ELECTROCHEMISTRY OF SEMICONDUCTORS AND ELECTRONICS

Processes and Devices

Edited by

John McHardy and Frank Ludwig

Hughes Aircraft Company
El Segundo, California

np NOYES PUBLICATIONS
Park Ridge, New Jersey, U.S.A.

Library of Congress Catalog Card Number: 91-46659
ISBN: 0-8155-1301-1
Printed in the United States

Published in the United States of America by
Noyes Publications
Mill Road, Park Ridge, New Jersey 07656

10 9 8 7 6 5 4 3 2 1

Library of Congress Cataloging-in-Publication Data

Electrochemistry of semiconductors and electronics : processes and devices / edited by John McHardy and Frank Ludwig.
p. cm.
Includes bibliographical references and index.
ISBN 0-8155-1301-1
1. Semiconductors--Design and construction. 2. Electrochemistry. I. Ludwig, Frank.
TK7871.85.E42 1992
621.381'52--dc20 91-46659
CIP

MATERIALS SCIENCE AND PROCESS TECHNOLOGY SERIES

Editors

Electronic Materials and Process Technology

DEPOSITION TECHNOLOGIES FOR FILMS AND COATINGS: by Rointan F. Bunshah et al

CHEMICAL VAPOR DEPOSITION FOR MICROELECTRONICS: by Arthur Sherman

SEMICONDUCTOR MATERIALS AND PROCESS TECHNOLOGY HANDBOOK: edited by Gary E. McGuire

HYBRID MICROCIRCUIT TECHNOLOGY HANDBOOK: by James J. Licari and Leonard R. Enlow

HANDBOOK OF THIN FILM DEPOSITION PROCESSES AND TECHNIQUES: edited by Klaus K. Schuegraf

IONIZED-CLUSTER BEAM DEPOSITION AND EPITAXY: by Toshinori Takagi

DIFFUSION PHENOMENA IN THIN FILMS AND MICROELECTRONIC MATERIALS: edited by Devendra Gupta and Paul S. Ho

HANDBOOK OF CONTAMINATION CONTROL IN MICROELECTRONICS: edited by Donald L. Tolliver

HANDBOOK OF ION BEAM PROCESSING TECHNOLOGY: edited by Jerome J. Cuomo, Stephen M. Rossnagel, and Harold R. Kaufman

CHARACTERIZATION OF SEMICONDUCTOR MATERIALS–Volume 1: edited by Gary E. McGuire

HANDBOOK OF PLASMA PROCESSING TECHNOLOGY: edited by Stephen M. Rossnagel, Jerome J. Cuomo, and William D. Westwood

HANDBOOK OF SEMICONDUCTOR SILICON TECHNOLOGY: edited by William C. O'Mara, Robert B. Herring, and Lee P. Hunt

HANDBOOK OF POLYMER COATINGS FOR ELECTRONICS: by James J. Licari and Laura A. Hughes

HANDBOOK OF SPUTTER DEPOSITION TECHNOLOGY: by Kiyotaka Wasa and Shigeru Hayakawa

HANDBOOK OF VLSI MICROLITHOGRAPHY: edited by William B. Glendinning and John N. Helbert

CHEMISTRY OF SUPERCONDUCTOR MATERIALS: edited by Terrell A. Vanderah

CHEMICAL VAPOR DEPOSITION OF TUNGSTEN AND TUNGSTEN SILICIDES: by John E.J. Schmitz

ELECTROCHEMISTRY OF SEMICONDUCTORS AND ELECTRONICS: edited by John McHardy and Frank Ludwig

HANDBOOK OF CHEMICAL VAPOR DEPOSITION: by Hugh O. Pierson

(continued)

Ceramic and Other Materials–Processing and Technology

SOL-GEL TECHNOLOGY FOR THIN FILMS, FIBERS, PREFORMS, ELECTRONICS AND SPECIALTY SHAPES: edited by Lisa C. Klein

FIBER REINFORCED CERAMIC COMPOSITES: by K.S. Mazdiyasni

ADVANCED CERAMIC PROCESSING AND TECHNOLOGY–Volume 1: edited by Jon G.P. Binner

FRICTION AND WEAR TRANSITIONS OF MATERIALS: by Peter J. Blau

SHOCK WAVES FOR INDUSTRIAL APPLICATIONS: edited by Lawrence E. Murr

SPECIAL MELTING AND PROCESSING TECHNOLOGIES: edited by G.K. Bhat

CORROSION OF GLASS, CERAMICS AND CERAMIC SUPERCONDUCTORS: edited by David E. Clark and Bruce K. Zoitos

HANDBOOK OF INDUSTRIAL REFRACTORIES TECHNOLOGY: by Stephen C. Carniglia and Gordon L. Barna

Related Titles

ADHESIVES TECHNOLOGY HANDBOOK: by Arthur H. Landrock

HANDBOOK OF THERMOSET PLASTICS: edited by Sidney H. Goodman

SURFACE PREPARATION TECHNIQUES FOR ADHESIVE BONDING: by Raymond F. Wegman

FORMULATING PLASTICS AND ELASTOMERS BY COMPUTER: by Ralph D. Hermansen

HANDBOOK OF ADHESIVE BONDED STRUCTURAL REPAIR: by Raymond F. Wegman and Thomas R. Tullos

CONTRIBUTORS

Giulio Di Giacomo
IBM
Hopewell Junction, NY

Robert C. DeMattei
Center for Materials Research
Stanford University
Stanford, CA

Robert S. Feigelson
Center for Materials Research
Stanford University
Stanford, CA

Ian D. Raistrick
Los Alamos National Laboratory
Los Alamos, NM

R. David Rauh
EIC Laboratories, Inc.
Norwood, MA

Keshra Sangwal
Institute of Chemistry
Pedagogical University of
Czestochowa
Czestochowa, Poland

Robert T. Talasek
Texas Instruments
Dallas, TX

Micha Tomkiewicz
Department of Physics
Brooklyn College
Brooklyn, NY

NOTICE

To the best of our knowledge the information in this publication is accurate; however, the Publisher does not assume any responsibility or liability for the accuracy or completeness of, or consequences arising from, such information. Mention of trade names or commercial products does not constitute endorsement or recommendation for use by the Publisher.

Final determination of the suitability of any information or product for use contemplated by any user, and the manner of that use, is the sole responsibility of the user. We recommend that anyone intending to rely on any recommendation of materials or procedures for use in electrochemistry involving semiconductors and/or electronics mentioned in this publication should satisfy himself as to such suitability, and that he can meet all applicable safety and health standards. We strongly recommend that users seek and adhere to the manufacturer's or supplier's current instructions for handling each material they use.

PREFACE

This book reflects the confluence of two trends. On the one hand, Electrochemistry is reemerging as a vital scientific discipline after many years of relative obscurity. Issues such as the space race, the energy crisis, and the environmental movement have prompted rapid expansion in electrochemical research and the subject is becoming an important foundation of modern technology. On the other hand, the relentless drive towards faster, more compact electronic devices continues to probe the limits of materials science, setting ever higher goals for semiconductor purity, crystal uniformity, and circuit density. The following chapters discuss possible electrochemical avenues towards these goals. The aim is to highlight opportunities in electronics technology to match current advances in areas such as energy conversion, batteries, and analytical chemistry.

In Chapter 1, R.C. De Mattei and R.S. Feigelson review electrochemical methods for the deposition and doping of semiconductors. Potential advantages of these methods over thermally driven processes include electrical control over the deposition rate, relatively low deposition temperatures and applicability to a wide range of materials. Despite these advantages, electrochemical methods have been overlooked as a route to electronic semiconductors. The incentive for research described in this chapter has come largely from photovoltaic applications.

The next three chapters deal with electrochemical aspects of semiconductor processing. In Chapter 2, K. Sangwal reviews the principles and applications of chemical etching. Although the technology

is well established, the electrochemical viewpoint of this article provides fresh insight for the development of improved processes.

In Chapter 3, R.T. Talasek reviews the anodic passivation of II-VI semiconductors such as the (Hg,Cd)Te alloys used in infrared imaging detectors. This is one area of electronics in which electrochemical methods have already become the industrial standard.

In Chapter 4, R.D. Rauh introduces the relatively new subject of photoelectrochemical processing. The injection of photon energy at an electrochemical interface adds an extra dimension to the processing capability, be it for selective etching, patterned electrodeposition, or the fabrication of optical elements. These concepts offer intriguing possibilities for the future of both electronic and opto-electronic technologies.

In Chapter 5, Micha Tomkiewicz reviews photoelectrochemical methods for characterizing the defect structure and doping levels of semiconductor wafers. Application of these techniques on a real-time basis should provide feedback which can be used to fine-tune the manufacturing process, assuring consistently high quality wafers.

The quest for ever more compact circuitry requires progressive reductions first in the width and spacing of conductor lines and second in the size of individual circuit elements. As conductors become finer and more closely spaced, the incidence of electrochemical migration phenomena become increasingly critical. In Chapter 6, G. DiGiacomo reviews the principles underlying these phenomena. Understanding gained from this review will provide a basis for controlling or avoiding migration-related failures in future circuit designs. The final chapter by I.D. Raistrick reviews the subject of electrochemical capacitors: devices which promise to reduce the size of capacitors and/or batteries utilized in electronic circuits.

August, 1991 John McHardy
El Segundo, California

CONTENTS

1

ELECTROCHEMICAL DEPOSITION OF SEMICONDUCTORS

Robert C. DeMattei
Robert S. Feigelson

1.0 INTRODUCTION

Prior to the invention of the transistor and the birth of the semiconductor industry, the field of electrochemistry was already very advanced with respect to both theoretical understanding and industrial applications. It is therefore surprising that electrochemical preparative techniques did not play a significant role in the development of semiconductor materials. The reason for this is unclear, but during the nearly forty years that have elapsed since then, there have only been a few scattered papers published in this field. When you compare this miniscule effort with the vast body of published papers on the research, development, and manufacturing of semiconductor materials by other methods, it is not surprising that electrochemical methods have not yet made a serious impact on this multibillion dollar industry.

Most semiconductor materials for opto-electronic applications must be in the form of single crystals with exceptional crystalline perfection and purity. Typically, large boules are sliced into wafers, and devices are prepared by either diffusing dopants into them and/or by depositing on them compounds of either similar composition (homoepitaxy) or different composition (heteroepitaxy). Some semiconductors in polycrystalline film or bulk form have also been found useful in a few applications, the most important being low cost solar cells. This latter application has stimulated much of the recent work on the electrolytic deposition of semiconductor materials.

Electrochemical preparative methods can be conveniently divided into two categories: 1) low temperature techniques (usually aqueous

solutions, but organic electrolytes are sometimes used), and 2) high temperature techniques (molten salt solutions). By far, the greater effort has gone into low temperature processes because these systems are simple to construct, operate and control, and because aqueous solution chemistry is much better understood then complex molten salts. The large metal plating industry (Cr, Au, Ag, Cu, etc.) is based on aqueous electrochemical techniques.

The choice of solvent or electrolyte depends to a large extent on the ability to put appropriate ions in solution. Low temperature solvents are not readily available for many refractory compounds and semiconductor materials of interest and, although aqueous techniques are preferable for the reasons stated above, they are often unsuitable. As a result, molten salt electrolysis has found utility for the synthesis and deposition of elemental materials such as Al, Si and a wide variety of binary and ternary compounds such as borides, carbides, silicides, phosphides, arsenides, and sulfides, and the semiconductors SiC, GaAs, and GaP and InP(1)(2)(3). Molten salt electrolysis has proven to be a commercially important means for refining aluminum from bauxite ore (the Hall process) and for alkali metal separation.

While small single crystals of many compounds have been produced electrolytically from molten salts as well as aqueous solutions, scaling up to large size has generally been difficult. The subject of using molten salt electrolysis for crystal growth was reviewed by Feigelson (3).

One of the unique features of electrodeposition is that it is an electrically driven process capable of precise control. This offers a potential advantage over most other processing techniques which are thermally driven. Other attractive advantages include: 1) growth temperatures are well below the melting point so that the point defect concentration is low, 2) the solvents have a fluxing action on the cathode surface dissolving oxide impurities, 3) purification occurs during electrodeposition because of differences in deposition potential between major and minor components in solution (however, doping with certain elements is possible and can be controlled through changes in concentration), 4) a wide range of compounds and elements can be electrodeposited, and 5) electrolysis is convenient for epitaxial deposition since growth occurs uniformly over the sample area.

The ability to produce thin uniform films on both simple and complex shapes has been one of the traditional strengths of electrochemical methods, and it is not surprising that the majority of the semiconductor electrodeposition studies have concentrated on thin film deposition.

Semiconductor materials can be divided into two broad categories: elements and compounds. The latter category may be further subdivided by reference to the column in the periodic table from which the constituent elements come, and whether the compound is a binary or higher order.

This article reviews the history and most recent results of electrodeposition of various semiconductors, including: 1) Si; 2) the III-V compounds, GaAs, GaP and InP; 3) the II-VI compounds, CdS and CdTe; 4) SiC; and 5) the important ternary compound $CuInSe_2$.

2.0 THEORY

The electrodeposition of semiconductor compounds, like any other chemical process, is governed by thermodynamic considerations. In the case of electrodeposition, the reactions are thermodynamically unfavorable; that is, the overall free energy change (ΔG) for the reaction is positive and the electrical energy supplies the needed energy to drive the reaction. Consider, the case of an ion M^{+m} being reduced to M:

Eq. (1) $$M^{+m} + me^- \longrightarrow M$$

The change in free energy is given by (4)(5):

Eq. (2) $$\Delta G = \Delta G^\circ + RT \ln(a_M / a_{M^{+m}})$$

where R is the gas constant, T is the absolute temperature and a_i is the activity of species i. Activity is used instead of concentration in Eq. 2 to account for the interaction of ions in solution, or for the difference in reactivity of an atom in a molecule vs. that of an atom in the elemental state where the activity would be 1. In the solution case, activity is related to the concentration by the activity coefficient,

Eq. (3) $$a = \gamma [M^{+m}]$$

A more complete discussion of activity and activity coefficients can be found in references 4 and 5. For the sake of practicality, concentrations will be used in the following discussion. Thus, Eq. 2 becomes:

Eq. (4) $$\Delta G = \Delta G^\circ + RT \ln(1 / [M^{+m}])$$

It can be shown that (5)

Eq. (5) $$\Delta G = - n F E$$

where n is the number of moles of electrons involved in the reaction, F is Faraday's constant and E is the potential. Equation 4 may now be written:

Eq. (6) $$E = E_o - \frac{RT}{nF} \ln \frac{1}{[M^{+m}]}$$

where E_o is the standard electrode potential for reaction (Eq. 1) referenced to the standard electrode with $[M^{+m}] = 1$ mole/liter. Tables of standard electrode potentials exist for aqueous solutions and some non-aqueous systems.

A single electrode reaction such as given in Eq. 1 can not stand alone since there must be a compensating reaction involving an oxidation process. The overall reaction can be represented by:

Eq. (7) $$b\,A^{+a} + a\,B^{-b} = b\,A + a\,B$$

and the electrode reactions by:

Eq. (8a) $$A^{+a} + a\,e^- \longrightarrow A \quad \text{(reduction at cathode)}$$

Eq. (8b) $$B^{-b} \longrightarrow B + b\,e^- \quad \text{(oxidation at anode)}$$

The cell potential is given by

Eq. (9) $$E = E_o^A + E_o^B - \frac{RT}{abF} \ln \left[\frac{1}{[A^{+a}]^b [B^{-b}]^a} \right]$$

The reactions described in Eqs. 7 thru 9 are typical of those involved in the deposition of an elemental semiconductor such as silicon or germanium. The situation is somewhat more complicated for the formation of a compound semiconductor such as GaAs or CdTe. In this case, two materials must be codeposited at the cathode, and one of the species, the non-metal (As or Te above), is normally considered an anion. This component of the semiconductor must be introduced into the solution in a form such that it can be reduced at the cathode. This is usually accomplished by using a starting compound that incorporates the desired non-metal as part of an oxygen-containing ionic species (AsO_4^{-3} or TeO_4^{-2} for example). In general terms, the reactions involved in this deposition would be:

Eq. (10a) $$M^{+m} + m\,e^- \longrightarrow M$$

Eq. (10b) $$N\,O_y^{-n} + (2y - n)\,e^- \longrightarrow N + y\,O^{-2}$$

Eq. (10c) $$O^{-2} \longrightarrow 0.5O_2 + 2e$$

yielding an overall reaction:

Eq. (10d) $$2M^{+m} + 2NO_y^{-n} + (m - n)O^{-2} \rightarrow 2MN + (y + (m - n)/2)\ O_2$$

The cell potential is then given by:

Eq. (11) $$E = E_o' - \frac{RT}{(2y + m - n)F} \ln \frac{1}{[M^{+m}]^2[NO_y^{-n}]^2[O^{-2}]^{(m-n)}}$$

where E_o' is the sum of the E_o's for reactions 10a,b,c. From a practical point of view, it is important to ensure that reactions 10a and 10b occur simultaneously. This will occur if the potentials for the two reactions are equal. The two cell reactions are:

Eq. (12a) $$2M^{+m} + mO^{-2} \rightarrow 2M + 0.5mO_2$$

Eq. (12b) $$2NO_y^{-n} \rightarrow 2N + (y - n/2)\ O^2 + nO^{-2}$$

with cell potentials given by:

Eq. (13a) $$E^M = E_o^M - \frac{RT}{2mF} \ln \frac{1}{[M^{+m}]^2\ [O^{-2}]^m}$$

and

Eq. (13b) $$E^N = E_o^N - \frac{RT}{2[2y - n]F} \ln \frac{(O^{-2})^n}{(NO_y^{-n})^2}$$

where E_o^M and E_o^N are the sum of the standard potential for reactions 10a plus 10c, and 10b plus 10c, respectively. Since the desired condition for codeposition is $E^M = E^N$, Eqs. 13a and 13b can be combined to yield an expression for determining the solution composition for codeposition:

Eq. (14)

$$E_o^N - E_o^M = \frac{RT}{2F}\left[\frac{1}{m} \ln\left[\frac{1}{[M^{-m}]^2\ [O^{-2}]^m}\right] - \frac{1}{(2y - n)} \ln\left[\frac{[O^{-2}]^n}{[NO_y^{-n}]^2}\right]\right]$$

Equation 14 is useful only if the E_o's are known for the various species in the solvent system being used. Often the investigator does not have this information. The solution to this problem is the use of voltammetry. In this technique, the voltage across an electrochemical cell is slowly increased and the current is monitored. Ideally, there is no current flow until the

deposition potential is exceeded, as shown in Fig. 1. In most practical cases, some extrapolation of both the baseline and rising portion of a current vs. voltage plot (I-V plot) is necessary to determine the deposition potential (Fig. 2). A series of I-V plots with differing solution concentrations will give the variation of deposition potential with concentration. Repeating this procedure for each element in the semiconductor will give the range of solution conditions under which codeposition of the elements is possible.

The foregoing discussion is a brief introduction to those parameters which influence the thermodynamic aspects of electrodeposition. Kortum and Bockris (6), and Bockris and Reddy (7) present a much more complete discussion of the nature of ions in solution and the processes occurring at electrified interfaces.

Thermodynamics is concerned with the equilibrium aspect of deposition. Once the potential between the electrodes is raised above the deposition potential, the system is in a non-equilibrium condition and kinetics must be considered. While it is possible to determine some aspects of the deposition process such as the electron transfer processes occurring at the electrodes and the rate-controlling step for deposition, from a practical point of view, it is more important to determine those conditions which will yield a smooth deposit and what the expected growth rate will be under those conditions.

In most cases, the rate of electrodeposition is limited by the onset of dendritic growth on the electrode. This will occur if some critical current density (i_c) is exceeded. Despic and Popov(8) developed an equation to determine this current density:

Eq. (15) $$i_c = i_o\left[\exp\frac{-\alpha_c F\eta}{RT} - \exp\frac{\alpha_a F\eta}{RT}\right] \leq i_{L,1}$$

where i_o is the exchange current density, α_c and α_a are the cathodic and anodic transfer coefficients, respectively, and η is the overpotential (the difference between the potential measured between an electrode and a reference electrode with and without current flowing) (7). The values of i_o, α_c and α_a can be determined (7). The value of $i_{L,1}$, the limiting current density to a flat plate, may be calculated from the expression (9):

Eq. (16) $$\eta = (RT/nF)\ln(i_{L,1}/i_o)$$

If the values are available in the literature or if an investigator wishes to determine them for his system, it is possible to calculate the critical current density for dendritic growth and thus carry out the deposition at its highest rate. The alternative is to accept the suggestion of Kroll (10) that for most systems $i_{L,1}$, which is less then or equal to i_c (Eq. 15), equals 40

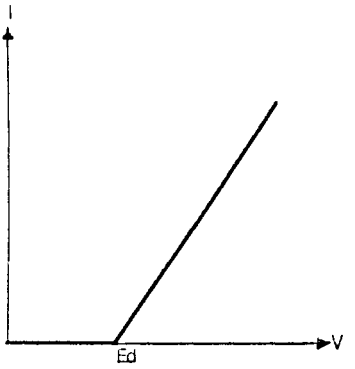

Figure 1. Theoretical current vs. voltage (I-V) plot showing deposition potential (E_d).

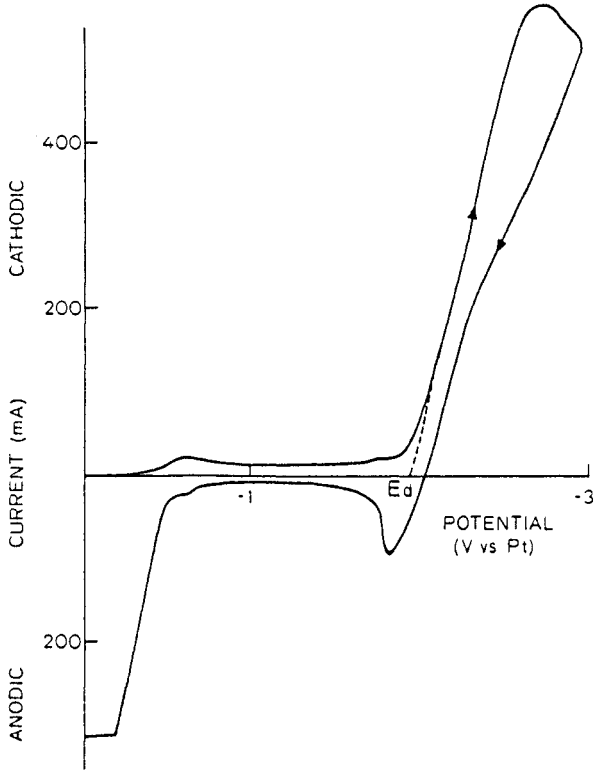

Figure 2. I-V (voltammogram) plot of 1 m/o K_2SiF_6 in Flinak at 750°C showing extrapolated deposition potential (E_d).

mA/cm^2.

In order to determine the rate of growth of the depositing layer, the amount of material deposited per unit of time must be determined. Faraday's law of electrolysis gives the weight of material deposited by a given amount of charge (q) as

Eq. (17) $$w = (M q \epsilon) / (n F)$$

where M is the molecular weight of the material and ϵ is the deposition efficiency. The volume is given by:

Eq. (18) $$v = (M \epsilon q) / (\rho n F) = Ay$$

where ρ is the density of the material, A is the area of deposition and y is the deposit thickness. The rate of growth (dy/dt) is given by:

Eq. (19) $$\frac{dy}{dt} = \frac{M \epsilon}{\rho n F A} \frac{dq}{dt} = \frac{M \epsilon}{\rho n F} \frac{I}{A} = \frac{M \epsilon}{\rho n F} i$$

The term $M/\rho nF$ is a constant for any given deposition process and *i* is in amps/cm^2. As an example, consider the deposition of cadmium sulfide (CdS) from cadmium ions (Cd^{+2}) and sulfate ions (SO_4^{-2}). From Eq. 11, the number of electrons transferred in Eq. 19 is 8, the density is 4.82 gm/cm^3 and the molecular weight is 144.46 gm, which yields a value for the growth rate constant of 3.88×10^{-5} cm^3/(amp-sec). Using a value of 40 mA/cm^2 (0.040 amp/cm^2) as a practical current density, the maximum growth rate for CdS (with $\epsilon = 1$) is 5.59×10^{-3} cm/hr or 55.9 μm/hr. In practice, the actual value is somewhat less since ϵ is usually less than 1.

3.0 ELEMENTAL SEMICONDUCTORS

The most important elemental semiconductor material for industrial applications is silicon. Because of its commercial importance, the electrodeposition of silicon has been studied to a greater extent than all of the other semiconductor materials combined.

3.1 Silicon

Introduction. The first attempts to produce silicon electrolytically date from the mid 1800's. St. Claire De Ville (11) claimed that he produced silicon as the result of the electrolysis of impure molten $NaAlCl_4$. Since the

material did not oxidize at white heat, the claim was probably not true. Monnier(12) reports that De Ville did deposit silicon as platinum silicide on a platinum electrode from a melt of NaF/KF containing SiO_2 at a later date. In 1854, Gore (13) claimed to have produced silicon by the electrolysis of an aqueous solution of potassium monosilicate. This was never confirmed and silicon has never been deposited from any aqueous system. Ullik (14), in 1865, was probably the first to deposit elemental silicon when he electrolized a solution containing K_2SiF_6 in KF. Iron- and aluminum-silicon alloys were produced from solutions containing SiO_2 and iron or aluminum oxide in NaCl + $NaAlF_4$ by Minet (15). Warren (16) produced a silicon amalgam from SiF_4 in alcohol using a mercury cathode. All of this work before 1900 established that both SiO_2 and fluorosilicates could be used as source materials for silicon electrodeposition. This work also showed that alkali halides as well as organic solvents were suitable solvent materials for the process.

More systematic studies of silicon electrodeposition began in the 1930's with Dodero's (17)(18) investigation of the electrolysis of molten silicates at temperatures of 800 to 1250°C. The very high potentials used in these studies would be expected to liberate not only silicon but also alkali and alkaline earth metals. There is no conclusive proof in Dodero's work that silicon was the primary cathode product or the result of a reduction of the silicon containing compounds by alkali or alkaline earth metals that had been produced by electrolysis. His best result was 72% silicon produced from a melt composition of 5 SiO_2 - 1Na_2O - 0.2NaF electrolyzed at 1150°C.

The melts used for the electrodeposition of silicon can be broadly classified by the silicon-containing species used: silicates and fluorosilicates. Each will be discussed separately.

Silicate-Based Melts. Silicate or SiO_2 melts have been studied by several investigators in an effort to develop a commercial process for electrowinning silicon. The molten solutions most often studied contained SiO_2 in cryolite.

Cryolite, Na_3AlF_6, was a logical choice as a solvent for use with SiO_2 because of its ready availability and its successful use in the Hall process for electrowinning aluminum. The SiO_2/Na_3AlF_6 system was studied both in a laboratory environment and in pilot plant trials, first by Monnier, et al. (12)(19)(20), whose interest was in producing pure silicon, and later by Grjotheim, et al. (21-24), whose primary interest was in Al-Si alloys. This high temperature solution chemistry is not simple, leading to mixtures of aluminum silicates and sodium aluminosilicates (12).

Monnier and his co-workers were able to obtain 99.9 to 99.99% pure silicon from SiO_2 - cryolite solutions in a two step process. The first step was the deposition of silicon to form a molten copper-silicon alloy at the

cathode. The anode in this cell was graphite and the measured deposition potentials at zero current could be calculated from thermodynamic data. The second step involved using the cooper-silicon alloy as an anode and electrorefining the silicon.

Monnier (12)(19) was also responsible for the only reported pilot plant study of the electrodeposition of silicon from SiO_2-cryolite. The study began in 1957 and the pilot plant was built and operated between 1960 and 1966. Two versions were built. One used auxiliary carbon heating electrodes and operated at a maximum deposition current of 300 amp. The second furnace operated at currents of up to 3000 amp and was self heated as in the Hall cell for aluminum. Figure 3 is a diagram of Monnier's cell. The current densities ran as high as 800 mA/cm and the deposits were in the form of 1 - 3 mm crystals. After removal from the solidified melt and zone refining, the silicon was reported to be of semiconductor quality.

The limitation of this process is that silicon is deposited as a solid which limits the rate of deposition as discussed earlier in this chapter and also by Huggins and Elwell (26). Monnier's approach of depositing into a liquid alloy cathode is one solution to this problem, but it does require a second step to remove the alloying metal. The Hall process for aluminum gets around this problem by depositing the metal above its melting point. A second benefit arises from the high currents used; after initial start up, the electrolysis currents used provide enough Joule heating to keep the system molten. A process similar to the Hall process was developed for silicon by DeMattei, Elwell and Feigelson (27)(28) in 1981.

The main problem in using the Hall process for silicon electrodeposition is that silicon melts at a much higher temperature than aluminum (1412°C compared to 660°C). Cryolite can not be used at this temperature due to volatization problems, so a binary or ternary melt containing SiO_2 had to be developed that would be stable above this temperature. Johnson (29) indicated that calcium and magnesium based silicate melts looked favorable, while other alkaline earth and alkali metal silicates were less desirable.

DeMattei, Elwell and Feigelson (27) were the first to successfully demonstrate a process for the electrodeposition of Si above its melting temperature. The actual melt composition they preferred was the eutectic composition in the BaO-SiO_2 system (53% - 47% by weight). About 15% barium fluoride was added to reduce viscosity. These melts were electrolyzed at about 1450°C in the furnace shown in Fig. 4 using graphite crucibles and graphite electrodes. Potentials in the range of 1 to 8 volts were used together with currents of 0.1 to 2.0 amps for an electrode area of about 2 cm^2. The electrodeposited silicon formed into spherical droplets (Fig. 5) and, because of their lower density, floated to the top of the melt. Faradaic efficiency ranged from 20% to a high of 40% which is less than desired for

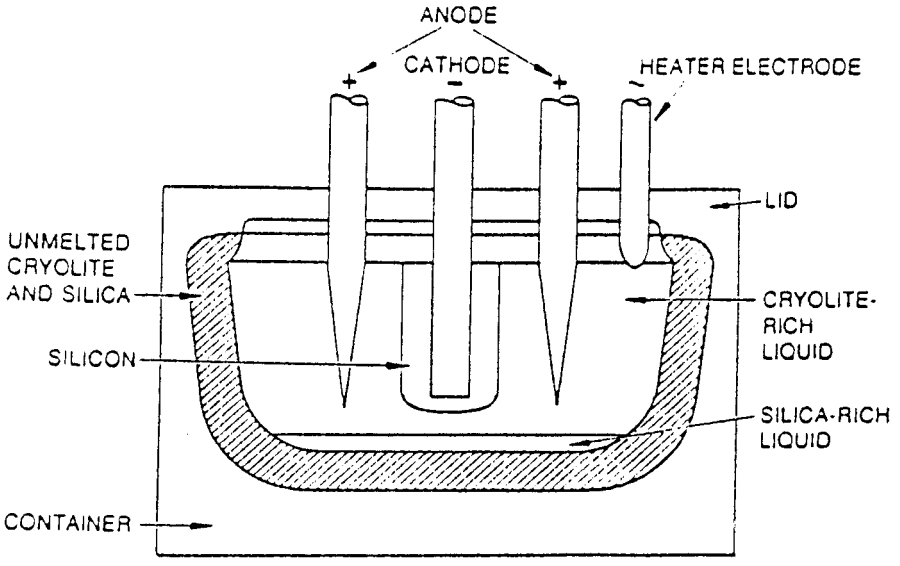

Figure 3. Cell for silicon production in which the electrolyte is contained in an unmelted solid of the same composition (12)(19).

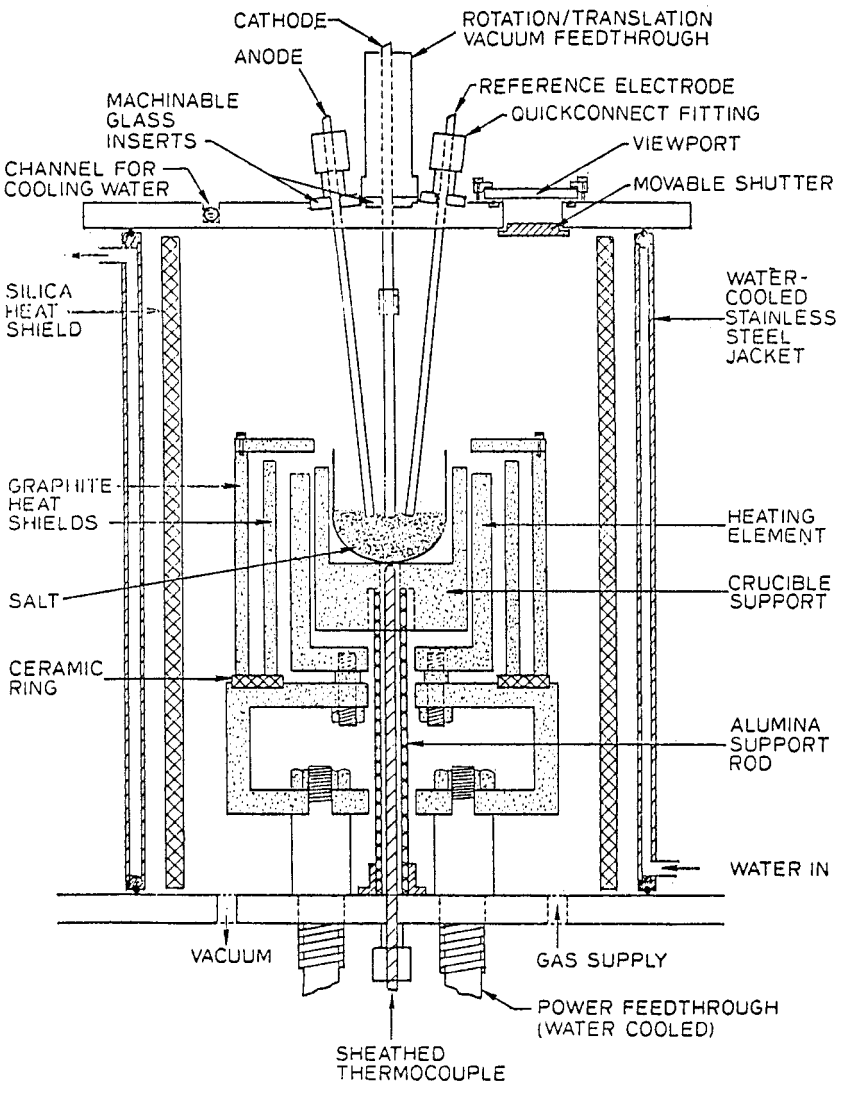

Figure 4. Furnace used for electrodeposition of silicon and silicon carbide.

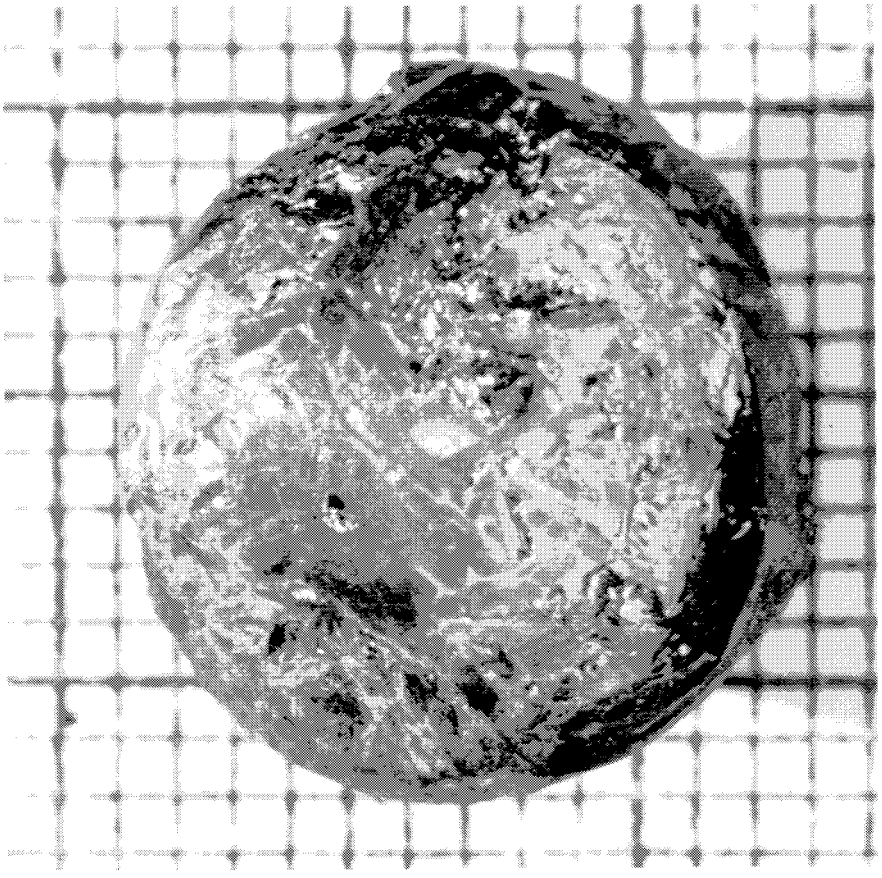

Figure 5. Silicon lump (1.6 gm) produced by electrodeposition above the melting point (27).

commercial applications. The silicon produced by this method had a typical purity of 99.98% with the main impurities being titanium (60 ppm), and aluminum and iron (20 ppm). This is close to the purity required to produce 10% efficient solar cell with one step of purification (30). The heat generated by Joule heating in a commercial sized plant was judged sufficient to maintain the temperature at 1450°C or above. Olson and Kibbler (31) used tin in place of the aluminum or copper used in Monnier's (12) earlier work. This eliminated the shallow and deep-level traps which these elements can induce in silicon. Their silicon was deposited from a melt containing SiO_2 dissolved in Na_3AlF_6/LiF. Solidification of the Sn-Si solution produced 1 - 10 mm crystals of silicon which contained 10 ppm of transition metals and exhibited a resistivity of 0.05 - 0.1 Ω cm. The major drawback of this approach (like Monnier's case) was the need to separate the silicon from the solidified tin.

Fluorosilicate-Based Melts. Compounds containing fluorosilicate ions (SiF_6^{-2}) are a relatively inexpensive by-product of the fertilizer industry. They may also be produced by the reaction of SiO_2 with alkali and alkaline-earth fluorides at 1000 - 1100°C (32). The process for deposition of Si from fluorosilicates is analogous to that used for titanium (33)(34)(35) and suffers from the same limitations which makes it attractive only for special applications which may include films for solar cells, surface coatings, and (in the form of powder or sponge) as a replacement for metallurgical grade silicon.

A study of silicon film deposition using K_2SiF_6 was begun at Stanford University in the Center for Materials Research in the early 1970's. Of the several fluoride systems studied, only LiF-KF and LiF-KF-NaF melts proved suitable. In 1977, Cohen (36) reported that epitaxial Si layers could be deposited from a LiF-KF eutectic containing K_2SiF_6. He also produced continuous films using a dissolving silicon anode.

Similar melts were studied for the electrowinning of Si for use in further processes. Initial work was done using graphite anodes and either LiF-KF-NaF or LiF-KF eutectics at 750°C. In initial experiments by Rao, et al. (37)(38), silver was used as a cathode. Later experiments (39)(40) used inexpensive graphite substrates. The concentration of K_2SiF_6 was maintained between 4 - 20 m/o to prevent the formation of powdery deposits (38). Typical deposition conditions were: 1) constant current experiments at 10 to 25 mA-cm^{-1}, and 2) constant potential experiments at -0.74 ± 0.04 volts versus Pt. Columnar growths (250 μm grain size) of 3 - 4 mm thickness were produced in 2 to 4 days. The electrodeposited silicon was typically 99.99% pure although the best samples had impurity levels less than 10 ppm. Current efficiencies could be as high as 80%.

Olson and Carleton (41) extended the use of these melt systems by using a copper-silicon anode to simulate electrorefining metallurgical

grade silicon. In the same vein, Sharma and Mukherjee (42) investigated the semi-continuous production of 99.99% pure silicon powder from 97.5% pure metallugical grade silicon. Bouteillon, et al. (43)(44), demonstrated that improvements in both morphology and purity (to less than 1 ppm impurity) could be obtained using pulsed electrolysis as currently applied in copper refining.

Organic Electrolytes. One of the major drawbacks of any molten salt process for electrodeposition is the energy needed to maintain the system in its molten state. The energy that is added either by external heaters or by Joule heating must add to the cost of the final product.

Austin (45) was the first to report the electrodeposition of amorphous silicon from organic solvents in the temperature range of 20 to 100°C. Amorphous Si (a-Si) has been used commercially for a number of years in low cost solar cell applications (particularly calculators and watches). The solvents of choice were aprotic materials such as propylene carbonate or tetrahydrofuran using silane or a silicon halide as a source of silicon. The deposits which contained impurities of less than 10 ppm showed a resistivity of about 20 Ω cm.

Attempts by Bucker and Amick (46) to reproduce Austin's work produced films which were unstable in air. Heat treatment at about 350°C was recommended to remove hydrogen from the films before they were exposed to air. Their recommended solvents were tetrahydrofuran/benzene, tetrahydrofuran/toluene, dioxolane/benzene and dioxolane/toluene, with silicon tetrachloride or trichlorosilane as solutes. The films contained both chlorine and chromium in trace amounts.

Kroger and co-workers (47)(48) did a series of detailed studies on the deposition of amorphous silicon including the influence of dopants. Lee and Kroger (47) investigated the deposition of fluorinated a-Si which should have higher stability than hydrogen-containing films. Since fluorine would normally be deposited at the anode, they used solutions of SiF_4 in ethyl alcohol, dimethyl sulfoxide and acetonitrile. Potassium fluoride was added to produce K_2SiF_6, which contains a cathodic fluorine-containing ion, and HF was added to increase conductivity. Deposition onto either nickel or stainless steel cathodic substrates was carried out in a Teflon vessel under an argon atmosphere using a platinum anode. The film resistivity was about 10^{12} Ω cm. Phosphorus doping could change the film from p- to n- type. The lowest resistivity observed was 10^{11} Ω cm.

Rama Mohan and Kroger (48) investigated the deposition of a-Si using tetraethyl orthosilicate or silicic acid in ethylene glycol or formamide-ethylene glycol containing HF. Undoped fluorine containing films were p-type. Doping with phosphorus from triethyl phosphate reduced the resistivity to $\sim 10^5$ Ω cm.

A more complete discussion of silicon electrodeposition can be found in Elwell and Rao (49).

Next Page

Previous Page

4.0 COMPOUND SEMICONDUCTORS

Compound semiconductors can be chosen to match their optoelectronic properties to a particular application. This is particularly true of ternary and higher order alloys and compounds in which the stoichiometry as well as dopants can be used to vary the semiconductor properties. These compounds are classed by the chemical groups to which their constituent elements belong. Thus there are II-VI, III-V and IV-IV type semiconductors. In the following discussion, ternary and higher order compounds will be classed with the group of compounds which contain the same non-metallic element.

4.1 II-VI Compounds

Aqueous Solvents. The interest in the electrodeposition of II-VI semiconductors arose from the use of these compounds in solar cells and photoelectrochemical energy conversion and storage. What appear to be the initial two articles in this area were published almost simultaneously in 1971. Hodes, et al. (50), reported the growth of a 1 cm^2 polycrystalline layer of CdSe on titanium. The cadmium and selenium were codeposited from a solution of $CdSO_4$ and SeO_2. Using 4.5 coulombs per electrode-side, about 7.5 mmol of CdSe was deposited. No concentrations, voltages, currents or current densities were reported. Two months later, Miller and Heller (51) produced layers of CdS and Bi_2S_3 by the anodization of cadmium and bismuth in polysulfide solutions. CdS was produced using a 1F Na_2S solution and Bi_2S_3 using 1F Na_2S - 0.05F S. Again no voltages, currents or current densities were reported.

The mechanism for the formation of sulfide films on cadmium was studied by Peter (52). The anodization was performed on polished 99.999 (5N) polycrystalline cadmium rods in a solution of 0.1 M Na_2S and 1.0 M $NaHCO_3$. A reference electrode consisted of a pool of mercury in contact with red mercuric sulfide. The potential of this electrode was estimated to be -0.74 volts on the hydrogen scale. A voltammogram (current versus potential referenced to the reference electrode) showed three features (Fig. 6).

A peak beginning at -0.5 volts corresponded to the formation of the first monolayer of the sulfide. The plateau region and the rise following it were investigated by a series of electrochemical experiments and comparison to models which will not be detailed here. The results showed that in the plateau region the film grew to a thickness of about 5 nm by high field ion migration. The donor concentration in this region was as high as $10^{25}\ m^{-3}$. Above approximately 1.0 volt, the film grew to approximately 500 nm by a diffusion controlled process. This portion of the film was

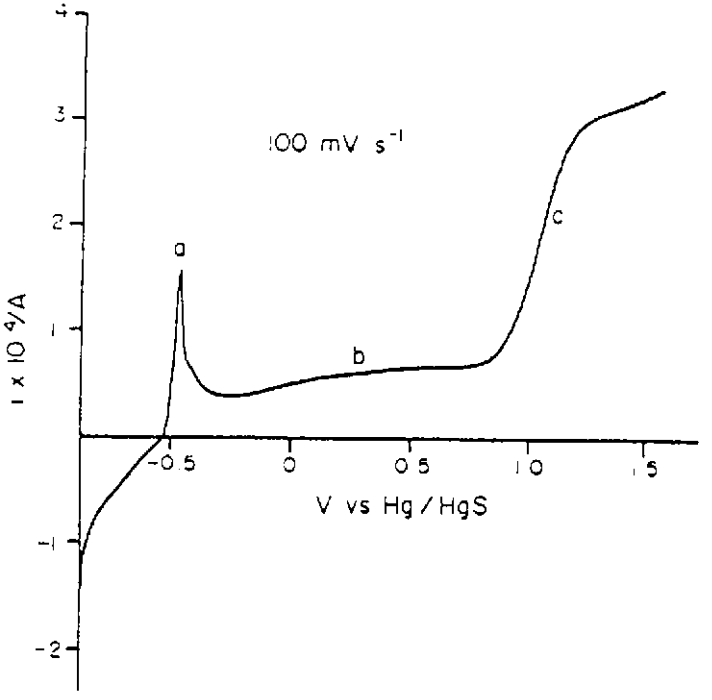

Figure 6. Linear sweep voltammogram. Polycrystalline cadmium electrode (area 0.125 cm^2) in 1 M $NaHCO_3$ + 0.1 M Na_2S. Sweep rate 100 mVs^{-1}. a) monolayer region, b) plateau region, c) transpassive region (52).

porous or polycrystalline. The process ended when the layer began to crack.

Panicker, et al. (53), investigated the cathodic codeposition of cadmium and tellurium to form CdTe layers. This paper analyzed the deposition reactions in light of the existence range of CdTe and the equilibrium potentials developed in this range. Under all conditions cadmium is the potential-determining species and the deposition potential is given by:

Eq. (20) $$V_{dep} = -0.403 + 0.295 \log a_{Cd^{2+}} - \Delta V$$

at the CdTe/Cd phase boundary and by:

Eq. (21) $$V_{dep} = 0.143 + 0.295 \log a_{Cd^{2+}} - \Delta V$$

at the CdTe/Te phase boundary. ΔV is the overpotential and is given by

Eq. (22) $$\Delta V = \eta + iR$$

where η is the discharge overpotential, i the current density and R the resistance per square centimeter of electrode between the cathode contact and the saturated calomel electrode (SCE) used to measure the cathode voltage. Depositions were done from aqueous solutions of cadmium sulfate (1 mole/liter) at a pH of 2.5 to 3. In some cases the Cd solution was purified by pre-electrolysis. Tellurium oxide was added to the cadmium solution. Concentrations of 10^{-5} to 10^{-3} moles/liter were used for unsaturated solutions and excess TeO_2 was used for saturated solutions. In the unsaturated solutions, two anodes were used, one was Te (to maintain the Te concentration) and the other an inert material. The ratio of current density (i_{Te}/i_{inert}) was 2. After a number of experiments, Panicker and his co-workers were able to establish that the films deposited from $CdSO_4$/Te solutions having a rest potential (see ref. 53) between 0.2 volts and 0.6 volts vs. SCE were CdTe. When these films were deposited at room temperature, they were amorphous. Between 35 and 90°C, the films were semicrystalline with a grain size of 500 to 1000 angstroms, and annealing at 350°C in argon increased the grain size to > 5000 angstroms. The deposited films were n-type when $-E_{rest} > 0.3$ volts and p-type when $-E_{rest} < 0.3$ volts. Films could also be doped with In (donor) or Cu (acceptor) and were n- or p-type respectively for all deposition conditions.

Similar studies were done for cadmium sulfide films by Power, et al. (54). The films were cathodically deposited according to the reaction:

$$Cd^{2+} + [S] + 2e^- = CdS$$

The source of [S] was thiosulfate ($S_2O_3^{2-}$). A voltammogram of a 0.1 M

thiosulfate/0.002 M cadmium sulfate solution (pH 6.7) on a rotating platinum cathode demonstrated that the reaction producing CdS did not proceed to any appreciable extent (Fig. 7). The dominant reactions were the deposition and stripping of cadmium. Lowering the pH to 2.8 by addition of dilute sulfuric acid caused the decomposition of the thiosulfate to give colloidal sulfur and altered the voltammogram (Fig. 8). The cathodic (deposition) peak is increased (probably due to hydrogen deposition) and the anodic peak is diminished and shifted to a more positive potential. The authors attributed this anodic peak to the stripping of excess cadmium from the CdS film. Reduction of the excess cadmium ion in solution eliminated this peak. Repeated cycles under these conditions gave a deep yellow, uniform, translucent film. These films were shown to be photoactive in sulfide, thiosulfate, sulfite and sulfate solutions. The shape of the I-V curves of the cathodically deposited films under illumination in 0.1 M sodium sulfide solutions is different in both shape and efficiency from anodically deposited films. The donor density of the cathodic film was shown to be considerably higher by capacitance measurements. Microprobe analysis of the cathodically deposited films showed roughly equal amounts of Cd and S with no detectable contaminants.

CdTe film electrodeposition and photochemical behavior studies were continued by Takahashi, et al. (55). These films were deposited on either nickel or titanium electrodes from solutions of cadmium sulfate, tellurium oxide and sulfuric acid. The I-V plot of a solution which was 1 M, 1 mM and 0.05 M in the respective reactants showed a current plateau between -0.30 and -0.65 volts vs. a Ag/AgCl standard electrode. The I-V curves were strongly affected by the TeO_2 concentration and a linear relation was found between the limiting current and the concentration of tellurium oxide (Fig. 9). The concentration of the cadmium ion had little effect on the I-V curves. The thickness of the deposited films could be correlated to the total charge passed through the cell (Fig. 10). X-ray diffraction data confirmed that the films were CdTe (56). At the more positive deposition potentials, a peak for Te was observed in the x-ray patterns which became stronger as the potentials became more positive. The authors developed an exact expression for the total current based on the reactions:

Eq. (23) $$HTeO_2^+ + 3H^+ + 4e^- = Te + 2H_2O$$

Eq. (24) $$Cd^{++} + 2e^- + Te = CdTe$$

Under the conditions of the experiment, the exact expression reduced to:

Eq. (25) $$i = -6DFC_{HTeO_2^+} / d$$

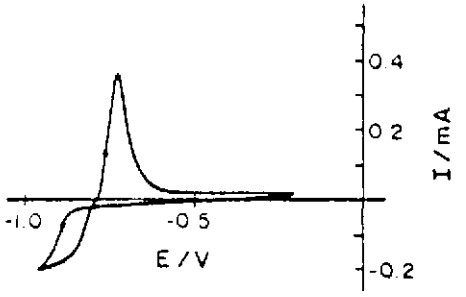

Figure 7. I-V plot of a solution containing 0.1 M $Na_2S_2O_3$ and $2x10^{-3}$ M $CdSO_4$, pH 6.7, at a Pt rotating disc electrode. Rotation speed 500 rpm. Potential ramps speed 10 mVs^{-1}. Temperature 25.0°C (54).

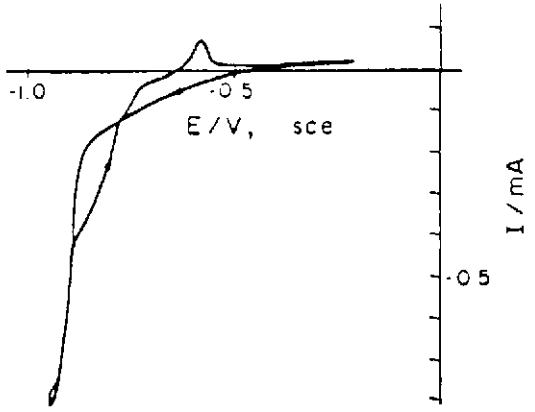

Figure 8. I-V plot of a solution containing 0.1 M $Na_2S_2O_3$ and $2x10^{-3}$ M $CdSO_4$, pH 2.8, at a Pt rotating disc electrode. Rotation speed 500 rpm. Potential ramp speed 10 mVs^{-1}. Temperature 25.0°C (54).

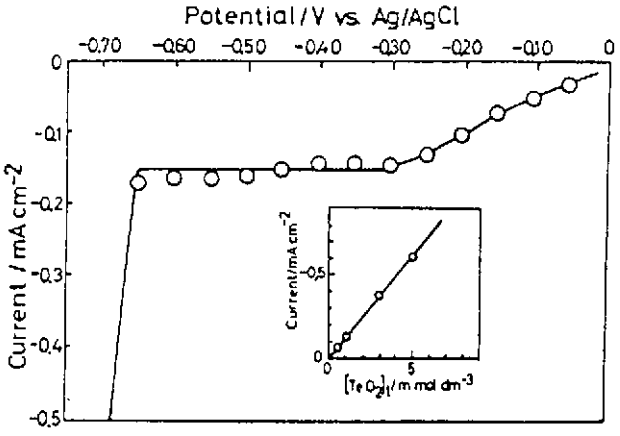

Figure 9. I-V plot of Ni electrode in a sulfuric acid solution (pH 1.4) containing 1 M $CdSO_4$ and 1 mM TeO_2. Insert: TeO_2 concentration dependence of the current at -0.35 volts (vs. Ag/AgCl) (55).

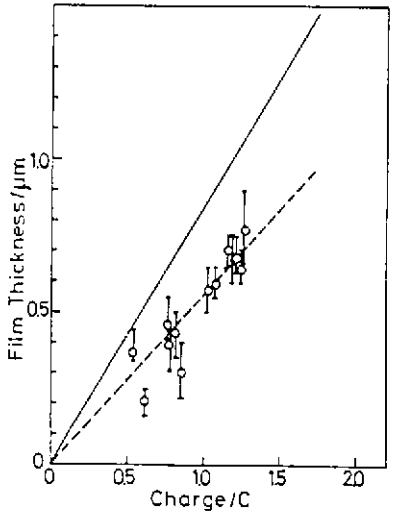

Figure 10. The thickness of the electrochemically deposited films of Ni as a function of charge passed. The deposition was carried out at -0.35 volts (vs. Ag/AgCl) in a sulfuric acid solution (pH 1.4) containing 1 M $CdSO_4$ and 1 mM TeO_2. Solid line shows the theoretical value calculated by assuming six-electron process (55).

where D is the diffusion coefficient, F Faraday's constant, $c_{HTeO_2^+}$, the concentration of $HTeO_2^+$ and d the diffusion boundary thickness. Using a density of 6.2 gm/cc for CdTe and the fact that the deposition is a six electron process as indicated by the above equation, the authors calculated a deposition efficiency of 75%.

The authors also studied both the diffuse reflection spectrum and the photochemical behavior of the deposited films. The efficiency of cathodic photocurrent production was dependent on the deposition potential. The efficiency peaked at a deposition potential of -0.40 volts. The authors attributed this to the presence of excess Te at potentials more positive than -0.40 volts and to the n-type character of the CdTe at potentials more negative than -0.40 volts. The effects of heat treatment and etching were also studied. Heat treatment improved the photocurrent due to the increased grain size which eliminated grain boundaries. Etching had the effect of removing the surface layer of Te and improving photocurrents.

One of the potential advantages of electrochemical growth techniques is in controlling impurities. Pre-electrolysis of the solution can reduce or eliminate impurities. The proper selection of deposition conditions and potential can prevent the codeposition of impurities, and complexing agents can be added to render the impurities inactive. An example of the latter approach is seen in the work of Pandey and Rooz on CdSe films (57). The authors grew CdSe films from solutions of 0.3 M cadmium sulfate and 0.009 M selenium oxide. The cadmium sulfate contained Cu (100 ppm), Fe (46 ppm), Pb (62 ppm), Zn (39 ppm), Al (95 ppm), Ca (320 ppm) and alkaline earths (0.1%). Ethylene diamine tetraacetic acid (EDTA) (probably the disodium salt) was used as the complexing agent. A typical film deposited at 0.67 volts (referenced to a saturated calomel electrode) showed impurities of Zn, Pb, Fe and Cu when depth profiled by Auger analysis (Fig. 11). The typical concentration was an order of magnitude less than that of either the Cd or Se. Additions of EDTA removed these impurities due to the formation of stable complexes. However the addition of EDTA alters the Cd:Se ratio from 1:1.6 to 1:3. The photoresponse of the CdSe films formed from EDTA containing solutions was improved. Careful heat treatment and etching further improved the film performance. A CdSe film deposited from the basic starting solutions showed an open circuit voltage (OCV) of 200 mV and a short circuit current (SCC) of 1.7 mA/cm^2, but the efficiency (eff) and fill factor (ff) were very low. The addition of EDTA raised the values to: OCV 400 mV, SCC 4.0 mA/cm^2, eff 0.9% and ff 0.28. The best annealed and etched film had values of OCV 500 mV, SCC 10.0 mA/cm^2, eff 3.6% and ff 0.38. These compared favorably with the best films produced by co-evaporation of high purity Cd and Se (58).

It has also proved possible to deposit CdTe films without the use of

(a)

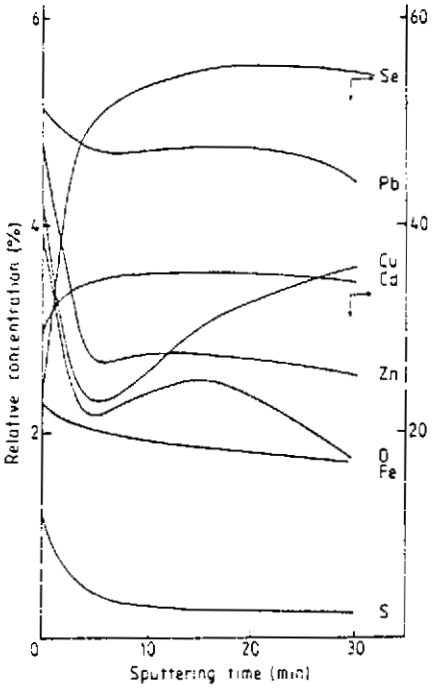

(b)

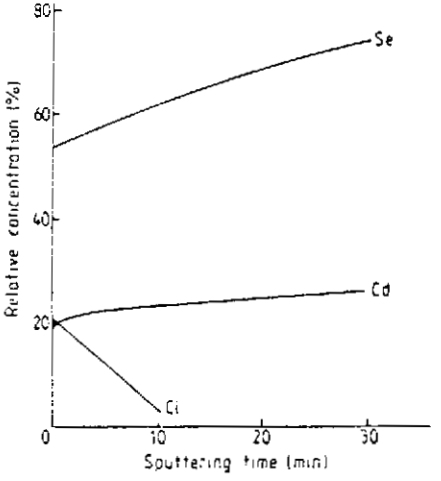

Figure 11. a) Auger depth profile of a typical CdSe sample deposited in the absence of EDTA at 0.67 volts (57). b) Auger depth profile of a typical CdSe sample deposited at 0.67 volts in the presence of 1.5×10^{-2} mol l^{-1} EDTA (57).

an external potential source. This method, electroless deposition, has been studied by Bhattacharya and co-workers (59). The solutions used were basically the same as had been used for conventional electrodeposition; 0.01 M cadmium acetate and 0.01 M tellurium oxide with the pH adjusted to 2 with 10% sulfuric acid. Either titanium or Nesatron™ glass (PPG Industries) were used as substrates. The necessary deposition potential was generated by short circuiting the substrate to an easily oxidizable redox component. Aluminum, for example, undergoing the reaction

Eq. (26) $Al = Al^{3+} + 3e^-$

has an electrode potential of 1.66 volts. Films were easily grown on substrates shorted to both aluminum and cadmium foils. Optical absorption measurements gave a band gap of 1.4 eV. EDAX measurements showed that the films, as deposited, had a Cd:Te ratio of 25:60. Annealing the films for 30 min. at 590°C changed the ratio to 55:45. X-ray data provided more evidence for compositional changes on annealing. Films, as deposited, contained CdTe in both the hexagonal and cubic forms as well as hexagonal Te. After annealing, only the hexagonal form of CdTe remained; there was no free Te. The films exhibited photoelectrochemical behavior.

Non Aqueous Solvents. Several II-VI compounds have also been electrodeposited from non-aqueous solvents. The first report was by Baranski and Fawcett (60) in 1980. Their approach was to deposit cationic species electrochemically from a solution containing elemental chalcogenide, dimethylsulfoxide (DMSO), dimethylformamide (DMF) and ethylene glycol (EG). A typical CdS deposition utilized a solution of 6 gm/l of sulfur and 10 gm/l of cadmium chloride. This was electrolyzed at 110°C with a current density of $\leq$ 2.5 mA/cm^2. The quality of the CdS deposit was independent of both the sulfur and cadmium chloride concentration used and was not affected by the addition of 10% water. The deposit composition was solution temperature dependent, however, becoming highly non-stoichiometric below 90°C. X-ray diffraction data showed that the crystallites in the film were all oriented with their [111] planes parallel to the electrode surface. The resistivity of these films was about 10^6 Ω cm which could be lowered by addition of sodium iodide to the solution.

The sulfides of lead, bismuth, nickel, cobalt and thallium were also produced by changing the salt in solution. CdTe was obtained from a DMF solution saturated with tellurium containing 10 gm/l cadmium chloride and 10 gm/l potassium iodide.

The photochemical properties of the films were determined in a cell using 1 M sodium sulfide and 1 M sodium hydroxide as the electrolyte. The sulfides of cadmium and bismuth were n-type while that of thallium was p-

type. Nickel and cobalt sulfides were metallic conductors and showed catalytic properties for electrode processes involving sulfur compounds.

A second paper by Baranski and co-workers (61) extended the previous work (60) on CdS. Again a DMSO solution was used. The reactant concentrations were 0.055 M cadmium chloride and 0.19 M sulfur. Cadmium/cadmium chloride was used as a reference electrode. The films were grown on platinum substrates. Measurements of the deposition potential versus time at constant current densities showed a sharp rise characteristic of the formation of a double layer (Fig. 12). This was followed by a nucleation step which lasted 100 to 200 sec. depending on the current density. The curves then became linear until the film "broke down" at about 5 volts. This "breakdown" was due to a cracking of the film which the authors attribute to a secondary piezoelectric effect. The cracking was eliminated by reducing the current density throughout the deposition.

X-ray diffraction analysis confirmed the results of the previous paper and showed only reflections from the <111> planes. The spacing was measured at 3.34 angstroms in good agreement with the theoretical value of 3.36 angstroms. Rutherford backscattering showed that the S:Cd ratio was 0.9 ± 0.1:1 and that the ratio was uniform throughout the depth of the film. There was some evidence of chloride impurities.

Plots of the average thickness of the film versus time at constant current density were compared to the thickness expected from Faraday's law and the deposition efficiency was calculated to be 81%. A similar plot of depth versus current density at constant time indicated a more rapid deposition at higher current densities which was attributed to increased deposition of cadmium.

Addition of thallium ions to the deposition solution changed the conductivity of the films as evidenced by a lowering of the necessary deposition potential as the thallium concentration was increased. It was thus possible to tailor the electrical characteristics of the film by the selective addition of various ions.

The deposition of CdTe from propylene carbonate (PC) was studied by Darkowski and Cocivera (62). This work was unusual in that unlike previous non-aqueous deposition which used elemental chalcogenides dissolved in a non-aqueous medium, this investigation used an organometallic source - tri(n-butyl)phosphine telluride [$(C_3H_8)_3PTe$] (phosphine telluride). The solution concentrations employed were 2 - 10 mM cadmium perchlorate or cadmium trifluoromethane sulfonate, 120 mM lithium perchlorate or sodium trifluoromethane sulfonate, and 7 - 26 mM phosphine telluride. A silver/silver chloride reference electrode was used throughout. Cyclic voltammograms were made for solutions of the cadmium alone, the phosphine telluride alone and for the combined

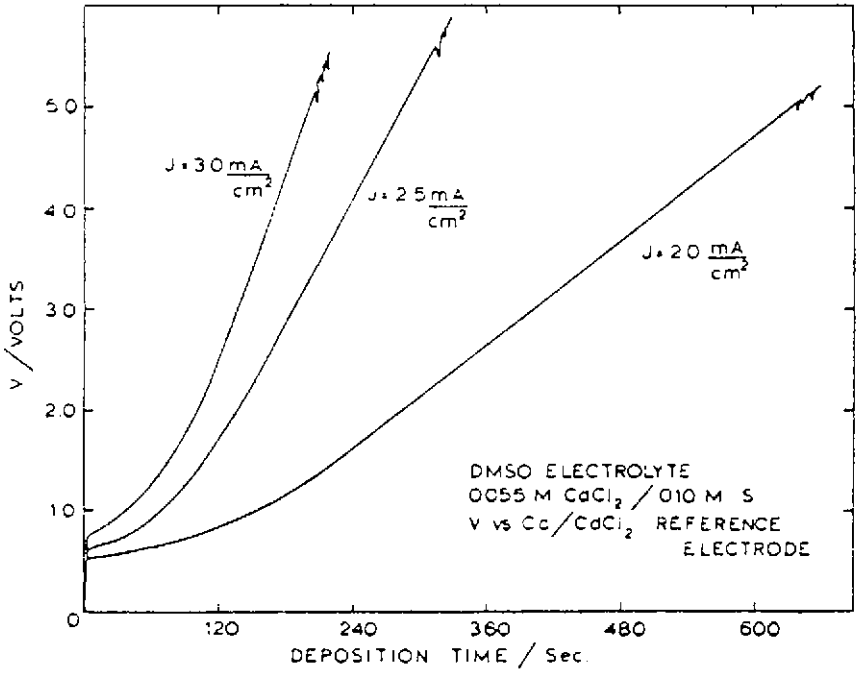

Figure 12. Plots of voltage against deposition time during the deposition of CdS films at several current densities as indicated (61).

solution (Fig. 13). The deposition potential of the cadmium was considerably more cathodic than that of the phosphine telluride. The phosphine telluride peak was shifted slightly in the anodic direction in the combined solution and the currents were larger. This seemed to indicate a weak interaction between the cadmium ions and the phosphine telluride.

CdTe films were deposited at potentials between -650 and -1600 mV from solutions containing 3 mM Cd(II) and 12 and 18 mM phosphine telluride. The stoichiometry of these films was determined by dissolving the films and using polarography (see ref. 62 for details). The Te:Cd ratio in these films reached 1 (0.95 ± 0.05) at -1200 mV and remained at that value up to -1600 mV. The ratio and deposition current depended somewhat on the concentrations of the reactants.

The current density decreased with time during constant potential deposition. The rate of decrease was dependent on the concentration of the Cd(II) relative to the phosphine telluride. The rate of decrease was shown to be slower at higher relative concentrations indicative of a complicated deposition mechanism, perhaps involving Cd-tri(n-butyl) phosphine telluride complexes.

The photoelectrochemical activity of these films was measured in the same cell and solutions in which they were grown. They produced a cathodic photocurrent indicating that the films were p-type. Scanning above the shut-off potential produced negligible photoanodic current assuring that the photocurrent was not due to increased photoconductivity (Fig. 14). The best films were produced from a solution of 3 mM Cd(II), 12 mM phosphine telluride, and 100 mM lithium perchlorate electrolyzed at -1200 mV versus Ag/AgCl.

Fatas, et al. (63), have also done a study on the electrodeposition of CdS from nonaqueous solutions, in this case on stainless steel and tin oxide. They studied two solvents: DMSO and PC. The solutions were 0.19 M sulfur and 0.055 M cadmium chloride in DMSO, and PC saturated with sulfur, cadmium chloride and potassium chloride. The depositions were carried out at a constant current at 120°C. All voltages were referenced to a cadmium/cadmium chloride electrode.

The plots of deposition potential versus time for the two different solutions were markedly different (Fig. 15). The PC solution maintained essentially a constant potential after the initial transient while the potential for the DMSO rose continuously. The initial transient potential was also higher in DMSO which was attributable to the stronger solvation action of this solvent.

Film thickness versus current density was also measured (Fig. 16). At the same current density, the PC films were thicker than those deposited from DMSO. Part of the explanation for this behavior was the possibility of cracks forming in the films deposited from DMSO due to the higher

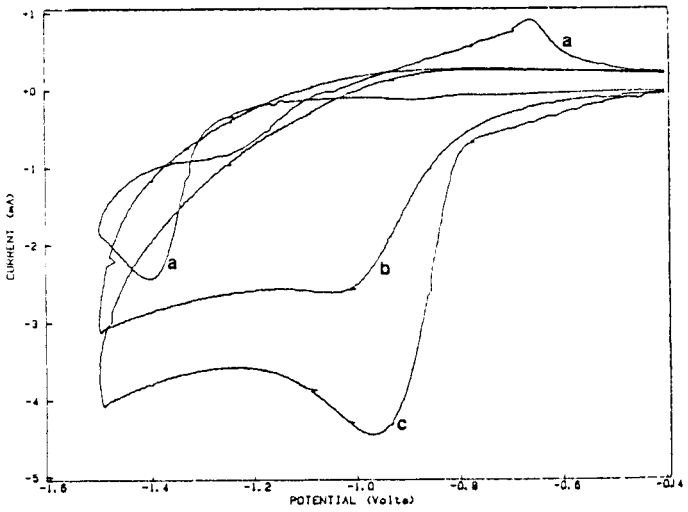

Figure 13. I-V plots in propylene carbonate under N_2 at 100°C and a scan rate of a) 100 mV/s for 0.003 M Cd(II) and 0.10 M $LiClO_4$, b) 0.01 8 M tri-n-butylphosphine telluride and 0.10 M $LiClO_4$, and c) 0.0003 M Cd(II), 0.018 M tri-n-butylphosphine telluride, and 0.10 M $LiClO_4$ (62).

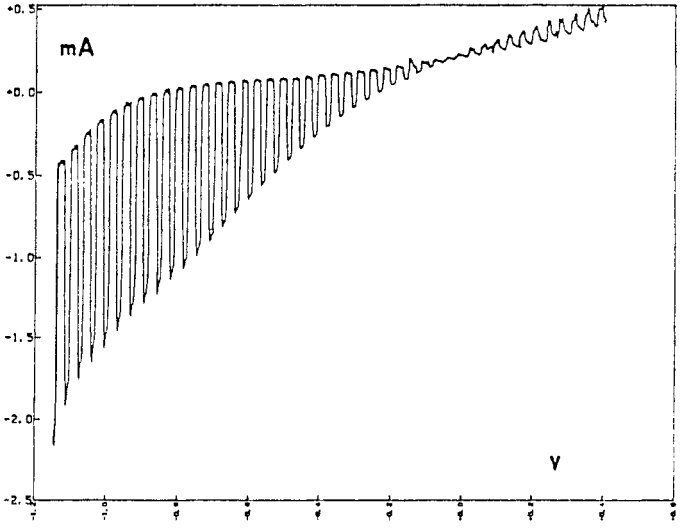

Figure 14. Photoresponse at 100°C of electrodeposited CdTe film in PEC containing 0.003 M Cd(II), 0.018 M tri-n-butylphosphine telluride, and 0.10 M $LiClO_4$ in propylene carbonate under nitrogen with no stirring (62).

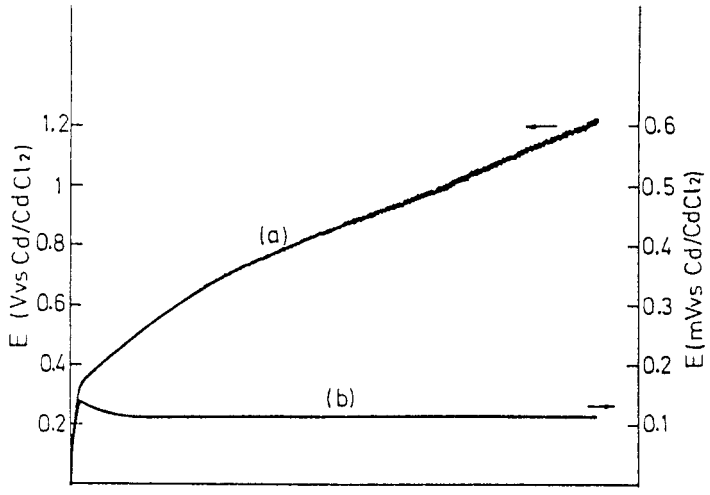

Figure 15. Plots of voltage against deposition time during the deposition of CdS films, a) in DMSO, b) in PC (63).

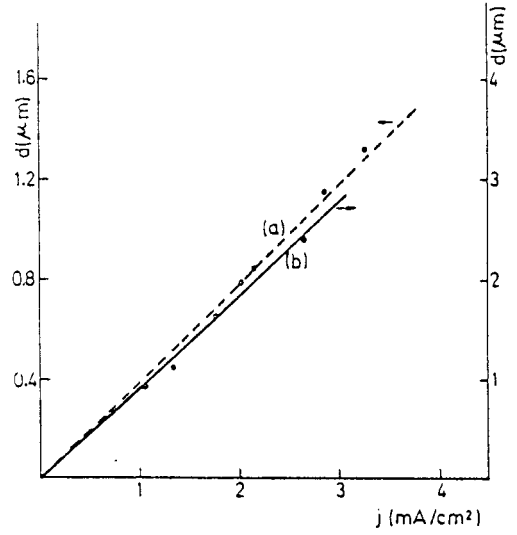

Figure 16. Plots of thickness of CdS film deposited on stainless steel against current density. Deposition time, solution composition and temperature were constant during the deposition, a) in DMSO, b) in PC (63).

potential required. This seemed to occur at thicknesses greater than 0.8 μm. It may also have involved the decomposition of the solvent. Cracking did not appear when PC was the solvent. By comparing the thicknesses to that expected from Faraday's law, the efficiencies were found to be 90% for PC and 70% for DMSO (additional evidence for the decomposition of the DMSO).

The photoelectrochemical properties of these films were measured using an electrolyte that consisted of 0.1 M sodium hydroxide, 0.1 M sodium sulfide and 0.01 M sulfur. The films showed typical photochemical behavior (Fig. 17).

X-ray diffraction data for films deposited between 100 and 140°C exhibited hexagonal symmetry and were c oriented. At temperatures above 140°C, the films gave patterns very similar to powder patterns (Fig. 18). The grain size and the influence of deposition conditions on that size were obtained from the x-ray data.

The films, as grown, had resistivities between 2.4×10^5 and 9.0×10^5 Ω cm. Heat treatment reduced this value to 500 Ω cm.

Molten Salts. ZnSe has been grown electrochemically on silicon and germanium substrates by Yamamoto and Yamaguchi (64). Two melts were studied: 1) 0.02 zinc chloride, 0.02 selenium chloride, 0.12 potassium chloride and 0.18 lithium chloride (in mole ratio), and 2) 0.003 zinc oxide, 0.003 sodium selenite, 0.4 potassium chloride and 0.5 lithium chloride. In both cases, the potassium and lithium chlorides were the solvent. The melts were operated under dry argon between 430 and 550°C.

Melt 1 not only produced ZnSe, but also zinc oxide. Moreover the results were not reproducible and the melt attacked germanium. Melt 2 produced high quality, reproducible films of ZnSe. These films showed good orientation to the substrate (<111> Ge) and exhibited red photoluminescence at room temperature.

The optimum current density for growth lies between 0.5 and 3 mA/cm^2. Below 0.5 mA/cm^2 no deposit was obtained, while above 3.0 mA/cm^2 the deposit was polycrystalline. The ideal range of growth temperatures was 450 to 500°C.

Ternary Alloys and Compounds. Baranski and co-workers (65), in an extension of their previous work, grew solid solution films of cadmium sulfur selenide (CdS_xSe_y). They used a solution of 0.055 M cadmium chloride and 0.19 M sulfur with varying amounts of selenium in DMSO. Good quality films were electrodeposited and the color varied from yellow-gold for CdS to dark reddish-purple for films deposited from saturated solution of Se (approximately 0.01M Se). The morphology of these alloy films was crystalline, but highly cracked at low Se concentrations and smooth and glass-like at high Se concentrations. These structural

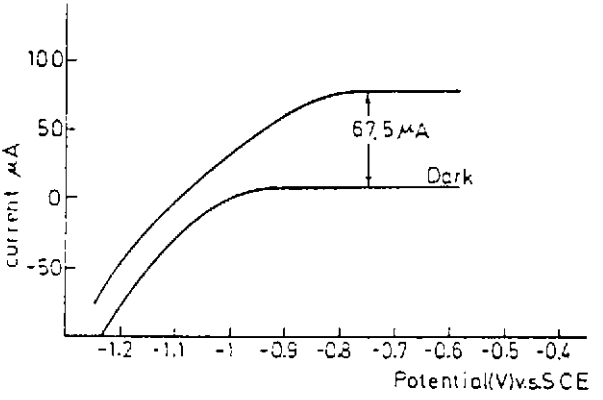

Figure 17. Current-voltage properties for n-type CdS electrode exposed to the 0.1 M NaOH, 0.1 M $Na_2S \cdot 9H_2O$ and 0.01 M S electrolyte. The sweep rate is 0.1 Vs^{-1} (63).

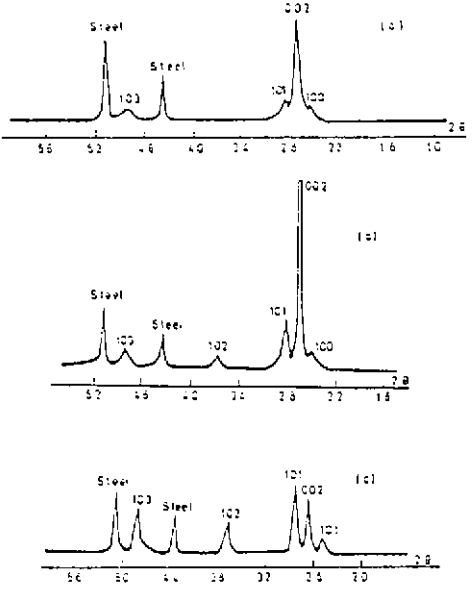

Figure 18. X-ray diffraction spectra for CdS films obtained at different temperatures during deposition, a) 70°C, b) 140°C, and c) 160°C (63).

changes were also reflected in the x-ray patterns.

Plots of the S/Cd ratio versus the Se/Cd ratio in the films showed a trend of decreasing S/Cd for increasing Se/Cd. This indicates that the deposition mechanisms for the two chalcogens are similar. A plot of Se/Cd versus Se concentration in the film revealed that it is possible to vary the amount of selenium in the film over a wide range. The ratio reached a maximum value of 0.75.

The photoelectrochemical response of these films was measured. As was to be expected, it and the band gap varied with film composition.

Some ternary compounds are also technologically important. The I-III-VI_2 chalcopyrite compounds are included here because the anion is from group VI and the average cation valence is 2. $CuInSe_2$ is an important candidate material for highly efficient thin film solar cells.

The electrodeposition of copper indium selenide and telluride was discussed by Bhattacharya and Rajeshwar (66). The deposition solutions were made in a multistep process. A 0.5 M solution (A) of indium chloride was prepared. The copper solution (B) was prepared from cuprous chloride dissolved in 30 ml of triethanolamine, 40 ml of 30% ammonia and 150 ml of water. The copper concentration was 0.5 M. Solutions A and B were mixed in equal amounts, diluted 10 times and adjusted to pH 1 with HCl. This solution (C) was aged for 24 hrs. The actual deposition bath was made from 20 ml of either 0.1 M selenium oxide or 0.1 M tellurium oxide and 60 ml of solution C. The triethanolamine was added to the copper solution as a complexing agent to shift the deposition potential. Depositions were carried out at -1.0 volt versus a saturated calomel electrode. The initial current density was 12 mA/cm^2.

Before deposition, the behavior of the copper-indium and chalcogen solutions were investigated separately. The I-V plot of the copper-indium solution showed both deposition and stripping peaks indicating a reversible behavior (Fig. 19). The addition of the triethanolamine decreased the separation of deposition potential between copper and indium to 0.37 volts instead of 0.68 volts. The I-V plots of the chalcogen oxide solutions demonstrated irreversible behavior (Fig. 20).

X-ray diffraction patterns of the films showed peaks characteristic of the chalcopyrite copper indium selenide or copper indium telluride compounds. Auger spectra and depth profiles showed the expected signal plus some carbon and surface oxidation. The stoichiometry varied with depth.

A heterojunction of copper indium selenide on n-type cadmium sulfide indicated that the films, as deposited, were p-type. These films yielded an OCV of 100 mV and SCC of 2 mA/cm^2. The main problem with these films was poor grain morphology.

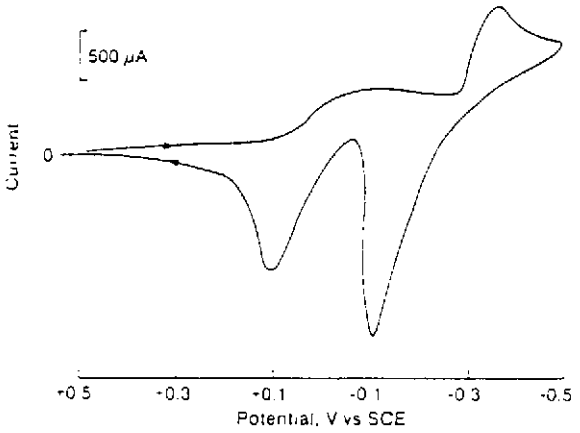

Figure 19. I-V plot recorded using a Pt micro-electrode (potential scan rate, 0.10 Vs^{-1}) for a solution of $CuCl_2$ and $InCl_3$ ($5x10^{-2}$ M each) in 0.1 M HCl (66).

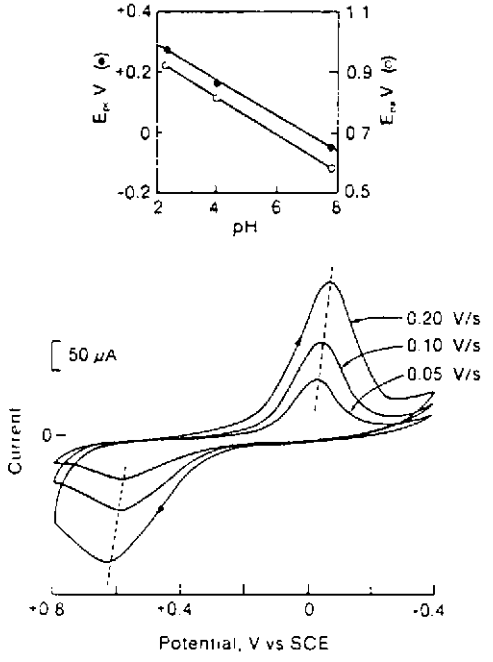

Figure 20. I-V plot on a Pt micro-electrode (parameter shown is the potential scan rate) for a $5x10^{-3}$ M solution of SeO_2 in H_2SO_4 (pH 7.8). Inset: dependence on pH of CV peak potentials for reduction and oxidation, E_{pc} and E_{pa} respectively (66).

There is a review article by Hodes and Cahen (67) which outlines numerous approaches for depositing copper indium sulfide and selenide. It also outlines a technique whereby the copper and indium can be codeposited and converted to the chalcogenide by annealing in hydrogen sulfide or selenide.

4.2 III-V Compounds

Gallium Phosphide. Cuomo and Gambino (68), in 1968, were the first to electrochemically synthesize a III-V compound (GaP). Gallium phosphate is an important electroluminescent material. By molten salt electrolysis, they prepared up to 100 mm thick epitaxial layers of GaP on <111>, <100> and <110> silicon substrates (cathodes) at current densities of up to 50 mA/cm^2. A fused salt bath contained (in molar ratio) 2.0 $NaPO_3$, 0.5 NaF and 0.1225 - 0.25 Ga_2O_3. It was held at 800°C during electrodeposition. They were able to dope their layers both p- or n- type during growth, using small concentrations of ZnO and Na_2SeO_4 respectively. An electroluminescent p-n junction was fabricated using electrochemical techniques.

A schematic diagram of Cuomo and Gambino's furnace is given in Fig. 21. The quartz chamber was heated by a resistance furnace. The graphite crucible, in addition to containing the melt, acted as the anode. Two types of cathodes were used; 1/4 inch diameter graphite rods (spectrographic grade) immersed in the melt to a depth of 1 inch were used for synthesis experiments, while two oriented silicon single crystal wafers mounted back to back on graphite rods were used for epitaxial growth. Both constant current and constant voltage experiments were studied. They used reagent grade chemicals except for the Ga_2O_3, which was 99.999% pure. The gallium phosphide layers were readily removed from the substrate by dissolving away the silicon substrate in HF:HNO_3. The GaP was coated with apiezon wax during the etching process. The silicon wafers were placed back-to-back to prevent GaP depositing on both surfaces of a single wafer and preventing Si removal.

The liquidus temperature of the melt composition (750°C) set the lower limit for the bath and deposition temperature while extensive volatization at 1000°C fixed the upper limit. Voltages below 0.6 volts did not produce solid products, while voltages of around 0.9 produced the best results. The growth rates were typically 10 - 20 mm/hr initially, but these decreased due to the relatively high resistivity of the GaP formed. Doped layers with lower resistivities could be grown to thicker dimensions. Typical deposits consisted of an epitaxial layer covered with a dendritic polycrystalline overgrowth. The GaP films usually cracked along cleavage planes. This problem was minimized by carefully cooling the layer after

growth. Deposits were found to contain the following impurities (in atomic percent); Si (0.0001), Mg (0.0001), Al (0.05), Te (0.01), and Cu (0.001). Cuomo and Gambino (68) also showed that alkali halide salts could also be used as solvents for GaP electrodeposition, but the results were not as good.

DeMattei, et al. (69), in a limited study in 1978, studied the conditions necessary for the stable growth of GaP epitaxial layers on Si and GaP substrates. They identified the variables critical to controlling the morphology and uniformity of electrodeposited GaP layers. They used the same fused salt composition and range of deposition temperatures (750 - 900°C) as Cuomo and Gambino. The electrochemical cell reactions for GaP at the cathode were probably:

Eq. (27) $8e^- + Ga^{+3} + 4PO_3^- \rightarrow GaP + 3PO_4^{-3}$, or

Eq. (28) $8e^- + Ga^{+3} + PO_3^- \rightarrow GaP + 3O^{-2}$

and at the anode:

Eq. (29) $2O^{-2} \rightarrow O_2 + 4e^-$, or

Eq. (30) $2PO_4^{-3} \rightarrow 2PO_3^- + O_2 + 4e^-$

A schematic of the apparatus used by DeMattei, et al. (69), is shown in Fig. 22. As in Cuomo and Gambino's experiments, they used their graphite crucible as the anode. Three different cathode materials were studied: 1) Graphite, 2) P-doped, n-type (100) Si (0.3 Ω-cm) wafers polished on one side, and 3) S-doped, n-type (111) as-cut wafers of GaP (0.05Ω-cm). The (100) Si orientation has a close lattice match to GaP (a_{Si} = 5.431, a_{GaP} = 5.449). The minimum deposition potential for Si substrates was about 0.5 volts, somewhat lower than observed by Cuomo and Gambino (68), but the deposits grown at 40 mA/cm^2 (Fig. 23) had surface craters due to excess P forming gas bubbles on the substrate surface. Dendrites grew beneath the bubbles due to restricted solute transport in these regions. These craters also appeared on graphite and GaP substrates under certain conditions. Excess P evolution was also seen by Cuomo and Gambino at low potentials and most of their experiments were carried out at cell potentials of about 1 volt. More uniform, epitaxial crystalline layers were produced at lower current densities (20 mA/cm^2). Current density is related to growth rate (G) and there is a maximum allowable value of G above which the quality of single crystal films deteriorate for all epitaxial growth methods used. The morphology of the crystallites in the electrodeposited layers were comparable to that produced by early

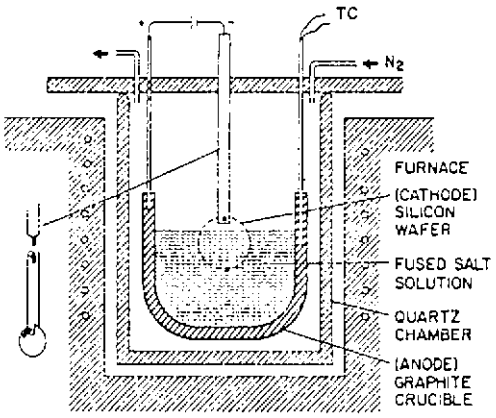

Figure 21. Schematic of the apparatus for the preparation of GaP by fused salt electrolysis (68).

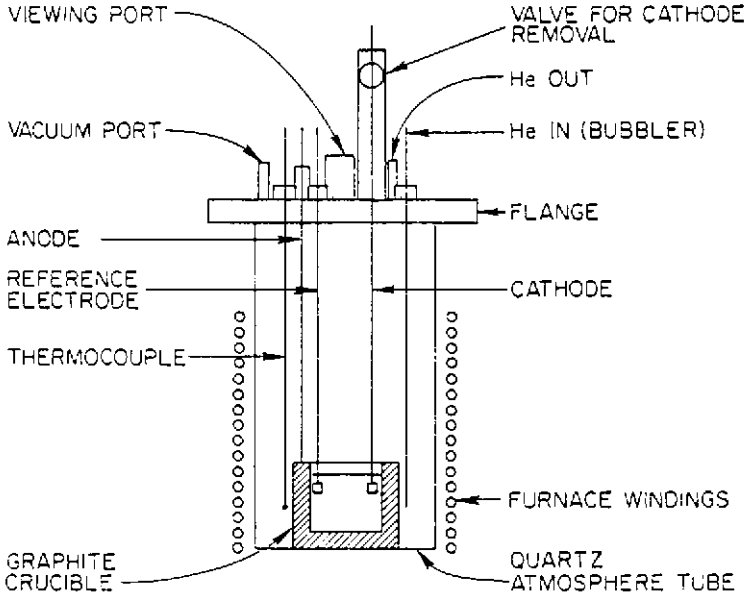

Figure 22. Diagram for apparatus used for growth of GaP layers (69).

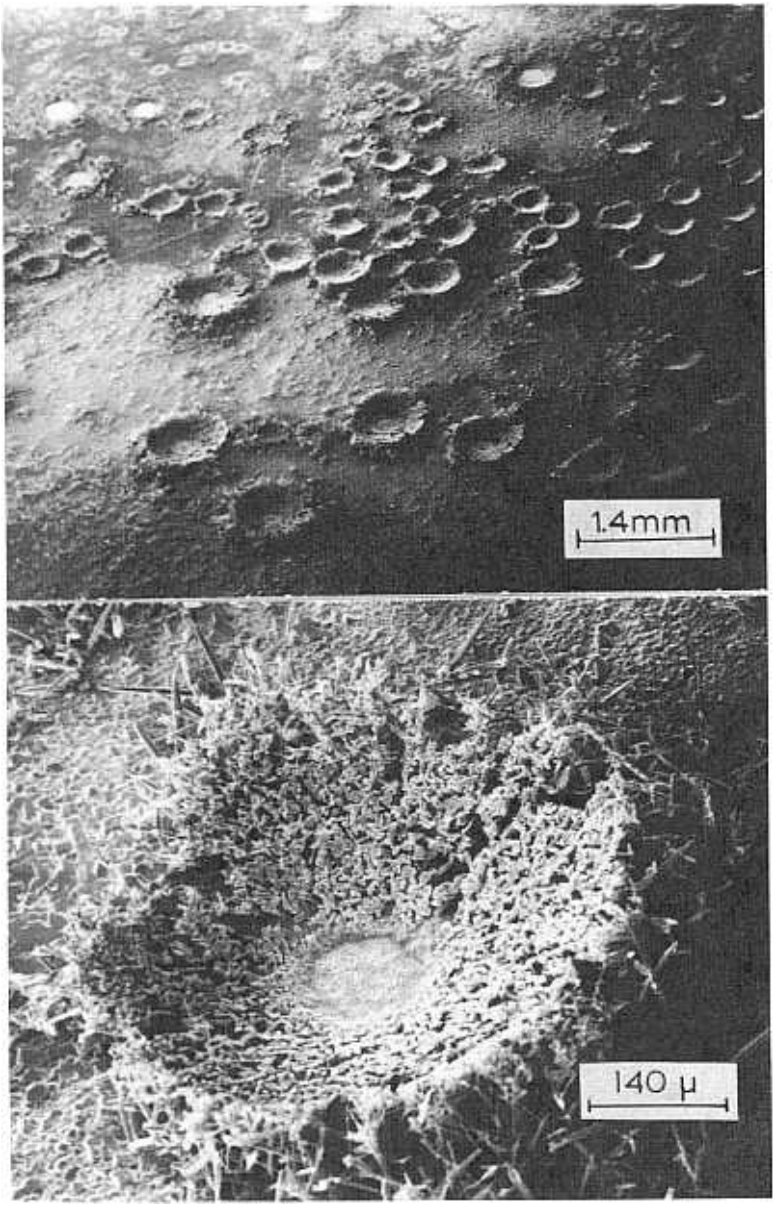

Figure 23. High current density deposit of GaP on silicon done early in investigation. Shows layer with dendritic over-growth around "craters" (40 mA/cm^2) (69).

MOCVD deposition techniques (70).

In order to gain a better understanding of the deposition process and to improve control of the epitaxial growth process for GaP on Si, DeMattei, et al. (69), did a series of nucleation experiments at a constant cell potential of 0.6 volts (slightly above the minimum deposition potential). While analysis did not reveal a consistent pattern, SiO_2 was found together with the deposited GaP layer. The SiO_2 may have formed because the electrodeposition potential was not applied until 5 minutes after the substrate was dipped into the melt (part of the substrate cleaning process). This conjecture was confirmed by a later experiment in which it was found that an applied potential was not necessary for the formation of GaP and SiO_2 on a Si substrate. The results suggest that the silicon substrates can react with the melt by the following reaction:

Eq. (31) $$8Si + 2Ga_2O_3 + 4PO_3^- \rightarrow 4GaP + 8SiO_2 + 2O^{-2}$$

This reactivity of silicon with the melt and the poor thermal expansion mismatch between Si and GaP, which was probably responsible for the cracking observed by Cuomo and Gambino (68), led DeMattei, et al. (69), to study the homoepitaxy of GaP on GaP substrates. The minimum deposition potentials for GaP on (111) GaP at 800°C and at 900°C are shown in Table 1, along with data for the electrodeposition of GaP on Si and graphite substrates at 900°C.

Table 1

Minimum Deposition Potentials for GaP on Various Cathodic Materials

Cathode Material	800°C	900°C
Graphite	-	0.68 volts
Si (100)	-	0.55 volts
GaP (111)	1.16 volts	0.86 volts

All deposition experiments were carried out at potentials 0.1 volts greater than the minimum depositon voltages. Since substrate surfaces were etched somewhat at 900°C, most depositions were carried out at 800°C. Current densities over 10 mA/cm^2 gave layers with craters, as seen in Fig. 23. At 48 mA/cm^2, large dendritic craters on thin epitaxial layers were formed. In Fig. 24, a plot of current (I) versus overpotential is given. DeMattei, et al. (69), related the first linear region to the growth rate being controlled either by volume diffusion of solute ions or by interface mechanisms, and the second linear region at higher current densities to possible interface attachment mechanisms. The limit of this linear region (η = 1.4 volts) corresponds to the maximum current density for stable growth.

Both the preliminary work of Cuomo and Gambino (68), and DeMattei, et al. (69), have shown that electrodeposition of GaP is possible. More carefully controlled systematic experiments should lead to much improved epitaxial deposits. It is not likely, however, considering the major advances of vapor deposition techniques, that a strong need for this technology will be forthcoming.

Indium Phosphide. Indium phosphide, an important material for high frequency electronic devices, is also of some interest for CdS/InP heterojunction solar cell applications. The only reported work on the electrodeposition of InP was by Elwell, et al. (71), in 1981. They explored a wide range of solute/solvent systems and developed, for the first time, the conditions necessary for the electrodeposition in InP on [0001] CdS and [111] and [100] InP substrates.

The use of molten salt electrolysis for InP synthesis and growth is complicated by the high volatility of the most convenient sources of In ions (In_2O_3 and InF_3) above 650°C, and also by the decomposition of InP at elevated temperatures in an inert atmosphere. These factors limited the temperature regime for stable deposition of InP to 600 - 650°C.

After trying a number of low melting solvents as listed in Table 2, Elwell, et al. (71), were able to successfully deposit InP from a $NaPO_3$/KPO_3/NaF/KF eutectic mixture named "Pofonak". Current densities in the range of 1 - 3 mA/cm^2 were used.

InP probably forms electrochemically by the following cathode and anode reactions:

Eq. (32) $$In^{3+} + 4PO_3^- + 8e \longrightarrow InP + 3PO_4^{3-}$$

Eq. (33) $$4PO_4^{3-} \longrightarrow 4PO_3^- + 2O_2\uparrow + 8e$$

The anode used in these experiments was normally graphite, which reacts with the O_2 evolved to form CO or CO_2. The minimum deposition

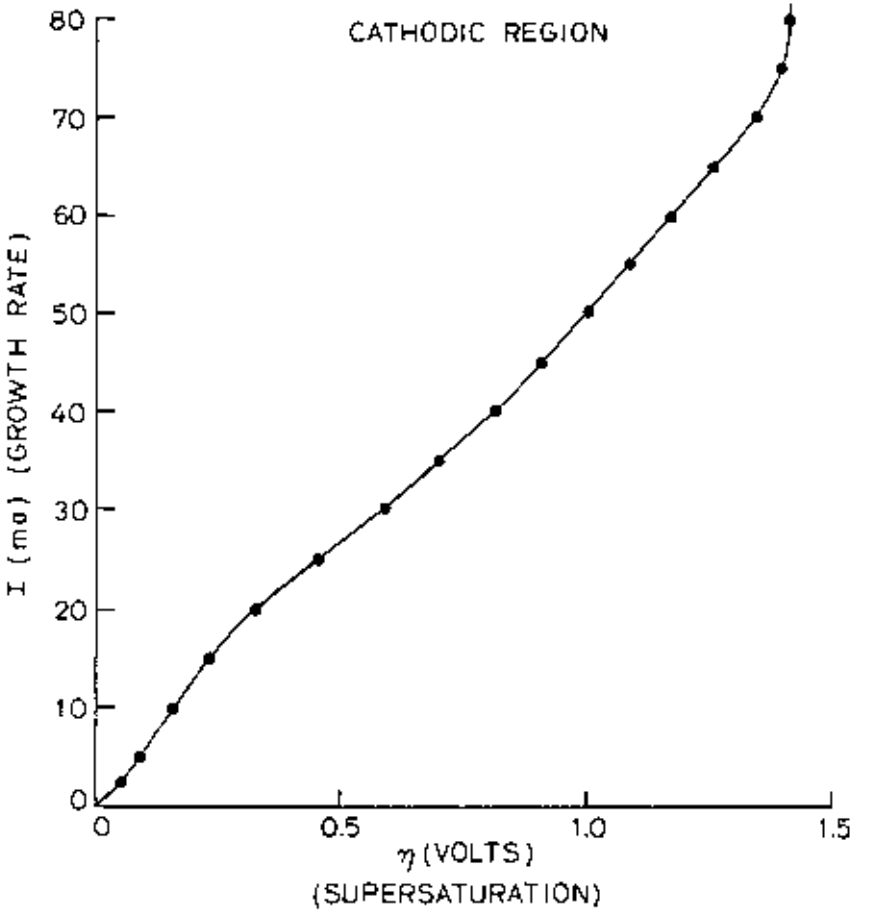

Figure 24. Plot of current (I) vs. overpotential (η) for deposition of GaP on GaP (69).

potential was 0.85±0.05 volts and was not sensitive to In_2O_3 concentration. The chemicals used were reagent grade (98 - 99%) and major melt impurities were 0.01% Si, 0.001% Al and Ca.

While cathode materials made of graphite, Ni, Ge, Au, Mo, Nb, Pt and Ta were tried, Ni was the only metal suitable for the deposition of polycrystalline InP, due to poor adhesion on the other materials. Fig. 25 shows a deposit on Ni foil. The CdS substrates came from various sources and had resistivities in the range of 3 - 10 Ω cm at 600°C. Commercial crystals had to be annealed in a Cd vapor to reduce their initially high resistivities (10^4 - 10^7 Ω cm). These substrates had to be carefully cleaned to prevent dendritic growth. An example of a InP layer on CdS is shown in Fig. 26 in cross-section. Films 2 - 5 μm in thickness were deposited at rates of 1 - 2 μm/hr at potentials of 0.9 to 1.0 volts. Deposition efficiencies were around 50%.

Table 2

Solvent/Solute Composition Studied for InP Electrodeposition (17).

Composition	Comment
$NaPO_3/NaF(In_2O_3$ or $InF_3)$	Low solubility of In_2O_3 and InF at 600°C High viscosity No InP deposits
KCl/LiCl eutectic + $NaPO_3/In_2O_3$ or InF_3	Chlorides volatile
LiF/NaF/KF eutectic + InF_3/KPF_6	All fluoride system Gas evolution due to reaction of components, non-reproducible InP formation
$Li_2O/B_2O_3/LiF/In_2O_3$ $Na_{0.814}K_{0.186}(PO_3)_{0.75}F_{0.25}/In_2O_3$	Low Solubility of In_2O_3 Successful for InP electrodeposition Solubility of In_2O_3 only ≈ 1 %
(Li,K)(PO_3,F) and (Li,Na)(PO_3,F) with $LiPO_3$ and LiF_3	InP deposits not obtained

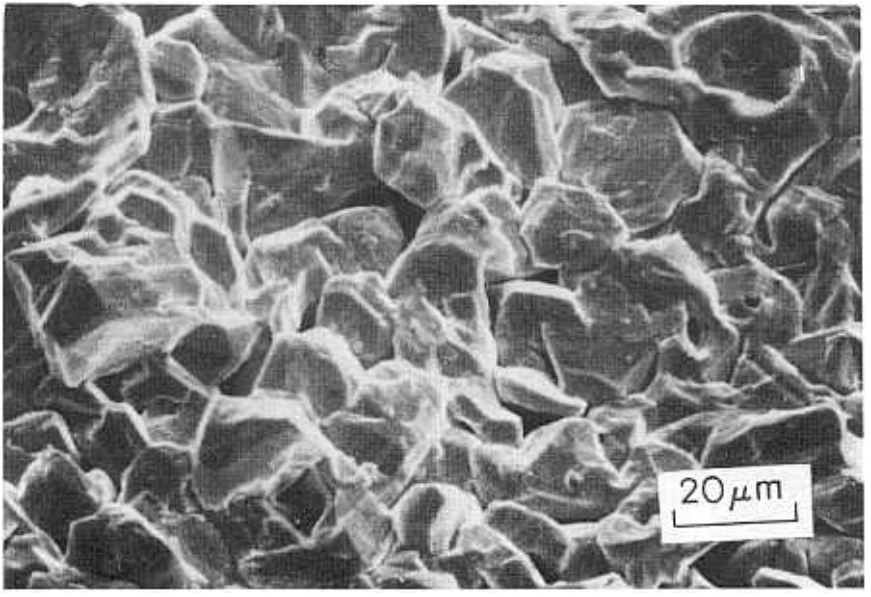

Figure 25. Polycrystalline InP deposit on nickel foil (71).

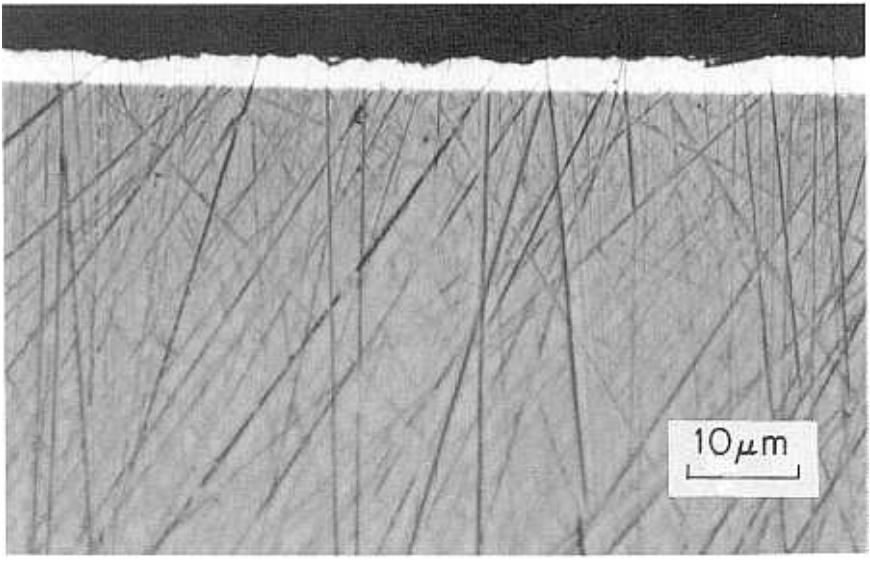

Figure 26. Cross-section of fairly uniform layer of InP on CdS. (The scratches are polishing marks on the CdS.) (71).

The deposition of InP on doped [100] and [111] n-type InP wafers was less successful. The preliminary work of Elwell, et al. (71), showed that the deposition of InP films by the fused salt electrolysis method is possible, but challenging.

Gallium Arsenide. GaAs is the next most commercially important material after silicon. It is useful for light emitting diodes, diode lasers, substrates for high speed integrated circuits and other optoelectronic applications. It is surprising, therefore, that there has been only one published paper to date on the electrolytic synthesis and deposition of GaAs (DeMattei et al., Ref. 72). A molten salt solution was used which contained $NaAsO_2$ and Ga_2O_3 in a B_2O_3-NaF solvent at 720 - 760°C. The specific source of As used was very important. $NaAsO_3$ is easily reduced by conversion of As^{5+} to As^{3+} or As° in the presence of either carbon, metals, or GaAs. Melts using As_2O_3 or $NaAsO_2$ are more stable but volatile at high temperature. Following the work of Weiss (73), who employed $NaAsO_2$ for the growth of MoAs and reduced deposition temperatures using a $Na_4B_4O_7$-NaF flux, DeMattei, et al. (72), reduced the liquidus temperature even lower to (720 - 760°C) by using 20.3 wt% NaF, together with 67.3 wt% B_2O_3 in the solvent, and 4.3 wt% Ga_2O_3 and 8.2 wt% $NaAsO_3$ as the solute. More than a stoichiometric amount of arsenic was needed to prepare single phase GaAs deposits. The minimum deposition potentials were 1.7 volts for GaAs cathodes and 2 volts in nickel at the deposition temperatures used. The apparatus used was described by Zubeck, et al. (74). Vitreous carbon crucible and gold anodes were used.

Epitaxial GaAs layers 10 μm thick were deposited on (100) n-type (0.05 Ω cm) GaAs substrates.

4.3 IV-IV Compounds

Silicon Carbide. Silicon carbide is a complex compound which has a large number of structural polytypes. The α or 6H (hexagonal) form is the most commonly found while the cubic β-phase is of greatest technological interest. The promise of silicon carbide as a high temperature, radiation resistant semiconductor and blue-green light-emitting diode, has tantalized researchers for at least three decades. The problem of growing large crystals or epitaxial films with the appropriate structure and crystalline perfection has been very challenging. Many approaches have been pursued without much success until 1981 when Tairov and Tsvetkov (75) developed a vapor-phase process to grow large bulk crystals.

While the electrochemical synthesis and deposition of various metal carbides was first reported in 1946 (73), the one and only study on the electrocrystallization of SiC (Elwell et al., Ref.76) was not reported until 1982. After experimenting with a variety of molten salt mixtures containing

alkali metal fluorides and sources of Si and C such as K_2SiF_6 and Na_2CO_3, they succeeded in electrodepositing single phase α-SiC. Best results were obtained with Li_2CO_3/SiO_2 melts, which yielded thin layers of α-SiC without excess C or Si. Deposition was on (0001) α-SiC single crystal seeds (cathode) held at 1000 - 1050°C. These seed crystals were obtained from a commercial source and were the by-product of the carbothermic reduction process for silicon dioxide.

The overall simultaneous cathodic deposition reactions involved in SiC deposition were

Eq. (34) $Li_2CO_3 \longrightarrow Li_2O + C$ (cathode) + O_2 (anode)

and

Eq. (35) $SiO_2 \longrightarrow Si$ (cathode) + O_2 (anode)

Electrodeposition was carried out in a furnace system having a graphite heater and heat shields and a water-cooled stainless steel jacket, as described by DeMattei, et al. (69). The potential difference used with a polycrystalline SiC anode was -0.5 volts. Molten Li_2CO_3 was found to be very reactive with a variety of crucible materials. Vitreous carbon crucibles were found to be the least reactive but were prone to cracking and, therefore, zirconium metal crucibles which were almost as good, were used routinely by Elwell, et al. (76). Care had to be taken so that the temperatures were low enough (< 1200°C) to prevent the evolution of CO_2 from the decomposition of Li_2CO_3. The upper temperature limit was found to depend on the container and electrode materials used. The lower temperature limit was related to the requirement that the SiO_2/Li_2CO_3 ratio be sufficiently high for the formation of SiC without excess C. Melt compositions (expressed as [1 - x] Li_2CO_3 x SiO_2), which contained $x \geq 70.3$ were too viscous. Deposits from melts containing $x < 0.1$ had irregular texture and poorly formed grains. A small quantity of LiF (1%) added to the melt was found useful in lowering the viscosity. While the lowest temperature used to deposit SiC from SiO_2-Li_2CO_3 melts was 950°C, it was possible to electrodeposit this compound at 750°C from a 5 m/o K_2SiF_6-20 m/o Li_2CO_3 mixture in a LiF/KF eutectic melt. Unfortunately, the deposits from these melts had poor morphology.

Figure 27 shows a slow scan voltammogram for SiO_2-Li_2CO_3 melts at 1000°C containing different compositions. Although no waves for Si and C can be seen, an unexpectedly large increase in current with SiO_2 concentration was observed. The best deposits (shown in Fig. 28a & b) were made using potentials of -0.4 to -0.5 volts, deposition time of 3 hrs and a melt composition of 0.8 Li_2CO_3 and 0.2 SiO_2. While conditions for

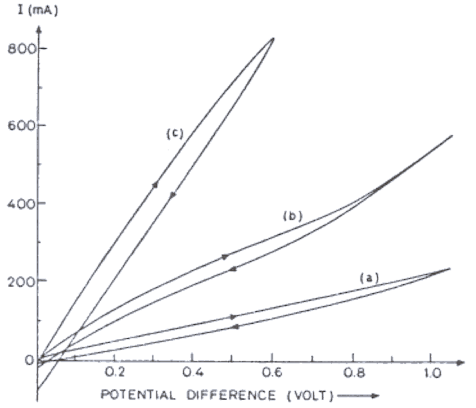

Figure 27. Slow-scan I-V plots for melts of different composition at 1000°C, using SiC electrodes: a) Li_2CO_3 only; b) 0.9 Li_2CO_3 + 0.1 SiO_2; c) 0.8 Li_2CO_3 + 0.2 SiO_2 (75).

(a)

(b)

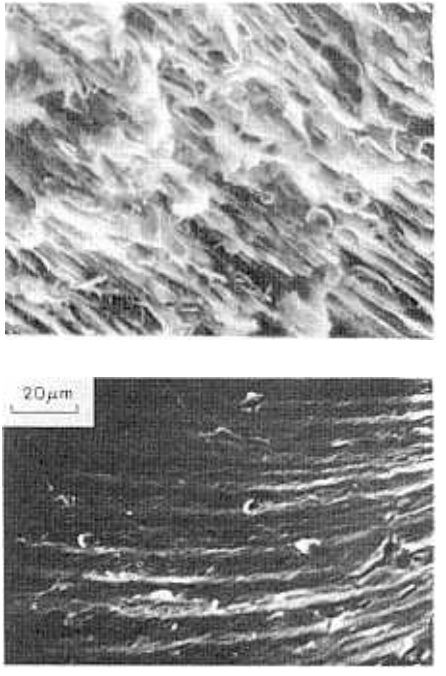

Figure 28. a) SEM photograph of SiC deposit on [0001] α-SiC from melt of composition of 0.8 Li_2CO_3; 0.2 SiO_2, using -0.5 volts vs. SiC. Deposition time, 3 hrs. b) SiC deposit under similar conditions to a) but at -0.4 volts for 30 mins (76).

long-term deposition stability were found, attempts to produce thick layers were hampered by delamination of the seed crystals.

5.0 CONCLUSION

It has been demonstrated that most of the technologically important semiconductors can be synthesized and deposited as thin films by electrolysis techniques. By far, the greatest amount of effort has gone into the development of electrodeposition methods for low cost silicon solar cells.

Although there are important advantages associated with electrodeposition processes, the demanding requirements for purity and structural perfection of materials for semiconductor devices and the continued development of advanced alternative growth and deposition methods, such as molecular beam epitaxy and metalorganic chemical vapor deposition, make it unlikely that a strong interest to pursue electrolytic processes will emerge during the next decade. If semiconductor films with complex shapes become needed sometime in the future, then electrodeposition techniques might become more important.

6.0 REFERENCES

1. Kunnmann, W., *Preparation and Properties of Solid State Materials,* (R. A. Leferer, ed.), p. 1, Dekker, New York (1971)

2. Wold, A. and Bellavance, D., *Preparative Methods in Solid State Chemistry,* (P. Hagenmiller, ed.), p. 279, Academic Press, New York (1972)

3. Feigelson, R. S., Crystal Growth by the Electrolysis of Molten Salts, in: *Solid State Chemistry: A Contemporary Overview*, (S. Hold, J. Milstein and M. Robbins, eds.), pp. 243, Amer. Chem. Soc., Washington, D.C. (1980)

4. Wall, F. T., *Chemical Thermodynamics*, V. H. Freeman and Company (1958)

5. Barrow, G. M., *Physical Chemistry*, McGraw-Hill (1961)

6. Kortum, G. and Bockris, J. O'M, *Textbook of Electrochemistry*, Elsevier Publishing Company (1951)

7. Bokris, J. O'M. and Reddy, A. K. N., *Modern Electrochemistry*, Plenum Publishing Corporation (1970)

8. Despic, A. P. and Popov, K. I., Transport-Controlled Deposition and Dissolution of Metals, *Modern Aspects of Electrochemistry,* (B. E. Conway and J. O'M. Bockris, eds.), 7:99 (1972)

9. Despic, A. P., Diggle, J. and Bockris, J. O'M., *J. Electrochem. Soc.* 115:507 (1968)

10. Kroll, W. J., *Trans. Electrochem. Soc.* 87:551 (1945)

11. St Claire De Ville, H., *Compt. Rend. Acad. Sci. Paris* 39:323 (1854)

12. Monnier, R., *Chimia* 37:109 (1983)

13. Gore, C., *Phil. Mag.* 7:227 (1854)

14. Ullik, F., *Ber. Akad. Wien* 52:1115 (1865)

15. Minet, A., *Compt. Rend. Acad. Sci. Paris* 112:1215 (1891)

16. Warren, H. N., *Chem. News* 67:303 (1893)

17. Dodero, M., *Compt. Rend. Acad. Sci. Paris* 109:556 (1934)

18. Idem., *Bull. Soc. Chim. France* 6:209 (1939)

19. Monnier, R. and Barakat, D., *Helv. Chim. Acta* 40:204 (1957)

20. Monnier, R. and Giacometti, J. C., *Helv. Chim. Acta* 47:345 (1964)

21. Grjotheim, K. and Matiasovsky, K., *Chem. zvesti* 25:249 (1971)

22. Grjotheim, K., Matiasovsky, K., Fellner, P. and Silny, A., *Can. Met. Quart.* 10:79 (1971)

23. Boe, G., Grjotheim, K., Matiasovsky, K. and Fellner, P., *Can. Met. Quart.* 10:179,281,463 (1971)

24. Grjotheim, K., Matiasovsky, K. and Fellner, P., Light Metals 1982, (J.E. Anderson, ed.), p. 333, *AIME* (1982)

25. Monnier, R., and Barakat, D., U.S. Patents 3,219,561 (23 Nov 1965) and 3,254,010 (31 May 1966)

26. Huggins, R. A. and Elwell, D., *J. Crystal Growth* 37:159 (1977)

27. DeMattei, R. C., Elwell, D. and Feigelson, R. S., *J. Electrochem. Soc.* 128:1712 (1981)

28. DeMattei, R. C., Elwell, D. and Feigelson, R. S., "Electrodeposition of Molten Silicon," U.S. Patent No.4,292,145 (September 29, 1981)

29. Johnson, K. E., *High Temperature Technology*, p. 493, Butterworths, London (1967)

30. Davis, J. R., Rohatgi, A., Hopkins, R. H., Blais, P. D., Rai-Choudhury, P., McCormick, J. R. and Mollenkopf, H. C., *IEEE Trans.* ED-27:677 (1980)

31. Olson, J. M. and Kibbler, A., *Abstracts 5th Amer. Conf. Crystal Growth*, p. 248, San Diego (1981)

32. Hitachi Ltd., Japanese Patent 58,144,485, (27 Aug 1983); see *Chem. Abs.* 100:14515s (1984)

33. Ito, Y. and Yoshizawa, S., *Advances in Molten Salt Chemistry*, Vol. 4, (G. Mamantov and J. Braunstein, eds.), p. 391, Plenum Press, New York (1981)

34. Paulsen, E. R. and Hall, J. A., *J. Metals* 35:60 #6 (1983)

35. Lovering, D. G. and Williams, D. E., *Molten Salt Technology*, (D. G. Lovering, ed.), p. 91, Plenum Press, New York (1982)

36. Cohen, U., *J. Electron. Mater.* 6:607 (1977)

37. Rao, G. M., Elwell, D. and Feigelson, R. S., *Surface Technology* 13:331 (1981)

38. Rao, G. M., Elwell, D. and Feigelson, R. S., *J. Electrochem. Soc.* 127:1940 (1980)

39. Idem., ibid. 128:1708 (1981)

40. Idem., ibid. 130:1021 (1983)

41. Olson, J. M. and Carleton, K. L., *J. Electrochem. Soc.* 128:2698 (1981)

42. Sharma, I. G. and Mukherjee, T. K., *Metall. Trans.* 17B:395 (June 1986)

43. Boen, R. and Bouteillon, J. *J. Appl. Electrochem.* 13:277 (1983)

44. De Lepinay, J., Bouteillon, J., Traore, S., Renaud, D. and Barner, M. J., *J. Appl. Electrochem* 17:294 (1987)

45. Austin, A. E., U.S. Patent 3,990,953 (Nov. 9, 1976)

46. Bucker, E. R. and Amick, J. A., U.S. Patent 4,192,720 (Mar. 11, 1980)

47. Lee, C. H., and Kroger, F. A., *J. Electrochem. Soc.* 129:936 (1982)

48. Rama Mohan, T. R. and Kroger, F. A., *Electrochimica Acta* 27:371 (1982)

49. Elwell, D. and Rao, G. M., *J. Appl. Electrochem.* 18:15 (1988)

50. Hodes, G., Manassen, J. and Cahen, C., *Nature* 261:403 (1971)

51. Miller, B. and Heller, A., *Nature* 262:680 (1971)

52. Peter, L., *Electrochim. Acta* 23:165 (1978)

53. Panicker, M., Knaster, M. and Kroger, F., *J. Electrochem. Soc., Electrochem. Sci. and Technol.* 125:566 (1978)

54. Power, G. P., Peggs, D. R. and Parker, A. J., *Electrochimica Acta* 26:681 (1981)

55. Takahashi, M., Uosaki, K. and Kita, H., *J. Electrochem. Soc., Electrochem. Sci. and Technol.* 131:2304 (1984)

56. Takahashi, M., Uosaki, K. and Kita, H., *J. Appl. Phys.* 55:3879 (1984)

57. Pandey, P. K. and Rooz, A. J. N., *J. Phys. D: Appl. Phys.* 19:917 (1986)

58. Russak, M. A., Reichmann, J., Witzke, H., Deb, S. K. and Chen, S. N., *J. Electrochem. Soc.* 127:725 (1980)

59. Bhattacharya, R. N., Rajeshwar, K. and Noufi, R. N., *J. Electrochem. Soc.: Accelerated Brief Communication* 131:939 (1984)

60. Baranski, A. S. and Fawcett, W. R., *J. Electrochem. Soc.* 127:766 (1980)

61. Baranski, A. S., Fawcett, W. R., McDonald, A. C., de Nobriga, R. M. and MacDonald, J. R., *J. Electrochem. Soc.: Electrochem. Sci and Technol.* 128:963 (1981)

62. Darkowski, A. and Cocivera, M., *J. Electrochem. Soc.: Electrochem. Sci. and Technol.* 132:2768 (1985)

63. Fatas, E., Herrasti, P., Arjona, F., Camarero, E. Garcia and Medina, J. A., *Electrochem. Acta* 32:139 (1987)

64. Yamamoto, A. and Yamaguchi, M., *Japan. J. Appl. Phys.* 14:561 (1975)

65. Baranski, A. S., Fawcett, W. R., Gatner, K., MacDonald, A. C., MacDonald, J. R. and Selen, M., *J. Electrochem. Soc.: Electrochem. Sci. and Technol.* 130:579 (1983)

66. Bhattacharya, R. N. and Rajeshwar, K., *Solar Cells* 16:237 (1986)

67. Hodes, G. and Cahen, D., *Solar Cells* 16:245 (1986)

68. Cuomo, J. J. and Gambino, R. J., *J. Electrochem. Soc.* 115:755 (1968)

69. DeMattei, R. C., Elwell, D. and Feigelson, R. S., *J. Crystal Growth* 44:545 (1978)

70. Andre, J. P., Hallais, J. and Schiller, C., *J. Crystal Growth* 31:147 (1975)

71. Elwell, D., Feigelson, R. S. and Simkins, M. M., *J. Crystal Growth* 51:171 (1981)

72. DeMattei, R. C., Elwell, D. and Feigelson, R. S., *J. Crystal Growth* 43:643 (1978)

73. Weiss, G., *Ann. Chim.* 1:446 (1946)

74. Zubeck, I. V., Feigelson, R. S., Huggins, R. A. and Pettit, P. A., *J. Crystal Growth* 34:85 (1976)

75. Tairov, Y. M. and Tsvetkov, V. K., *J. Crystal Growth* 52:146 (1981)

76. Elwell, D., Feigelson, R. S. and Simkins, M. M., *Mat. Res. Bull.* 17:697 (1982)

2

CHEMICAL ETCHING: PRINCIPLES AND APPLICATIONS

Keshra Sangwal

1.0 INTRODUCTION

When a crystal is in contact with its undersaturated environment or some other corrosive medium, it undergoes decrystallization (dissolution, etching). Depending on the experimental conditions and the duration of the process, the crystal may yield etch figures (depressions and elevations) and dissolution layers on its surfaces without loss of its macroscopic appearance, or may acquire a macroscopic form different from the initial one. The former are produced when the process is carried out for short durations, while a change in the macroscopic appearance of the crystal takes place only after prolonged dissolution. Honess (1) gives a chronological description of the literature prior to 1927 on etch figures produced on crystal surfaces by corrosive solvents, while a recent monograph by Sangwal (2) describes various etch figures from the standpoint of dissolution theories. Heimann's book (3), on the other hand, concentrates on the theories of dissolution and dissolution forms of crystals.

A variety of etch figures are observed on etched surfaces of crystals. In general, they are depressions and elevations. Among the former type are pits, depression spirals and etch grooves, while among the latter are crystallographically-oriented and noncrystallographic hillocks. Etch pits are the most frequently observed figures on etched crystal surfaces, and often they are formed at the emergence points of dislocations.

The present chapter treats the subject of etching of crystals from the viewpoint of electrochemical processes. The fundamental mechanisms of dissolution and selective etching are first outlined in Secs. 2 through 7. The morphology of etch pits and the reliability of etch figures in locating the emergence points of dislocations are then briefly discussed in Secs.

8 and 9, respectively. Finally, the application of chemical etching in producing etch profiles is presented in Sec. 10. Chemical etching techniques are well known regarding the determination of the symmetry of a crystal face from the shape of etch pits, the study of the density and distribution of structural defects in crystals, the detection of nuclear tracks in solids and in the fabrication of electronic devices. In the present chapter, however, these aspects are either omitted completely or considered marginally because they are adequately covered in the above monographs. Similarly, all types of the theories of dissolution and etch-pit formation, proposed so far, are not described.

2.0 MECHANISM OF DISSOLUTION

2.1 Driving Force for Dissolution: Some Basic Concepts and Definitions

Under constant temperature and pressure conditions, any change in a system proceeds from a state of higher to a state of lower Gibbs free energy. Consequently, Gibbs function, G, is taken as a thermodynamic potential, and the change in the system as a passage from a state of higher to a state of lower potential. Thus the reaction,

Eq. (1) $$aA + bB \longrightarrow cC + dD + \Delta G$$

is thermodynamically possible if the change in the free energy

Eq. (2) $$\Delta G = (cG_C + dG_D) - (aG_A + bG_B) < 0$$

Since ΔG is related to changes in the Helmoltz free energy, ΔH, and entropy, ΔS, by the equation

Eq. (3) $$\Delta G = \Delta H - T\Delta S$$

a reaction possible at one temperature may not occur at another temperature.

If n_1, n_2, n_3,..., n_i represent the number of moles of components 1, 2, 3,..., i in a particular phase, we define chemical potential, μ_i, by,

Eq. (4) $$\mu_i = (\partial G/\partial n_i)_{T,p,n_i}$$

It is the change in the Gibbs free energy of the phase with a change in the number of moles of component i, while the temperature, the pressure and the number of all other components are held constant. If a_i is the activity

of the *i*-th component, the chemical potential of the *i*-th component is expressed by

Eq. (5) $$\mu_i = \mu_i^* + RT \ln(a_i)$$

where μ_i^* is the chemical potential of i in some standard state of activity a_i^*. Thus the difference in the chemical potentials of the *i*-th component corresponding to two activities, a and a*, may be expressed as

Eq. (6) $$\Delta\mu_i = \mu_i - \mu_i^* = RT \ln(a_i/a_i^*)$$

The difference in the chemical potentials, $\Delta\mu_i$, is the driving force for dissolution.

When a crystal is immersed in an etching solution, an electrical double layer is produced. The double layer is developed as a result of the adsorption of molecules of solvent, solute and reaction products at the dissolving surface. The surface may be composed of the following:

1. Charged ions of the same sign as on metal surfaces.
2. Oppositely charged ions of different sizes as on the surfaces of halite-type structures.
3. Free dangling bonds as in the case of II-VI and III-V semiconductors.

It is believed that the double layer is composed of a rigid layer of adsorbed ions with a thickness equal to ionic diameters (the Stern or Helmoltz rigid layer) followed by a diffuse layer (Gouy-Chapman diffuse layer) extending up to several hundred microns into the solution. Below we describe the surface potentials of this double layer.

A homogeneous material containing an excess electrical charge and situated in vacuum has an outer potential, or Volta potential, Ψ, which is the amount of work necessary to bring a unit electric charge from infinity to a point close to the surface where Ψ attains the maximum value.

The presence of charge on the surface of a material causes the formation of a surface dipole layer. Thus further work is needed to take the test charge from just outside the surface to it. The potential change resulting from the presence of the dipole layer is the surface potential χ. The inner, or Galvani, potential is defined as (4),

Eq. (7) $$\phi = \Psi + \chi$$

where Ψ and χ are mainly due to surface charge and surface dipoles, respectively.

From the foregoing, it follows that the work done in taking the test charge (or ion) from infinity to the material surface is chemical and

electrochemical in nature. Thus the electrochemical potential $\bar{\mu}_i$ for an ion of charge z_i may be given by (4)

Eq (8) $$\bar{\mu}_i = \mu_i + z_i F \phi$$

where μ_i is the chemical potential of the ions of component i (Eq. 5) and F is the Faraday constant. The work required to take 1 mole of ions of the component i across the double layer is given by

Eq (9) $$\Delta\bar{\mu}_i = \Delta\mu_i + z_i F \Delta\phi_i$$

where $\Delta\mu_i$ is expressed by Eq. 6.

2.2 Dissolution Process Controlled by Surface Reactions and Volume Diffusion

We now consider the rates of dissolution of a crystal surface in solution. The processes taking place during dissolution are essentially similar to those in heterogeneous catalysis. We may take a crystal surface as a catalytic surface that facilitates the transfer of ions or molecules to and from the etching medium. Thus, the dissolution process may be viewed as a succession of steps:

(1) Diffusion of reactant ions/molecules to the surface.
(2) Reaction in the interfacial layer.
(3) Adsorption of reactant onto the crystal surface.
(4) Reaction between the crystal and the adsorbed reactant species.
(5) Desorption of reaction products from the surface.
(6) Reaction of products in the interfacial layer.
(7) Diffusion of the ultimate reaction products away from the surface.

The sequence of ultimate reactions does not necessarily include steps 2 and 6, but such steps are indeed involved, for example, in the decomposition or formation of complex ions in the solution phase before or after a chemical reaction with the surface ion/molecules. However, for the sake of clarity we did not include steps representing the formation of activated complexes during the processes of adsorption and in the chemical reactions in steps 2 through 6.

Any of the above consecutive steps may control the etching process, but it is always the slowest step that is rate limiting. Steps 1 and 7 of the transport of the reacting species and reaction products are controlled by diffusion kinetics, while surface reactions control the remaining steps. Some of the above steps may be very important in certain systems, while

they may play no role at all in the etching process in others. For example, steps 2 and 6 are of minor importance in the etching of water-soluble crystals in undersaturated aqueous solutions, but the same steps, to a large extent, control the etching of metals and semiconductors, in which a supplemented reagent removes reaction products tending to adhere to the crystal surface.

Whether etching is controlled by diffusion or by surface reactions can be determined by using a number of criteria (2). One of these criteria is the activation energy, E, for dissolution, obtained from data on the temperature dependence of dissolution rates. If the activation energy has relatively low values (of the order of 20 kJ/mol or less) such that the dissolution rate increases only slightly with temperature, dissolution is diffusion controlled. In the case of dissolution controlled by surface reactions, E has relatively high values of about 50 kJ/mol or more. Another criterion of diffusion-controlled dissolution is that the activation energy for dissolution is of the order of the activation energy for viscous flow. Dissolution rates controlled by diffusion and the associated activation energies increase with stirring, while those of surface-reaction-controlled dissolution remain invariant. The rates of dissolution of faces of different orientations are usually anisotropic and isotropic in the case of surface-reaction- and diffusion-controlled dissolution, respectively (see also Sec. 10).

Recalling that crystal-medium interfacial layer is composed of the rigid layer 1 - 2 atomic diameters wide and the diffuse layer extends up to some 10^{-2} cm deep into the solution, we may view the diffusion-controlled dissolution process as one in which the reactant species and reaction products have to traverse the wide diffuse layer in order to enable the surface reactions to proceed. In this case, the rate of dissolution, expressed as the amount, m, of material removed per unit time, t, is described by Fick's first law, namely:

Eq. (10) $$dm/dt = DA(c_o - c)/\delta$$

where D is the bulk diffusion coefficient of diffusing species in the medium, A is the dissolving surface area, δ is the thickness of the diffuse layer, and, in solution etching, c and c_o are the concentrations of solute in the bulk solution and at the crystal surface, respectively. In "pure" chemical and electrochemical etching, these concentrations may be replaced by chemical (Eq. 5) and electrochemical potentials (Eq. 9), respectively.

In the case of surface-reaction-controlled dissolution, there is no diffuse layer and the exchange of reacting species and reaction products

proceeds directly at the rigid layer. Depending on the type of surface reactions (i.e. solvation, simple chemical or electrochemical), surface-reaction-controlled dissolution process is different for different types of materials. After a brief description of the classification of types of dissolution in the following section, we shall discuss these mechanisms in Sec. 2.4.

2.3 Types of Dissolution

As mentioned above, the formation of activated complexes is a prerequisite for a chemical reaction. In order to attain the activated state, the system requires some source of energy. There are three main sources by which the molecules can acquire the necessary activation energy:

1. Thermal energy associated with translation of molecules and their internal vibrations and rotations.
2. Energy supplied by an electric field.
3. Absorption of radiation.

Taking the above three sources as the basis, we can distinguish between the traditional terminology of dissolution as follows:

Chemical etching (1)
- (a) Solvation or solution etching.
- (b) "True" chemical etching.
- (c) Electrochemical etching.

Electrolytic etching (2)

Photoetching
- (a) Photoelectrochemical etching (1 + 3)
- (b) Photoelectrolytic etching (2 + 3)

The subdivision of chemical etching stems from the types of reactions taking place on a dissolving surface. In solvation or solution etching the ions/molecules on a surface are severed by solvation, in true chemical etching by double displacement reactions, e.g.,

Eq (11) $$MgO + 2HCl \longrightarrow MgCl_2 + H_2O$$

in which the oxidation state of the ruptured ions remains the same as in the crystal, and in electrochemical etching by charge transfer, e.g.,

Eq (12) $$Zn^{\circ} + 2HCl \longrightarrow ZnCl_2 + H_2$$

in which the ruptured atoms/ions undergo a change of oxidation states.

Finally, it should be pointed out that since photoetching and electrolytic etching are carried out at $T > 0$, there is always a thermal contribution to the activation enegy.

2.4 Dissolution Kinetics in Terms of Interfacial Layer Potential

Dissolution of Ionic Compounds in Aqueous Solutions (5). The potential of a double layer developed on the surface of a crystal placed in an aqueous solution is given by (cf Eqs 6 and 8),

Eq. (13) $$\phi = (RT/zF)\ln(a/a_o)$$

where a and a_o, respectively, are the actual and equilibrium solute activity in solution. In the absence of an additional source, other than diffusion, for the activation energy for the addition of ions to the crystal, the exchange rate, v_e, for ions across the double layer in a saturated solution is given by

Eq. (14) $$v_e = Dc/\delta$$

Equation 14 gives a maximum exchange rate due to bulk diffusion of ions in the solution in the absence of any additional source of activation energy.

If the crystal is charged in the solution, the rates of removal, v_r, and deposition, v_a, of each ion may be given by

Eq. (15a) $$v_r = nk_r \exp\{\alpha zF\phi/RT\}$$

Eq. (15b) $$v_a = ck_d \exp\{-(1-\alpha)zF\phi/RT\}$$

where n is the number of ions per cm^2, α is a transfer coefficient (see below), and k's are rate constants. For pure diffusion, $k_d = D/\delta$. Thus the net rate of exchange $(v_r - v_a)$ is,

Eq. (16) $$(v_r - v_a) = nk_r \exp\{\alpha zF\phi/RT\} - ck_d \exp\{-(1-\alpha)zF\phi/RT\}$$

For a freely dissolving crystal MX in an undersaturated solution for which, at the isoelectric point, the rates of exchange for M^+ and X^- are $(v_{r1} - v_{a1})$ and $(v_{r2} - v_{a2})$, the net removal rates must be equal, i.e.,

Eq. (17) $$n_1k_{r1} \exp\{\alpha_1 z_1 F\phi/RT\} - c_1k_{d1} \exp\{-(1-\alpha_1)z_1F\phi/RT\} = n_2k_{r2} \exp\{\alpha_2 z_2 F\phi/RT\} - c_1k_{d2} \exp\{-(1-\alpha_2)z_2F\phi/RT\}$$

In this equation, the suffixes 1 and 2 denote cations and anions, respectively.

In the case of dissolution in pure solvents, i.e., when the concentration of both ions in the solution is zero, such that $v_a = 0$, from Eq. 17 one gets

Eq. (18) $$n_1k_{r1} \exp\{\alpha_1 z_1 F\phi/RT\} = n_2k_{r2} \exp\{\alpha_2 z_2 F\phi/RT\}$$

and from Eq. 18,

Eq. (19) $\phi = [RT/F(\alpha_2 z_2 - \alpha_1 z_1)] \ln[(n_1 k_{r1})/(n_2 k_{r2})]$

Using the values of ϕ from Eq. 19, one can estimate the dissolution rate from Eq. 18.

For an undersaturated stoichiometric solution, the potential may be written from Eqs. 15a and 15b as:

Eq. (20) $\phi = (RT/zF) \ln(nk_r/ck_d)$

Equating Eq. 20 for both cations and anions, one gets,

Eq. (21) $$n_2 k_{r2} = \{n_1 k_{r1}/n_2 k_{r2}\}^{z_2/(z_1 - z_2)} * \{(c_2 k_{d2})^{z_1/(z_1 - z_2)}/(c_1 k_{d1})^{z_2/(z_1 - z_2)}\}$$

where c_1 and c_2 are the concentrations of cations and anions, respectively, in the stoichiometric solution.

Substituting into Eq. 15a the values of ϕ from Eq. 19, one obtains the dissolution rate,

Eq. (22) $v = n_2 k_{r2} (n_1 k_{r1}/n_2 k_{r2})^{\alpha_2 z_2/(\alpha_1 z_1 - \alpha_2 z_2)}$

in pure solvents. Introducing Eq. 21 into Eq. 22, and taking $\alpha_1 = \alpha_2$, one gets,

Eq. (23) $$v = \frac{(c_2 k_{d2})^{z_1/(z_1 - z_2)}}{(c_1 k_{d1})^{z_2/(z_1 - z_2)}}$$

in undersaturated solutions. Equation 23 gives the maximum dissolution rate of a crystal, and reduces to Eq. 13 for $c_1 = c_2$ and $k_{d1} = k_{d2}$.

Dissolution of Ionic Crystals in Acidic and Alkaline Media (5). All ionic crystals are not soluble and many insoluble substances are etched in acidic and alkaline media. The ideas of dissolution in terms of double layer potentials can be extended to such situations in which it is considered that protons or hydroxyl ions of an acid or an alkali are complexing agents for anions or cations, respectively. For example, in the dissolution of MgO in aqueous HCl, H^+ ions are the complexing agents for O^{2-} such that OH^- and H_2O are produced.

Assuming that, for the dissolution of a hydroxide crystal, the rate of removal of hydroxide ions as water is much greater than that of OH^- so that

the latter is negligible, then, following Vermilyea (5), we may write the rates of removal of cations and hydroxyl ions as

Eq. (24a) $v_{r1} = n_1 k_{r1} \exp\{\alpha_1 z_1 F\phi/RT\}$

Eq. (24b) $v_{r2} = n_2 k_{r2} c_i \exp\{\alpha_2 z_2 F\phi/RT\}$

where c_i is the H^+ ion concentration. For a freely dissolving crystal with $v_{r1} = v_{r2}$, from Eqs. 24a and 24b we obtain,

Eq. (25) $\phi = [RT/(\alpha_1 z_1 - \alpha_2 z_2)] \ln[(n_2 k_{r2} c_i)/(n_1 k_{r1})]$

This equation shows that the potential ϕ increases with H^+ ion concentration. Substitution of Eq. 25 into Eq. 24a yields:

Eq. (26) $v = nk\,[(n_2 k_{r2} c_i^{\alpha_1 z_1/(\alpha_1 z_1 - \alpha_2 z_2)})/(n_1 k_{r1})]$

Thus if $\alpha_1 = \alpha_2$, the dissolution rate increases as $c_i^{1/2}$, $c_i^{2/3}$, $c_i^{3/4}$, and $c_i^{4/5}$ for cations of charge 1, 2, 3 and 4, respectively.

The dissolution mechanism of an oxide may be complicated. The following situations are possible:

1. Surface oxide ions may first hydrate to form OH^- ions. The dissolution mechanism then is like that for a hydroxide.
2. Oxide ions may be removed by reaction with a proton to form OH^-, which is subsequently removed as water as a result of the reaction with another proton. Since $z_2 = 2$, the dissolution rate will increase as $c_i^{1/3}$, $c_i^{1/2}$, $c_i^{3/5}$, and $c_i^{2/3}$ for cations of charge 1, 2, 3 and 4, respectively.
3. Oxide ions may react directly with two protons to form water. Then c_i^2 will replace c_i in Eq. 24b and the dissolution rate will increase as $c_i^{2/3}$, c_i, $c_i^{6/5}$, and $c_i^{4/3}$ for cations of charge 1, 2, 3 and 4, respectively.

Dissolution of an oxide or hydroxide in an alkaline solution, in which OH^- ions are the possible complexing ions, may be treated similarly. However, in this case the reverse reaction for the crystal anion cannot be neglected and the equations become complicated. The dissolution of compounds other than oxides and hydroxides may also be treated in a similar way.

Finally, two comments should be made in connection with the above mechanism. First, the assumption $\alpha_1 = \alpha_2$ may yield higher rates than the actual ones. Second, since hydrogen and hydroxyl ion concentrations are related to the pH of a solution, the dissolution rate is expected to depend on solution pH, as has been observed experimentally (6)(7).

Dissolution of Metals. A pair of electrodes immersed in an electrolyte solution and connected by an external metallic conductor represents a typical electrochemical cell in which reaction at the surface of an electrode takes place by the transfer of charge. If the cell is converting chemical energy into electrical charge, it is a galvanic cell; if it is using externally applied electrical energy to carry out a chemical reaction, it is called an electrolytic cell. The distinction between a galvanic and an electrolytic cell is given by the conditions (4):

Eq. (27a) $\Delta\phi < \mathbf{E}$ galvanic cell,

Eq. (27b) $\Delta\phi > \mathbf{E}$ electrolytic cell,

where $\Delta\phi$ is the potential difference due to the electric double layer at the electrode-electrolyte interface, and $\mathbf{E}$ is the cell emf.

A metal dipped in an electrolyte solution dissolves as a result of electrode (electrochemical) reactions. Electrochemical reactions differ from other heterogeneous reactions in that their rate constants depend on the value of $\Delta\phi$. According to the electrochemical nature of metal dissolution, there are anodic or cathodic sites on the dissolving surface, where oxidation of metal M and reduction of species N of the electrolyte take place, respectively. Thus all metals give electrons and pass into the ionized state.

Eq. (28) $M^{\circ} \longrightarrow M^{x+} + N^{x-}$

so that the metal itself is charged positively and acts as an anode (oxidation process). Here x is a small integer. In order for the metal ions, M^{x+}, to be removed from the surface, the reaction (reduction process),

Eq. (29) $N^{\circ} + xe^{-} \longrightarrow N^{x-}$

proceeds on the cathode, with the result that negatively charged ions are formed. Equations 28 and 29 are called half-cell or partial reactions occurring at the metal-electrolyte interface. Thus the following overall reaction takes place:

Eq. (30) $M^{\circ} + N^{\circ} \longrightarrow M^{x+} + N^{x-}$

These M^{x+} and N^{x-} ions then go into the solution. If the reaction product is soluble, then an atom has been removed; if it is insoluble or poorly soluble, then a complexing agent is required to remove it by an independent subsequent reaction.

When positively charged metal ions, M^{x+}, leave the metal surface, the metal surface remains negatively charged. The attraction of positively charged metal ions in solution to the negatively charged metal surface leads to the development of the double layer and the potential difference, $\Delta\phi$, across it, as mentioned in Sec. 2.1.

Under nonequilibrium conditions, there is a net anodic or cathodic current, i.e.,

Eq. (31) $$i = i_c - i_a$$

where i_a and i_c are the currents in anodic and cathodic directions, respectively. The electric potential difference between the terminals of the electrochemical cell then departs from the equilibrium value $\Delta\phi = E$. The actual value of $\Delta\phi$ depends on the current density, i, at the electrodes. The difference,

Eq. (32) $$\Delta\phi(i) - \Delta\phi_o = \eta$$

is the polarization (also called overpotential or overvoltage) of the cell, and its value is determined by the potential necessary to overcome the resistance in the electrolyte and the leads.

When a diffusion layer is present in a solution, the concentration of the latter at the double-layer interface is c* rather than c_o in the bulk. Because of the concentration dependence of chemical affinity, a potential difference is developed across the diffusion layer. This potential difference is called *concentration* or *diffusion overpotential* and is given by,

Eq. (33) $$\eta_D = (RT/zF)\ln(c^*/c_o)$$

From Fick's first law, the rate of diffusion of ions to the double layer is given by,

Eq. (34) $$-dn/dt = DA(dc/dx) = DA(c_o - c^*)/\delta$$

Therefore the current density to the cathode is,

Eq. (35) $$i_r = -(zF/A)(dn/dt) = -zFD(c_o - c^*)/\delta$$

Therefore for $c = 0$, a limiting current density,

Eq. (36) $$i_{lim} = -zFDc_o/\delta$$

occurs. Using Eq. 36, Eqs. 33 and 35 may be written as:

Eq. (37) $\eta_D = (RT/zF) \ln\{1 - (i/i_{lim})\}$

Eq. (38) $i_r = i_{lim} \{1 - \exp(zF\eta_D/RT)\}$

The values of i_r (see Eq. 36) can be increased by increasing the values of D (by increasing temperature) and by decreasing the value of δ (by stirring the solution). The dependence of current density on electrode potential showing concentration overpotential is schematically shown in Fig. 1. The curve has three regions, which we will describe in Sec. 6 on electrolytic etching.

At equilibrium, the currents of each ionic species to and from the electrode should be equal, i.e.,

Eq. (39) $i_o = i_c = i_a$

When $\Delta\phi$ is different from its equilibrium value, $\Delta\phi_o$, at low current densities, the net anodic or cathodic current is associated with the extra electric potential difference, called the *activation overvoltage* or *activation overpotential*, given by

Eq.(40) $\eta_r = \Delta\phi - \Delta\phi_o$

At equilibrium, the anode and cathode current densities are given by:

Eq. (41a) $i_a = i_o \exp\{-(1-\alpha) zF\eta_r/RT\}$, and

Eq. (41b) $i_c = i_o \exp\{\alpha zF\eta_r/RT\}$

where i_o is the exchange current. The net current density, therefore, is given by

Eq. (42) $i = i_c - i_a = i_o [\exp\{\alpha zF\eta_r/RT\} - \exp\{(1-\alpha) zF\eta_r/RT\}]$

If $\eta_r >> RT/zF$, we have the well known equations:

Eq. (43a) $\ln i_a = \ln i_o - [(1-\alpha)zF/RT]\eta$, and

Eq. (43b) $\ln i_c = \ln i_o - [\alpha zF/RT]\eta$

Depending on the current density across an electrode, the surface reactions or the transport of ions may become rate determining. At lower current densities, with ionic reactants, the Galvani potential difference, $\Delta\phi$, will

favor the transfer of an ion through the layer in one direction but it will hinder its transport in the opposite direction. Thus in the process, only a fraction, α, of the electrical energy difference $zF\Delta\phi$ is used. This fraction is the transfer coefficient.

The electrochemical mechanism of dissolution is illustrated schematically by the simplified polarization diagram shown in Fig. 2. The open circuit potentials of the cathode process, E_c, and the anodic process, E_a, are the equilibrium potentials of the corresponding partial reactions of Eqs. 28 and 29. The dissolution current corresponds to the steady-state rate of dissolution. The corresponding dissolution potential of the dissolving solid lies between the equilibrium values of the cathodic and anodic reactions. From the figure, it also follows that conditions which shift the point of intersection of the anodic and cathodic polarization curves by decreasing their slopes, lead to an increase in dissolution rate. Conversely, an increase in the slopes of the curves lowers the dissolution rate.

It should be emphasized that activation overpotential, η_r, is caused by slow reactions in the solution close to the electrode (reaction overpotential) and in the process of deposition of a solid product on the electrode (crystallization or ohmic overpotential). Concentration or diffusion overpotential, η_D, on the other hand, develops when the activity of the potential generating substance decreases substantially at the electrode in comparison with that in the bulk solution.

Finally, we note that different faces of a crystal dissolve at different rates. This aspect has been discussed by Despic'(10). The difference has been attributed to structural changes at the surface and the varying participation of different crystal planes at a face of a given orientation.

Dissolution of Semiconductors. The mechanism of dissolution of semiconductors is essentially similar to that of metals, described above. The basic difference in the dissolution behavior of metals and semiconductors lies in the concentration and type of charges responsible for surface reactions. In semiconductors, the concentration of charge carriers is much smaller than in metals because of the predominantly covalent nature of bonding. The electron transfer process may involve either valence band or conduction band electrons at the semiconductor electrode while only conduction band electrons take part at metal electrodes. Furthermore, the kinetics of dissolution of metals is determined by electrochemical reactions occurring in the solution or at the solution-metal interface, whereas the rate-determining process in the dissolution of semiconductors may also involve phenomena taking place inside the surface.

In contrast with metals, there are two types of carriers that can take part in the anodic and cathodic partial reactions involved in the dissolution of semiconductors: electrons in the conduction band and holes in the

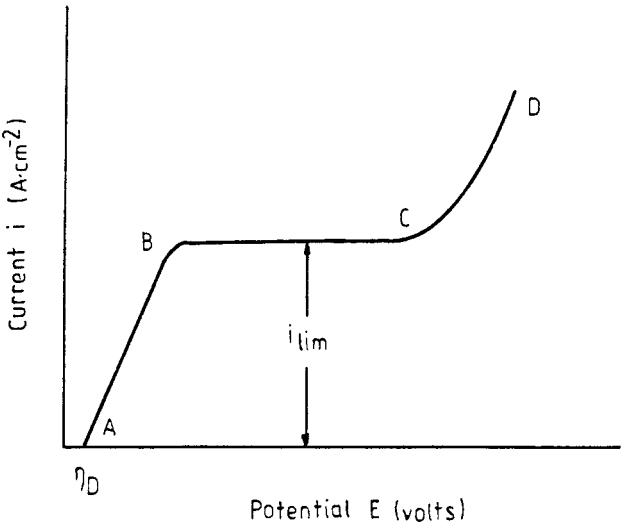

Figure 1. Schematic illustration of the dependence of current density on electrode potential showing concentration overpotential (8).

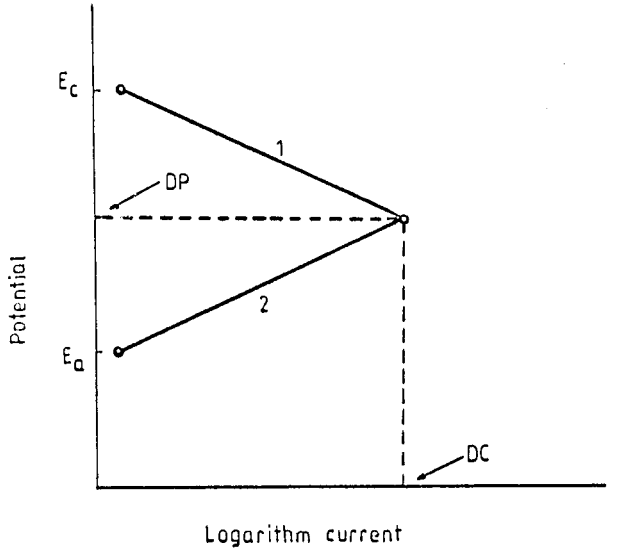

Figure 2. Simplified polarization diagram illustrating the electrochemical mechanism of dissolution (9): (DP) dissolution potential, (DC) dissolution current, (1) cathodic polarization, and (2) anodic polarization.

valence band. Thus in acidic solutions such as HNO_3, the anodic reaction is as follows (9):

$$Si + 3H_2O \longrightarrow H_2SiO_3 + 4H + 4ae^-, \text{ valence band,}$$

$$Si + 3H_2O \longrightarrow H_2SiO_3 + 4H + 4(1\text{-}a)e^-, \text{ conduction band,}$$

or,

Eq. (44) $$Si + 3H_2O + 4ae^+(\text{holes}) \longrightarrow H_2SiO_3 + 4H + 4(1-a)e^-$$

where a is the fraction of electrons entering the valence band. The negative charges left in the silicon are used up in the cathodic reaction, but they are not directly taken up by the acid. Instead they are used up by the products of the acid that are stronger oxidizing agents. An initial reaction is believed to take place between nitric and nitrous acids:

Eq. (45a) $$HNO_2 + HNO_3 \longrightarrow 2NO_2 + H_2O$$

The charges are then taken up by NO_2

Eq. (45b) $$2NO_2 + 2e^- \longrightarrow 2NO_2^-$$

The nitrite ions subsequently react again to yield more HNO_2 that feeds back to reaction (45a):

Eq. (45c) $$2NO_2^- + 2H^+ \longrightarrow 2HNO_2$$

Therefore the overall cathodic reaction may be given by,

Eq. (46a) $$2HNO_3 + 4H^+ + ce^- \text{ (valence band)} + (1-c)e^- \text{ (conduction band)} \longrightarrow 2HNO_3 + 2H_2O, \text{ or}$$

Eq. (46b) $$2HNO_3 + 4H^+ + (1-c)e^- \longrightarrow 2HNO_2 + 2H_2O + ce^+$$

where c is the fraction of electrons that enter the valence band.

By combining the anodic and cathodic reactions given by Eqs. 44 and 46b, one gets

Eq. (47a) $$Si + H_2O + 2HNO_3 \longrightarrow H_2SiO_3 + 2HNO_2 + 4(c-a)e^- + 4(c-a)e^+$$

In the steady state, sufficient HNO_2 is provided by reaction (45c) to feed

reaction (46c). Once a reaction initiates, it provides its own starting material (autocatalytic reaction).

In place of the cathodic reaction of Eq. 46, an alternative reaction:

Eq. (48) $HNO_3 + H^+ + (1-c)e^- \longrightarrow NO + 2OH^- + ce^-$

has also been used (11)(12). This equation gives the following overall reaction:

Eq. (47b) $3Si + 4HNO_3 + 9H_2O \longrightarrow 3H_2SiO_3 + NO + 4(c-a)e^- + 4(c-a)e^+$

The oxide H_2SiO_3 is insoluble. Therefore, HF or some other reagent is used in the solution to convert it into a soluble compound, e.g.,

Eq. (49) $H_2SiO_3 + 6HF \longrightarrow H_2SiF_6 + 3H_2O$

Thus the overall dissolution may be written by combining this equation with Eqs 47a and 47b, i.e.,

Eq. (50a) $Si + 2HNO_3 + 6HF \longrightarrow H_2SiF_6 + 2HNO_2 + 2H_2O$

Eq. (50b) $3Si + 4HNO_3 + 18HF \longrightarrow 3H_2SiF_6 + NO + 8H_2O$

From Eqs. 47a and 47b, we note that the rate of production of electrons and holes is proportional to (c - a), and is equal to (c - a) times the dissolution rate. For $c > a$, there is a net generation of electrons and holes, implying, thereby, that the dissolution process is not controlled by charge carriers (carrier control). For $c < a$, on the other hand, there is a net consumption of electrons and holes by the dissolution reaction. This means that, in this case, the supply of carriers controls the dissolution process (diffusion control). It should be noted that electrons and holes are produced in equal numbers during the electrochemical dissolution of semiconductors (Eqs 47a, 47b).

If there is a net consumption of carriers during dissolution, then the rate of consumption of holes by the anodic reaction exceeds their rate of production by the cathodic reaction, so that the supply of holes by thermal generation and diffusion could determine the rate when an n-type material is used for dissolution. Similarly, when the rate of consumption of electrons by the cathodic reaction exceeds their rate of production by the anodic reaction, the supply of electrons could be the rate-determining step when a p-type material is used.

The stoichiometry of reactions 47 and 50 predicts the value of the

molar ratio, γ_m, of oxidant to complexing reagent* (i.e. $[HNO_3]/[HF]$) corresponding to the maximum rate of dissolution. The reaction of Eq. 50b, for example, gives the maximum dissolution rate for $\gamma_m^* = 0.22$ (11)(13), while that of Eq. 50a predicts $\gamma_m^* = 0.33$, but because of the autocatalytic charater of the oxidation process, the ratio will probably be lower (14). Equation 50 corresponds to the stoichiometry of the reaction determined by surface reactions, but Eq. 47, involving reaction by autocatalytically formed HNO_2, indicates that the stoichiometry is determined by reactions between the electric double layer and the bulk solution.

The reactions of Eqs. 50a and 50b correspond to complete oxidation of the semiconductor as SiO_2. However, if the depletion of the oxidizing agent in the vicinity of the interfacial layer is fast, incomplete oxidation takes place in which the number of charges involved in the oxidation process is less than that predicted by these equations. For example, corresponding to Eq. 50b for the dissolution of Si we have (15):

Eq. (51) $$Si + (z/3)HNO_3 + 6HF \longrightarrow H_2SiF_6 + (z/3)NO + (2z/3)H_2O,\ z < 4$$

The value of z decreases in the order 4, 3, 2 and 3/2 for SiO_2, Si_2O_3, SiO *and* Si_3O_2, *respectively. Similarly, corresponding to the maximum rate,* the molar ratio also decreases for z = 4, 3, 2 and 3/2, in the order $\gamma_m^* =$ 0.22, 0.16, 0.11 and 0.083.

The above basic ideas on the etching of elemental semiconductors are equally valid for compound semiconductors. However, in the latter case, the partial reaction at the anode gives two oxidation products, e.g., (16)

Eq. (52) $$GaAs + 10OH^- + 6e^+ \longrightarrow GaO_2^- + AsO_3^{3-} + 5H_2O$$

where OH^- ions are formed by the well known electrolysis reaction:

Eq. (53) $$2H_2O + 2e^- \longrightarrow 2OH^- + H_2$$

The mechanism of dissolution of semiconductors usually involves a number of discrete steps in which intermediate reactions corresponding to surface states take place (17-25). For example, to describe the dissolution kinetics of GaAs in CrO_3-HF solutions, the following oxidation and reduction steps have been proposed (19)(25). Oxidation of GaAs takes place in a series of consecutive steps:

Eq. (54) $$\backslash\ /\ Ga{:}As\ /\ \backslash + e^+ \xrightarrow{k_1} \backslash\ /\ Ga \bullet As\ /\ \backslash$$

Eq. (55) 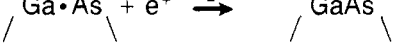

Eq. (56) 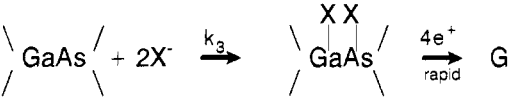

In these equations, X^- is a nucleophilic reagent. Thus, in all, six holes are required to dissolve one GaAs molecule. The reduction reaction in which holes are injected into the valence band, is given by:

Eq. (57) $$[Cr^{VI} - Cr^{VI} - Cr^{VI}] \xrightarrow{k_4} [Cr^{III} - Cr^{III} - Cr^{III}]_{ads} + 6e^+$$

where it is assumed that the trichromate ion $[Cr^{VI} - Cr^{VI} - Cr^{VI}]$ is the electroactive species. The model involves a depassivation of the adsorbed complex with activated surface states from the GaAs oxidation process, i.e.,

Eq. (58) 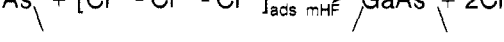

Here k's are rate constants of the reactions. The overall partial reactions are:

Eq. (59a) $$GaAs + 6e^+ \longrightarrow Ga^{III} + As^{III}$$

Eq. (59b) $$[Cr^{VI} - Cr^{VI} - Cr^{VI}] \longrightarrow Cr^{II} + 2Cr^{III} + 10e^+$$

Thus the surface coverage due to the adsorbed film is important in etching kinetics, and the injection of holes from Cr^{VI} and dissolution of GaAs via nucleophilic attack are possible only at the free surface.

Information about the mechanism of dissolution of semiconductors may be obtained from investigations of current-potential characteristics of a semiconductor-electrolyte system (16)(18-23), and from photoluminescence and electroluminescence spectra of semiconductor-electrolyte interface (26-28). For details of surface reaction mechanisms, the reader is referred to the above cited literature.

Figures 3a and b show the current-potential curves for p-type (100) GaAs electrodes in 0.05 and 0.5 M $K_3Fe(CN)_6$, respectively, at pH 13. It is obvious from the figures that the total current-potential curves (1) show three distinct plateaus. The partial cathode current due to $Fe(CN)_6^{3+}$ reduction (curve 2) (obtained by using a ring-disk electrode) and the partial anodic current due to GaAs reduction (curve 3) (obtained by subtracting the cathodic current from the total current) reveal a number of

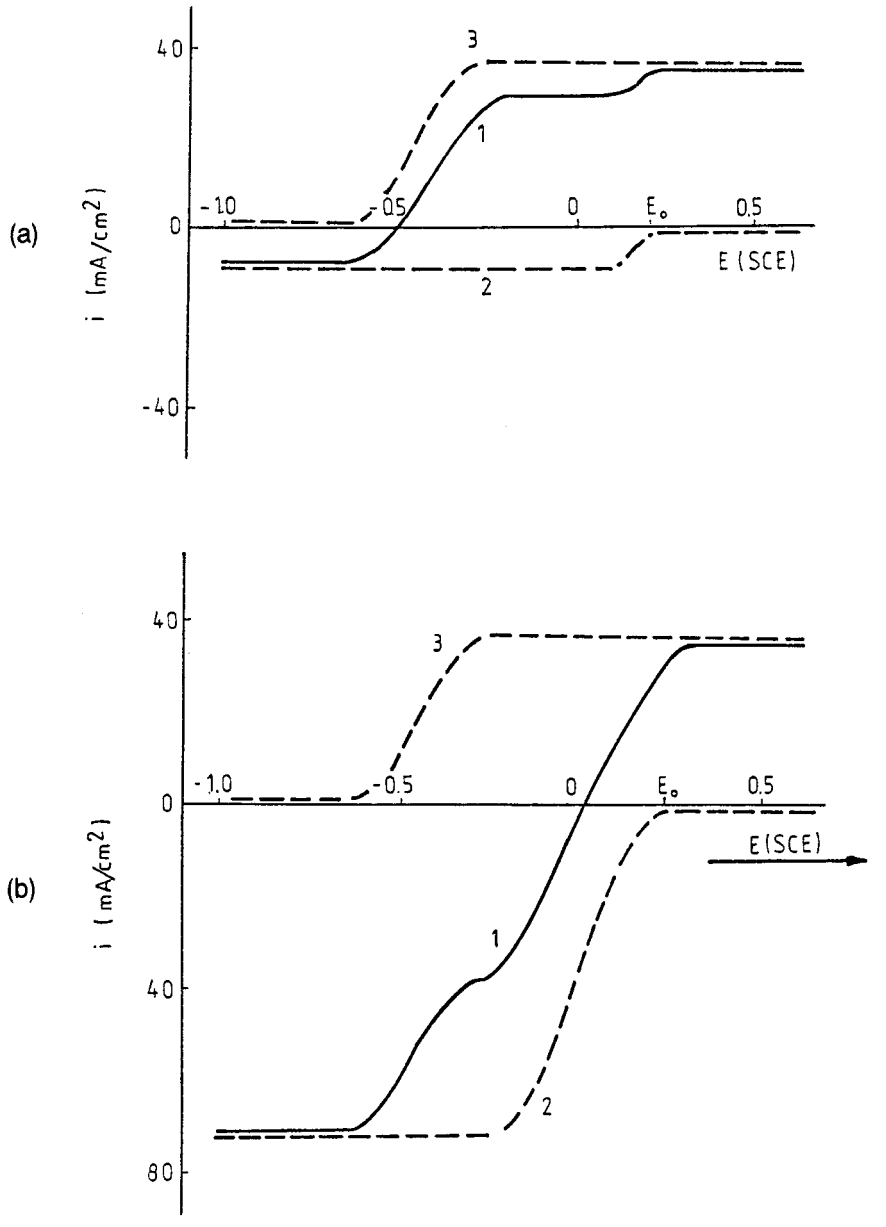

Figure 3. Current-potential curves for p-type (100) GaAs electrode in (a) 0.05 M and (b) 0.5 M $K_3Fe(CN)_6$ solutions at pH 13: (1) total curve; (2) and (3) are the cathodic and anodic partial curves. Electrode rotation rate 200 rpm. From Ref. (16).

features:

1. At relatively large positive potentials, anodic partial current is constant.
2. The limiting anodic partial current is much larger than the correponding cathodic current.
3. At higher electrolyte concentrations, the limiting current is considerably larger than the corresponding anodic current..

There are two general aspects of the curves of Fig. 3. At voltages greater than E_c, the anodic partial current is constant at both low and high concentrations. Dissolution, in this case, depends on the transport of OH^- ions to the electrode surface. At voltages smaller than E_c, the cathodic partial current is larger than the corresponding anodic current for higher electrolyte concentration, while the cathodic current is smaller than the corresponding anodic current at lower electrolyte concentrations. This difference is due to the fact that, at low electrolyte concentration, the dissolution kinetics are determined by the reduction of the oxidizing agent, while at high concentration, they are controlled by the anodic reaction (i.e. OH^- diffusion), and the rest potential of the system is much more positive than that at low concentrations.

2.5 Dissolution Kinetics in Terms of Surface Adsorption Layers

In the area of crystal growth from solution, the growth process is considered to occur according to the following consecutive steps:

1. Transport of solvated growth units from the supersaturated bulk solution to the crystal surface.
2. Adsorption of the growth units onto the surface to constitute a loosely adsorbed surface layer.
3. Migration of adsorbed growth units over the surface.
4. Integration of growth units at energetically favorable sites (i.e. kinks) available at ledges, and release of solvent molecules from the solvated growth units.
5. Transport of the released solvent molecules to the bulk solution.

These steps are very similar to those described Sec. 2.3. Steps 1 and 5 are controlled by the usual diffusion kinetics, while steps 2, 3 and 4 are controlled by the kinetics of surface adsorption, surface diffusion and of integration of growth units at kinks.

The source of kinks is a crucial factor in the theories based on the concept of surface adsorption layers. In the case of a perfect crystal, the kinks may be supplied by two-dimensional nuclei forming on its smooth, flat surface, but, if there are dislocations emerging on the surface, they may serve as unending sources of kinks.

In dissolution, the sequence of steps is reverse to that in growth. Therefore, as in growth, we have the following two types of models: two-dimensional nucleation models, and surface diffusion models.

Two-dimensional Nucleation Models. Dissolution of a perfect, flat surface can occur if there is a change in the free energy of the system (Fig. 4), i.e.,

Eq. (60) $\Delta G_p = 2\pi r h\gamma - \pi r^2 h\Delta\mu / \Omega$

where r is the radius of the developing circular disk-shaped nucleus of height h, γ is the surface energy, Ω is the molar volume, and $\Delta\mu$ is the potential difference given by Eqs. 6 and 9. The critical radius r* of a nucleus that can grow larger to give a dissolution ledge may be obtained by taking $dG_p / dr = 0$, i.e.,

Eq. (61) $r^* = \gamma\Omega / \Delta\mu$

and the corresponding free energy change (cf Eq. 60),

Eq. (62) $\Delta G_p^* = \pi h\gamma^2\Omega / \Delta\mu$

The rate of two-dimensional nucleation (i.e. number of nuclei of radius, r*, formed per unit area per unit time) is given by,

Eq. (63) $J = J_o \exp\{-\Delta G_p^*/kT\}$

with pre-exponential factor $J_o \approx 10^{12}$ /sec.

Depending on the rate of movement and the nature of formation of two-dimensional nuclei, we have three types of two-dimensional nucleation models (29). In the mononuclear model, the rate-limiting step is the formation of a critically-sized nucleus of height, h, and once it is formed, it spreads across the surface at an infinite rate, i.e., $v_\infty = \infty$. The surface dissolution rate, v_p, is given by

Eq. (64) $v_p = AJh$

where A is the total area of the dissolving crystal. In the polynuclear model, the lateral spreading velocity $v_\infty = 0$, but dissolution takes place by the accumulation of critically-sized nuclei. The surface dissolution rate then is

Eq. (65) $v_p = \pi r^{*2} Jh$

The mononuclear model predicts that v_p depends on the area, A, of the dissolving crystal, while the polynuclear model predicts that the dependence of v_p on undersaturation, $\sigma = (c_o - c) / c_o = \Delta\mu / kT$, should show a maximum. Such dependences have not been observed experimentally.

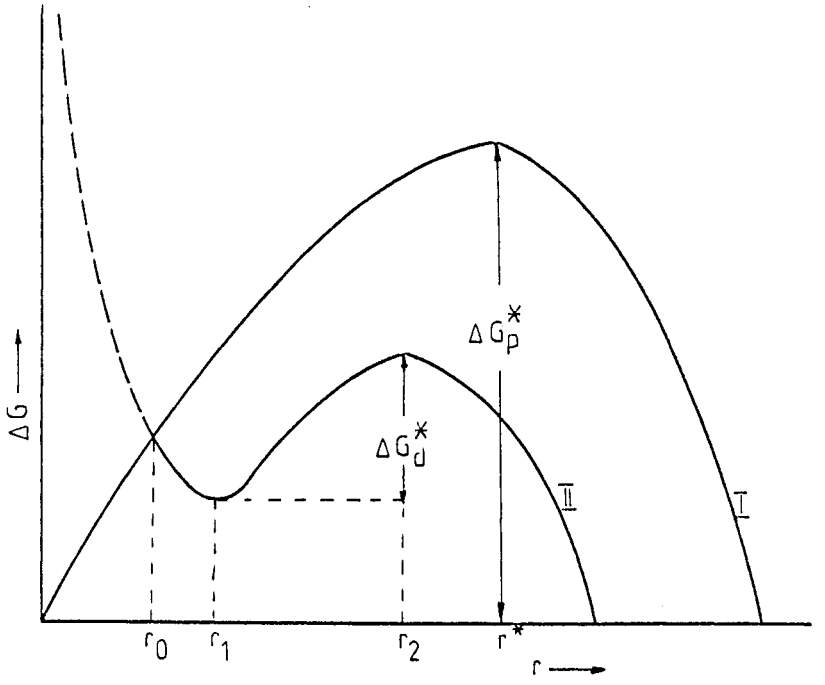

Figure 4. Schematic representation of the free energy change involved during the formation of two-dimensional circular dissolution nuclei on: (I) a perfect surface, and (II) at the emergence points of a dislocation.

Thus it is believed that these models probably represent extreme situations of the rate of lateral spreading of the stable nuclei.

In the birth-and-spread model, it is assumed that nuclei develop and spread at finite velocities. Here the dissolution rate

Eq. (66) $v_p = hJ^{1/3} v_\infty^{2/3}$

and the spreading velocity of a straight ledge is given by,

Eq. (67) $v_\infty = 2c_o' D_s \Omega \{\exp(-\Delta\mu/kT) - 1\} \beta\Lambda / h\lambda_s$

where c_o' is the equilibrium solute concentration on the surface, λ_s is the interdiffusion distance, β and Λ are retardation factors connected with interstep and interkink distances, respectively, and are always less than unity, and D_s is the surface diffusion coefficient. Then from Eqs. 63, 66 and 67, one obtains

Eq. (68) $v_p = B (\Delta\mu/kT)^{5/6} \exp\{-(\Delta G_p^*)/(3kT\Delta\mu)\}$, with

Eq. (69) $B = 2h^{1/6} \Omega^{5/6} (\bar{v}/\pi)^{1/3} (n_1 D_s \beta\Lambda c_o'/\lambda_s)^{2/3}$

where $\bar{v}$ and n_1 are the mean velocity and concentration of surface adsorbed molecules/atoms, respectively.

According to Eq. 68, $v_p = B(\Delta\mu/kT)^{5/6}$ at relatively high values of $(\Delta\mu/kT)$, while $v_p/(\Delta\mu/kT)^{5/6}$ is an exponential function of $(\Delta\mu/kT)^{-1}$ at low $(\Delta\mu/kT)$ values.

Surface Diffusion Model. This model, developed by Burton, Cabrera and Frank (30) postulates the presence of screw dislocations which ensure a constant source of kinks by virtue of the geometrical arrangement of atoms/molecules at their cores. Thus dissolution can proceed by the removal of atoms from these unending sources of kink sites. Since the unwinding ledge is fixed at the emergence point of a dislocation and its inner parts move radially at a faster rate than the outer parts, the ledge will yield a depression spiral.

The spacing, y_o, between successive ledges emanating from the dislocation is given by (31)

Eq. (70) $y_o = 19r^*$

and the velocity of the step is given by (30),

Eq. (71) $v_\infty = (\Omega/h\lambda_s) 2D_s c_o' \beta\Lambda(\Delta\mu/kT) \tanh(y_o/2\lambda_s)$

The dissolution rate normal to the surface is expressed as

Eq. (72) $v_p = v_\infty h/y_o = C\{(\Delta\mu)^2/kT\Delta\mu_1\}\tanh(\Delta\mu_1/\Delta\mu)$, where

Eq. (73) $\Delta\mu_1 = 19\gamma\,\Omega/2\lambda_s$, and

Eq. (74) $C = \Omega\beta\Lambda\, c_o' D_s/\lambda_s^2$

Equation 20 predicts that $v_p = C(\Delta\mu/kT)$ for $\Delta\mu >> \Delta\mu_1$, and $v_p = (CkT/\Delta\mu_1)(\Delta\mu/kT)^2$ for $\Delta\mu << \Delta\mu_1$.

Edge dislocations have their Burgers vector in the plane of the dissolved crystal surface. Therefore they are not expected to act as nucleation centers for dissolution. However, Keller (32), and Bauser and Strunk (33)(34) showed that edge dislocations can also act as persistent sources of steps for growth and dissolution. Bauser and Strunk (33)(34) attributed the nucleation at an edge dislocation to its dissociation into two partial dislocations with a possible reconstruction of the dislocation emergence point to yield a step at the surface. Frank (35) suggested that surface stresses of the same order of magnitude as their surface free energies associated with an edge dislocation provide regions compressed on one side and dilated on the other side. These surface stresses supply the extra energy required for the formation of nuclei even if no dislocation component perpendicular to the surface is present.

Information about the actual dissolution mechanism based on surface adsorption layers may be obtained from analysis of kinetic data on the undersaturation dependence of dissolution rate and observation of surface morphology of etched surfaces (36).

3.0 MECHANISM OF SELECTIVE ETCHING

In the preceding section, we were dealing with general dissolution of a crystal without considering some specific points on its surface, which may dissolve selectively. However, it is usually observed that, apart from the general dissolution, etching also leads to the formation of etch pits or hillocks at the sites of defects emerging on the crystal surface. All types of defects ranging from one- to three-dimensional ones act as the sites of preferred or selective etching. The resulting etch figures are characteristic of the distribution and nature of defects revealed during etching. In this section we describe briefly the mechanism of formation of etch pits at the sites of dislocations.

The formation of etch pits at the sites of dislocations is possible when the rate of nucleation of pits of unit depth along the dislocation line,

v_n, the rate of lateral motion of steps of these nuclei away from the source of nucleation, v_t, and the rate of dissolution of the defect-free surface, v_p, are properly related (Fig. 5). Etch pits are formed only when $v_n > v_p$ but their contrast is determined by the ratio v_n/v_t. Under an optical microscope, etch pits are visible when $v_n/v_t > 0.1$ (37). In the other case, when v_p/v_n, etch hillocks are produced. A decrease in v_n may be caused by insoluble or sparingly-soluble impurities segregated along the dislocation lines or at random sites in the form of precipitates, or by insoluble or sparingly soluble impurities supplied by the etching medium.

Revelation of different types of defects as etch pits is explained in terms of either stresses associated with, or impurities segregated at, them. In the former case, the energy localized at a defect site accelerates the rate of nucleation of unit pits, while in the latter case the rate is increased as a result of enhanced solubility of the material. Impurities may also affect the rate of motion of steps, i.e., v_t, by poisoning them. Thus the whole process of etch-pit formation may be viewed to be comprised of two aspects: thermodynamic and kinetic. The thermodynamic aspect, as we shall see below, is associated with the free-energy change involved, and deals with the rate of etch-pit nucleation. The kinetic aspect, connected with the lateral motion of steps, involves mutual interaction between steps and adsorption of impurities at them.

In Sec. 2 the overall surface dissolution was considered. Except in the case of surface diffusion, we assumed that a dissolving surface is free from defects. Since real crystals usually contain dislocations and other defects, it is necessary to know their effect on dissolution rates and the mechanism of formation of etch pits at their emergence points.

3.1 Models of Etch-Pit Formation

From the geometrical arrangement of atoms around dislocations, it is immediately obvious that screw dislocations should yield etch pits with slope, m, given by:

Eq. (75) $$m = \tan\theta = v_n/v_t = h/y_o = h\Delta\mu/19\gamma\Omega$$

where h is the height of the dissolution ledge, and y_o is given by Eq. 70.

We can check the validity of this model, which is basically the BCF growth model as applied to dissolution, from the experimental data on the etching of the (101) and (100) faces of KH_2PO_4 (36). In this case, dislocation etch pits are produced at undersaturation $\sigma > 0.06$ (i.e., $\Delta\mu > 2.33\times10^{-22}$ J at T = 300°K). Taking $\gamma = 0.01$ J/m^2, $h = 7.4\times10^{-10}$ m and $\Omega = 1.73\times10^{-28}$ m^3, one obtains m = 0.00524, a very small slope indeed with $\theta = 0.3°$. Such spiral etch pits cannot be visible. Moreover, according to

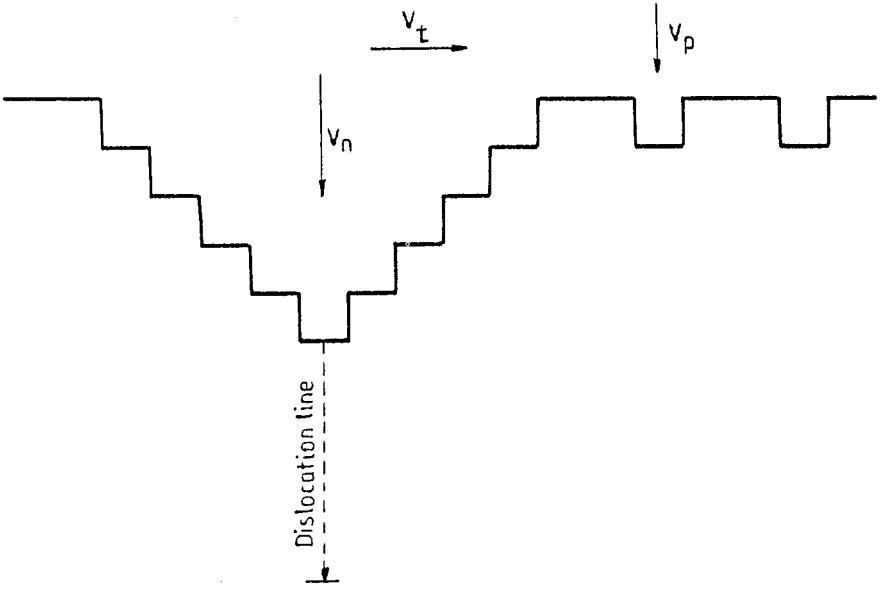

Figure 5. Illustration of the mechanism of the formation of a dislocation etch pit in terms of different etch rates.

this model, the height of dissolution ledges should be equal to the Burgers vector of the screw dislocation being etched. Such etch spirals have not been reported in the literature (2)(35-38). The observed spiral etch pits have ledges of heights of several tens to several thousands of nm (2)(38-40). These spiral depressions are formed by the etching of helical dislocations (38)(39) or by the occurrence of a mistake in the early stages of formation of atomic steps and subsequent bunching of these steps during their motion (40). From the foregoing, the mechanism of formation of visible etch pits at screw dislocations by the unwinding of their helicoidal turns is ruled out. Moreover, etch pits are revealed almost equally at edge and screw dislocations. Thus there should be some other mechanism of etch-pit formation.

Cabrera (31)(41) realized that the elastic strain energy associated with a dislocation can lead to the successive generation of two-dimensional nuclei at its point of emergence on the surface. According to Schaarwächter (42), the core energy of a dislocation ensures this preferred two-dimensional nucleation at dislocations. Hoek, et al. (43), and Koziejowska and Sangwal (44) treated the process of etch-pit formation using equations of total dislocation energy. Here we describe the essential features of the formation of dislocation etch pits according to Cabrera's theory.

The change in the free energy, ΔG_d, for the nucleation of a disk-shaped cavity of depth, h, and radius, r, at the site of a dislocation is given by:

Eq. (76) $$\Delta G_d = 2\pi h \gamma r - \pi r^2 h \Delta\mu / \Omega - h(Gb^2\alpha/4\pi) \ln(r/r_o)$$

where the last term on the right represents the dislocation energy outside its core, the parameter $\alpha = 1/(1-\nu)$ and $\alpha = 1$, respectively, for clean edge and screw dislocations (where ν is Poisson's ratio), r_o is the radius of the dislocation core outside which the elastic continuum theory is valid, G is the shear modulus, and b is the Burgers vector of the dislocation.

The behavior of the free-energy curve is determined by taking the first two derivatives of ΔG_d and equating them to zero. The first derivative, $d\Delta G_d/dr$, gives a quadratic equation having two roots:

Eq. (77) $$r_{1,2} = (\gamma \Omega/2\Delta\mu)(1 \pm \xi), \text{ and}$$

Eq. (78) $$\xi = (Gb^2\alpha/2\pi^2\gamma^2\Omega)\Delta\mu$$

Figure 5 shows the dependence of free-energy change on the radius r of a two-dimensional nucleus. For $\xi < 1$, the critical free-energy change for nucleation of a unit pit at a dislocation is:

Eq. (79) $\Delta G_d^* = \Delta G_d(r_2) - \Delta G_d(r_1)$

and using Eqs. 76 and 77, one gets:

Eq. (80) $\Delta G_d^* = (\pi h \gamma^2 \Omega / \Delta\mu)(1-\xi)^{1/2} + (hGb^2\alpha/4\pi)\ln\{[1-(1-\xi)^{1/2}]/[1+(1-\xi)^{1/2}]\}$

which is valid for $r > r_o$ and $\xi < 1$. Equation 80 gives the decrease in the free energy of nucleation at a dislocation site with respect to that on a perfect surface. When $\xi < 1$, we get:

Eq. (81) $\Delta G_d^* = (\pi h \gamma \Omega / \Delta\mu)(1-\xi)^{1/2} = \Delta G_p^*(1-\xi)^{1/2}$

Thus for $\xi < 1$, there is an energy barrier for etch-pit nucleation at a dislocation site but the value of this barrier is less than that at the perfect surface. For $\xi = 1$, there is a double root:

Eq. (82) $r^{**} = r_1 = r_2 = \gamma\Omega / 2\Delta\mu = r^*/2$, and

Eq. (83) $\Delta G_d^* = 0$

The values of r^* and ΔG_p^* of Eqs. 81 and 82 are given by Eqs. 61 and 62, respectively.

When $\xi > 1$, there is no real root, which means that there is no nucleation barrier for etch-pit formation. Thus, since ξ increases with $\Delta\mu$ (Eq. 78), there is a particular value of $\Delta\mu$ above which dislocations open up spontaneously. The critical value of this $\Delta\mu$ is obtained from Eq. 78 for $\xi = 1$, i.e.,

Eq. (84) $\Delta\mu^* = 2\pi^2\gamma^2\Omega / Gb^2\alpha$

In the region of undersaturation corresponding to $0 < \Delta\mu < \Delta\mu^*$, stationary spiral dissolution or a repeated two-dimensional nucleation process favored by an edge dislocation may take place.

A test of the validity of Cabrera's model is the condition that r_1, r_2 and r^{**} should be greater than r_o, which is believed to be 2 - 3 b. In the case of KH_2PO_4 (36), with the appropriate values of γ, Ω and $\Delta\mu$ given above, one obtains $r^{**} = 37.2\times10^{-10}$ m = 5 b. This means that here Cabrera's model holds true. For the electrochemical etching of {0001} faces of Zn (45), with $\Delta\mu/kT = 30\times10^{21}$ J, $\gamma = 0.1$ J/m^2 and $\Omega = 2.46\times10^{-30}$ m^3, one obtains $r^{**} = 4.1\times10^{-12}$ m = 0.02 b. Thus Cabrera's mechanism is not applicable in this case. Schaarwächter (42) also found that etch-pit formation on metal surfaces requires the consideration of dislocation

core energy. Here we shall not go into the details of the theory which is given elsewhere (2) together with other models.

3.2 The Slope of Dislocation Etch Pits

The slope of etch pits is determined by the normal and tangential etch rates, given by (46),

Eq. (85) $v_n = h\nu \exp\{-(\Delta G_d^* + \Delta H)/kT\}$, and

Eq. (86) $v_t = 2\beta\lambda_s\nu(\Delta\mu/kT)\exp(-\Delta H/kT)$

where ν is the frequency factor of the order of 10^{13}/sec, and ΔH is the free energy change for a molecule going from the crystal surface into the etching medium. Then the slope,

Eq. (87) $$m = [h/2\beta\lambda_s(\Delta\mu/kT)]\exp(-\Delta G_d^*/kT)$$
$$= [h/2\beta\lambda_s(\Delta\mu/kT)]\exp\{-(\pi h\gamma^2\Omega/kT\Delta\mu)(1-\xi)^{1/2}\}$$

It is easy to see from this relation that with an increase in $\Delta\mu$, the pit slope first increases to a maximum value at $\Delta\mu^*$, and finally decreases again. However, for $\Delta\mu > \Delta\mu^*$, depending on the behavior of β, the pit slope may even increase with $\Delta\mu$. The factor β is largely determined by the dissolution kinetics which are governed by the potential difference $\Delta\mu$ and adsorption processes taking place on crystal surface.

The above considerations hold good for fresh dislocations. Several experimental results, however, show that the segregation of impurities at dislocations facilitates the process of etch-pit formation. This behavior is associated with the fact that impurity segregation leads to an increased potential difference and decreases the free-energy change required for the formation of critically-sized two-dimensional nuclei. In such cases, the size and slope of etch pits can vary from those at fresh dislocations, if $v_p << v_n$. This feature may be understood from the model given by Ives and McAusland (47).

If v_p is independent of v_n, the rate of pit widening is

Eq. (88) $dD/dt = v_n - v_p$

where D is the diameter of a pit after time, t. Then, using the equation of pit slope $m = v_n/v_t$, from Eq. 88 one obtains, after rearrangement,

Eq. (89) $m = (1/v_t)(dD/dt) - (v_p/v_t)$

Under steady-state conditions when the etch pits are formed at a constant

rate, we have

Eq. (90) $$m = (1/v_t)\,(D/t) - (v_p/v_t).$$

The following two conclusions can be drawn from Eq. 90:

1. For pits at different defects (different v_n) produced by the same etchant (constant v_p and v_t), a plot of m against (D/t) will be a straight line. The values of v_t and v_p may be estimated from the slope and intercept of the straight line.
2. If $v_p << v_n$, the straight line will pass through the origin and all pits on a given surface, regardless of the type of defect, will have the same width. If v_p is significant, steep pits will be wider than shallow ones.

Several experimental observations in support of the above model are available in the literature. For example, on the (100) face of NaCl etched in ethanol containing $CdCl_2$ impurity (48), pits of different sizes are produced at low impurity concentrations when v_p is large, but the pits have a tendency to acquire the same size when impurity concentration in the etchant is high enough to decrease v_p markedly. These features may be noted from the etch-pit patterns and the kinetic data presented in Figs. 6 and 7, respectively.

According to the above model, the rate of pit widening, v_t, is a function of the composition of an etchant. Such dependences have been noted in the case of Zn (47) and LiF (37)(49). In the case of LiF, the main effect of the impurity FeF_3 was found to decrease v_t. This is expected if it is assumed that v_n is unaffected by the impurity. In the case of NaCl (48), both v_t and v_n decrease or increase simultaneously (Fig. 7). This means that an impurity can not only change v_t as a result of inhibition of ledges and kinks, but also affects v_n through surface energy as a result of adsorption.

3.3 The Role of Impurities

Among the effects of impurities on selective etching, two deserve particular attention. Impurities present in an etching solution facilitate the revelation of etch pits at dislocation and often change the pit morphology. The actual process of impurity adsorption may be quite complicated for different crystal-etchant systems, but certain features are common for different systems.

In the case of etching of the (100) face of NaCl in ethanol containing $CdCl_2$ impurity, it may be seen from Fig. 7 that with an increase in impurity concentration c_{imp}, v_p regularly decreases, but both v_t and v_n first slowly increase and then, at high c_{imp} values after attaining a maximum value,

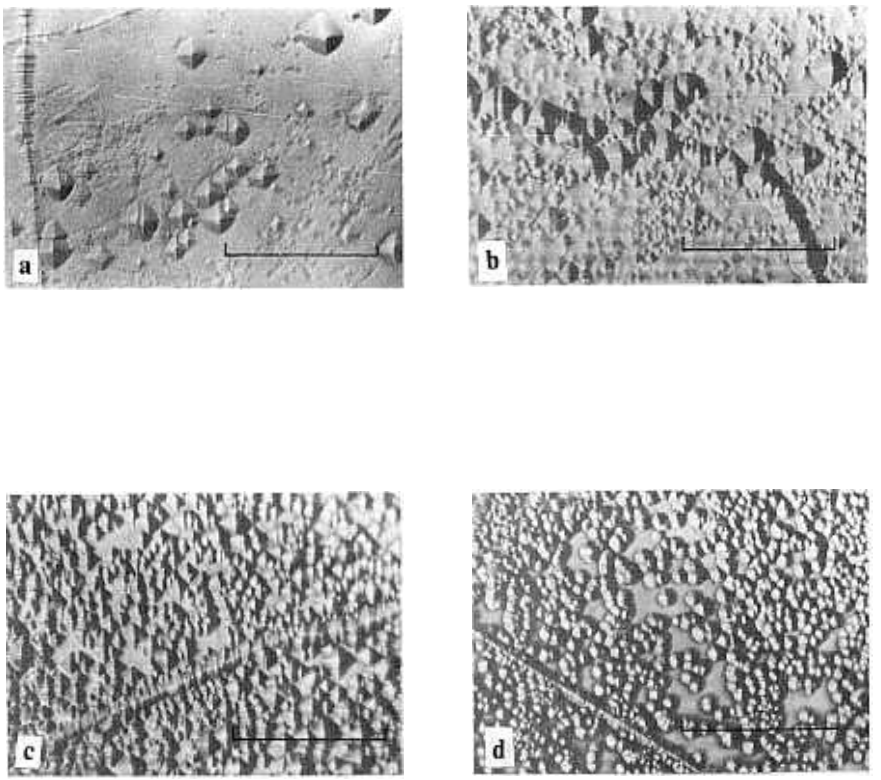

Figure 6. Etch-pit patterns produced after 20 min at 25°C on the (100) face of NaCl by C_2H_5OH containing: (a) 10^{-6} M, (b) 10^{-5} M, (c) 10^{-4} M and (d) 10^{-3} M $CdCl_2$ impurity (48). Marker = 0.1 mm.

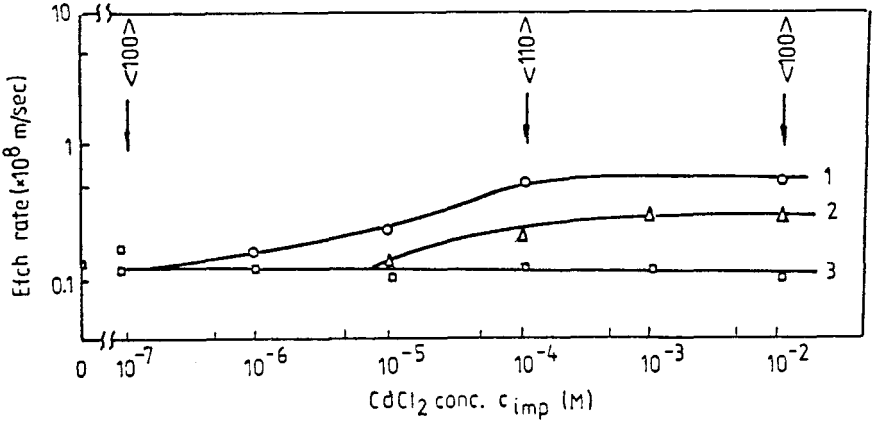

Figure 7. Dependence of etch rates (1) v_t, (2) v_n and (3) v_p for the (100) face of NaCl crystals on $CdCl_2$ concentration in C_2H_5OH (48). The arrows indicate the relationship between impurity concentration and morphology of dislocation etch pits.

show a slow decreasing tendency. The region of c_{imp} in which v_t and v_n increase with impurity content corresponds to the region in which pits of different size are formed (Fig. 6); pits of the same size are produced at or beyond impurity concentrations which give maximum values of v_t and v_n. At very high impurity concentrations, the impurity starts depositing on the dissolving surface (50).

The formation of etch hillocks on the (001) face of white tin with increasing concentration of $CuSO_4$ impurity (51)(52) provides a close similarity with the etching behavior of NaCl. The results on the morphology of etched surfaces and the dependence of hillock size on the impurity content in the etchant are presented in Figs. 8 and 9, respectively. The dependence of hillock size on c_{imp} shows three distinct regions, as indicated in Fig. 9. In Region I the rate of hillock development increases, in Region II it decreases, while in Region III the displaced metal precipitates epitaxially and hillocks are not produced. As in the case of etch pits on the (100) face of NaCl, at low c_{imp} the hillocks have different sizes, but at higher salt concentrations, around the maximum rate, their sizes are uniform.

It is well known that dislocation etch pits on the surfaces of metals are produced in solutions of salts of other metals as a result of contact displacement reactions (53)(54). The size of pits formed by these solutions depends on the concentration of a salt and the time of etching. However, prolonged etching often leads to the precipitation of mono- or polycrystalline displaced metal at relatively more active sites where dissolution is faster than that at the rest of the surface. Subsequent etching can yield etch hillocks, as observed in the case of etching white tin in acidic solutions of $CuSO_4$. Whether etch hillocks or etch pits will be formed at dislocation sites is determined by the exchange kinetics at the electric double layer and by the diffusion kinetics.

If A is the metal being etched and B is in the form of the salt, the condition for the displacement reaction to occur is that the electrode potential of B in the solution of B^{n+} ions is higher than that of the crystal A in the solution of A^{m+}, i.e., $E(B^{n+}/B) > E(A^{m+}/A)$, or,

$$\text{Eq. (91)} \qquad E^{\circ}(B^{n+}/B) + (RT/nF) \ln [a(B^{n+})] > E^{\circ}(A^{m+}/A) + (RT/mF) \ln [a(A^{m+})]$$

where $E^{\circ}(A^{m+}/A)$ and $E^{\circ}(B^{n+}/B)$ are, respectively, the standard electrode potentials of A and B, and $[a(A^{m+})]$ and $[a(B^{n+})]$ are the activities of the cations in solution.

Taking displacement reactions as the basis and assuming that the adsorption potential at the site of a dislocation (D), double kink, i.e., a pair of neighboring kinks of opposite sign in a ledge (DK), ledge (L), and surface terrace (T) changes in the sequence D > DK > K > L > T, one finds

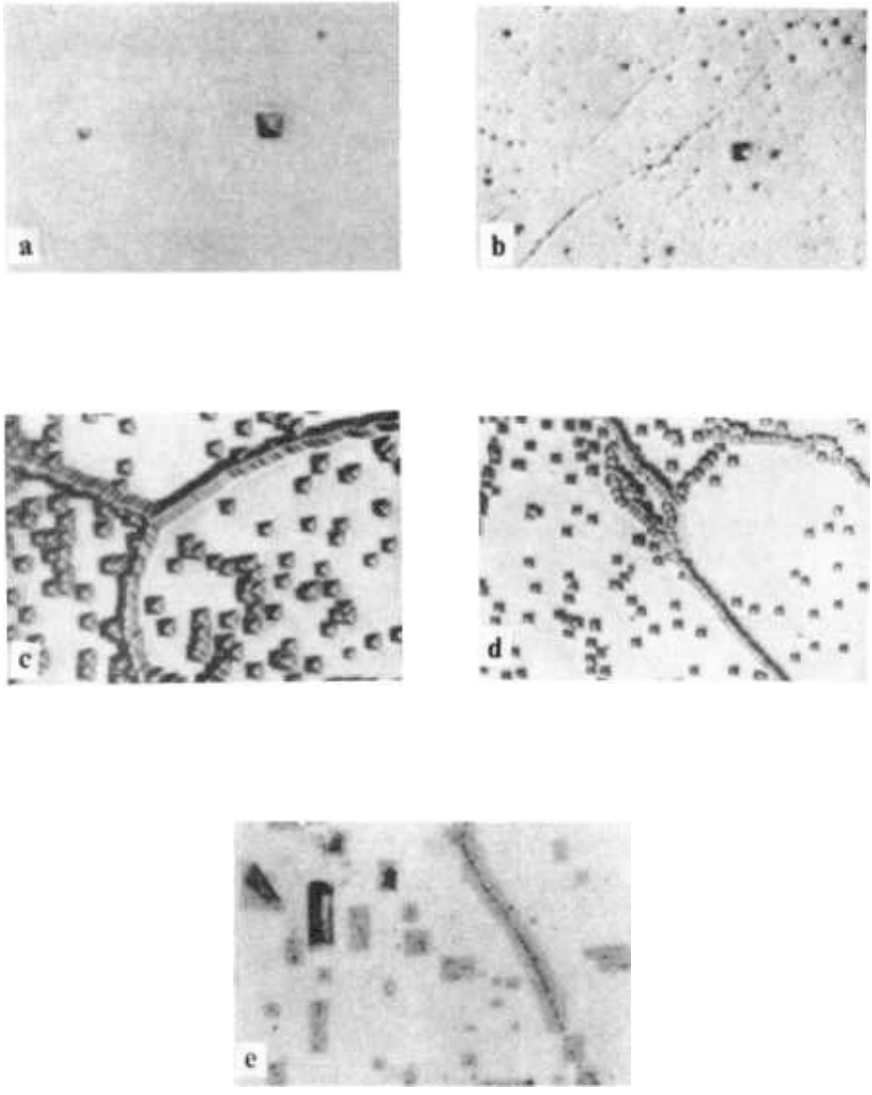

Figure 8. Effect of addition of $CuSO_4$ to an etching solution composed from 10 ml HCl + 10 g NH_4NO_3 + 50 ml H_2O on the formation of etch hillocks on the (001) face of white tin: (a) no impurity (b) 9.4×10^{-6} M, (c) 9.4×10^{-5} M, (d) 1.9×10^{-4} M, and (e) 9.4×10^{-3} M $CuSO_4$; etching time: (a - d) 3 min. and (e) 30 sec. From Ref. (51).

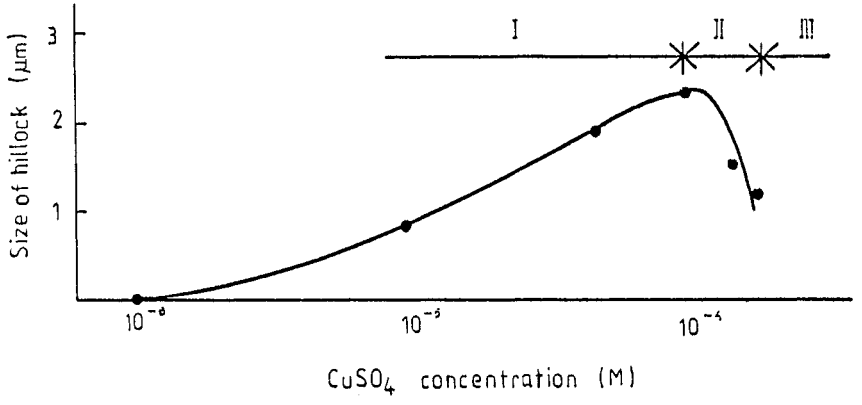

Figure 9. Dependence of the size of hillocks produced after 3 min etching on the (001) face of white tin on the concentration of $CuSO_4$ in the etching solution of Fig. 8 (51).

that the reaction is fastest at the dislocation site. Hence, in the absence of deposition of products, dissolution is more along the dislocation line than at the perfect surface. This mechanism also explains simultaneous changes in v_n and v_t as well as etch pit morphology with changes in impurity concentration. The effects of impurity on dislocation etch-pit morphology are discussed in detail elsewhere (2).

4.0 COMPOSITION OF ETCHING AND POLISHING SOLUTIONS

Etching solutions reported in the literature for revealing dislocations and surface polishing of crystals have been formulated by trial and error, and are often widely different from each other. The concepts on the chemistry of dissolution and the mechanism of etch-pit formation, described in the preceding sections, are useful in explaining their etching behavior. For the sake of clarity in discussion on the composition of etching and polishing solutions, the crystals are classified below according to chemical bonding and their dissolution behavior towards an etching solution.

4.1 Ionic crystals

Water-soluble Crystals. Typical etching solutions that produce etch pits on the surface of ionic crystals, fairly-soluble in water, are composed of a solvent with or without an added impurity. The solvents commonly used are water, lower aliphatic alcohols such as CH_3OH and C_2H_5OH, and acids such as HCOOH and CH_3COOH. However, the ability of a solvent to reveal the emergence points of dislocations decreases in the homologous series of organic alcohols and acids with the addition of a CH_2 group (55-57). This behavior is due to the existence of a critical undersaturation barrier (57) (Sec. 3.1, Eq. 84) whose value decreases with a decrease in the value of interfacial tension γ as a result of an increase in the solubility of the crystal in a solvent. However, it is also observed that the etch pits formed on a crystal surface by a fast solvent are somewhat shallow. This is connected with the lowered value of undersaturation in the immediate vicinity of the dissolving crystal because of the impeded exchange of subsaturated solution with the fresh solvent due to the diffusion-controlled nature of dissolution in fast solvents.

Acids, organic or inorganic, always react with the crystalline substance. Therefore, addition of an acid can increase etch rates as a result of chemical reactions (Sec. 2.4). However, by virtue of their low dielectric constant, which determines the solubility of the substance, their addition also decreases the rate. In the case of organic acids the latter effect is predominent, while in strong inorganic acids the former effect is predominent.

Next Page

Previous Page

that the reaction is fastest at the dislocation site. Hence, in the absence of deposition of products, dissolution is more along the dislocation line than at the perfect surface. This mechanism also explains simultaneous changes in v_n and v_t as well as etch pit morphology with changes in impurity concentration. The effects of impurity on dislocation etch-pit morphology are discussed in detail elsewhere (2).

4.0 COMPOSITION OF ETCHING AND POLISHING SOLUTIONS

Etching solutions reported in the literature for revealing dislocations and surface polishing of crystals have been formulated by trial and error, and are often widely different from each other. The concepts on the chemistry of dissolution and the mechanism of etch-pit formation, described in the preceding sections, are useful in explaining their etching behavior. For the sake of clarity in discussion on the composition of etching and polishing solutions, the crystals are classified below according to chemical bonding and their dissolution behavior towards an etching solution.

4.1 Ionic crystals

Water-soluble Crystals. Typical etching solutions that produce etch pits on the surface of ionic crystals, fairly-soluble in water, are composed of a solvent with or without an added impurity. The solvents commonly used are water, lower aliphatic alcohols such as CH_3OH and C_2H_5OH, and acids such as HCOOH and CH_3COOH. However, the ability of a solvent to reveal the emergence points of dislocations decreases in the homologous series of organic alcohols and acids with the addition of a CH_2 group (55-57). This behavior is due to the existence of a critical undersaturation barrier (57) (Sec. 3.1, Eq. 84) whose value decreases with a decrease in the value of interfacial tension γ as a result of an increase in the solubility of the crystal in a solvent. However, it is also observed that the etch pits formed on a crystal surface by a fast solvent are somewhat shallow. This is connected with the lowered value of undersaturation in the immediate vicinity of the dissolving crystal because of the impeded exchange of subsaturated solution with the fresh solvent due to the diffusion-controlled nature of dissolution in fast solvents.

Acids, organic or inorganic, always react with the crystalline substance. Therefore, addition of an acid can increase etch rates as a result of chemical reactions (Sec. 2.4). However, by virtue of their low dielectric constant, which determines the solubility of the substance, their addition also decreases the rate. In the case of organic acids the latter effect is predominent, while in strong inorganic acids the former effect is predominent.

Consequently, addition of small amounts of strong acids to slow solvents is found to have a marked favorable effect on the revelation of dislocation etch pits, while in organic acid the etch-pit contrast is poor.

Addition of trace amounts of ionic salts to slow solvents is found to be equally effective in producing contrasting etch pits as, for example, on the surfaces of alkali halide crystals (see Fig. 6).

Water-insoluble Crystals. Aqueous solutions of mineral acids, acidic salts and alkalies, and melts of alkalies and salts are the usual dislocation etchants for water-insoluble crystals. However, in order to reveal dislocations in some cases, particularly hard crystals, it is desirable to manipulate etching conditions, such as etchant composition, temperature and time of etching. Low concentrations and low temperatures are generally suitable for revealing dislocations in these crystals by mineral acids (58-60). At high concentrations and elevated temperatures, H_2SO_4 and H_3PO_4 often exhibit polishing action.

Figure 10 shows a typical curve of the temperature dependence of the polishing rate of the (111) face of gadolinium gallium garnet single crystals in H_3PO_4. Etch pits are observed in the temperature interval of the ascending part of the curve but for higher temperatures, at which the rate decreases, polishing takes place.

It should be pointed out that during the etching of water-insoluble crystals, an insoluble or sparingly-soluble reaction product may deposit on the crystal surface.

4.2 Molecular Crystals

The selective etching behavior of molecular crystals is similar to that of ionic crystals. Etch pits can be revealed by solvents in which a crystal is soluble or solutions which can react with the crystal (61).

4.3 Metallic Crystals

The etching of metals takes place according to one of the following mechanisms:

(i) *Simple reactions.* Here the metal is directly converted into reaction products. For example, etching of Zn in non-oxidizing acids and alkalies takes place according to the reactions:

Eq. (92a) $Zn + 2HCl \longrightarrow ZnCl_2 + H_2$

Eq. (92b) $Zn + 2NaOH \longrightarrow Zn(OH)_2 + 2Na^+$

(ii) *Redox reactions.* In this case a metal atom is oxidized, while

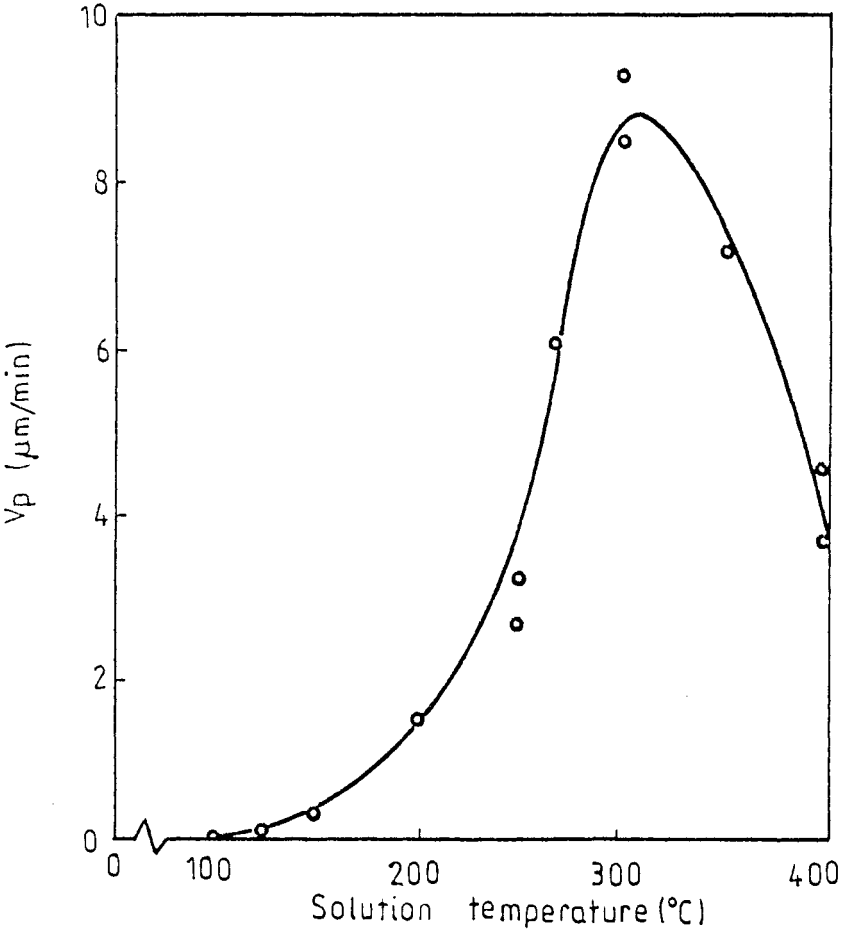

Figure 10. Dependence of the polishing rate of the (111) face of gadolinium gallium garnet in H_3PO_4 on etching temperature (60).

an atom or radical of the reagent is simultaneously reduced (Sec. 2.4). Oxidation of the metal is caused by an oxidizing reagent such as HNO_3, Br_2, I_2, or by a cation of variable valency (e.g., Cr^{3+}, Fe^{3+}, Cu^{2+}, Ni^{2+}, etc.):

Eq. (93a) $2Cu + HNO_3 \longrightarrow Cu_2O + HNO_2$

Eq. (93b) $Cu + 2FeCl_3 \longrightarrow CuCl_2 + 2FeCl_2$

(iii) *Contact displacement reaction.* Here etching takes place according to Eq. 91:

Eq. (94) $Cu + 2AgNO_3 \longrightarrow Cu(NO_3)_2 + 2Ag$

Any metal can be etched by mechanisms (ii) and (iii), but mechanism (i) holds true only for crystals of negative standard potentials. Thus selective etchants for metals dissolving according to mechanism (i) are confined to one-component systems. The composition of typical etchants for metals according to the above mechanisms are summarized in Table 1. The role of complexing agents, given in the last column of the table, is to dissolve insoluble reaction products forming on the crystal surface by oxidants.

Finally, it should be mentioned that etch pits on metal surfaces are produced when the concentration of the complexing agent in a three-component etching solution, or the diluent in a two-component solution, is moderately high. At low concentrations of the complexing agent or diluent, polishing takes place. However, it should be remembered that etchant pH is also an important parameter during the etching of metals (62).

4.4 Semiconductors

The mechanism of etching of semiconductors is similar to that of metals (Sec. 2.4). Consequently, the compositions of typical etchants for metals and semiconductors are similar. Although melts of KOH and mixtures of KOH and NaOH, and Br_2 or I_2 in CH_3OH are known as etching solutions, the usually-employed etchants for elemental and compound semiconductors are based on an oxidant (HNO_3, H_2O_2 or CrO_3), a complexing reagent (HF, HCl, HBr, H_2SO_4 or H_3SO_4) and a diluent (H_2O or CH_3COOOH).

The salient features of the etching of semiconductors by redox etchants are common for all three-component systems (25)(63)(64). Thus, to describe the etching behavior of semiconductors, consider the CrO_3-HF-H_2O system, whose original components or chemically similar components in different proportions constitute various well known etchants. Si and GaAs, two semiconductors of great interest due to device application, are used for discussion.

Table 1

Composition of typical etchants for metals

Mechanism	Equation	Reactant or oxidant	Diluent or medium	Complexing agent
(i)	(92a)	Acid	H_2O, alcohols, glycerine	-
(i)	(92b)	Alkali	H_2O, alcohols, glycerine	-
(ii)	(93a)	HNO_3	H_2O, alcohols, organic acids	HCl, HF, H_2SO_4
		H_2O_2	H_2O, NH_4OH, organic acids	HF, H_2SO_4
		Br_2, I_2	Alcohols	-
	(93b)	$K_2Fe(CN)_6$	H_2O	-
		Cr^{3+}, Fe^{3+}, Cu^{2+}, Ni^{2+}	H_2O	NH_4OH
(iii)	(94)	Ag^+	H_2O	-

Figure 11 shows the rate of dissolution, v_p, of the (111) face of silicon as a function of the molar concentration $\gamma_m = [CrO_3]/[HF]$ at 10 and 50°C. The rates first increase and then, after passing through a maximum rate at γ_m^*, decrease. In the ascending and descending parts of these curves, the dissolution rate follows the relations:

Eq. (95) $v_{p1} = k_1 \gamma_m^{1/2}$ for $\gamma_m < \gamma_m^*$, and

$v_{p2} = k_2 \gamma_m^{-p}$ for $\gamma_m > \gamma_m^*$

where v_{p1} and v_{p2}, respectively, denote the rates in the ascending and descending parts of the curves of the dependence of the overall dissolution

rate v_p on γ_m, k_1 and k_2 are the corresponding rate constants, and p is a constant. The temperature dependence of the rate constants is given by the Arrhenius equation:

Eq. (96) $k_i = A_i \exp(-E_i/kT)$

The overall dissolution rate for the whole range of the molar ratio is expressed by the empirical equation:

Eq. (97) $v_p = (k_1 k_2 \gamma_m^{1/2})/(8.5 k_1 \gamma_m^{p} + k_2)$

which can be written in the form,

Eq. (98) $1/v_p = (1/v_{p1}) + (8.5/v_{p2})$

The form of Eq. 98 is typical of equations of processes involving simultaneous surface reactions and volume diffusion. Thus it may be believed that at low concentrations of oxidant, the oxidation process is the rate-limiting step, and that at high concentrations, the supply of the oxidant to the surface is the rate-determining step. Information about the rate-determining step can also be obtained from the value of activation energy for dissolution calculated from Arrhenius-type plots of etch-rate data at different temperatures, and from the effect of stirring on etch rates (see also Sec.2.2).

Yang (65) investigated the etching behavior of the (100) and (111) faces of Si in CrO_3-HF-H_2O system using different ratios of γ_m, given in Table 2. It was observed that at low CrO_3 concentrations, rounded etch pits are formed, but with an increase in CrO_3 concentration, the pits become better defined. However, for the (100) and (111) faces, the capability of preferential etching decreases at $\gamma_m > 0.04$ and 0.204, respectively. At higher ratios, although the pits correspond to the emergence points of dislocations, all dislocations are not revealed. These results showed that preferential etching of dislocations takes place only at a proper molar ratio of CrO_3 and HF. The effect of this ratio was more critical on the (100) face than on the (111) face.

In order to describe the etching characteristics of GaAs, consider the iso-etch-rate contours for the (100) face as a function of composition of CrO_3-HF-H_2O system (Fig. 12). Depending on the etching kinetics, the ternary diagram can be divided into three main regions. In the region A corresponding to the ratio $\gamma_m > 0.1$, the contour lines of iso-etch-rate run parallel to the H_2O-CrO_3 axis. This means that the lines of iso-etch rate are also the lines of constant HF concentration, and the rate depends on HF concentration. In the concentration region B with $\gamma_m < 0.05$, the etch rate

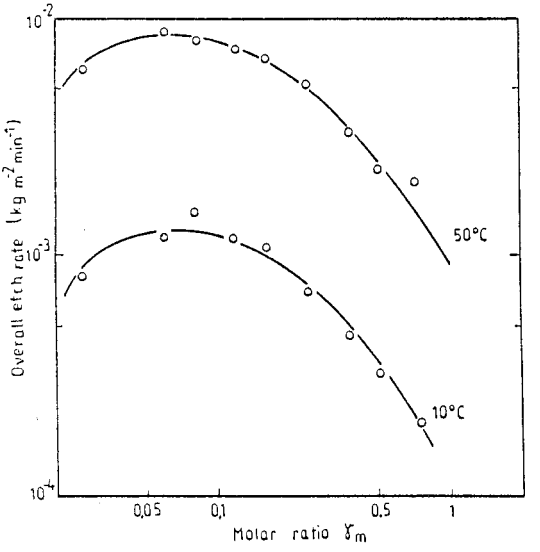

Figure 11. Dependence of the overall etch rate of the (111) face of Si on the molar ratio $\gamma_m = [CrO_3]/[HF]$ at two different temperatures (15).

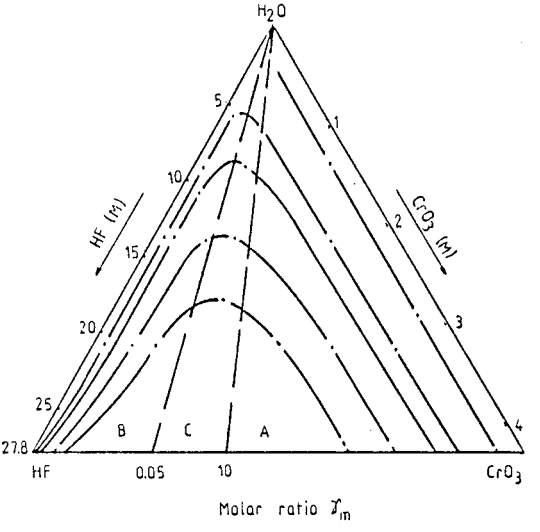

Figure 12. Iso-etch-rate contours for the (100) face of n-type GaAs in the dark. The numbers on the contour lines denote etch rates in μm/min. From Ref. (25).

increases with CrO_3 concentration, whereas in the region C in between regions A and B with $0.10 > \gamma_m > 0.05$, the system follows mixed kinetics.

Table 2

Etching Behavior of (100) and (111) Faces of Si in CrO_3-HF-H_20 System [65]

Plane	Etchant	CrO_3(M)	γ_m	Etching Characteristics,
(100)	Y1	0.5	0.010	Rounded etch pits.
	Y2	1.0	0.020	Poorly defined etch pits.
	Y3	1.5	0.031	Well-defined etch pits.
	Y4	2.0	0.041	Well-defined etch pits.
	Y5	2.5	0.051	Capability of selective etching decreases. Reveals low etch-pit density.
	Y6	3.0	0.062	Reveals very low etch-pit density.
(111)	Y1	0.5	0.010	Rounded etch pits.
	Y3	1.5	0.031	Well-defined etch pits.
	Y15	5.0	0.102	Well-defined etch pits.
	Y16	10.0	0.204	Well-defined etch pits.
	Y17	10.0	0.408	Capability of selective etching decreases. Reveals low etch-pit density.
	Y18	10.0	0.612	Reveals very low etch-pit density.

In region A, with $\gamma_m > 0.1$ and [HF] < 10 M, crystal defects are revealed as defect-related hillocks. The surface between these hillocks remains smooth for solutions with $\gamma_m > 0.14$. For solutions of region B and a part of A with $\gamma_m < 0.14$, surface microroughness and defect-related hillocks are observed. In the concentration region C with [HF] < 10 M, in addition to microroughness and defect-related hillocks, general macroroughness accompanied by the formation of large hillocks unrelated to crystal defects results. They are produced as a result of the inhibition of etching by the adhesion of gas bubbles to the surface (66).

5.0 PHOTOETCHING

As discussed in Sec. 2.3, dissolution of semiconductors is electrochemical in nature and takes place by the depletion of electrons and holes at the surface. Therefore, the kinetics of etching may be influenced by any mechanism that creates or supplies extra carriers. This can be caused by applying a potential with or without light (67)(68), by heating the sample or by illuminating the surface during traditional chemical etching (69)(70). In the case of illumination, the enhanced concentration of photocarriers not only increases the rate of surface dissolution but also influences the rate of reaction at the emergence points of dislocations. Since dislocations are effective sites for the recombination of electrons and holes, the concentration of carriers is reduced. This leads to the formation of etch hillocks as a result of dissolution at dislocations rather than at the perfect surface. Kuhn-Kuhnenfeld (69) showed that a photovoltage is developed at the surfaces of GaAs crystals etched in $3H_2SO_4$ - $1H_2O_2$ - $1H_2O$ under illumination, and attributed it to the separation of light-induced electron-hole pairs in the built-in electric field of the semiconductor surface.

The general features of the effect of illumination on etching kinetics may be described by referring to Fig. 12 of the etching of GaAs in CrO_3 - HF solutions, studied by Ven, et. al. (25). For CrO_3:HF molar ratios greater than 0.1 (region A in Fig. 12), the kinetics are independent of the CrO_3 concentration but slowly depend on the HF concentration for both p- and n-type GaAs (Fig. 13). For the etching of n-type GaAs in the dark, the etch rate increases slowly with the HF concentration at low concentrations, but then it tends to increase linearly at high HF concentrations. Under illumination, the rate increases linearly with HF concentration. The dependence of etch rate of p-type samples on HF concentration is similar to that of n-type crystals in the dark, but the etch rate remains unaffected by illumination.

The effect of light intensity on the etch rate of the (100) face of n-type

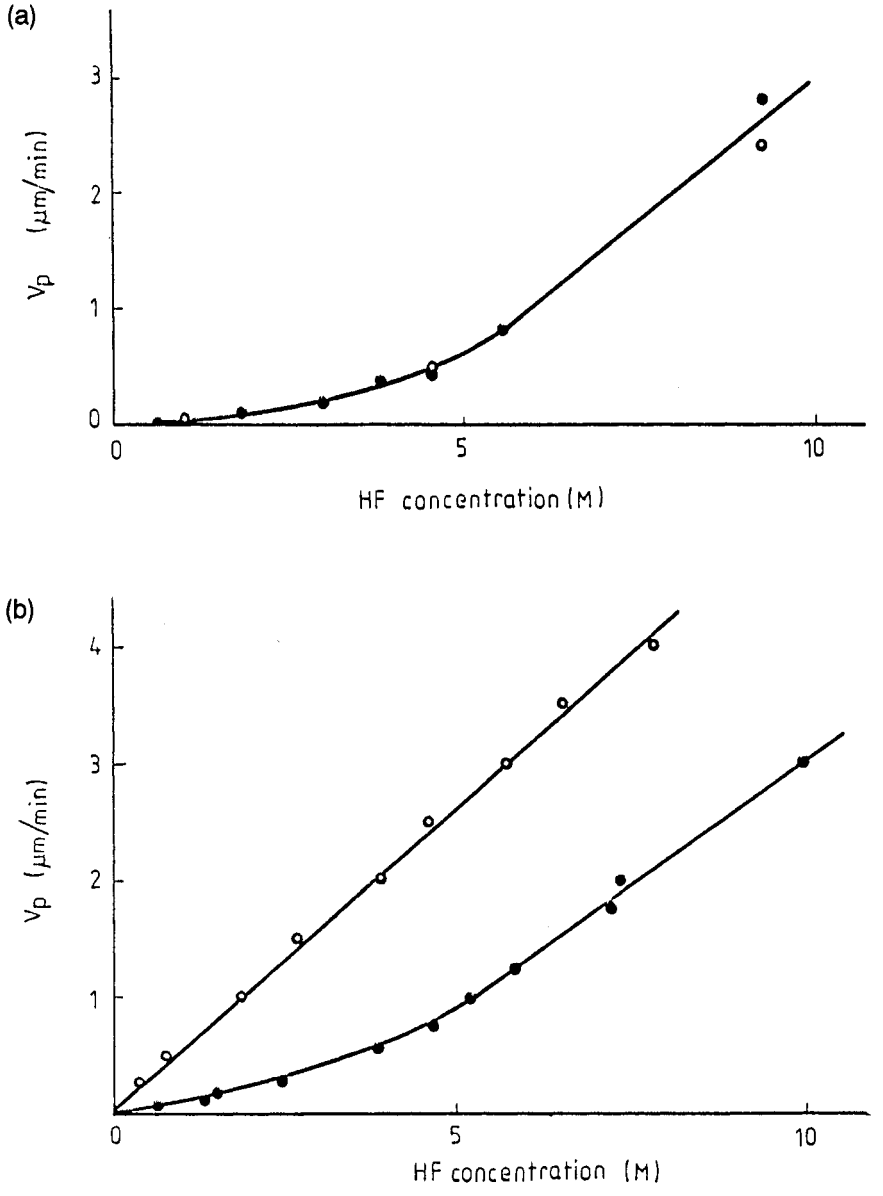

Figure 13. Etch rate v_p of (a) p- and (b) n-type (100) GaAs as a function of HF concentration for etchants from the HF-controlled region A of Fig. 12; solid and open circles are, respectively, for etching in dark and under illumination (18).

GaAs in a solution containing 1.55 M HF and 1.2 M CrO_3 is shown in Fig. 14. The curve reveals that, after an initial steep linear rise, the rate tends to attain a limiting value at high light intensities. The initial linear slope suggests that one GaAs molecule is dissolved when three photons are absorbed. Thus two holes are transferred for every photon absorbed because GaAs dissolution is a six-hole process (see Sec. 2.4).

From analyses of current-potential plots for n- and p-type materials, and the dependence of limiting cathodic current and cathodic peak currents on HF concentration, it was shown (18) that a passivation layer containing both Cr^{III} and Cr^{VI} species is formed on the dissolving surface. In the region of high CrO_3 concentration (region A), the surface coverage by the film is high, but with the aid of HF the layer is removed by intermediates from the GaAs oxidation process. In the case of dissolution of n-type GaAs under illumination, it was proposed (17)(19)(25) that recombination of holes and electrons takes place via surface intermediates of the GaAs oxidation process (see Eqs 54-56).

6.0 ELECTROLYTIC ETCHING AND POLISHING

By virtue of the chemical nature of the processes involved during dissolution, electrolytic etching (also called electroetching or electrochemical etching) is used for metals and semiconductors. Electrolytic etching and polishing take place only when dissolution kinetics are controlled by volume diffusion and the general dissolution characteristics usually observed on the surfaces of metals and semiconductors may be described with reference to the current-voltage characteristics of Fig. 1.

The current-voltage curve of Fig. 1 can be divided into three regions. In region AB the current density increases with the applied voltage, in region BC the current density is independent of the voltage, and in region CD the current density increases again with the voltage. It is found that in region AB crystal defects are selectively revealed, in region BC polishing takes place, while in region CD localized pitting, often unrelated to defects, occurs. Thus electropolishing takes place in the plateau region of the current-voltage curve.

The above features are illustrated in Fig. 15, which shows the experimental current-voltage chatacteristics of an electrolytic cell containing an electrolyte prepared by adding one part of a mixture consisting of equal parts by volume of a saturated KOH solution and saturated Na_2SO_3 solution, to 5 parts of glycerol (71), used for the etching of the (100) face of $Pb_{0.97}Sn_{0.03}Se$ crystal. This solution gives a cell conductivity of 14 mA cm^{-2}, but by adding small amounts of KOH-Na_2SO_3 mixture, the cell conductivity could be increased. High quality polished surfaces were

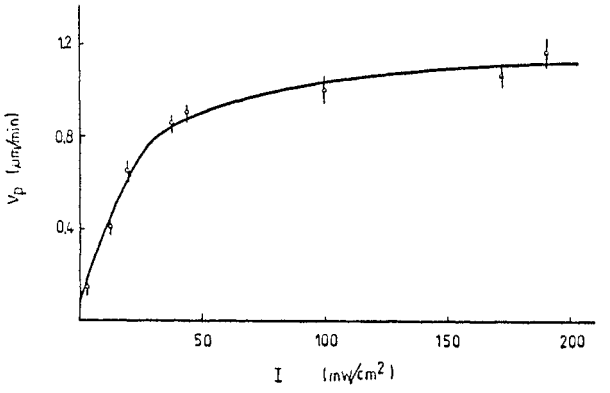

Figure 14. Etch rate v_p of n-type (100) GaAs as a function of laser-light intensity I for a solution containing 1.55 M HF and 1.2 M CrO_3 (25).

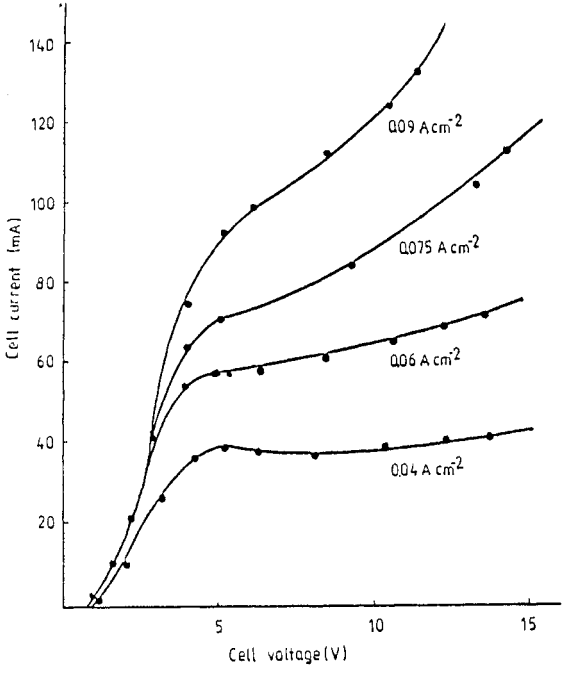

Figure 15. Dependence of current on voltage for electrolytic cells of different cell conductivities. The conductivities were measured at a cell voltage of 6 volts. After Ref. (71).

obtained only for 4 and 6 mA cm^{-2} cells in which there is little change in current with the cell voltage (i.e., in the 6 - 10 volt region). Use of 7.5 mA cm^{-2} cell gave non-uniform polishing with slight pitting while 9 mA cm^{-2} cell yielded a badly pitted surface with no polishing.

Electropolishing is the elimination of surface roughness of height > 1 μm (macrosmoothing) and of height < 1 μm (microsmoothing) (72). Macrosmoothing results from the concentration of current lines on peaks of a surface profile thus leading to a locally higher dissolution rate. The rate of macrosmoothing, therefore, is equal to the difference in dissolution rate between peaks and recesses of a rough surface. It is determined by the current distribution present on the surface profile and, therefore, depends on geometrical and electrochemical parameters. Microsmoothing, on the other hand, results from the suppression of the influence of defects and crystallographic orientation on the dissolution process. Consequently, it requires the study of surface kinetics and passivation behavior. In most cases we deal with microsmoothing.

There is evidence (8)(21-24)(71-75) that during electrodissolution, a passivation film is formed on the anode. The film is gradually eliminated by diffusion when the current is switched off. The etching and polishing behavior of an anode are perhaps associated with the chemical stability of this passive film whose composition is usually speculative (21-23)(72)(74).

A variety of electrolytic cells have been in use for electrolytic etching and polishing (73)(75-77). They all have a sample as the anode, a platinum foil as the cathode, a vessel containing an electrolyte, temperature controller, and a power supply. Additionally, stirring may be provided by a magnetic stirrer or by bubbling an inert gas through the electrolyte. Measurements of potential of an anode are made against a saturated calomel electrode (SCE).

Figure 16 illustrates the current-voltage curves for < 100 > oriented n-type InP samples with different carrier concentrations. These curves show that with an increase in carrier concentration the dissolution rate increases, but the higher the carrier concentration the smaller is the increase in dissolution rate. This behavior is due to a decreasing contribution of holes to the anodic dissolution rate (77). It was observed that the sample with the highest carrier concentration is simply polished both in the dark and with illumination, but that structural defects are revealed as etch hillocks in samples of lower carrier concentrations. The effect of illumination in revealing structural defects in n-type crystals is profound in mild etching systems (75)(77-79). In mild etching electrolytes, photoelectrolytic etching is also dependent on crystal orientation in n-type materials (80). However, it is not known whether this anisotropy is due to a difference in the rates of recombination at the surfaces due to the surface structure or in the kinetics of dissolution of reaction products.

Obviously, in mild etching systems the dissolution kinetics are controlled by surface reactions.

7.0 GAS-PHASE CHEMICAL ETCHING

Prior to epitaxy or chemical vapour deposition, surfaces of crystals, especially semiconductors, are frequently polished with chemically reactive gaseous mixtures. In contrast with traditional wet chemical etching, the procedure has the advantage of cleaning the surface by removing the metallic impurities. The degree of polish depends on the ratio of components in the reactive mixture, its total pressure, partial pressure of the reactant and the temperature at which etching is carried out (81-86). Generally, etching is carried out at atmospheric pressure (81-84), but low-pressure etching has also been studied (86)(87).

Depending on the etching conditions, gas-phase etching of crystal wafers reveals etch pits, bunch formation and surface polishing (81-85). Figure 17 shows the surface morphology of the (111) face of silicon single crystals etched in gaseous HCl with Ar or H_2 as a carrier gas as a function of temperature. The continuous and the dashed curves represent the transition lines between smooth and bunched surface structures when H_2 and Ar are used, respectively, as the carrier gas. When argon is used as a carrier gas, the transition line is shifted to lower input concentrations of HCl and higher temperatures. Also shown is the transition line from a smooth to a pitted surface for HCl-H_2 system. In the region of high HCl concentrations and low temperatures both etch pits and bunches are produced. The shape of the observed bunches is determined by the misorientation of the etched surface from the real (111) plane and by the directions of the etching vectors in the (111) surface. It is also observed (81)(83) that beyond a critical HCl concentration formation of block patterns (facet formation) takes place on the (111) surfaces with very small ($<0.5°$) misorientations. The block patterns are composed of shallow triangular etch pits.

The etching behaviour of Si in HCl-H_2 mixtures at low-pressure CVD conditions shows (85) that, at constant HCl concentration and total pressure, the polishing effect improves with an increase in temperature. With an increase in the concentrations of HCl and H_2 or with an increase in the total pressure, a roughening of the surface takes place. The effect of temperature observed in this case is similar to that described above in Fig. 17.

As in the case of wet chemical etching, the temperature dependence of etch rates of crystals in gas-phase etching shows the reaction-rate and diffusion controlled nature of the process. Figure 18 illustrates the

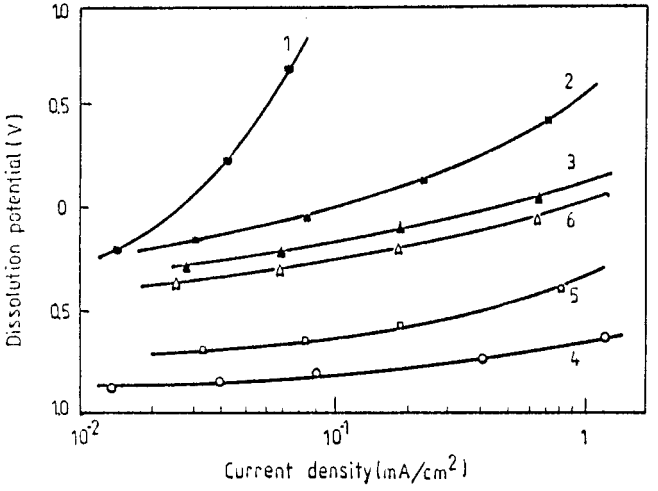

Figure 16. Curves of dissolution potential against current density for n-type (100) InP of different carrier concentrations (77); carrier concentration n: (1,4) 1×10^{16} cm^{-3}, (2,5) 4×10^{18} cm^{-3}, (3,6) 2×10^{19} cm^{-3}; (1,2,3) in the dark, (4,5,6) under illumination.

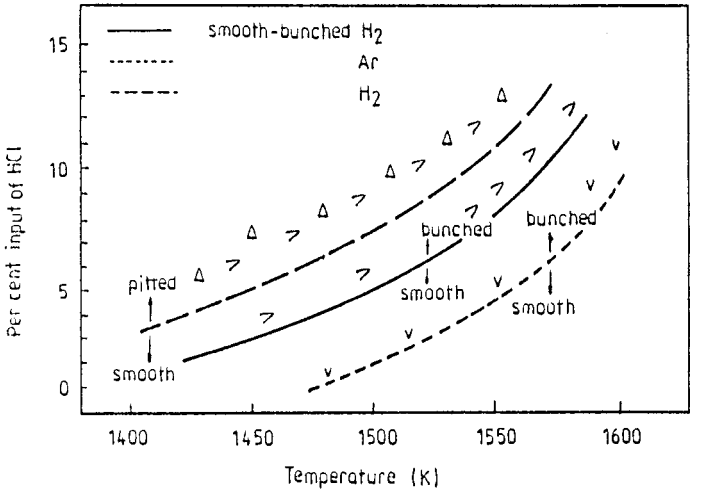

Figure 17. Surface morphology of the (111) face of Si etched in gaseous HCl. Transition lines from smooth to bunched structures are for the H_2/HCl and Ar/HCl systems; the transition line from smooth to pitted structures is for the H_2/HCl system. From Ref. (83).

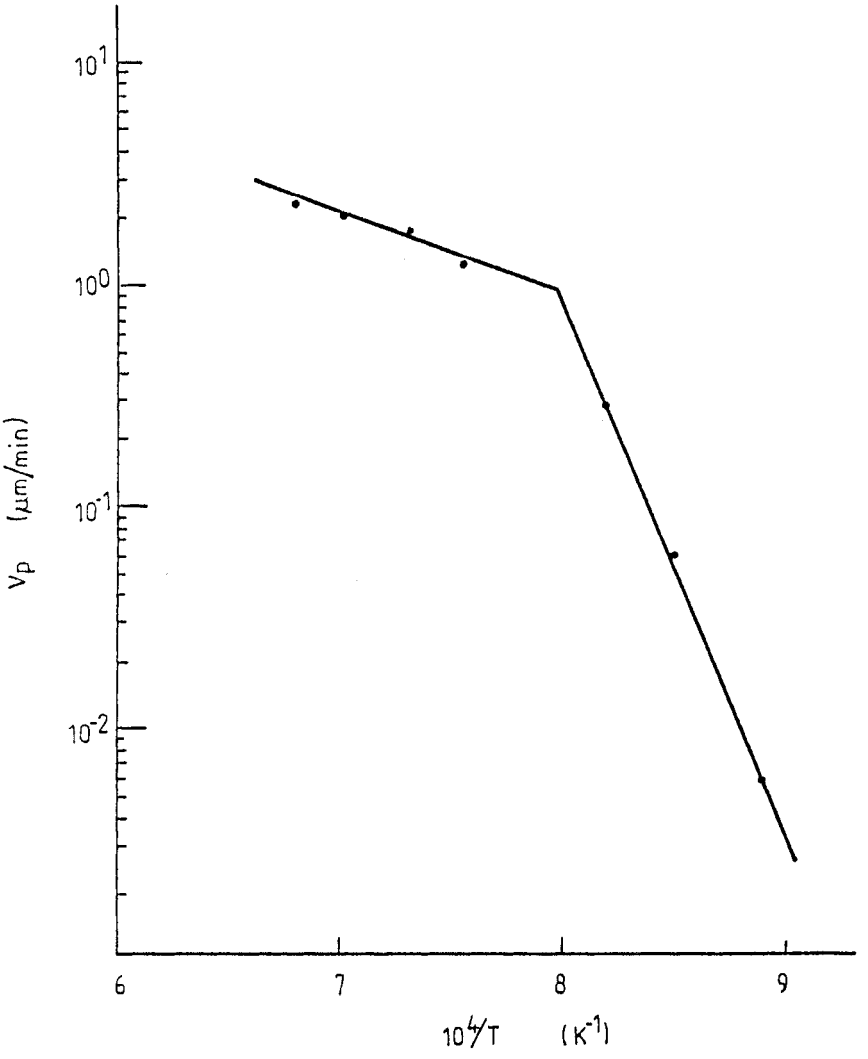

Figure 18. Dependence of etch rate v_p on the reciprocal temperature 1/T at a pressure of 1.0 torr and molar fraction of HCl of 0.1 (85).

Arrhenius-type plot of the dependence of etch rate of the (111) face of Si on temperature, at a pressure of 1.0 torr and HCl molar fraction of 0.1. The dependence clearly shows two regions. At temperatures below 1000°C, where the temperature dependence is very strong, corresponding to an activation energy of 105 kcal/mol, etching is kinetically controlled. At temperatures above 1000°C corresponding to an activation energy of 16 kcal/mol, etching is controlled by diffusion. Etching at atmospheric pressure also exhibits a similar behaviour (87)(88), but the values of the activation energy corresponding to kinetically- and diffusion-controlled regimes are 42 and 0 - 4 kcal/mol, respectively.

The change in the morphology of surfaces etched in the gaseous phase can be correlated with the theoretical predictions (2). For example, if we take the reactant concentration as a measure of undersaturation, the transition from a region of smooth morphology to pitted structures is predicted by the thermodynamic theories of dislocation etch-pit formation, while the bunched morphology may be interpreted by the kinematic theory of step motion. The kinetic data, on the other hand, have been explained (82-84)(86) in terms of surface reactions, commonly used in heterogeneous catalytic reactions, involving adsorption of molecules of reactant and carrier gas onto the surface and subsequently, desorption of different thermodynamically stable species generated at the surface. In the case of etching Si in HCl-H_2 mixtures, the the following reactions have been proposed (85)(86):

Eq. (99) $(1/2)H_{2(g)} + * \rightarrow H*$

Eq. (100) $HCl_{(g)} + * \rightarrow HCl*$

Eq. (101) $HCl* + Si_{(s)} \rightarrow SiH_xCl_{1-x}*$

Eq. (102) $SiH_xCl_{4-x}* \rightarrow SiH_xCl_{4-x(g)}$

where * denotes an adsorption site on the surface. Eqs. (99) and (100) represent the adsorption reactions, Eq. (101) chemical reaction on the surface, while Eq. (102) represents the desorption reaction. Below 1000°C, the rate-limiting step is the surface reaction given by Eq. (101), while above this temperature the control of the surface reaction is diffusional and may be determined by any of the steps of Eqs. (99), (100) and (102).

Depending on experimental conditions, which ultimately determine the concentration of adsorbed hydrogen and chlorine on the surface, the number of HCl molecules reacting with a silicon atom may be different, forming different species containing Si-Cl bonds (86). The stable species forming at high and low temperatures are $SiCl_2$ and $SiCl_4$, respectively, but

their stability also depends on pressure and Cl/H ratio (i.e., HCl concentration).

8.0 MORPHOLOGY OF CHEMICAL ETCH PITS

Etch pits always possess an external outline, which may be crystallographic, rounded or circular. Etch pits with a crystallographic outline are called preferential while those without a crystallographic contour non-preferential. The process leading to the formation of crystallographically-oriented (or preferential) etch pits is termed preferential or anisotropic etching, while the one corresponding to the formation of circular (or non-preferential) etch pits is called non-preferential or isotropic etching.

The external outline of etch pits depends on the conditions of etching (i.e., composition of etchant and etching temperature). In the case of etching water-soluble crystals of lower symmetry in simple solvents, even a change of solvent leads to a marked change in the geometry of pits (56). On the surfaces of crystals of higher symmetry, on the other hand, the outline of etch pits undergoes a change when the composition of the etchant or temperature of etching is changed. This feature is illustrated in Fig. 19 for etch pits produced on the (100) and (110) faces of MgO by H_2SO_4. The figure shows that by changing the etchant concentration both anisotropic and isotropic etching may be achieved.

It has been suggested (89) that isotropic etch pits are produced when etching is controlled by diffusion, while anisotropic etch pits are produced when the process is kinetically controlled. An analysis of the experimental observations reveals that it is not always so. For example, the process of etching of a crystal in a solvent in which it is highly soluble, is expected to be diffusion-controlled, yet, as observed in the case of etching of potassium dihydrogen phosphate (KDP) (57) and potassium bichromate (KBC) (56) in water, the pits are anisotropic. Similarly, in the case of etching of the (100) face of MgO, the kinetics at low acid concentrations are controlled by chemical reactions but the pits produced are isotropic (90).

The geometry of etch pits is determined by the relative rates of removal of atoms along different directions. Factors, such as adsorption of added impurities or reaction products, temperature of etching and stirring, affect the absolute values of these rates and thus lead to a change in the geometry of etch pits. In the absence of adsorption and diffusion effects, a situation difficult but possible to be realized, the shape of etch pits may be determined from a consideration of the binding energy between nearest neighbors (2) or from Periodic Bond Chain vectors

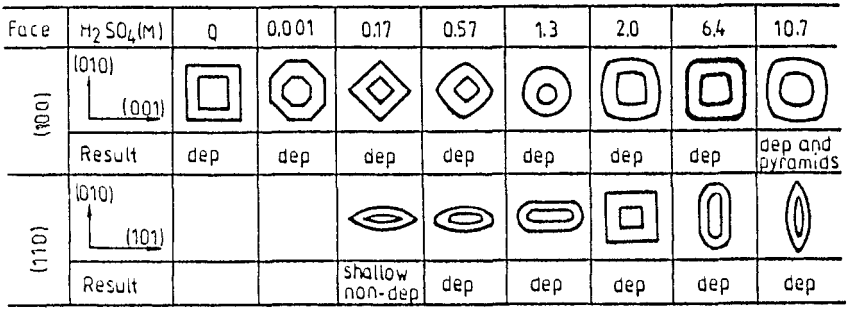

Figure 19. Schematic representation of the geometry of etch pits on the (100) and (110) faces of MgO at various H_2SO_4 concentrations; dep: dislocation etch pits. After Refs. (7)(58).

(PBCs) (2)(3)(91). The deviation in the observed morphology of etch pits from the one predicted by the PBC theory is a consequence of adsorption and diffusion processes.

Since the geometry of etch pits is determined by the arrangement of ions, atoms or molecules composing a crystal surface, the shape of etch pits formed on crystallographically different or on opposite faces of a crystal is different. This difference forms a basis for the distinction of various faces of a crystal and, in many cases, serves as a quick method for the identification of the faces or the directions on the face of a crystal. Figure 20 presents dislocation etch-pit patterns on the (001) and (00$\bar{1}$) faces of a KBC crystal. The difference in the shape of etch pits as well as in the distribution of dissolution layers is evident. Similarly, the non-equivalence of the [110] and [$\bar{1}$10] directions in the (001) plane of zinc-blende-type crystals leads to the formation of elongated or elliptical (93-95) and rectangular etch pits (93)(96)(97). However, an appropriate choice of the etching solution is a crucial factor in these observations, as illustrated in Fig. 21 for the (001) face of InP crystals.

The side walls of dislocation pits with a crystallographic outline usually correspond to high-index planes (47), but low-index planes of the equilibium form are also observed (see Refs (47)(98-100) and literature cited therein). The latter type of etch pits, customarily called crystallographic etch pits, are observed on the surfaces of metals and semiconductors. The sites for the origin of the crystallographic etch pits are either the emergence points of dislocations or random points corresponding to pinholes developed in a surface film formed during dissolution, permiting localized etching action. These surface films are favorably formed by redox etchants during the dissolution of metals and semiconductors. Figure 22 presents the successive stages of the development of etch pits on the (111) face of Si in a solution of $3HNO_3 + 1HF + 1.6CH_3COOH$. The figure shows that most of the pits have turned flat-bottomed on successive etching, indicating their non-dislocation origin.

Several factors, such as etchant composition, etching temperature and surface treatment (e.g., prepolishing, surface damage, etc.) contribute to the formation of etch pits by the pinhole dissolution mechanism and different tests may be applied to demonstrate the validity of this mechanism. If etch pits are produced by this mechanism, successive etching leads to the development of shallower and more rounded etch pits which were initially small and relatively flat (Fig. 22). The growth of etch pits with time also shows a parabolic dependence (99). Furthermore, prepolishing may greatly enhance the density of etch pits.

Finally, it should be mentioned that under certain experimental conditions etch pits formed by this pinhole mechanism may be non-preferential. Such shallow saucer-shaped pits, often called S-pits, of non-

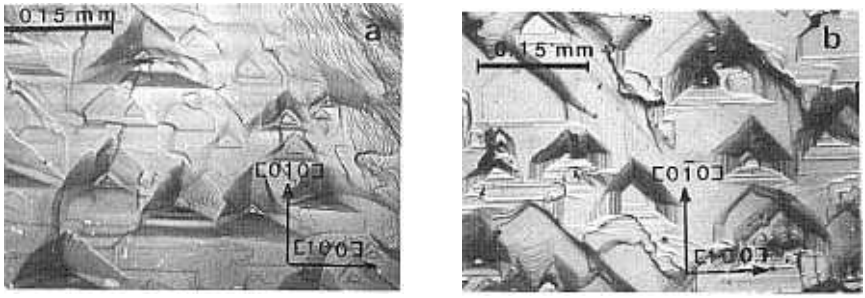

Figure 20. Dislocation etch pits produced on the (001) and (00$\bar{1}$) faces of potassium bichromate crystals by etching with water at room temperature (92).

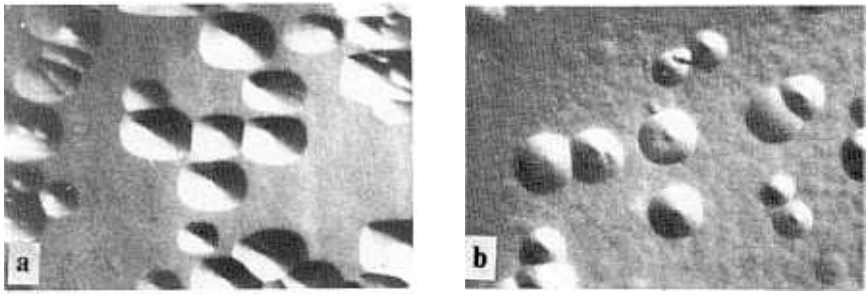

Figure 21. Etch pits of different shapes produced on the (001) plane of InP; etchants: (a) 10HBr + 10CH_3COOH + 1(1N)$K_2Cr_2O_7$, and (b) 2HBr + 2H_3PO_4 + 0.07(1N)$K_2Cr_2O_7$. From Ref. (96).

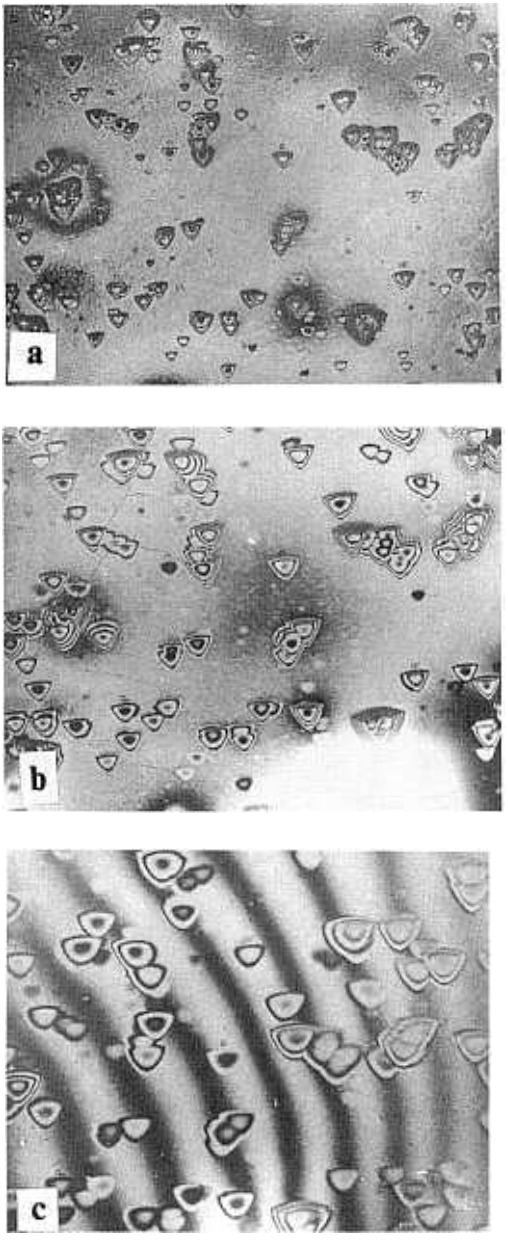

Figure 22. Successive stages of the development of non-dislocation etch pits on the (111) face of Si in $3HNO_3$ + 1HF + $1.6CH_3COOH$ etchant (99); etching time: (a) 30 sec., (b) 90 sec., (c) 330 sec.

dislocation origin are frequently observed during the etching of semiconductors.

9.0 CORRESPONDENCE BETWEEN ETCH FIGURES AND DISLOCATIONS

All types of linear (dislocations), planar (stacking faults, twin boundaries, grain boundaries, etc.) and volume defects (clusters of point defects and impurities) emerging on the surface of a crystal lead to the formation of etch figures (Sec. 3). Volume defects are localized at random positions in the crystal interior, planar defects extend to large areas, while linear defects do not terminate within a crystal. These geometrical properties of defects may be used to distinguish between them by studying etch patterns. Volume and linear defects produce etch figures at isolated positions; stacking faults, twin boundaries and impurity striations produce grooves or ridges, while grain boundaries yield rows of etch figures. Etch figures resulting from linear and volume defects may be recognized by examining the etch patterns on a surface after successive etching, or after alternate etching and polishing, or by comparing etch patterns on matched cleavage faces. Etch figures due to volume defects disappear continuously with successive etching or alternate etching and polishing. If an etch pattern persists after prolonged etching or alternate etching and polishing, or if the etch patterns produced on matched halves are essentially mirror images of each other, the etch figures correspond to the emergence points of dislocations.

If a crystal contains tilt boundaries, the following tests can be performed to identify etch figures at the emergence points of dislocations. In the case of an isolated low-angle tilt boundary, the distance between two etch figures in the boundary is equal to that between neighboring dislocations, D, as estimated by X-rays from the misorientation angle θ in accordance with the relation $\theta = b/D$ of the dislocation model of a low-angle tilt boundary (101). A simpler test without the measurement of angle θ is to look for three or four intersecting boundaries (Fig. 23). For symmetrical low-angle tilt boundaries there exists a relation between the linear dislocation densities ρ_i (i.e., number of etch figures per unit length) between different branches (103), namely,

Eq. (103) $$\rho_1 + \rho_2 = \rho_3 = \rho_4$$

If a crystal can be deformed plastically, the appearance of slip bands and indentation rosettes (Fig. 24) on a surface implies that the etch figures locate the emergence points of dislocations. Comparison of etch

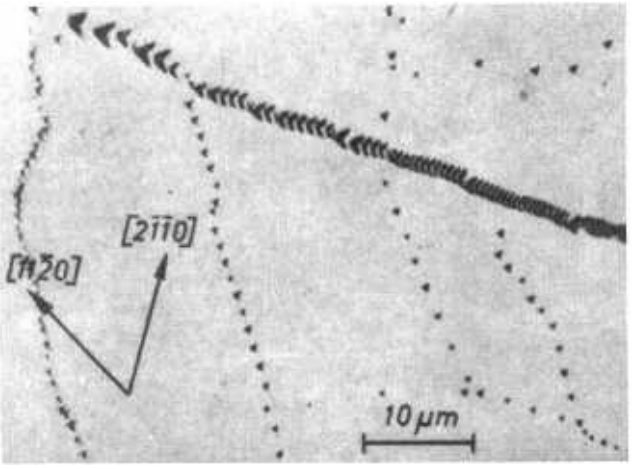

Figure 23. Low-angle tilt boundaries revealed by electrolytic etching on the (0001) face of Sb -2.5% Bi alloy (102).

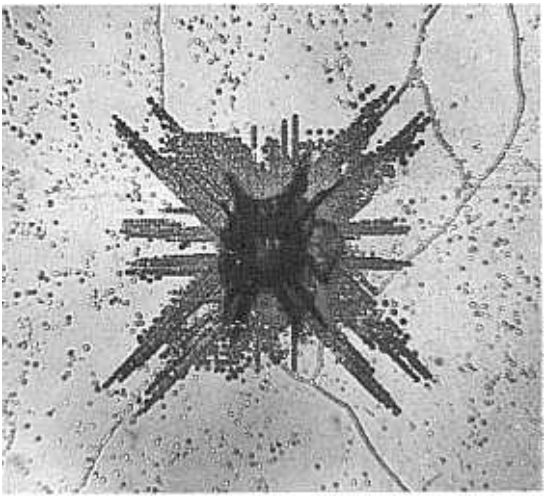

Figure 24. Indentation rosette revealed on the (100) face of MgO by dilute H_2SO_4.

figures with dislocation patterns revealed by other techniques (e.g., decoration, X-ray topography, recombination techniques) also provides evidence of the one-to-one correspondence between etch figures and dislocations (Fig. 25).

10.0 ETCHING PROFILES

The fabrication of electron devices involves a sequence of steps,and the production of etching profiles in the form of grooves and mesas in the surface of a semiconductor by chemical etching is an important step. The shape of an etching profile is determined by the composition of the etching solution, the temperature of etching, the surface orientation, degree of undercutting beneath the mask and the chemical aggressiveness of the etchant towards the mask.

The surfaces for the formation of etching profiles for semiconductors are (001), and single-crystal wafers of Si (105), GaAs (24)(64)(94)(106-110) and InP (93)(94)(96)(111)(112) and double-heterostructure (DH) wafers of InAlAs/InP (113), InGaAsP/InP (96)(114-117), and AlGaAs/GaAs (118)(119) have been used. However, depending on the type of wafer, and the chemical composition of the etchant used, the etching profile produced on the surface is different.

Etching profiles on the surfaces of elemental semiconductors are grooves, while those on the surfaces of the layers of compound semiconductors are both mesa-shaped and reverse mesa-shaped, depending on the direction in the (001) plane. This feature is shown in Fig. 26 for the profiles produced on (001) GaAs etched in different solutions. The profiles were obtained by cleaving the wafers in orthogonal directions along the (110) and ($\bar{1}$10) planes.

Figure 26 reveals that the profile walls are composed of individual planes. In Fig. 26a, the reverse mesa-shaped and the mesa-shaped planes form angles of 114° and 55° with respect to the (001) plane and correspond to {221} (or {1$\bar{1}\bar{1}$}Ga) , and {$\bar{1}$11}Ga planes, respectively (Fig. 27). In the case of Fig. 26b,c,d, the profiles on the (110) cleavage planes show vertically etched planes with a small tilt from a direction normal to the surface (001) plane. These vertical planes correspond to the {$\bar{1}$10} plane. Some etching solutions also produce profiles whose walls on the (110) cleavage plane make different angles with respect to the (001) plane. These profile walls correspond to {$\bar{1}\bar{1}$2}III, {$\bar{2}\bar{2}$1}III and {0$\bar{1}$1} planes. A summary of the etching profiles of semiconductor wafers is given in Ref. (2).

The most commonly used etching solutions for producing etching profiles on the (001) face of GaAs and InP are mixtures of various

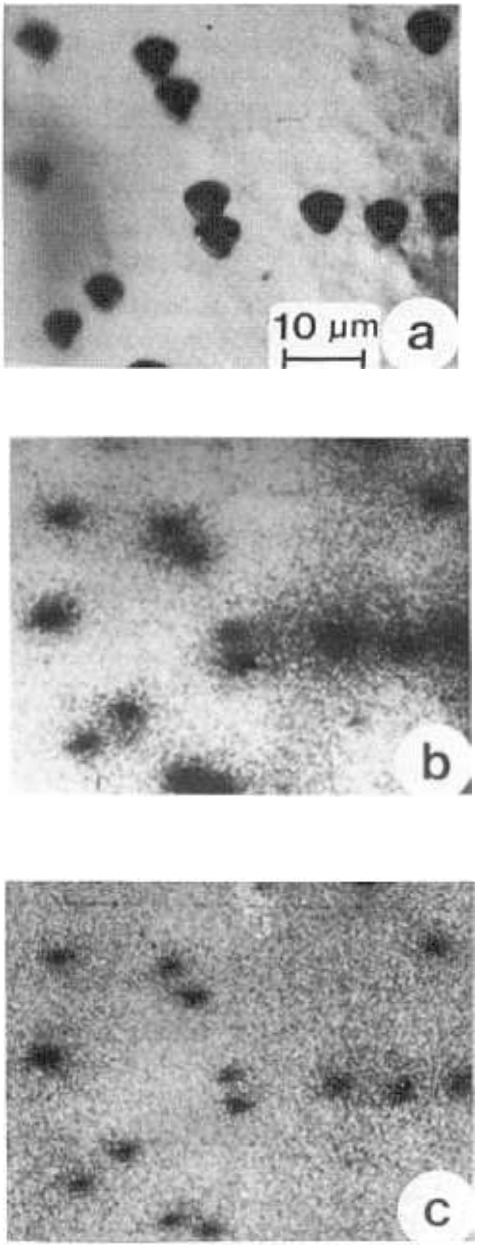

Figure 25. One-to-one correspondence between (a) dislocation etch-pit distribution, (b) cathodoluminescence images and (c) electron-beam-induced conductivity images of the same region of a GaP layer (104).

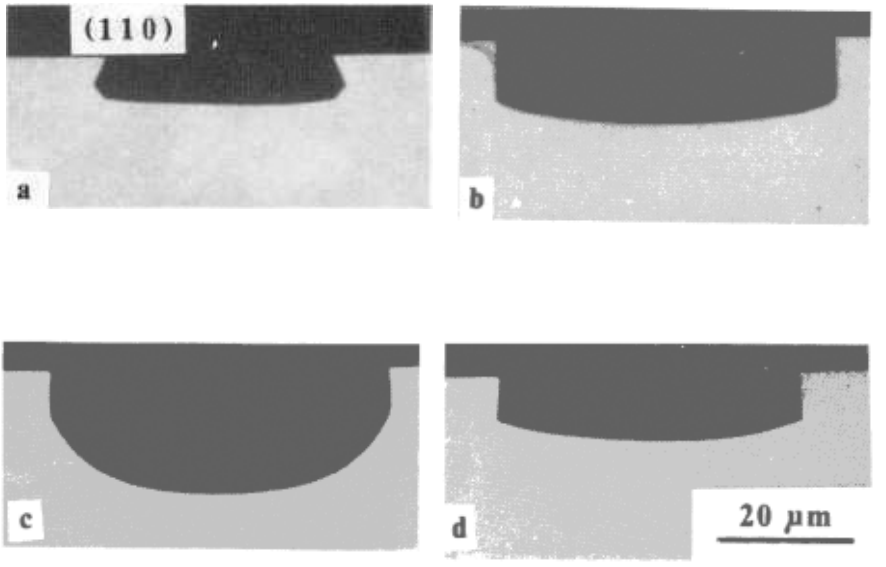

Figure 26. Etch profiles obtained on (001) GaAs etched in different etchants: (a) $1H_2SO_4 + 1H_2O_2 + 1H_2O$ (25°C, 30 sec); (b) $3(1M)K_2Cr_2O_7 + 1H_2SO_4 + 1HCl$ (60°C, 1 min); (c) $3(1M)K_2Cr_2O_7 + 1H_2SO_4 + 2HCl$ (60°C, 1 min); and (d) $3(1M)K_2Cr_2O_7 + 1H_2SO_4 + 12HCl$ (25°C, 2 min). From Ref. (94).

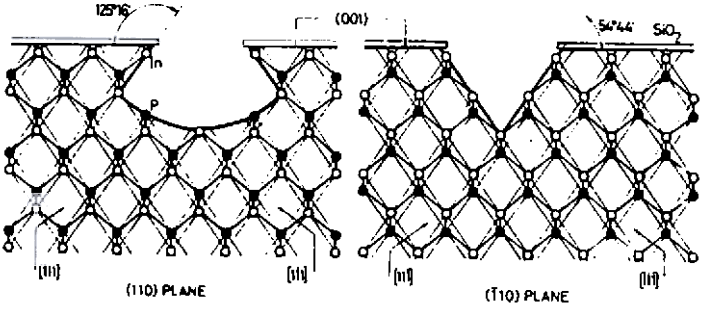

Figure 27. Schematic representation of etch profiles of (110) and ($\bar{1}$10) planes of a (001) InP crystal; the open and solid points represent III and V atoms, respectively (93).

compositions of H_2SO_4-H_2O_2-H_2O, HCl-H_2O_2-CH_3COOH(H_3PO_4), HNO_3-CH_3COOH, HF-HNO_3-H_2O(CH_3COOH), HCl-HNO_3-H_2O, HBr-HNO_3-H_2O, H_3PO_4-H_2O_2-H_2O(CH_3COOH), HBr (or HCl or H_2SO_4)-H_3PO_4 (or CH_3COOH)-$K_2Cr_2O_7$, Br_2-CH_3OH, and H_2O_2-NaOH (or KOH or NH_4OH)-H_2O. These etching solutions are the same as those used for the polishing and selective etching of these crystals. As in the case of selective etching, these solutions form etching profiles with crystallographically oriented walls or round profiles, and are called preferential (anisotropic) and non-preferential (isotropic). In order to mask the surface of the semiconductor crystals, either a photoresist or a layer of SiO_2 or Si_3N_4 are used. Commonly used photoresists are HNR-999, HPR-204 and AZ-1350.

A serious problem with most of the abovementioned etchants is a tendency towards an enhanced etch rate of the crystalline wafer near the edges of the mask (24)(106)(111)(120), probably due to the migration of etchant molecules along the mass. In the case of a photoresist mask, this effect results in the curling away of the masking layer. Both of these phenomena lead to the lateral etching of the wafer beneath the edges of the mask. This lateral etching is referred to as undercutting. The degree of undercutting can be reduced by using a masking material that firmly adheres to the substrate wafer. Metal coatings are often found to be suitable as masking material (105). However, acid etchants corrode metallic masks, while alkaline etchants tend to dissolve the oxide and nitride masks (106). In some etching systems the long etching times involved restrict their applicability (105).

For the reproducible production of etching profiles of good quality it is of utmost importance that the etching solution does not erode the mask material and the degree of undercutting is controlled. The first problem can be overcome by choosing a proper etching solution and masking material, while the degree of undercutting can be regulated by improving the adhesion between the mask and the wafer. It has been reported (111) that photoresist coated wafers stored for long durations lead to a significant deterioration in the formation of etching profiles.

Like the rate of etching, v_n, of the wafer in a direction perpendicular to the etching plane, the ratio of the rate of undercutting, v_t, in the lateral direction and the etch factor v_t/v_n depend on the composition of etching solution as well as on the temperature of etching. The dependence of these rates for the etching of (001) wafer of InP in a mixture of 3HCl + $1H_3PO_4$ on the etching temperature is presented in Fig. 28 in the form of Arrhenius plots. The phenomenon of undercutting beneath the edges of the mask is shown in the insert of this figure. Obviously, the two rates are activation controlled, but with an increase in temperature, the increase in v_t is relatively more than in v_n because of a higher activation energy. Consequently, the etch factor, which is equal to v_t/v_n, increases with an

increase in etching temperature, as shown in Fig. 29. The figure also shows that the value of the etch factor decreases with an increase in HCl concentration in the mixture. This fact means that with an increase in HCl concentration etching becomes preferential.

When the dissolution rates for a crystalline solid are very high for all crystallographic planes, diffusion in the solution is rate determining and the etching is isotropic. Therefore, rounded etching profiles are predicted at mask edges and the etch depth near the edge is increased due to a more efficient supply of the etchant. However, it has been found that, while the etch rates of various planes are diffusion-controlled, etching at mask edges is anisotropic (24). Two examples of isotropic etching in diffusion-controlled systems are illustrated by the etching profiles of (001) GaAs etched in aqueous $K_3Fe(CN)_6$ solutions, shown in Fig. 30. Isotropic etching profiles at mask edges may also be seen in Fig. 26.

Etching kinetics of semiconductors may be diffusion-controlled in two ways (24). In the first case, the reduction reaction is diffusion limited and controls the etching kinetics. Under these conditions a well defined crystallographic facet is obtained. This behavior is observed at low pH. In the second case of high pH, the rate of anodic dissolution of the semiconductor wafer depends on the mass transport of OH^- ions to the electrode. Electroless etching based on this limitation shows rounded profiles typical of diffusion-controlled dissolution.

Etching solutions employed to produce patterns in DH layers are also similar to those used for etching profiles in elemental and compound semiconductor wafers. However, appropriate choice of the composition of an etching solution that will yield the desired, smooth profile in a DH layer has to be made by trial and error. This is so because the etch rates of two neighboring layers are different due to a difference in their chemical composition. Etching profiles for InGasP/InP and InAlAs/InP DH layers produced by various etching solutions are given by Adachi et al., (96)(114-117) and Stano (113), respectively, while a summary for different DH layers may be found in Ref. (2).

11.0 ACKNOWLEDGEMENT

This work has been partly financed under Research Project CPBP 01.20.3.

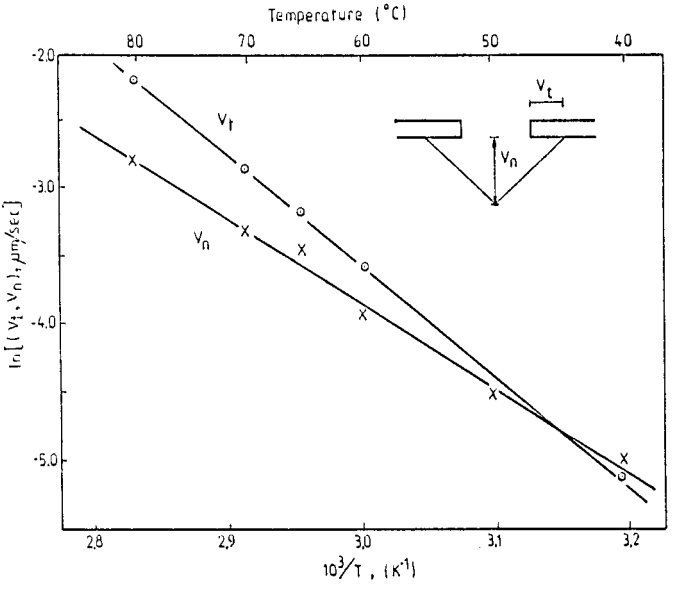

Figure 28. Arrhenius plots of v_t and v_n on temperature (111).

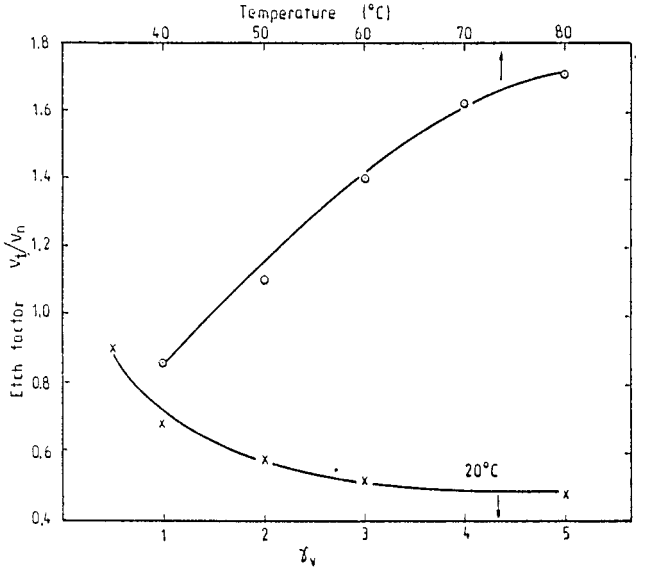

Figure 29. Dependence of etch factor v_t/v_n on etchant composition at 20°C and on etching temperature for $3HCl + 1H_3PO_4$ etchant. Based on the data of Ref. (111).

Figure 30. Etching profiles produced on n-type (001) GaAs by (a) 0.05 M and (b,c) 0.5 M $K_3Fe(CN)_6$ solutions at pH (a,b) 13 and (c) 14 (16).

12.0 REFERENCES

1. Honess, A. P., *The Nature, Origin and Interpretation of the Etch Figures on Crystals*, Wiley, New York (1927)

2. Sangwal, K., *Etching of Crystals: Theory, Experiment and Application*, North-Holland, Amsterdam (1987)

3. Heimann, R. B., *Auflösung von Kristallen - Theorie und Technische Anwendung,* Springer, New York (1975)

4. Moore, W. J., *Physical Chemistry, 5th edition,* Longman, London (1972)

5. Vermilyea, D. A., *J. Electrochem. Soc.* 113:1067 (1966)

6. Sangwal, K., *J. Mater. Sci.* 17:3598 (1982)

7. Borecka, B. and Sangwal, K., *J.Mater. Sci. Lett.* 1:364 (1982)

8. Lacombe, P., in: *The Surface Chemistry of Metals and Semiconductors,* (H. C. Gatos, ed.), p. 244, Wiley, New York (1960)

9. Gatos, H. C. and Lavine, M. C., in: *Progress in Semiconductors, Vol. 9,* (A. F. Gibson and R. E. Burgess, eds.), p. 1, Heywood, London (1965)

10. Despić, A. R., Electrochemistry, in: *Physical Chemistry Series 1, Vol. 6,* (J. O'M. Bockris, ed.), p. 115, Butterworths, London (1973)

11. Turner, D. R., in: *The Surface Chemistry of Metals and Semiconductors,* (H. C. Gatos, ed.), p. 285, Wiley, New York (1960)

12. Klein, D. L., and D'Stefan, D. J., *J.Electrochem. Soc.* 109:37 (1962)

13. Turner, D. R., *J.Electrochem. Soc.* 107:810 (1960)

14. Schwartz, B. and Robbins, H., *J.Electrochem. Soc.* 108:365 (1961)

15. Heimann, R. B., *J.Mater. Sci.* 19:1314 (1984)

16. Notten, P. H. L. and Kelly, J. J., *J.Electrochem. Soc.* 134:444 (1987)

17. Kelly, J. J. and Notten, P. H. L., *J.Electrochem. Soc.* 130:2452 (1983)

18. van de Ven, J., van den Meerakker, J. E. A. M. and Kelly, J. J., *J. Electrochem. Soc.* 132:3020 (1985)

19. Kelly, J. J., van de Ven, J. and van den Meerakker, J. E. A. M., *J. Electrochem. Soc.* 132:3026 (1985)

20. Palik, E. D., Glembocki, O. J. and Heard Jr., I., *J.Electrochem. Soc.* 34:404 (1987)

21. Glembocki, O. J., Stahlbush, R. E. and Tomkiewicz, M., *J. Electrochem. Soc.* 132:145 (1985)

22. Palik, E. D., Bermudez, V. M. and Glembocki, O. J., *J. Electrochem. Soc.* 132:135 (1985)

23. Palik, E. D., Bermudez, V. M. and Glembocki, O. J., *J. Electrochem. Soc.*. 132:871 (1985)

24. Raley, N. F., Sugiyama, Y. and van Duzer, T., *J. Electrochem. Soc.* 131:161 (1984)

25. van de Ven, J., Weyher, J. L., van den Meerakker, J. E. A. M. and Kelly, J. J., *J. Electrochem. Soc.* 133:799 (1986)

26. Beckman, K. H., and Memming, R. *J. Electrochem. Soc.* 116:368 (1969)

27. Decker, F., Pettinger, B. and Gerischer, H. *J.Electrochem. Soc.* 130:1335 (1983)

28. Decker, F., Abramovich, M. and Motisuke, P., *J. Electrochem. Soc.* 131:1173 (1984)

29. Ohara, M. and Reid, R. C., *Modeling Crystal Growth Rates from Solutions*, Prentice-Hall, NJ, (1973)

30. Burton, W.K., Cabrera, N. and Frank, F.C., *Phil. Trans. Roy. Soc. London* A243:299 (1951)

31. Cabrera, N. and Levine, M. M., *Phil. Mag.* 1:450 (1956)

32. Keller, K. W., in: *Crystal Growth and Characterization,* (R. Ueda and J. B. Mullin, eds.), p. 361, North-Holland, Amsterdam (1975)

33. Bauser, E., and Strunk, H., *J. Cryst. Growth* 51:362 (1981)

34. Bauser, E., and Strunk, H., *Thin Solid Films* 93:185 (1982)

35. Frank, F. C., *J. Cryst. Growth* 51:367 (1981)

36. Koziejowska, A. and Sangwal, K., *J. Mater. Sci.* 23:2989 (1988)

37. Gilman, J. J., Johnston, W. G. and Sears, G.W., *J. Appl. Phys.* 29:747 (1958)

38. Ives, M. B. and Ramachandaran, T. R., *J. Appl. Phys.* 38:2121 (1967)

39. Amelinckx, S., Bontick, W. and Dekeyser, W., *Phil. Mag.* 2:1264 (1957)

40. Lang, A. R., *J. Appl. Phys.* 28:497 (1957)

41. Cabrera, N., *J. Chim. Phys.* 53:675 (1956)

42. Schaarwächter, W., *Phys. Stat. Sol.* 12:375 (1965)

43. van der Hoek, B., van der Eerden, J. P. and Bennema, P., *J. Cryst. Growth* 56:621 (1982)

44. Koziejowska, A. and Sangwal, K., *Cryst. Res. Technol.* 20:455 (1985)

45. Nanev, Chr. N. and Dicheva, K., *Electrochim. Acta* 28:933 (1983); *Acta Phys. Hung.* 57:271 (1985)

46. Schaarwächter, W., *Phys. Stat. Sol.* 12:865 (1965)

47. Ives, M. B. and McAusland, D. D., *Surf. Sci.* 12:189 (1968)

48. Sangwal, K. and Zaniewska, G., *J. Mater. Sci.* 19:1131 (1984)

49. Ives, M. B., *J. Phys. Chem. Solids* 24:275 (1963)

50. Sangwal, K. and Urusovskaya, A. A., *J. Cryst. Growth* 41:216 (1977)

51. Honda, K. and Hirokawa, T., *Japan J. Appl. Phys.* 11:1763 (1972)

52. Hirokawa, T., Honda, K. and Shibuya, T., *J. Cryst. Growth* 24/25:484 (1974)

53. Pandya, N. S. and Bhatt, V. P., *J. Sci. Ind. Res.* B19:363 (1960)

54. Popkova, E.G. and Predvoditelev, A. A., *Kristallografiya* 15:91 (1970)

55. Baranova, G. K. and Nadgornyi, E. M., *Kristallografiya* 18:1028 (1973)

56. Sangwal, K. and Szurgot, M., *Cryst. Res. Technol.* 17:49 (1982)

57. Sangwal, K., Szurgot, M., Karniewicz, J. and Kolasinski, W., *J. Cryst. Growth* 58:261 (1982)

58. Sangwal, K. and Sutaria, J. N., *J. Mater. Sci.* 11:2271 (1976)

59. Sangwal, K., Patel, T. C. and Kotak, M. D., *J. Mater. Sci.* 14:1869 (1979)

60. Takagi, K., Fukazawa, T. and Ishii, M., *J. Cryst. Growth* 48:19 (1980)

61. McArdle, B. J. and Sherwood, J. N., in: *Advanced Crystal Growth,* (P. M. Dryburgh, B. Cockayne and K. G. Barraclaugh, eds.), Chap. 7 Prentice-Hall, London (1987)

62. Predvoditelev, A. A. and Popkova, E. G., in: *Rost Kristallov (Growth of Crystals),* (N. N. Sheftal, ed.), p. 259, Nauka, Moscow (1965)

63. Scwartz, B. and Robbins, H., *J. Electrochem. Soc.* 123:1903 (1976)

64. Mori, Y. and Watanabe, N., *J. Electrochem. Soc.* 125:1510 (1978)

65. Yang, K. H., *J. Electrochem. Soc.* 131:1140 (1984)

66. Weyher, J. L. and van Enckevort, W. J. P., *J. Cryst. Growth* 63:292 (1983)

67. Greene, L. I., *J. Appl. Phys.* 48:3739 (1977)

68. Faktor, M. M., Ambridge, T., Elliot, C. R. and Regnault, J. C., in: *Current Topics in Materials Science, Vol. 6,* (E. Kaldis, ed.), p. 1, North-Holland, Amsterdam (1980)

69. Kuhn-Kuhnenfeld, F., *J. Electrochem. Soc.* 119:1063 (1972)

70. Weyher, J. L. and van de Ven, J., *J. Cryst. Growth* 78:191 (1986)

71. Qadeer, A., Reed, J. and Bryant, F. J., *J. Electrochem. Soc.* 129:2145 (1982)

72. Landolt, D., *Electrochim. Acta* 32:1 (1987)

73. Barber, P. G. and Crouch, R. K., *J. Electrochem. Soc.* 131:2803 (1984)

74. Laser, D., Silberman, J. A., Spicer, W. E. and Wilson, J. A., *J. Electrochem. Soc.* 132:462 (1987)

75. Elliot, C. R. and Regnault, J. C., *J. Electrochem. Soc.* 128:113 (1981)

76. Takahashi, K., *Japan. J. Appl. Phys.* 18:1741 (1979)

77. Yamamoto, A., Tohno, S. and Uemura, C., *J. Electrochem. Soc.* 128:1095 (1981)

78. Bhat, R., *J. Electrochem. Soc.* 132:2284 (1985)

79. Carraba, M. M., Nguyen, N. M. and Rauh, R. D., *J. Electrochem. Soc.* 134:1855 (1987)

80. Carraba, M. M., Nguyen, N. M. and Rauh, R. D., *J. Electrochem. Soc.* 134:261 (1987)

81. Burmeister, J., *J. Cryst. Growth* 11:131 (1971)

82. van der Putte, P., Giling, L. J. and Bloem, J., *J. Cryst. Growth* 41:133 (1977)

83. van der Putte, P., van Enckevort, W. J. P., Giling, L. J. and Bloem, J., *J. Cryst. Growth* 43:659 (1978)

84. Bloem, J. and Giling, L. J., in: *Current Topics in Materials Science, Vol. 1,* (E. Kaldis, ed.), Chap. 4, North-Holland, Amsterdam (1978).

85. Dominguez, C., Pastor, G. and Dominguez, E., *J. Electrochem. Soc.* 134:199 (1987)

86. Dominguez, C., Pastor, G. and Dominguez, E., *J. Electrochem. Soc.* 134:202 (1987)

87. Kuyer, Th. J. M., Giling, L. J. and Bloem, J., *J. Cryst. Growth* 22:29 (1974)

88. Wilkes, J. G., Kingsnorth, R. L. and Low, H. E., in: *Proceedings of the Fourth European CVD Conference, Eindhoven, The Netherlands,* p. 183, (1983)

89. Ives, M. B. and Baskin, M. S., *J. Appl. Phys.* 36:2057 (1965)

90. Sangwal, K. and Arora, S. K., *J. Mater. Sci.* 13:1977 (1978)

91. Hartman, P., in: *Crystal Growth - an Introduction,* (P. Hartman, ed.), p. 367, North-Holland, Amsterdam (1973)

92. Sangwal, K., Szurgot, M. and Szczepaniak, M., *J. Cryst. Growth* 79:185 (1986)

93. Adachi, S. and Kawaguchi, H., *J. Electrochem. Soc.* 128:1342 (1981)

94. Adachi, S., Kawaguchi, H. and Iwane, G., *J. Mater. Sci.* 16:2449 (1981)

95. Caridi, E. A. and Chang, T. Y., *J. Electrochem. Soc.* 131:1440 (1984)

96. Adachi, S., *J. Electrochem. Soc.* 129:609 (1982)

97. Chu, S. N. G. and Jodlauk, C. M., *J. Electrochem. Soc.* 129:352 (1982)

98. Spink, G. M. and Ives, M. B., *J. Appl. Phys.* 42:511 (1971)

99. Heimann, R. B., Ives, M. B. and Zaya, P., *J. Cryst. Growth* 57:48 (1982)

100. Bojarski, Z. and Wokulska, K. B., *Prace Nauk. Uniw. Slaskiego, No. 209, Fiz. Chem. Metali* 3:56 (1978)

101. Vogel, F. L., Pfann, W. G., Corey, H. E. and Thomas, E. E., *Phys. Rev.* 90:489 (1950)

102. Doerschel, J., *Krist. Tech.* 7:197 (1972)

103. Amelinckx, S., *Acta Metall.* 2:848 (1954)

104. Werkhoven, C. J., Hengst, J. H. T. and Bartels, W. J., *J. Cryst. Growth* 42:632 (1977)

105. Petit, B., Pelletier, J. and Molins, R., *J. Electrochem. Soc.* 132:982 (1985)

106. Gannon, J. J. and Nuese, C. J., *J. Electrochem. Soc.* 121:1215 (1974)

107. Adachi, S. and Oe, K., *J. Electrochem. Soc.* 130:2427 (1983)

108. Adachi, S. and Oe, K., *J. Electrochem. Soc.* 131:126 (1984)

109. Chen, J. A., Lee, S. C. and Ho, L. I., *J. Electrochem. Soc.* 132:3016 (1985)

110. Barycka, I. and Zubel, I., *J. Mater. Sci.* 22:1299 (1987)

111. Huo, D. T. C., Wynn, J. D., Napholtz, S. S., Lenzo, F. R. and Wilt, D. P., *J. Electrochem. Soc.* 134:2850 (1987)

112. Uekusa, S., Oigawa, K. and Tacano, M., *J. Electrochem. Soc.* 132:671 (1985)

113. Stano, A., *J. Electrochem. Soc.* 134:448 (1987)

114. Iga, K. and Miller, B. I., *IEEE J. Quantum Electron. QE 18,* p. 22, Jan. 1982

115. Adachi, S., Noguchi, Y. and Kawaguchi, H., *J. Electrochem. Soc.* 129:1524 (1982)

116. Adachi, S., Noguchi, Y. and Kawaguchi, H., *J. Electrochem. Soc.* 129:1053 (1982)

117. Adachi, S., Kawaguchi, H. and Iwane, G., *J. Electrochem. Soc.* 129:883 (1982)

118. Kobayashi, T. and Sugiyama, K., *Japan. J. Appl. Phys.* 12:619 (1973)

119. Alferov, Zh. I., Gurevich, S. A., Mizerov, M. N. and Portnoi, E. L., *Zh. Tekh. Fiz.* 45:2602 (1975)

120. Shaw, D. W., *J. Electrochem. Soc.* 113:958 (1966)

3

ELECTROCHEMICAL PASSIVATION OF (Hg,Cd)Te

Robert T. Talasek

1.0 INTRODUCTION

For device technology based on silicon, thermal oxidation has emerged as the passivation method of choice. However, thermal oxides have proved less effective for the passivation of II-VI compound semiconductors such as (Hg,Cd)Te, used in infrared imaging detectors. Heating causes a loss of mercury from the semiconductor bulk (1)(2), changing both the bandgap and type of the material near the interface. For this and other reasons, anodic oxidation has become the most successful passivation method for these materials: an instance where electrochemistry is having significant impact on electronics technology.

1.1 Types of Infrared Detectors

Past generations of imaging detectors were based on photoconductor technology, which relies on bulk material effects. For these detectors, passivation, although necessary, has a relatively small effect on device performance. Present and future generations of imaging detectors are based on Metal-Insulator-Semiconductor (MIS) capacitor or p-n diode (photovoltaic) elements. These detectors are significantly affected by the properties of the passivation as well as the interface between the insulating passivation and the semiconductor.

Photoconductor Devices. Photoconductive detectors (3) used for infrared imaging are arrays similar to the basic structure in Figure 1. The (Hg,Cd)Te is thinned to an appropriate thickness through a combination of sawing and mechanical polishing, chemically treated to remove residual

mechanical damage and bonded to the thermally conductive substrate. The exposed area is passivated and coated with an antireflective coating. Electrical contacts to the (Hg,Cd)Te are created by chemically removing passivation and metal deposition, usually by evaporation. Many variations of this basic configuration are possible, some of which place the detector contacts on the side opposite illumination. No matter what the configuration, the basic operating principle remains the same.

For the intrinsic photoconductor (4), the conductivity of the material is given by:

Eq. (1) $$\sigma = q(\mu_n n + \mu_p p)$$

where:

σ = conductivity,
q = carrier charge,
μ_n, μ_p = carrier mobility, and
n, p = carrier concentration.

Since the narrow band-gap semiconductors used for this application are easily saturated with carriers by thermal generation of electron-hole pairs, the detector temperature is lowered sufficiently to reduce this generation to a manageable level. The detector is illuminated under bias, and the optically generated electron-hole pairs cause an increase in the conductivity of the material which can be sensed by the attached processing circuity. By rastering an array of these structures, an image can be electronically generated based on the infrared radiation striking each detector element with respect to its scanning position.

MIS Devices. Imaging detectors based on arrays of MIS structures (5) utilize variations of the basic structure shown in Figure 2. The surface of the material is mechanically polished to allow all detector elements to be in the same focal plane. The surface is then chemically polished or treated in some other manner to remove the mechanical damage caused by polishing grit. An insulator is deposited or grown on the prepared surface through one or more possible techniques. Gate metallization is deposited on the insulator and may be transparent to allow illumination through the gate or may be opaque in the case of illumination through the semiconductor.

The operation of the MIS structure is best explained in terms of the energy band diagrams and capacitance-voltage (C-V) behavior of a typical metal-oxide-semiconductor (MOS) capacitor (6). The energy bands vs. distance from the surface for a structure with zero surface potential ($\phi_s = 0$) is given in Figure 3. This condition is called the flat band. As the surface potential varies with applied gate potential in the positive or negative direction, the band positions are shifted at the surface, while

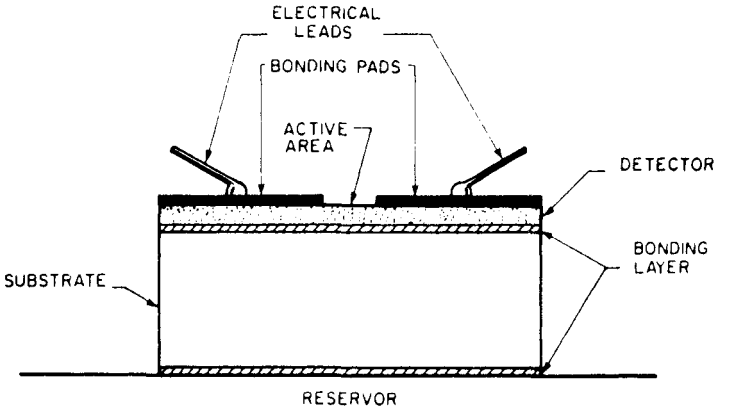

Figure 1. Principal elements of a typical photoconductive device. (With permission of Academic Press.)

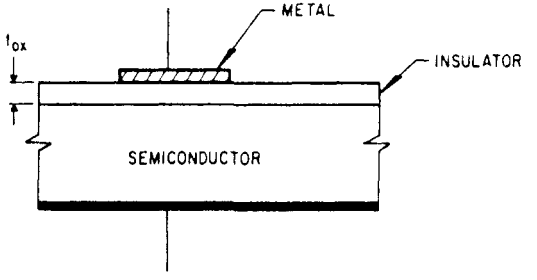

Figure 2. Metal-insulator-semiconductor (MIS) structure. (With permission of Academic Press.)

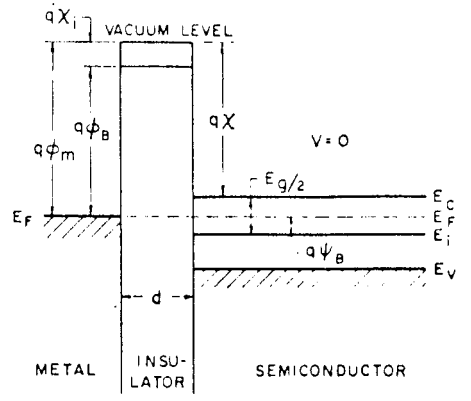

(a) IDEAL MIS DIODE (n-TYPE SEMICONDUCTOR)

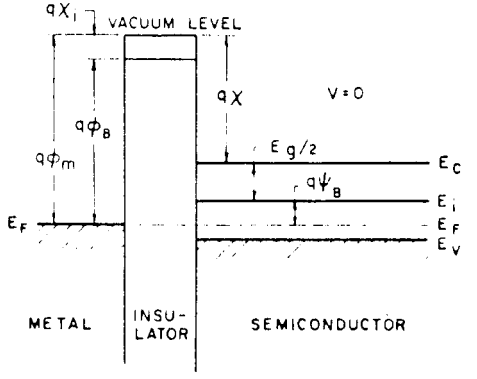

(b) IDEAL MIS DIODE (p-TYPE SEMICONDUCTOR)

Figure 3. Energy band diagrams for ideal MIS structures at V = 0. (With permission of Academic Press.)

remaining unaffected in the bulk. In the space-charge region between the surface and the bulk, the bands are bent to an extent dependent given by a form of the one-dimensional Poission equation:

Eq. (2) $$\partial^2 V/\partial x^2 = -\rho(x)/\epsilon_s$$

where: $\rho(x)$ = space charge density, and
ϵ_s = permittivity of semiconductor.

This equation, when integrated between the bulk and surface potentials, yields a quantitative description of the band bending in the space charge region. The results for three different potential conditions are shown in Figure 4.

For an n-type non-degenerate semiconductor, when the surface potential is positive, the conduction and valence bands are bent downward, while the Fermi level of the semiconductor remains fixed. Since the majority carrier density is dependent on the energy difference between the conduction band and the Fermi level (E_c - E_f), this produces an increase in the carrier density as compared to the bulk in the space-charge region. This condition is known as accumulation. As the surface potential is varied in the negative direction, E_c - E_f increases, producing a decrease in carrier density from the bulk, called depletion. This lower carrier density creates a "potential well" in which carriers have an extended life due to this lowered density (recombination rates increase with carrier density). As the surface potential is increased further in the negative direction, the hole concentration becomes larger than the electron concentration at the surface, and the surface is described as "inverted". The band behavior for p-type semiconductors is similar, but the polarity of the surface potential must be reversed.

The energy band behavior with respect to potential provides a qualitative explanation of the C-V behavior of the capacitor (Figure 5). More direct quantitative expressions have been derived, but are beyond the scope of this text. One may view the structure as a series of two capacitors, the fixed insulator capacitor (C_i) and a variable capacitor whose value is dependent on the capacitance of the space-charge region, often known as the depletion capacitor (C_D). In accumulation, the space-charge region is heavily populated with carriers and is essentially metallic. The capacitance in this region is therefore that of C_i. As the surface potential is varied in the negative direction (for n-type), the depletion of carriers begins, and C_D falls, causing a decrease in total capacitance. The minimum of the total capacitance is related to the carrier concentration by the Poisson equation, since carrier density affects the extent of band bending. As the onset of inversion begins, C_D rises and total capacitance

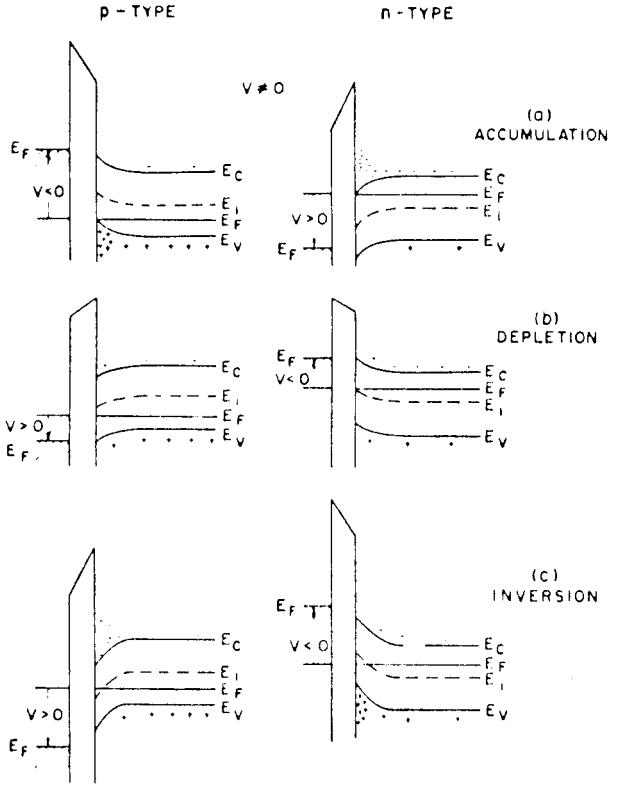

Figure 4. Energy band diagrams for ideal MIS structures when $V \neq 0$ for both *p*-type and *n*-type semiconductors. (With permission of Academic Press.)

increases until it reaches C_i again. This behavior is observed only when the gate bias controlling the surface potential is d.c. or low frequency a.c., and the resulting description is a low frequency C-V behavior. If the bias frequency is increased sufficiently, the recombination-generation rates of the minority carrier can no longer keep up with the small signal variations and do not show an increase in capacitance. Other conditions, such as deep depletion can also also be induced in this potential regime, but will not be discussed here.

In the case of a photocapacitor (6) used for infrared detection, an appropriate bias is placed on the gate to induce depletion. The potential well is created in which carriers are generated optically. These carriers can be stored for a period of time, due to their extended life, allowing the collection of signal for some "integration time." The bias is removed, which "collapses" the well, passing the carriers out to be processed by appropriate electronics. This type detector can be operated in a scanning mode similar to a photo conductor detector, or a "staring" mode. In a staring detector, a two dimensional array of MIS structures "stare" at the image without scanning for a specific integration time. The signal from each individual pixel is then recreated electronically by the appropriate circuitry.

Photovoltaic Devices. The basic structure of a photodiode array (7) is shown in Figure 6. Surface preparation is typically the same as for MIS structures, although structure thickness is probably a more critical consideration for photodiodes. An implantation mask of photoresist or photolithographically defined metal is then used to allow ion implantation of boron or other sources to produce n-type regions on a p-type substrate. Other methods of creating n-type (Hg,Cd)Te, such as impurity diffusion grown junctions or mercury in-diffusion or out-diffusion, are also used. The surface is then passivated, and contacts are etched through to the n-type islands which are connected to the silicon processing circuitry with evaporated metal. This process can be modified slightly to yield a backside illuminated device.

The basic operation of a p-n junction (8) as an infrared detector can be explained once again through the use of energy band diagrams (Figure 7). In the simplest case of an abrupt p-n junction, a region is formed where the transition between energy levels occurs which is depleted of carriers by recombination of holes from the p-side and electrons from the n-side. This region, called the depletion (or space-charge) region, has a width which is controlled by the difference in energy levels of the conduction bands of the p and n type regions. The difference in the energy levels of these two regions (and thus the width of the depletion region) is controlled by (among other things) the potential applied to the diode. Under zero bias conditions, a potential exists, known as the built-in potential (V_{bi})

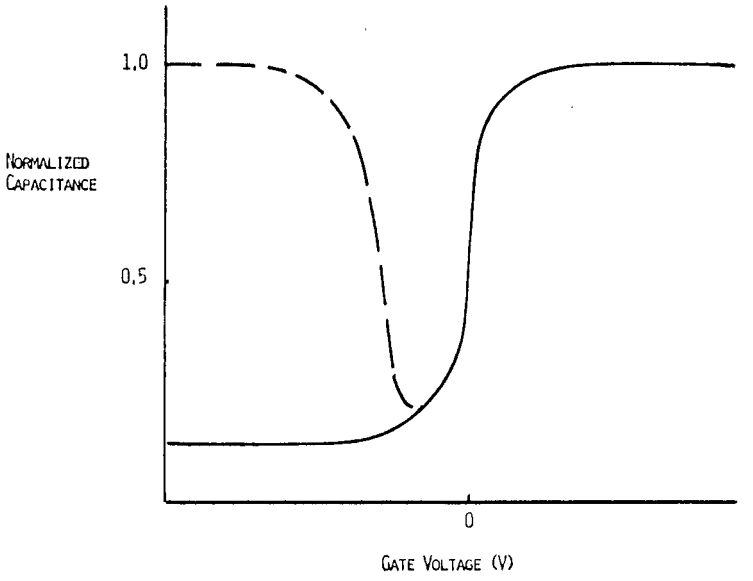

Figure 5. High frequency (solid line) and low frequency (dashed line) capacitance-voltage behavior for a typical *n*-type MIS structure.

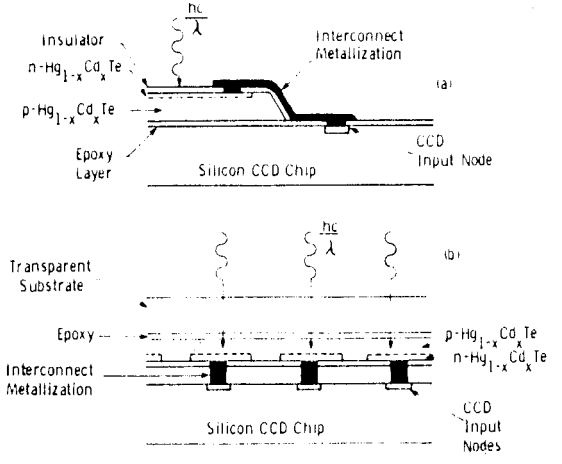

Figure 6. Schematic illustrations of the (a) planar processed and (b) backside-illuminated hybrid mosaic focal plane schemes utilizing a silicon CCD processing chip together with $Hg_{1-x}Cd_xTe$ junction photodiodes. (With permission of Academic Press.)

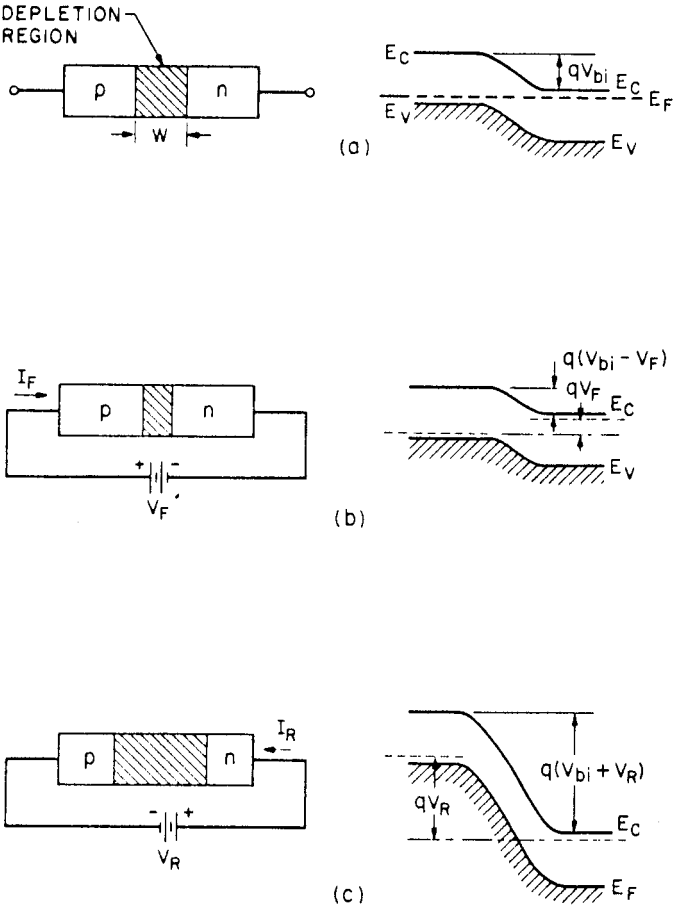

Figure 7. Schematic representations of depletion layer width and energy band diagrams of a *p-n* junction under various biasing conditions. (a) thermal-equilibrium condition, (b) forward bias condition, and (c) reverse-bias condition. (With permission of Academic Press.)

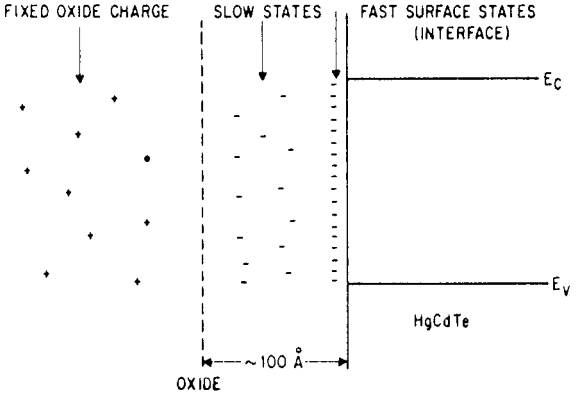

Surface states of (HgCd)Te.

Figure 8. Surface states of (HgCd)Te. (With permission of Academic Press.)

which is proportional to the difference between the two energy levels. In the presence of a forward bias, the difference in energy levels is proportional to the difference between the bias (V_F) and V_{bi}, and the depletion width is decreased. The inverse is true for the reversed bias (V_R) case. Photodiodes are operated either under zero bias or reversed bias. Photo generation of minority carriers is possible in this case because of the reduced carrier density of the depletion region. Because of the increased lifetime of majority carriers, integration can be used in a similar manner to MIS based devices, and both scanning and staring modes are feasible.

1.2 Electrochemical Passivation

Electrochemical oxidation of (Hg,Cd)Te has several shortcomings. Various reports have indicated a lack of thermal stability of the oxide (2)(10-13). Also, the oxide-semiconductor interface and oxide near the interface has relatively poor interface quality as compared to thermally oxidized silicon (14-18). Anodic oxidation at an elevated temperature has been used in one instance (9), and was reported to have increased stability over room temperature anodic oxides. This idea has not been further explored.

Oxide-related features that can impair detector performance include fast and slow interface states and fixed charges (5) (Figure 8). Fast interface states (N_{FS}) adversely affect the dark current by providing indirect transition paths for tunneling (Figure 9). Slow states within tunneling distance also contribute to dark current, acting as minority carrier traps. These contributions are most significant in material with $E_g \leq 0.12$ eV. Positive fixed charge in the oxide near the interface can make a significant contribution to the surface potential. Among other problems, this charge drives the surface of p-type material to inversion, requiring an isolating guard ring structure which allows the surface to be maintained in a depletion mode for infrared imaging.

In photovoltaic devices (7), fast interface states at the insulator-semiconductor interface can act as carrier generation-recombination centers, and may make a significant contribution to dark current which limits image contrast. Fixed oxide charge near the interface can modify the surface potential which can cause an increase in dark current through one of several mechanisms (Figure 10), including surface leakage.

Material Effects. Material also limits advanced infrared device performance. Material parameters such as carrier concentration, minority carrier lifetime, carrier mobility and crystalline perfection all have varying effects on the performance of the finished device. Compositional homogeneity also plays a significant role in device performance, since relatively small variations in composition can produce significant shifts in

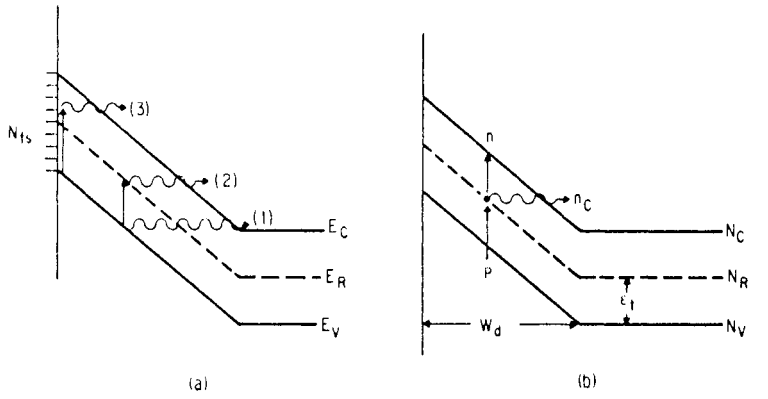

Figure 9. (a) Various tunneling mechanisms in (HgCd)Te, and (b) tunneling via bulk Shockley–Read centers. (With permission of Academic Press.)

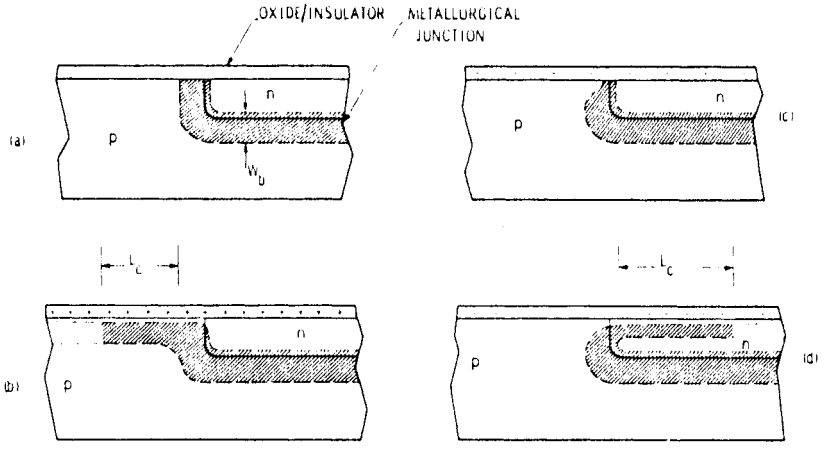

Figure 10. Effect of fixed oxide/insulator charge on the effective junction space-charge region: (a) flat-band condition; (b) positive fixed charge causes inversion of the *p* side and formation of a *n*-type surface channel; (c) negative fixed charge causes accumulation of the *p* side and a narrow field induced junction at the surface; (d) larger amount of negative fixed charge causes inversion of the *n* side and formation of a *p*-type surface channel. (With permission of Academic Press.)

the band gap (E_g) of the material. (Table 1 lists the variation of a number of parameters with composition (7)) All of these factors have resulted in a significant body of work to produce improved materials.

Numerous bulk crystal growth techniques (19) have been investigated. Although Czochralski growth methods have been investigated, technical difficulties (e.g., Hg pressure, maintaining melt composition) have prevented this technique from being as successful as with other semiconductors. A number of methods such as quench/recrystallization, often called solid state recrystallization (SSR), both horizontal and vertical Bargeman techniques, zone melting, travelling solvent zone melting and slush growth all have been used to varying extents. However, these methods generally are limited to small crystals. Efforts to increase crystal size include bulk techniques such as incremental quenching (20) and travelling heater method (THM) (21) as well as epitaxial methods (22). These methods include various liquid phase epitaxy (LPE) methods, vapor phase epitaxy (VPE), controlled diffusion of Hg into CdTe, vacuum sputter deposition, metal organic chemical vapor deposition (MOCVD) (22), molecular beam epitaxy (MBE) (23)(24), and laser assisted deposition (LADA) (25). (Note: This list is only partial and is for illustration. The reader is referred to the literature for a more complete review of material growth techniques). Each of these methods produces material with different compositional homogeneity and crystalline perfection.

Surface Preparation. Before passivation, various surface preparations may be used to remove surface damage induced by mechanical polishing which would otherwise significantly reduce carrier lifetime (26). Chemical etching or chemical-mechanical polishing with various concentrations of Br_2 in methanol (or other solvents) have been used, and have been shown to leave the surface depleted of Cd, and to a lesser extent, Hg (27-31). Electropolishing techniques (32) as well as oxidation and etchback (27)(28) have been used to address this problem, and seem to leave the surface closer to its original stoichiometry.

Such wide variances in material and surface preparation can be expected to have a significant effect on a surface process such as anodic oxidation. However, the literature is full of studies of anodic oxidation, with each study using the researchers favorite material and surface preparation, often with conflicting results. In the following pages, an attempt will be made to summarize these studies and find a common ground where one exists. Also, an attempt will be made to note material and surface preparation differences when they have been reported, so that conflicting results can be better understood.

With all of the problems associated with anodic oxidation, it is inevitable that an attempt be made to develop alternative passivation methods. Some, such as sulfidization, are electrochemical, others are

Table 1

SUMMARY OF $Hg_{1-x}Cd_xTe$ ELECTRICAL AND OPTICAL PROPERTIES (ALL VALUES SHOWN ARE HIGHLY APPROXIMATE)

$Hg_{1-x}Cd_xTe$ alloy composition	x	—	0.19		0.20		0.30			0.40		0.55
Temperature	T	(K)	77	170	30	77	77	125	200	200	300	300
Energy gap[a]	E_g	(eV)	0.079	0.107	0.080	0.094	0.251	0.260	0.275	0.425	0.433	0.656
Cutoff wavelength	λ_{co}	(μm)	15.8	11.6	15.4	13.2	4.9	4.8	4.5	2.9	2.9	1.9
Peak wavelength	λ_p	(μm)	14.4	10.5	14.0	12.0	4.4	4.3	4.1	2.6	2.6	1.7
Intrinsic carrier concentration[b]	n_i	(cm^{-3})	2×10^{14}	9×10^{15}	4×10^{9}	9×10^{13}	1×10^{9}	3×10^{12}	3×10^{14}	6×10^{12}	6×10^{14}	1×10^{13}
Electron mobility in n-type	μ_e	(cm^2/V sec)	2×10^{5}	3×10^{4}	3×10^{5}	2×10^{5}	5×10^{4}	2×10^{4}	1×10^{4}	4×10^{3}	3×10^{3}	2×10^{3}
Hole mobility in p-type	μ_h	(cm^2/V sec)	~1,400[d]	~400[d]	1,400[d]	800[d]	500[c]	300[c]	200[c]	140[f]	100[f]	20[f]
Conduction and light-hole mass[g]	m_c, m_{lh}	—	0.006	0.008	0.006	0.007	0.018	0.019	0.020	0.030	0.030	0.048
Heavy-hole mass[g]	m_{hh}	—	0.5		0.5			0.5		0.5		0.5
Kane's matrix element[e]	E_p	(eV)	19		19			19		19		19
Static dielectric constant[h]	ϵ_s	—	17		17			16		15		14
High-frequency dielectric constant[h]	ϵ_∞	—	12.5		12.5			12		11		10

[a] From Schmit and Stelzer (1969).
[b] From Schmit (1970).
[c] From Scott (1972).
[d] See Fig. 44b.
[e] From Riley *et al.* (1978b).
[f] From Scott *et al.* (1976).
[g] From Weiler (1981).
[h] From Dornhaus and Nimtz (1976).

Source: Reprinted from Reine, M.B., et al, *Semiconductors and Semimetals–Vol. 18,* Academic Press, 1981, with permission of Publisher.

not. A review of these methods will be given, with emphasis placed on the electrochemical techniques.

Finally, there have been other electrochemical processes involving II-VI semiconductors, the most significant being electrodeposition. Among the compounds deposited from solution are CdS (33), CdSe (34), (Cd,Se)Te (35) (of various compositions), HgS (36), and (Hg,Cd)Te (37). (The references listed are for example only). Various metal sulfides have also been anodically produced from sulfide containing electrolytes (38-40). These films have generally been used for solar cell application due to limitations in crystalline perfection, compositional control, and film purity, although a relationship between sulfide passivation and anodic deposition of sulfide films may exist. Since this text will deal with infrared detector technology, no further mention will be made of electrodeposition processes. Electrochemical doping, primarily with copper, has also been described (41). No published reports of device applications have been made, however, and this process will not be discussed further.

2.0 ANODIC OXIDATION

Throughout the body of research on anodic oxidation, many different electrolytes have been used. By far the most common is 0.1 N KOH in 90% ethylene glycol/10% water described by Catagnus and Baker (42). In a few instances, the concentration of KOH was varied for one reason or another. Hydrogen peroxide and 0.1 N KOH in methanol or water have also been used studied in instances. Also, the use of acetate, borate, and phosphate buffers have been used in investigative studies where it was necessary to control pH, and at least one study exists where Hg, Cd, and Te were added to the electrolyte. In almost no instance was the total ionic strength controlled. All of these factors as well as material and surface preparation must be considered when a comparison of various results are made.

Much research has been conducted to determine the oxide composition in the bulk and at the semiconductor oxide interface. Both calculated and experimentally-determined phase diagrams of various types have been reported. Also, numerous surface analysis and optical techniques have been used to evaluate bulk and interface composition.

An equally active area of research has been determination of the chemical processes involved in oxide formation. Many different electrochemical measurement approaches have met varying degrees of success in this endeavor. Various analytical techniques, such as those used in surface analysis have, also been employed in attempts to follow the progressive steps of oxide formation.

2.1 Oxide Composition - Phase Diagrams

Several attempts have been made to construct phase diagrams of the Hg, Cd, Te, O system. The earliest diagram constructed, however, contained only Cd, Te and O and were constructed from an effort to grow and characterize bulk crystals from various mixtures of CdO and TeO_2 (Figure 11) (43). Two compounds found were reported as cadmium ditellurite ($CdTe_2O_5$) and cadmium mono-tellurite ($CdTeO_3$). The later was reported to have two phases with a transition occurring at 700°C.

In 1983, two different types of phase diagrams were reported independently. First, a solid-state quaternary phase diagram was constructed for the Hg-Cd-Te-O system by Rhiger and Kvaas (44) through thermodynamic calculations of mutual stability as Gibb's free energy of various elements and compounds assumed to be possible components of the anodic oxide. The four ternary diagrams which represent the sides of the quaternary diagram are shown in Figure 12. In order to construct this diagram, a number of assumptions were made, as can be expected. One significant assumption is the absence of $CdTe_2O_5$ from consideration. Another is that no compounds containing both Hg and Cd were considered. Instead these compounds were considered as a two-phase mixture of compounds in a ratio to arrive at the appropriate stoichiometry. (Note: thermodynamic data for the quaternary compounds are not readily available). The calculated phase diagram was confirmed in some cases by attempted reaction of mutually stable or unstable compounds as predicted by tie lines within the phase diagram, and the composition of the reaction products was confirmed by Raman spectroscopy. Where evaluated, the phase diagram made correct predictions

A significant conclusion drawn from this diagram were that elemental mercury, HgTe, (Hg,Cd)Te and $CdTeO_3$ are thermodynamically stable with respect to mercury-tellurium oxides and mercury oxides. The prediction was made that the instability of the mercury-tellurium oxides and mercury oxides may decompose to yield Hg or HgTe at the oxide semiconductor interfaces, with potentially disastrous results to device performance. This instability has been demonstrated experimentally (1)(2)(10-12) with mercury loss and oxide compositional changes being demonstrated by various methods after thermal annealing. In a least one case (12), a change in semiconductor type as shown by capacitance-voltage behavior has been demonstrated. The presence of a multi-layered oxide structure has also been demonstrated by Auger and SALI (surface analysis by laser ionization) profiling (13). The layer closest to the interface was concluded to be $CdTeO_3$, with the mercury depleted at the interface being present in the outer layers as HgTe. Mercury enrichment as suggested by Rhiger and

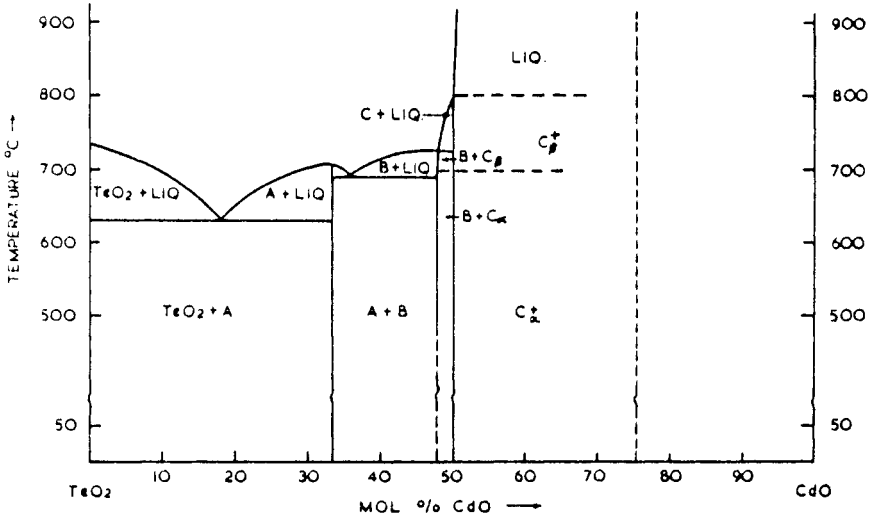

Figure 11. $CdO-TeO_2$ (phase diagram, major compositions and temperatures). 18 mol % CdO, 630 ± 3°C eutectic; 33.3 mol % CdO, 708 ± 3°C congruent point (A); 35.5 mol % CdO, eutectic 690 ± 3°C; 48 mol % CdO (approx.), 725 ± 3°C, incongruent point (B); 50 mol % CdO, 795 ± 3°C, incongruent point (C), phase change in (C). (With permission of Chapman Hall.)

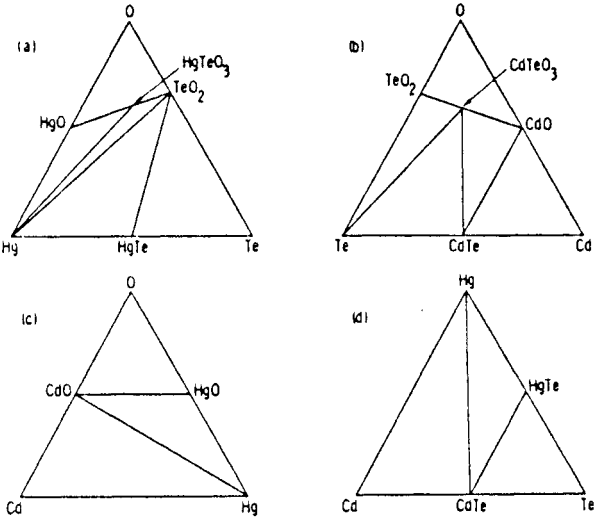

Figure 12. The four ternary phase equilibrium diagrams: (a) Hg-Te-O, (b) Cd-Te-O, (c) Hg-Cd-O, (d) Hg-Cd-Te. Tie lines connect pairs of mutually stable phases. (With permission of American Institute of Physics.)

Kvaas was only seen at the interface after thermal annealing.

Another type of phase diagram reported in 1983 was constructed by Davis, et al. (45), from depth profiling of anodic oxides by x-ray photoelectron spectroscopy (XPS) in conjunction with ion beam sputtering in Figure 13. This type diagram, called a surface behavior diagram, represented the oxide composition as a function of depth. This group concluded a bulk composition of a combination of $(Cd,Hg)Te_3$ and $(Cd,Hg)Te_2O_5$ with the mercury to cadmium ratio being considerably lower than that of the semiconductor. Mercury depletion of the interfacial region was also reported agreeing with the experimental results of Stahle, et al., cited earlier. Similar studies were performed by Seelmann-Eggebert and Richter by XPS with dissolution used in place of sputtering for depth profiling. The studies report an accumulation of HgTe at the interface. The extent of this accumulation is reported to be a function of electrolyte pH, anodization voltage, and presence of an organic solvent in the electrolyte.

A year later another stability diagram based on thermodynamic calculations was reported. Based on the methods developed by Pourbaix (48), this diagram presented regions of stability of various dissolved and undissolved species in a potential vs. pH format (Figure 14) (49). Thermodynamic calculations once again supported elemental mercury being stable with respect to various oxide components, although calculations were once again limited by the lack of data for the Hg-Cd-Te-O quaternary compounds. Also, the mercury and cadmium ditellurites were calculated to be electrochemically more stable than the monotellurite compounds. Experimentally determined diagrams from electrochemical measurements (potentiodynamic polarization measurements) made in various buffer solutions were also constructed using n-type, $x = 0.225$ material which had been mechanically polished (Figure 15). These measurements indicated that the onset of passivation corresponding with a current maximum did not occur until a much higher applied potential than what was predicted thermodynamically, thus suggesting that the anodic oxidation process might be significantly affected by the reaction kinetics.

2.2 Oxide Analyses

Perhaps the first investigation into the chemical composition of the anodic oxide of HgCdTe was reported by Nemirovsky and Finkman in 1979 (50). Anodic oxide films were grown on n-type slush grown (Hg,Cd)Te ($E_g = 0.1$ eV) in 0.1 N KOH in methanol and various concentrations (< 0.1 N) of KOH in 90% ethylene glycol / 10% H_2O. The material surface was mechanically polished and etched in 20% Br_2 in methanol prior to anodization. The refractive index and dielectric constant of the oxide were determined to be closer to TeO_2 than CdO or HgO, so the authors concluded that the

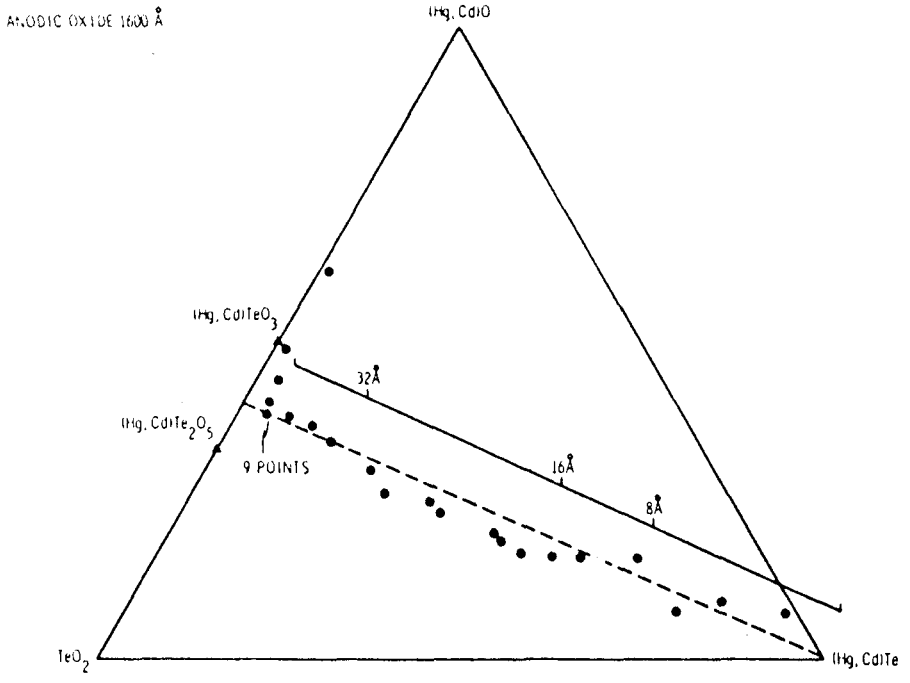

Figure 13. (HgCd)-TeO_2-(HgCd)Te surface behavior diagram of $Hg_{0.8}Cd_{0.2}Te$ with a 1600 Å thick anodic oxide. The superimposed depth scale gives the equivalent thickness of oxide for an abrupt interface and a mean free path of 16 Å. The dashed line represents the depth profile path for a stoichiometric oxide and semiconductor. (With permission of Elsevier Science Publishers.)

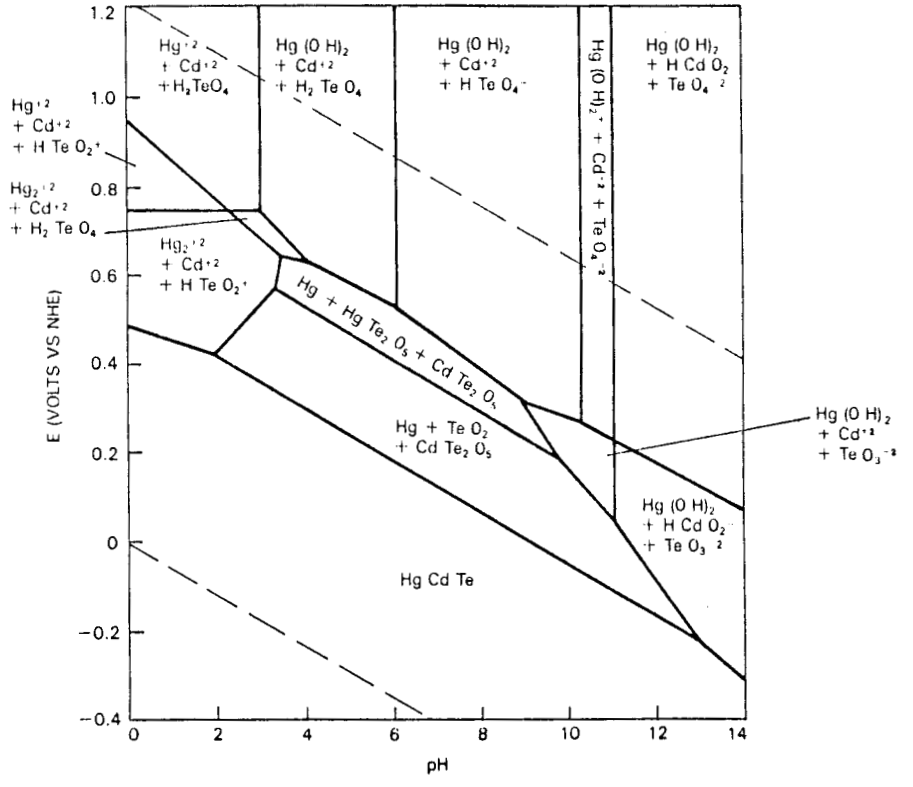

Figure 14. Potential-pH diagram for $Hg_{0.8}Cd_{0.2}Te$ constructed from thermodynamic data.

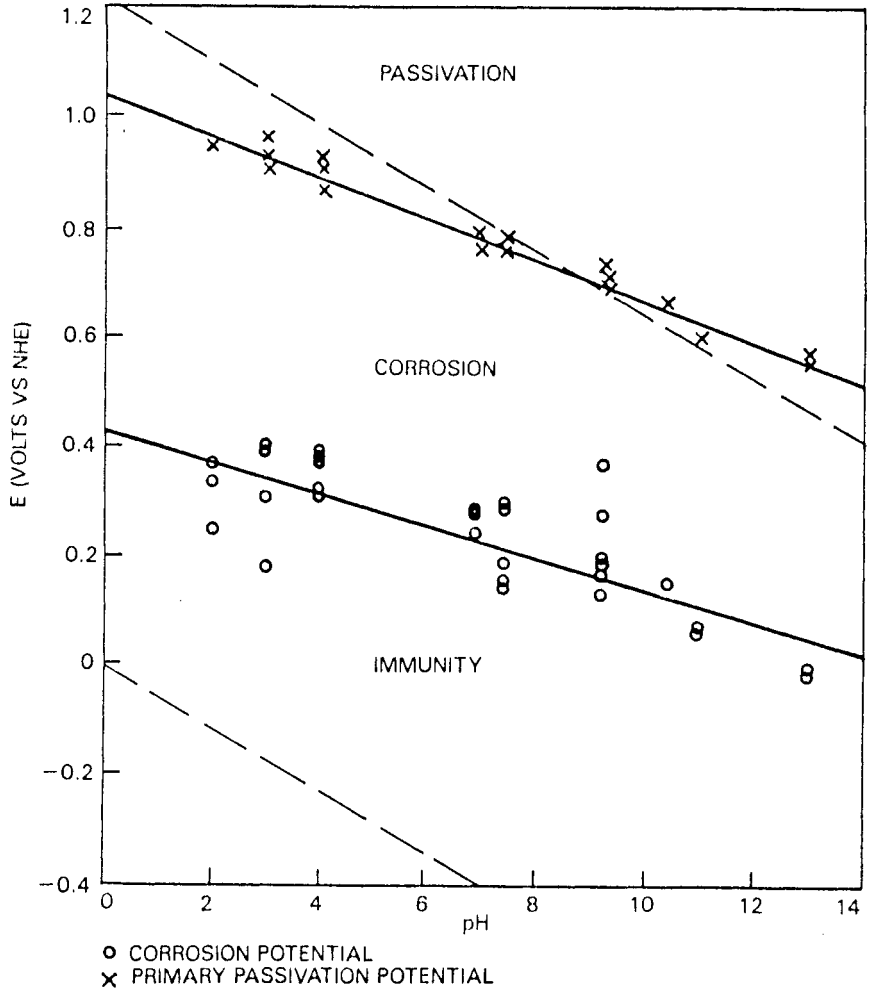

Figure 15. Potential-pH diagram for mechanically polished HgCdTe constructed from potentiodynamic polarization curves in various pH buffers.

passivation layer must be primarily TeO_2 (no other oxides were considered). The authors theorized that cadmium in the semiconductor was oxidized to Cd^{2+} and dissolved, but mercury was trapped in the TeO_2 as an elemental layer which is partially oxidized at the interface.

Shortly after this, however, the presence of cadmium in a Cd-Te-O oxide compound was demonstrated (51)(52) using sputtering and XPS depth profiling. Also, it was pointed out that the optical properties of $CdTeO_3$ were suitable to explain the behavior observed by Nemirovsky and Finkman. Finally, this group also reported the significant mercury depletion in the bulk and interface region discussed with the surface behavior diagrams.

From this point on, various groups have argued the extent of mercury depletion in the oxide. An extensive study (53) of mercury losses during various combinations of sputtering or thermal desorption used in conjunction with analytical techniques demonstrated that at least part of the mercury loss was due to preferential sputtering of mercury during depth profiling. However, the extent of this contribution to analytically determined composition of the oxide is still disputed. In fact as late as 1982, Farrow, et al. (54), still claimed that little mercury was present in the anodic oxide as determined by XPS, while Morgen et al. (55), claimed only that the oxide was depleted to some unknown extent through Auger electron spectroscopy (AES). Also, Farrow claimed spectroscopic evidence that $CdTe_2O_5$ could not be a major component of the oxide. Christie, et al. (56), stated that the oxide could be as much as 25% $CdTe_2O_5$ while stating that this was not necessarily in disagreement with Farrow since this would not be considered a major constituent of the oxide. Seelmann-Eggebert, et al. (57), strongly disputed Farrow's measurement as erroneous, stating that they measured the same oxygen Auger parameter (the parameter claimed by Farrow to be different in $CdTeO_3$ and $CdTe_2O5$) for both compounds. However, in the same paper, Seelmann-Eggebert claimed the composition of the oxide was primarily $HgTeO_3$ and $CdTeO_3$. Also, they made the first claim that the mercury to cadmium ratio in the oxide might be as high as in the semiconductor, and was certainly no lower than 1:1. Electron microprobe analysis by Kaiser, et al. (58), also supported a significant mercury concentration in the oxide, although somewhat less than Seelmann-Eggebert. Surface analysis by laser ionization (SALI), Rutherford backscattering (RBS) (59), and neutron activation analysis (NAA) (60) have also established a significant mercury content in the oxide. Along with the measurement artifacts which have been discussed in other publications, perhaps Strong, et al. (61), have demonstrated another significant cause of this wide disagreement concerning oxide composition. By determining the composition of oxides grown in different electrolytes (0.1 N KOH in 90% ethylene glycol /10% H_2O and H_2O_2, unspecified

concentrations), significant differences in oxide composition were found, the later being depleted of Hg and Cd to a much larger extent than the former. The oxide grown in alkaline solution showed significant quantities of mercury and cadmium, although somewhat depleted with respect to the bulk. In general, the oxide has been shown to be 30-40% depleted of mercury with respect to the bulk, and only slight (if any) depletion of cadmium. The multilayer model mentioned earlier (13) suggests that the mercury depletion is primarily near the interface, and precludes the conclusion of a single oxide composition.

2.3 Chemical Processes

Numerous attempts have been made to study the interactions which produce oxidation of the (Hg,Cd)Te surface. Several studies of the interaction of molecular oxygen in ground and excited states have been made with XPS and other surface analysis techniques (62-67). Pressure conditions have varied from atmospheric to high vacuum in situ studies. In one instance, Al was used instead of oxygen to study the behavior of this surface (68). These studies are of limited usefulness for studying anodic oxidation processes since the oxygen-containing species is chemically different and is contained in a significantly different matrix. (This is not a criticism since most of these studies were intended to study gas phase oxidation. In fact, in at least one case it was specifically concluded that anodic oxidation and gas phase oxidation must be significantly different processes) (67). Nevertheless, an important conclusion can be drawn from these works that should be applicable to anodic oxidation. Significant evidence has been produced that surface preparation had a significant affect on both the chemical processes involved in oxidation, and the oxide composition for the oxides (63-70). It was also suggested that the constituent elements may behave differently from one another and that impurity absorption (specifically organic acids) may impede the oxidation process (62). As will be shown, these conclusions will be supported by more direct studies of the anodic oxidation process.

A number of different techniques have been used to study the surface preparation techniques used prior to anodic oxidation. For device fabrication, mechanical polishing is usually necessary to insure a relatively flat surface. Some chemical treatment is necessary to remove the mechanical damage induced by grit polishing. Often etching or chem-mechanical polishing is used to remove this damaged layer. However, it has been shown that chemical treatments do not leave a stoichiometric surface (27-30)(63). A kinetic study of the reaction of 0.1N Br_2 in methanol with (Hg,Cd)Te under etch conditions found the relative rates of reaction of the individual constituents to be:

Cd:	10
Hg:	3
Te:	1

and the disparity in reaction rates worsened with the addition of mechanical action (29). Various attempts have been made to estimate the depth of the depletion layer caused by the inequity of the constituent reaction rates. Estimates as low as 0.7 nm (28) and as high as 60 nm (27) have been made either by optical techniques or a combination of oxidation-dissolution combined with optical techniques.

This depletion has been shown to have an effect on the chemical processes involved in anodic oxidation. Various authors have reported the presence of an additional dissolution peak in potentiodynamic polarization (I-V) curves of the etched or polished surface as opposed to a mechanically polished surface, although the two preparation techniques were only compared in case (49). Although no conclusive identification has been made of this species, it has been speculated that this additional peak could represent dissolution of excess tellurium on the surface or dissolution of some bromine-containing species. Several efforts have been made to develop surface treatment which removes this depleted layer from the surface. Anodic oxidation followed by acid stripping of the oxide with nitric acid, hydrochloric acid, or lactic acid in one or more steps have been shown to yield a stoichiometric surface (27)(28)(69)(70), as long as this process is stopped before consuming undepleted material (32)(70)(72). Also, electropolishing has been used to treat the surface, also resulting in a stoichiometric surface. Some limited description of the effects of this surface treatment on the capacitance-voltage behavior of an MOS capacitor fabricated from this surface were described as having negative fixed charge (Figure 16) (32), although the results are not improved with respect to fast surface states, as compared to Br_2/methanol polished surfaces.

Various efforts have been made to study the anodization process using common electrochemical techniques. One measurement used to evaluate the corrosion/passivation properties of alloys is potentiodynamic polarization curves (74). Potentiodynamic polarization measurements involve applying a voltage ramp (usually at a slow enough rate to approximate static behavior) and measuring the resulting current from electrochemical processes. Several characteristics of this curve are worth mentioning. First is the open circuit potential (OCP), the potential at which the anodic and cathodic currents are equivalent and total current is at a minimum. Between the OCP and the current maximum peak is a region in which only dissolution processes are occurring. The peak, the primary passivation

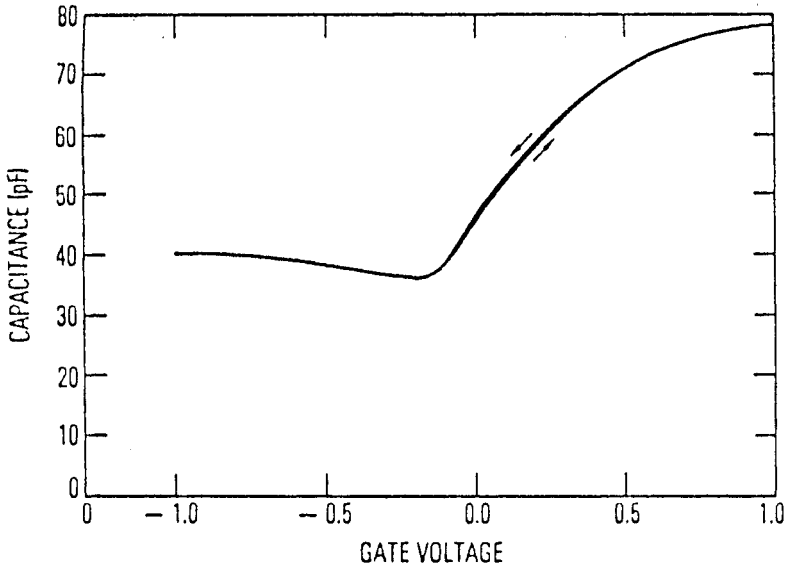

Figure 16. Capacitance voltage characteristic for electroetched MOS structure at 109 K. (With permission of American Institute of Physics.)

potential, represents the onset of passivation. Beyond this peak is the passivation region. Sometimes a drastic and sudden current increase is observed, representative of passivation breakdown. This is referred to as the transpassive region. The first potentiodynamic polarization on (Hg,Cd)Te appeared in 1982 (73). (See Figures 17-21). As is readily apparent, the appearance of these curves vary significantly, and one must take into consideration the wide variation in material, surface preparation, electrolyte, and scan conditions to understand this variation (See Table 2). However, one consistent result is apparent. In the absence of any pre-treatment designed to remove the depleted layer caused by bromine-methanol treatment, two current peaks appear. One study (49) demonstrates that one of these peaks appears at the same potential for mechanically polished and chemically polished samples. This was observed in a variety of electrolytes at a number of pH values. The second peak occurs at a more cathodic potential. Both vary with pH at the same rate (See Figure 22).

A closely related experiment attempted to determine the effect of hydroxide ion concentration on the rate of anodic processes in the absence of polarization (78). This was done with a series of Tafel plots (79) (I-V relationship near the region where the OCP) in varying hydroxide ion concentrations. The results indicated that the anodic current representative of dissolution rate in the absence of overpotential is independent of hydroxide concentration.

A second technique that has seen some use is ring-disk electrode measurements (78). Ring disk electrodes generally consist of a disk constructed of the material of interest (Hg,Cd)Te in this case) with a concentric ring insulated from the disk. In this manner, the ring and disk can be held or swept at separate potentials. Often the ring is split so that each part can be held at separate potentials. Using an electrode of this type allows various oxidation or reduction processes to be carried out while various dissolved species of interest can be reduced at the ring(s), producing an indication of increased or decreased concentrations. Mass transport processes can also be studied by rotating the electrode at various angular velocities. Sakashista, et al. (72)(73), performed two extensive studies of the first type with HgTe and (Hg,Cd)Te using a split ring set-up. Among the significant points of this study was an observed reduction of ring currents designed to demonstrate the decrease of Hg and Te dissolution under appropriate conditions (Fig 23); cadmium cannot be observed by the method due to its cathodic reduction potential. Also, a distinct difference in the dissolution processes occurring during anodization was demonstrated in an aqueous KOH electrolyte compared to the 90% ethylene glycol/10% water mixture. (Figure 24). It is readily apparent that there is an extreme difference in the extent of dissolution in the two

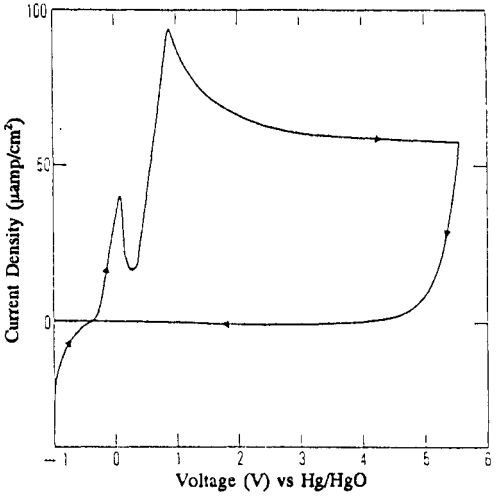

Figure 17

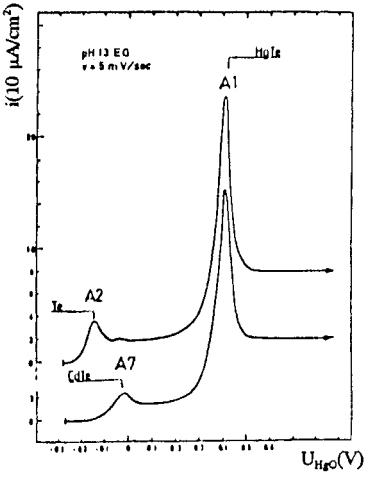

Figure 18

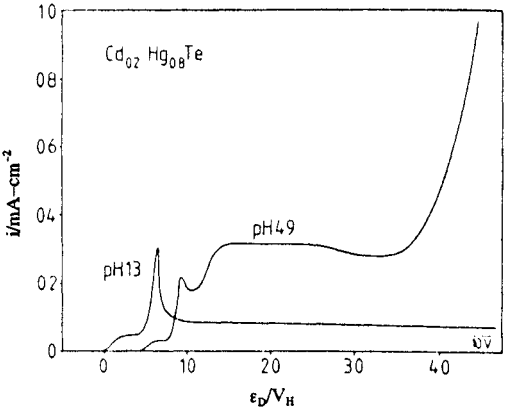

Figure 19

Figures 17-21. Current potential behavior for HgCdTe under conditions specified in Table 2. (With permission of The Electrochemical Society, Inc.)

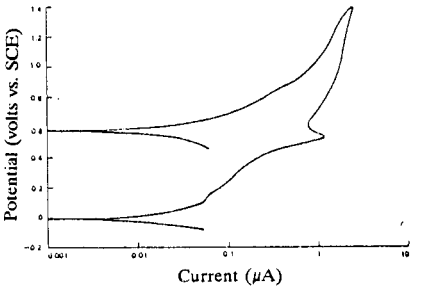

Figure 20a

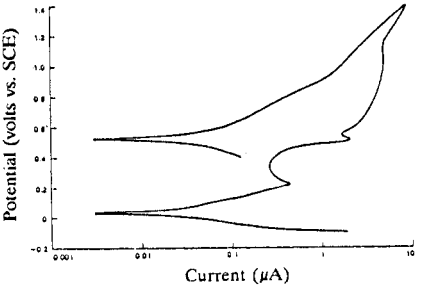

Figure 20b

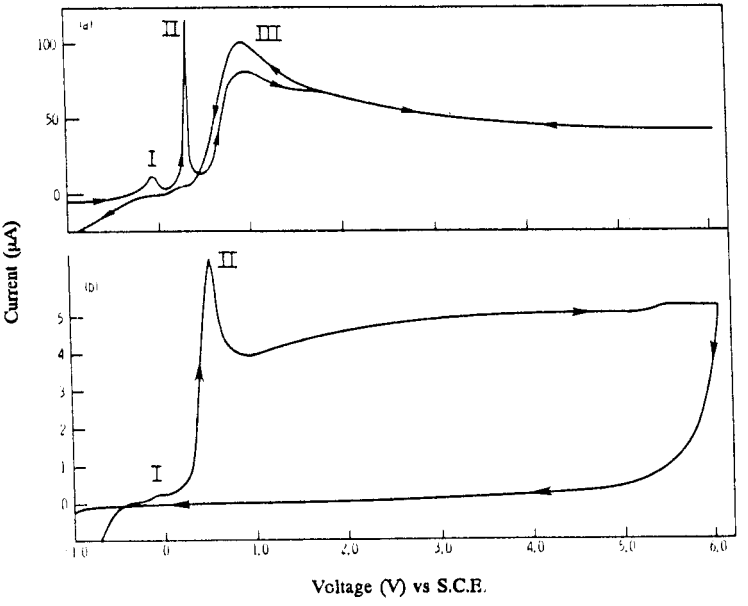

Figure 21

Figure 17-21 (continued). Current potential behavior for HgCdTe under conditions specified in Table 2.

Table 2

Figure	Reference	Material	Surface Preparation	Electrolyte/Scan Rate
17	32, 71	Slush growth n-type X = 0.3	5% Br_2/MeOH 1 min. etch	0.1M KOH in 90% Et Gly/ 10% H_2O Scan - 12 mV Sec^{-1}
18	46	"Device quality" type ? X = 0.2	Etch/polish in 3% Br_2/MeOH time ?	0.1 M KOH in 90% Et Gly/ 10% H_2O Scan - 5 mV Sec^{-1}
19	73	"Un-annealed" p-type X = 0.2	Mechanical polish 5% Br_2/MeOH etch reduced at 0.6V (vs SHE) in acetate buffer	a) pH 4.9 acetate buffer b) 0.1M KOH + 90% Et Gly/10% H_2O Scan - ?
20	49	SSR n-type X = 0.225	a) Mechanical polish 0.3 microns Al_2O_3 grit. b) Mechanical polish, 0.3 microns Al_2O_3 grit. 0.5% Br_2/MeOH Chem-mechanical polish	Buffer - pH = 6.86 Scan - 0.1mV Sec^{-1}
21	75	Slush growth p-type X = 0.2	Mechanical polish 1% Br_2/MeOH etch	a) 0.1 M KOH aqueous b) 0.01 N KOH Et Gly

(With permission of The Electrochemical Society, Inc.)

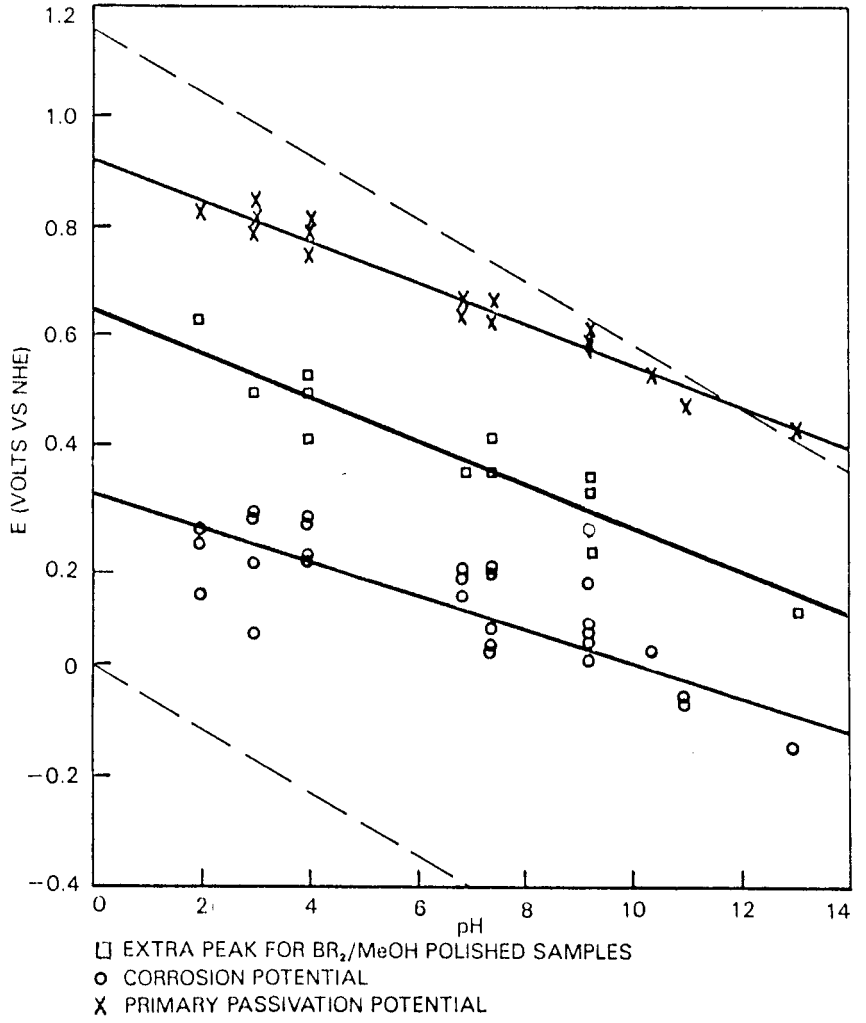

Figure 22. Potential-pH diagram for Br_2/methanol polished HgCdTe constructed from potentiodynamic polarization curves in various pH buffers.

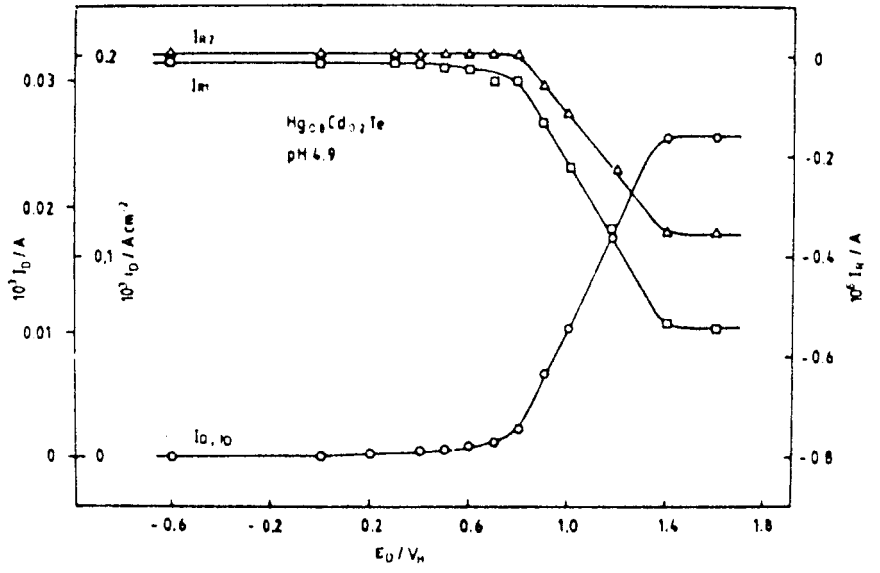

Figure 23. Quasipotentiostatic polarization curve of a CMT disk and the related ring currents I_{R1} and I_{R2} in pH 4.9 acetic buffer. Values after 10 min oxidation ε_{R1} = –0.30V, ε_{R2} = 0.40V. (With permission of The Electrochemical Society Inc.)

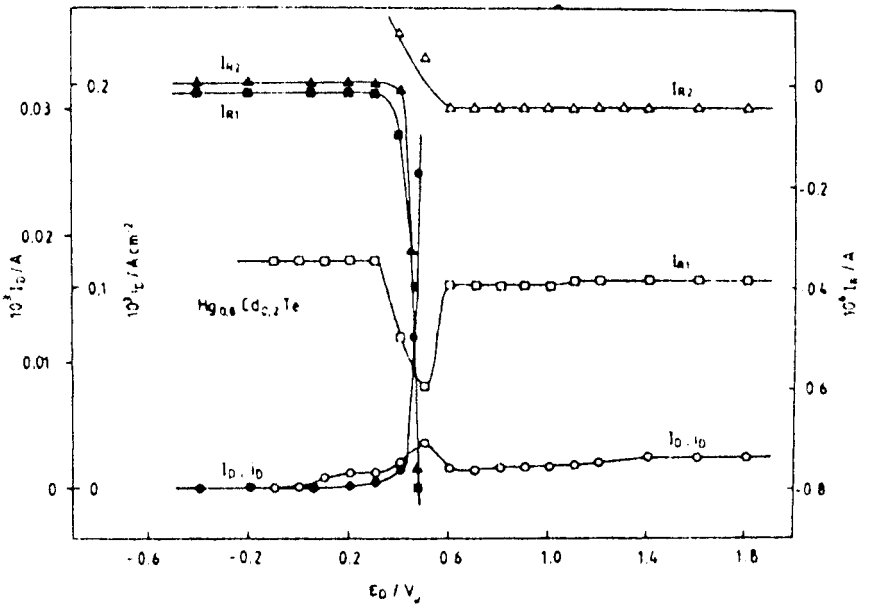

Figure 24. Quasipotentiostatic polarization curve of a CMT disk and related ring currents I_{R1} and I_{R2} in 0.1M KOH solid symbols (●, ■, ▲) and 0.1M KOH + 90% EG open symbols (○, □, Δ) after 10 min oxidation, ε_{R1} = -0.68V, ε_{R2} = -0.08V. (With permission of The Electrochemical Society, Inc.)

electrolytes. However, it is not clear from the data whether the difference is due to the variation of total KOH concentration (0.1 N vs. 0.01 N total concentration) or the difference in solubilities of the dissolved species due to the presence of ethylene glycol. Both could be expected to make major contributions. The ring-disk behavior of the oxidation of material which had been potentiostatically reduced was also studied, but the oxidation was carried out in pH 4.9 buffer, which has a significantly different potentiodynamic behavior and the results of this portion of the study are not directly comparable to others done in alkaline solution. A second set of ring-disk electrode experiments performed as a part of a kinetic study (79) has also been conducted to evaluate mass transport effects. These experiments were performed with a solid gold ring and incrementally quenched material under various potentiostatic conditions. The electrolyte used was 90% ethylene glycol/10% water with various concentrations of KOH added. The current observed at the ring of a ring-disk electrode is described by:

Eq. (3) $$I_{L,R} = 0.62nF\ [R_3^3 - R_2^3]^{2/3}\ D^{2/3}\ w^{1/2}\ v^{-1/16}\ C^B,$$

where:

$I_{L,R}$ = Limiting ring current,
n = Number of electrons transferred,
F = Faraday's constant,
R_3 = Outer ring radius,
R_2 = Inner ring radius,
D = Diffusion coefficient of active species,
w = Angular velocity,
v = Kinematic viscosity, and
C^B = Bulk concentration of species being reduced at ring.

Besides the factors that affect ring current that can be interpreted directly from the equation above, it should also be noted that the kinetic half-life of species being formed at the disk will affect the ring current, since it will affect the population of the species surviving long enough to reach the ring. Figure 25 represents the measured ring current at a function of rotational velocity for several concentrations of KOH.

For a simple system in which this relationship is only affected by the diffusion coefficient of the species being reduced, a straight line should be observed. This is the case for 0.1 N KOH. However, as the KOH concentration is dropped, non-linear behavior is observed which should be indicative of a change of species being reduced at the ring, resulting from an increased half-life of whatever species is reacting with the hydroxide ion.

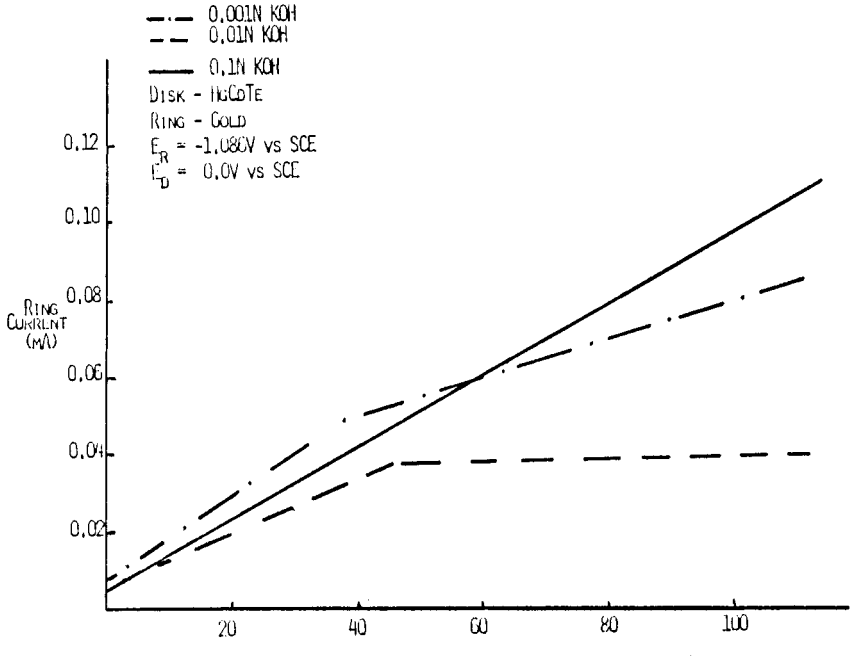

Figure 25. Ring current vs rotational velocity for various concentrations of KOH in 90% ethylene glycol/10% H_2O.

Another electrochemical study determined the potential behavior vs. time for constant current anodization conditions (32). The material used was n-type, slush-growth material with a composition of x = 0.3. The material was etched extensively in 5% bromine in methanol, to the extent of removing approximately 20 microns of material. The electrolyte used was 0.1 N KOH in 90% ethylene glycol/10% water. Figure 26 illustrates the behavior observed for various current densities. One significant aspect of this behavior is the period where potential is essentially independent of time. This portion of the curve (called the induction period) is indicative of no passivation being formed (no IR drop) with only dissolution supporting current, a characteristic of dissolution-precipitation type passivation processes. Furthermore, at sufficiently low current densities, the induction period becomes infinite, suggesting that the precipitation portion of the mechanism is prevented by mass transport of some species away from the (Hg,Cd)Te surface.

A different technique was used to study the fundamental processes involved in the initial oxide formation (76). A technique called a.c. impedance (80) studies the effects the system has on a.c. signals of varying frequency, thereby investigating the elementary mechanism steps on the timescale that they actually occur. This investigation was conducted on n-type material grown by solid state recrystallization where x = 0.225. The material was prepared by mechanically polishing with 0.3 micron grit only, so no effects of bromine etching were encountered. The electrolyte used was 0.1 N KOH in 90% ethylene glycol/10% water. Through mathematical models which have been constructed for the impedance behavior of various general mechanism types, it was concluded that the impedance behavior of this system best matched that of a mechanism consisting of three steps: an electron transfer, then chemical process, and finally a second electron transfer (ECE mechanism) for the special case where the first electron transfer is much faster than the second electron transfer. Considering this as well as the dissolution-precipitation effects presented earlier, the mechanism was concluded to be:

Eq. (4a) $$M \overset{k_{1,h}}{\rightleftharpoons} M^{n+} + ne^-, \quad k_{1,h} \propto 1/R_{ct}$$

Eq. (4b) $$M^{n+} + nOH^- \rightarrow M(OH)_n$$

Eq. (4c) $$M(OH)_n \overset{k_{2,h}}{\rightleftharpoons} MO_n + nH^+ + ne^-, \quad k_{2,h} >> k_{1,h}$$

(Authors Note: Corrections should be made in the hydroxide stoichiometry to account for basic solutions. This does not change the basic premise, however).

Another interesting component of the impedance that came to light

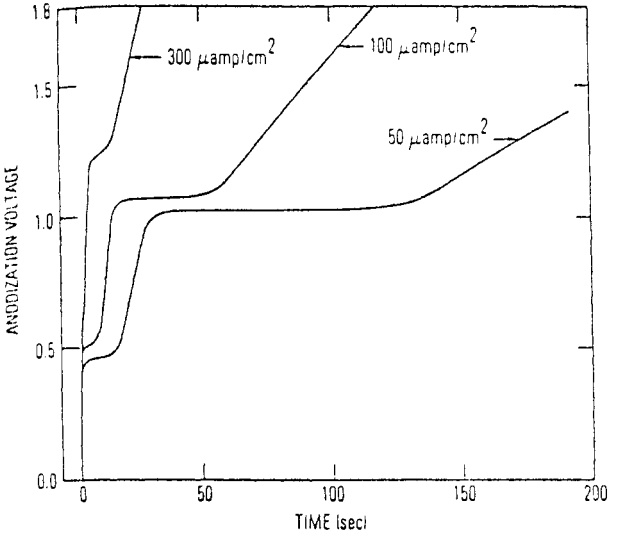

Figure 26. Anodization voltage vs time at constant current. (With permission of American Institute of Physics.)

is a complex impedance component, the Warburg impedance, which is normally attributed to mass transport effects. It had a significant potential dependence, and essentially disappeared at 0.8 volt vs. a saturated calomel electrode (SCE). A further conclusion from this fact was that mass transport was the controlling effect at low overpotentials, being taken over by charge transfer at some point. The rotating ring-disk electrode data (79) demonstrating a relationship between hydroxide concentration and mass transport suggests that the potential at which this change occurs could be affected by hydroxide concentration or mass transport rates, but this has never been concretely demonstrated.

This also tends to explain the observation by Janosek, et al. (32), that oxidation could be prevented at low current densities by stirring, but would occur eventually at higher current densities in the constant current studies. Further use of the a.c. impedance technique used the assumption that a component of the equivalent circuit, the charge transfer resistance (R_{CT}), is inversely proportional to the first step of the ECE mechanism, a valid assumption as long as the first charge transfer is much slower than the second. By saturating the electrolyte with one of the three constituent elements, the dissolution of that element could be stopped, or at least impeded significantly (79). Measuring R_{CT} could give relative dissolution rates of the three elements. In fact, the relative dissolution rates were shown to be:

Te:	1
Hg:	2.3
Cd:	10.3

which are very similar to those rates found for dissolution in bromine-methanol under etch conditions.

An interesting approach to evaluating the processes involved in (Hg,Cd)Te oxidation was taken by Lopes and Hart (81). They used microelectroephoresis to determine the effect of pH on surface charge density as expressed by zeta potential. As predicated by the experimental method, powdered samples of (Hg,Cd)Te (p-type with x = 0.2) were used. In order to cover large pH range, an aqueous solution of potassium phosphate was used, and the pH adjusted accordingly with acetic acid, hydrochloric acid, or potassium hydroxide. The measured relationship of the zeta potential to pH is shown in Figure 27. Significantly, this behavior agrees well with the dissociation of tellurous acid, H_2TeO_3 up to a pH of about 10. The authors associate this deviation with the decrease in solubility of the cadmium species in this range (Figure 28). This diagram demonstrates a similar behavior for mercury species, and this may be significant since the surface concentration of mercury is four times higher

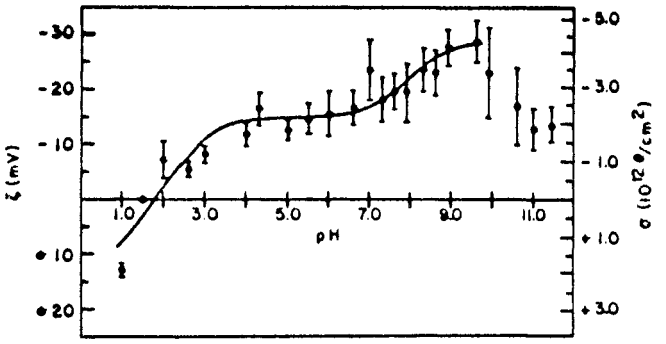

Figure 27. The zeta potential and surface charge density of $Hg_{0.8}Cd_{0.2}Te$ as a function of pH. The solid line is the best fit theoretical curve to the acid dissociation model with $pK = 12.7$, $pK_1 = 2.4$, $pK_2 = 7.6$, and $\gamma = 0.30$. The pK values correspond to the dissociation constants of the different phases of tellurous acid and γ is proportional to the total acid site density. The surface oxide chemistry is $HTeO_2^+$ (positive zeta potential, H_2TeO_3 (zero zeta potential), $HTeO_3^-$ (first step in the zeta potential), and $TeO_3^=$ (second step in the zeta potential). (With permission of American Institute of Physics.)

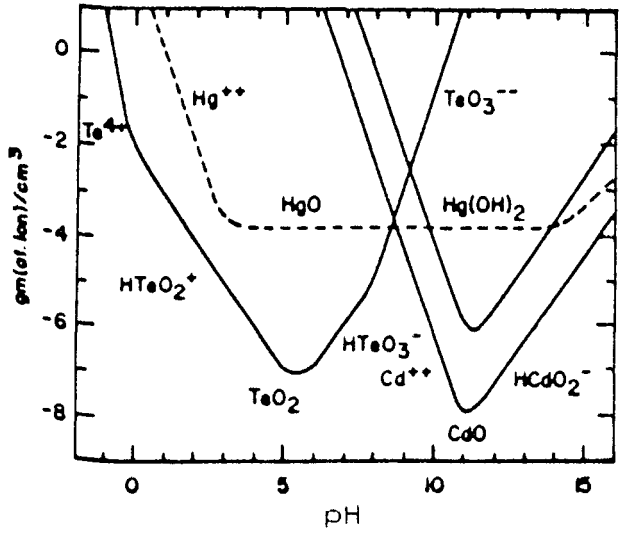

Figure 28. Solubility of various species containing Hg, Cd, and Te as a function of pH. (With permission of American Institute of Physics.)

than cadmium. At any rate, significant evidence of pH affecting the oxidation process is presented in this work.

A more limited amount of work has been done on the bulk growth of anodic oxide on (Hg,Cd)Te. However, two efforts are presented here. The first involved the growth of oxide in the presence of water which has been isotopically enriched with 18/8 O (28). The profile presented in Figure 29 was concluded to suggest bulk growth by successive jumps of hydroxide ions, although cation diffusion was not eliminated completely. The authors also suggested that the hump in the profile near the interface suggested that initial growth was by a separate mechanism, dissolution-precipitation, and had a direct effect on the oxide-semiconductor interface. Another series of studies (61)(83) were conducted using SIMS profiling of oxides grown in both hydrogen peroxide and 0.1N KOH in 90% ethylene glycol/ 10% water using various markers for the original surface or intermediate points in the growth. The material used was SSR grown with x = 0.22. One interesting sidelight of this study was the depletion of Cd at the surface of the H_2O_2 -grown oxide, and the lack of depletion in the basic electrolyte, apparently the result of solubility factors mentioned earlier. (The depletion of Cd was used as a marker in part of the study). Although the authors presented evidence for Hg, Cd and Te dissolution in the electrolyte and for metal out-diffusion in at least one instance, the bulk growth mechanism was concluded to be by oxygen vacancy out-diffusion. The later paper conceded the possibility of simultaneous oxide growth at the oxide-electrolyte interface. This work also demonstrated that the bulk growth mechanism could not be by dissolution-precipitation.

3.0 ALTERNATIVE PASSIVATION PROCESSES

A number of alternative passivation processes to anodic oxidation have been investigated for (Hg,Cd)Te. The primary motivations for this search have been the relatively high fixed charge associated with most anodic oxides, and low thermal stability. The fixed charge is especially a problem with p-type devices, since it produces surface inversion which requires additional device structures to compensate. The thermal stability has been pursued because of the likely association of thermal stability with thermodynamic stability, with the ultimate result being increased longevity and reliability of infrared imaging systems

3.1 Electrochemical

Perhaps the most significant development in alternative passivation has been another anodic electrochemical process, sulfidization. The

feasibility of this procedure was first published in 1984 by Nemirovsky and Burnstein (82), although the results were sketchy at this point. Later the same group revealed more details of the sulfidization procedure (83). The electrolyte used was described as a "non-aqueous basic sulfide solution in ethylene glycol." Films were grown at constant current densities of 100 ± 40 amp-cm^{-2} and the growth rate was reported on the order of 1 nm min^{-1}. The material used was p-type, x = 0.215, 0.225, and 0.285, but the crystal growth and surface preparation techniques were not mentioned. The voltage-time characteristics were reported (Figure 30) but showed little increase in potential as film growth occurred. The film composition was originally reported as entirely CdS, the absence of substantial Hg and Te being rationalized by the relatively high solubilities of the polysulfides, HgS_2^{2-} and TeS_3^{2}. More recent works (84) have indicated that the depletion of Hg and Cd, although severe, are not as complete as originally suggested. The sulfide passivation has been shown to have lower fixed charge and better thermal stability than the anodic oxide, and Nemirovsky, et al. (85), have reported the device characteristics of a photodiode structure built using this passivation process.

Little fundamental electrochemical information is presently available about anodic sulfidization. One work (86) using oxide marker and compositional profiling found the sulfide growth to be into the substrate, as the same report concluded for anodic oxidation. The original reports from Nemirovsky, et al. (83), suggested that the reaction was a six electron process:

Eq. (5)
$$Hg_{(1-x)}Cd_xTe + [4 + (1-x)]\,S^{2-} \rightarrow xCdS + TeS_3^{2-} + (1-x)HgS_2^{2-} + 6e^-$$

where $0 \leq x \leq 1$, based on a CdS film composition and the solubility of Hg and Te polysulfides mentioned earlier. This was later disputed and a two electron reaction was suggested (87):

Eq. (6)
$$Hg_{(1-x)}Cd_xTe + [1 + (1-x)]\,HS^- + S_3^{2-} + [1 + (1-x)]\,OH^- \rightleftharpoons xCdS + (1-x)\,HgS_2^{2-} + TeS_3^{2-} + [1+(1-x)]H_2O + 2e^-$$

where $0 \leq x \leq 1$.

Furthermore, this later work draws a possible connection between the anodic sulfidization process and photocorrosion of II-VI solar cells in polysulfide electrolytes. If this connection could be established, a well of knowledge could be applied to gain a better understanding of this passivation process. (For example: Ref 88-90).

Anodic fluoride films have also been produced on (Hg,Cd)Te as an

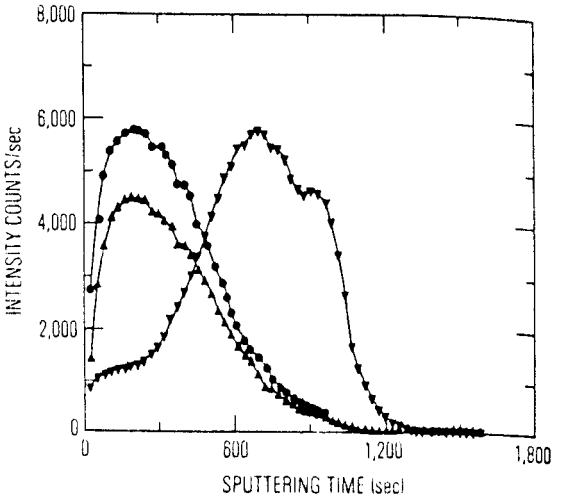

Figure 29. Concentration of O^{18} (▲) and O^{16} (▼) as a function of sputtering time in the sequentially grown film (growth current density = 300 $\mu A/cm^2$). The circles represent the O^{18}:O^{16} ratio for a film grown in the O^{18} anodization solution only. (With permission of American Institute of Physics.)

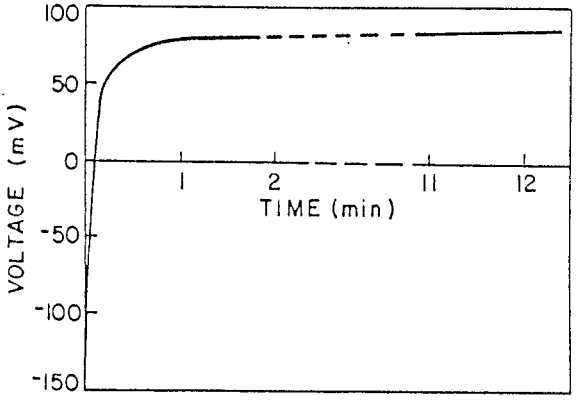

Figure 30. Electrochemical cell voltage as a function of the anodic sulfidization duration for $Hg_{1-x}Cd_xTe$ with x = 0.225. Current density is 130 $\mu A/cm^2$. (With permission of American Institute of Physics.)

alternative to anodic oxidation. Similar voltage-time behavior to that observed in anodic oxidation was reported, and initial film formation was concluded to proceed by dissolution-precipitation. The electrolyte used for film formation was potassium fluoride of various concentrations in ethylene glycol. The addition of water caused simultaneous incorporation of oxygen and fluorine in the film, and small additions of hydroxide produced oxides only. The film composition of the uncorrupted fluoride was reported as cadmium fluoride within a matrix of mercury, cadmium, and tellurium. The films were found to have a low positive fixed charge density with low surface state densities. By varying the oxygen and fluorine content of the film, the extent of band-bending at the interface could reportedly be stable to temperatures of 105°.

3.2 Non-Electrochemical Passivation

Other non-electrochemical passivation processes have been explored and have met with varying levels of success. Thermal oxidation of CdTe has been demonstrated (91), although it has not successfully been extended to the mercury-containing semiconductors. Plasma oxidation and photochemical oxidation (94-97) have been used to produce oxides with lower fixed charge than anodic oxides. However these passivation techniques suffer other problems thought to be associated with radiation damage caused by charged or excited oxygen species involved in the film formation. Chemical vapor deposition (CVD) of silicon dioxide has also been demonstrated both directly on (Hg,Cd)Te (98) and on thin native oxide layers (99)(100). However, SiO_2 has a transmission cutoff of 7 microns, limiting its use in devices operating in the 8 - 12 microns atmospheric window to those utilizing backside illumination. CVD deposition of Cd-Te-O compounds has been predicted to be thermally stable (101), but successful experimental results have not been published to date.

4.0 REFERENCES

1. Dimiduk, K. C., Opyd, W. G., Gibbons, J. F., Sigmon, T. W., Magee, T. J. and Ormond, R. D., *J. Vac. Sci. and Technol.*, A 1 (3), pp. 1661-1665 (1983)

2. Opyd, W. G., Dimiduk, K. C., Sigmon, T. W. and Bibbons, J. F., *J. Vac. Sci. and Technol.*, A 3 (1), pp. 276-279 (1985)

3. Broudy, R. M. and Mazurczyck, V. J., *Semiconductors and Semimetals*, (R.K. Willardson and A. C. Beer, eds.), Vol. 18, pp. 157-199, Academic Press, New York (1981)

4. Sze, S. M., *Semiconductor Devices - Physics and Technology*, pp. 278-281, John Wiley and Sons, Inc., New York (1985)

5. Kinch, M. A., *Semiconductors and Semimetals*, Vol 18, pp. 313-378, Academic Press, New York (1981)

6. Sze, S. M., *Physics of Semiconductor Devices*, pp. 425-504, John Wiley and Sons, Inc., New York (1969)

7. Reine, M. B., Sood, A. K. and Tredwell, T. J., *Semiconductors and Semimetals*, Vol. 18, pp. 201-312, Academic Press, New York (1981)

8. Sze, S. M., *Physics of Semiconductor Devices*, pp. 77-149, John Wiley and Sons, Inc., New York (1969)

9. Bertagnolli, E., Bettimi, M. and Gornik, E., *Appl. Phys. Lett.* 42 (9), pp. 824-826 (1983)

10. Kaiser, U., Ganschow, O., Wiedmann, L. and Benninghoven, A., *J. Vac. Sci. and Technol.*, A 1 (2), pp. 657-661 (1983)

11. Takita, K., Ipposhi, T., Murakami, K., Masada, K., Kudo, H. and Sek, S., *Appl. Phys. Lett.*, 48 (13), pp. 852-854, March 31, 1986

12. Stahle, C. M., Helmes, C. R., and Simmons, A., *J. Vac. Sci. and Technol.*, B 5 (4), pp. 1092-1096 (1987)

13. Stahle, C. M., Helms, C. R., Strong, R. L., Simmons, A., Schaake, H.

F., Pallix, J. and Becker, C. H., to be published, *J. Vac. Sci. and Techol.*, A 7

14. Nemirovsky, Y. and Kidron, I., *Solid State Elec*, 22 (10), pp. 831-837 (1979)

15. Janousek, B. K., Daugherty, M. J. and Schouler, R. B., *SPIE Infrared Detector Materials*, 285, pp. 118-125 (1981)

16. Schoolar, R. B., Janousek, B. K., Alt, R. L., Carscallen, R. C., Daugherty, M. J. and Fote, A. A., *J. Vac. Sci. and Technol.*, 21 (1), pp. 172-177

17. Beck, J. D., Kinch, M. A., Esposito, E. J. and Chapman, R. A., *J. Vac. Sci. and Technol.*, 21 (1), pp. 172-177 (1982)

18. Anderson, W. W. and Hoffman, H. J., *J. Vac. Sci. and Technol.*, A 1 (3), pp. 1730-1734 (1983)

19. Micklethwate, W. F. H., *Semiconductors and Semimetals*, Vol 18, pp. 48-120, Academic Press, New York (1981)

20. Columbo, L., Syllaios, A. J., Periaky, R. W. and Brau, M. J., *J. Vac. Sci. and Technol.*, A 3 (1), pp. 100-104 (1985)

21. Triboulet, R., Nguyen Duy, T. and Durand, A., *J. Vac. Sci. and Technol.*, A 3 (1), pp. 100-104 (1985)

22. Schmit, J. L., *J. Vac. Sci. and Technol.*, A 3 (1), pp. 89-92 (1985)

23. Faurie, J. P., Million, A., Boch, R. and Tissot, J. L., *J. Vac. Sci and Technol.*, A 1 (3), pp. 1593-1597 (1983)

24. Chow, P. O. and Johnson, D., *J. Vac. Sci. and Technol.*, A 3 (1), pp. 67-70 (1985)

25. Cheung, J. T. and Magee, T., *J. Vac. Sci. and Technol.*, A 1 (3), pp. 1604-1607 (1983)

26. Kannam, P. J., Murosaka, R. and Briere, T., *J. Electrochem. Soc.* 129 (3), pp. 656-660 (1982)

27. Lastsras-Martinez, A., Lee, U., Zehnder, J. and Racrah, P. M., *J. Vac. Sci. and Technol.*, 21 (1), pp. 157-160 (1982)

28. Aspnes, D. E. and Arwin, H., *J. Vac. Sci. and Technol.*, A 2 (3), pp. 1309-1315 (1984)

29. Talasek, R. T. and Syllaios, A. J., *J. Electrochem. Soc.*, 132 (3), pp. 656-659 (1985)

30. Talasek, R. T., Ohlson, J. J. and Syllaios, A. J., *IRIS Detector Specialty Group Proceedings* (1984)

31. Carey, G. P., Wahi, A. K., Silberman, J. A., Stahle, C. M., Spicer, W. E. and Wilson, J. A., *J. Vac. Sci. and Technol.*, A 5 (5), pp. 3203-3206 (1987)

32. Janosek, B. K. and Carscallen, R. C., *J. Appl. Phys.*, 53 (3), pp. 1720-1726 (1982)

33. Basol, B. M., Tseng, E. S. and Rod, R. L., U. S. Patent 4,388,483 (1983)

34. Kazacos, M. S. and Miller, B., *J. Electrochem. Soc.*, 127, p. 869 (1980)

35. Miller, B. and Rosamilia, J. M., *Electrochem. Soc. Extended Abstracts 86-1*, p. 485 (1986)

36. Baranski, A. S. and Fawcett, W. R., *J. Electrochem. Soc.*, 127 (3), pp. 766-767 (1980)

37. Biter, W. J., Epps, G. F. and Harns, R. D., *Electrochem. Soc. Extended Abstract 86-1*, pp. 487-488 (1986)

38. Miller, B., and Heller, A., *Nature* 262, p. 860 (1976)

39. Peter, L. M., *Electrochem Acta* 23, 1965, (1978)

40. Peter, L. M., *J. Electroanal. Chem.* 98, p. 49 (1979)

41. Talasek, R. T., Ohlson, M. J. and Syllalos, A. J., *J. Electrochem. Soc.*, 133 (1), pp. 230-232 (1986)

42. Catagnus, P. C. and Baker, C. T., U. S. Patent 3,977,018 (1976)

43. Robertson, D. S., Shaw, N. and Young, I. M., *J. Matl. Sci.*, 13, p. 1986-1990 (1978)

44. Rhiger, D. R. and Kvaas, R. E., *J. Vac. Sci. and Technol.,* A 1 (3), pp. 1712-1718 (1983)

45. Davis, G. D., Buchner, S. P., Beck, W. A. and Byer, N. E., *Appl. Surf. Sci.,* 15, pp. 238-246 (1983)

46. Seelmann-Eggebert, M. and Richter, H. J., *Proceedings of the 18th International Conference on the Physics of Semiconductors.* Stockholm, Sweden, Aug 11-15, 1986, World Scientific, p. 283. (1987)

47. Seelmann-Eggebert, M. and Richter, H. J., *Proceedings of the Optical Society of America*, Seattle, Washington, Oct 19-24, 1986

48 Pourbaix, M., *Atlas of Electrochemical Equilibria in Aqueous Solutions,* Celebcor Publication F59, Pergamon Press (1966)

49. Ohlson, M. J., Talasek, R. T. and Syllaios, A. J., *Electrochem. Soc. Extended Abstracts 84-1,* p. 213 (1984)

50. Nemirovsky, Y. and Finkman, E., *J. Electrochem. Soc.,* 126 (5), pp. 768-770 (1979)

51. Sun, T. S., Buchner, S. P. and Byer, N. E., *J. Vac. Sci. and Technol.,* 17 (5), pp. 1067-1073 (1980)

52. Davis, G. D., Sun, T. S., Buchner, S. P. and Byer, N. E., *J. Vac. Sci. and Technol.,* 19 (3), pp. 472-476 (1981)

53. Nitz, H. M., Ganschow, O., Kaiser, U., Wiedmann, K. and Benninghoven, A., *Surf. Sci.* 104, pp. 365-383 (1981)

54. Farrow, R. F. C., Dennis, P. N. J., Bishop, H. E., Smart, N. R. and Wotherspoon, J. T. M., *Thin Solid Films* 88, pp. 87-92 (1982)

55. Morgen, P., Silberman, J. A., Lindau, I., Spicer, W. E. and Wilson, J. A., *J. Vac. Sci. and Technol.,* 21 (1), pp. 161-163 (1982)

56. Christie, A. B., Sutherland, I. and Walls, J. M., *Surf. Sci.,* 135, pp. 225-242 (1983)

57. Seelmann-Eggebert, M., Brandt, G. and Richter, H. J., *J. Vac. Sci. and Technol.,* A 2 (1), pp. 11-15 (1984)

58. Kaiser, U., Ganschow, O., Wiedmann, L. and Benninghoven, A., *J. Vac. Sci. and Technol.*, A 1 (4), p. 657 (1983)

59. Stahle, C. M., Thomson, D. J., Helms, C. R., Becker, C. H. and Simmons, A., *Appl. Phys. Lett.*, 47 (5), pp. 521-523 (1985)

60. Gnade, B., Simmons, A., Little, D. and Strong, R., *Nuclr. Instr. and Meth. Phys. Res.*, B24/25, pp. 1014-1016 (1987)

61. Strong, R. L., Anthony, J. M., Gnade, B. E., Keenan, J. A., Norbeck, E., Li, L. W. and Helms, C. R., *J. Vac. Sci. and Technol.*, A 4 (4), pp. 1992-1995 (1986)

62. Kowalczyk, S. P. and Cheung, J. T., *J. Vac. Sci. and Technol.*, 18 (3), pp. 944-948 (1981)

63. Rhiger, D. R. and Kvaas, R. E., *J. Vac. Sci. and Technol.*, 21 (1), pp. 168-171 (1982)

64. Morgen, P., Silberman, J. A., Lindau, I., Spicer, W. E. and Wilson, J. A., *J. Electr. Matl.*, II (4), pp. 597-610 (1982)

65. Silberman, J. A., Laser, D., Lindau, I. and Spicer, W. E., *J. Vac. Sci. and Technol.*, A 1 (3), pp. 1706-1711 (1983)

66. Silberman, J. A., Laser, D., Lindau, I., Spicer, W. E. and Wilson, A., *J. Vac. Sci. and Technol.*, A 3 (1), pp. 222-225 (1985)

67. Wager, J. F. and Rhiger, D. R., *J. Vac. Sci. and Technol.*, A 3 (1), pp. 212-217 (1983)

68. Daniels, R. R., Margaritordo, G., Davis, G. D. and Byer, N. E., *Appl. Phys. Lett.*, 42 (1) pp. 50-52 (1983)

69. Arwin, H., Aspnes, D. E. and Rhiger, D. R., *J. Appl. Phys.*, 54 (12), 7132-7138 (1983)

70. Aspres, D. E. and Arwin, H., *J. Vac. Sci. and Technol.*, A 2 (2), pp. 600-601 (1984)

71. Janousek, B. K. and Carscallen, R. C., *J. Vac. Sci. and Technol.*, 21 (2), pp. 443-445 (1982)

72. Sakashita, M., Strehblow, H. H. and Bettini, M., *J. Electrochem. Soc.*, 129 (4), pp. 739-746 (1982)

73. Sakashita, M., Strehblow, H. H. and Bettini, M., *J. Electrochem. Soc.*, 129 (8), pp. 1710-1716 (1982)

74. Uhlig, H. H. and Revie, R. W., *Corrosion and Corrosion Control*, 3rd Ed., pp. 60-89, John Wiley and Sons, Inc., New York (1985)

75. Ahearn, J. S., Davis, G. D. and Byer, N. E., *J. Vac. Sci. and Technol.*, 20 (3), pp. 756-759 (1982)

76. Talasek, R. T., Ohlson, M. J. and Syllaios, A. J., *J. Vac. Sci. and Technol.*, A 3 (1), pp. 218-221 (1985)

77. Dean, S. W., *Electrochemical Techniques for Corrosion*, (R. Baboian, ed.) NACE pp. 52-60 (1977)

78. Bard, A. J. and Faulkner, L. R., *Electrochemical Methods*, pp. 280-311, John Wiley and Sons, New York.

79. Talasek, R. T., *Electrochem. Soc. Extended Abstracts 85-1*, p. 241 (1985)

80. MacDonald, D. D., *Transient Techniques in Electrochemistry*, Plenum Press, New York (1981)

81. Lopes, V. C., Hart, T. R., *J. Vac. Sci. and Technol.*, A 5 (2), pp. 174-178 (1987)

82. Nemirovsky, Y. and Burstein, L., *Appl. Phys. Lett.*, 44 (4), pp. 443-444 (1984)

83. Nemirovsky, Y., Burstein, L. and Kidron, I., *J. Appl. Phys.*, 58 (1), pp. 366-373 (1985)

84. Strong, R. L., Luttmer J. D., Little, D. D., Teherini, T. H. and Helms, C. R., *J. Vac. Sci. and Technol.*, A 5 (5), pp. 3207-3210 (1987)

85. Nemirovsky, Y. Adar, R., Kornfeld, A. and Kidron, I., *J. Vac. Sci. and Technol.*, A 4 (4), pp. 1986-1991 (1986)

86. Strong, R. L., *J. Vac. Sci. and Technol.*, A 5 (4), pp. 2003-2006 (1987)

87. Ziegler, J. P. and Hemminger, J. C., *Electrochem. Soc. Extended Abstracts.*

88. Hodes, G. and Miller, B., *J. Electrochem. Soc.,* 122 (10), pp. 2177-2180 (1986)

89. Licht, S., Tenne, R., Flaisher, H. and Manassen, J., *J. Electrochem. Soc.,* 133 (1), pp. 52-59 (1986)

90. Licht, S. and Manassen, J., *J. Electrochem. Soc.,* 132 (5), pp. 1076-1081 (1985)

91. Wang, F., Schwartzman, A., Fahrenbruch, A. L., Sinclair, R., Bube, R. H. and Stahle, C. M., *J. Appl. Phys.,* 62 (4), pp 1469-1476 (1987)

92. Weiss, E. and Mainzer, N., *J. Vac. Sci. and Technol.,* A 6 (4), pp. 2765-2771 (1988)

93. Mainzer, N., et. al., to be published *J. Vac. Sci. and Technol.,* A 7

94. Nemirovsky, Y. and Goslen, R., *Appl. Phys. Lett.,* 37 (9), pp. 813-815 (1980)

95. Nemirovsky, Y., Goshen, R. and Kidron, I., *J. Appl. Phys.,* 53 (7), pp. 4888-4895 (1982)

96. Buchner, S. P., Davis, G. D. and Byer, N. E., *J. Vac .Sci. and Technol.,* 21 (2), pp. 446-447 (1982)

97. Janousek, B. K. and Carscallen, R. L., *J. Vac. Sci. Technol.,* A 3 (1), pp. 195-199 (1985)

98. Kao, T. M. and Sigmon, T. W., *Electrochem. Soc. Extended Abstracts.*

99. Davis, G. A., Buchner, S. P. and Byer, N. E., *J. Vac. Sci. and Technol.,* A 1 (2), pp. 670-671 (1983)

100. Wilson, J. A. and Cotton, V. A., *J. Vac. Sci. and Technol.,* A 1, (3), pp 1719-1722 (1983)

101. Rhiger, D. R. and Kvaas, A. E., *J. Vac. Sci. and Technol.,* 21 (2), pp. 448-452 (1982)

102. Janousek, B. K., Carscallen, R. C. and Bertrand, P. A., *J. Vac. Sci. and Technol.*, A 1 (3), pp. 1723-1725 (1983)

103. Diehl, R., Nolang, B. I., *J. Cryst.. Growth,* 66, pp. 91-105 (1984)

4

PHOTOELECTROCHEMICAL PROCESSING OF SEMICONDUCTORS

R. David Rauh

1.0 INTRODUCTION

Photoelectrochemistry is a general category encompassing light-induced electrochemical reactions of semiconductors in contact with liquid electrolytes arising from the primary generation of minority carriers. In the field of electronics and electro-optics, photoelectrochemical processing has been a subject of considerable recent interest (1). Photoelectrochemical etching has been used in the fabrication of diffraction gratings, integral lenses for light emitting diodes, fiber optic couplers, and via holes in a variety of semiconductor materials. Photoelectrochemically induced electroplating has been employed for both ohmic and non-ohmic contacts. Photoelectochemistry has also been used in the modification of semiconductor surfaces to reduce surface state densities prior to device fabrication.

When immersed in an electrolyte, a semiconductor undergoes an exchange of electrons with the liquid at the interface to equalize the work functions of the two phases. The result is often a rectifying barrier between the semiconductor and liquid that has properties similar to a Schottky barrier. Like semiconductor-metal contacts, the barrier height can be fixed by the semiconductor surface state distribution, or, in the case of a low density of surface states, by the difference between the work functions of the bulk semiconductor and the liquid. Similarly, a reaction between the semiconductor surface and the electrolyte can produce a surface layer that fixes the barrier height.

The contact barrier that is produced is characterized by a bending of the semiconductor's conduction and valence bands. Such barriers are

well known to be photoactive. Thus, when light of energy greater than the bandgap strikes the interface and is absorbed by the semiconductor, electrons and holes are produced, with minority carriers being swept to the semiconductor surface. In the case of n-type semiconductors, these minority carriers are valence band holes which, upon arrival at the interface, can be consumed by a chemical reaction with the electrolyte or by (non-productive) surface recombination with majority carriers. For most technologically significant semiconductors (Si, Ge, III-V and II-VI compounds), valence band holes are sufficiently energetic to decompose the semiconductor in aqueous media. This phenomenon forms the basis for photoelectrochemical etching/micromachining processes. In the case of p-type semiconductors, photogenerated minority carriers at the interface are conduction band electrons. Many semiconductors are stable toward reduction by such electrons. However, metal ions added to the electrolyte can, in some cases, be reduced to the parent metal, leading to localized electroplating.

Light-localized, wet processing of semiconductors which is not photoelectrochemical in nature is also known. Localized surface heating can reduce the overpotential for electroplating (2) or accelerate etching, for example. In addition, reactive intermediates can be produced by photolysis of electrolyte species (e.g., Br_2), which then go on to react chemically with the semiconductor surface (3). These nonphotoelectrochemical approaches will not be dealt with further in this chapter.

2.0 EXPERIMENTAL PROCEDURES

There are three major components in an apparatus for photoelectrochemical processing. First is the cell for exposing the semiconductor working surface to the electrolyte while also accommodating auxiliary electrodes for controlling the semiconductor potential. Second is the control apparatus, typically a potentiostat and a means for monitoring current and charge. Finally is a light source, which can be broad band or monochromatic laser radiation.

The choice of a cell will be largely dependent on the type of processing to be accomplished. An example used in our laboratory for etching diffraction gratings is illustrated in Figure 1. The cell body should be machined from a polymer stable to the electrolyte of choice. Examples are nylon for many aqueous electrolytes and Teflon for HF-based etchants or nonaqueous media. The semiconductor electrodes must be mounted in such a way to prevent contamination of the ohmic contact (or other corrosive elements) by the electrolyte. In the approach illustrated in

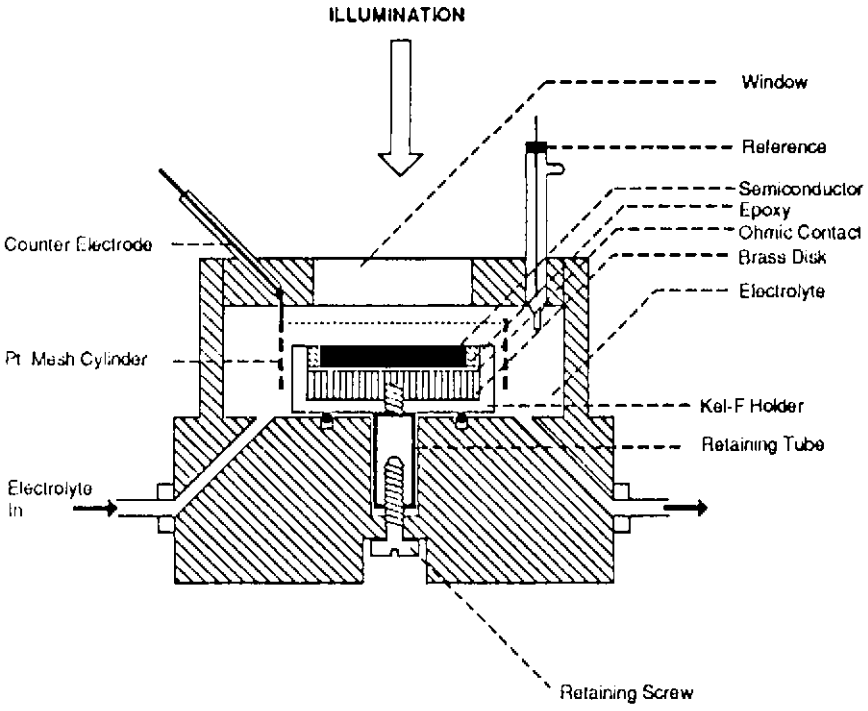

Figure 1. Cell design and semiconductor mounting for laboratory investigations of photoelectrochemical processing of semiconductors.

Figure 1, the semiconductor "working" electrode incorporates an ohmic contact on the back side. The electrode is mounted onto a brass disk using conductive silver-filled epoxy. The assembly is potted into a Kel-F holder with epoxy cement, save for a threaded hole in the rear of the brass disk. A screw assembly is used both as a contact and to tighten the electrode onto the cell via a liquid-tight O-ring seal. A cylindrical platinum gauze counter electrode surrounds the working electrode, giving rise to a uniform current distribution. A standard calomel (SCE) reference electrode is placed as close as possible to the electrode surface without occluding the light path.

When photoelectrochemical processing is to be used on a production scale, the cell will be of utmost importance. In that case, special holders would be necessary to incorporate multiple wafers. Nevertheless, the basic design philosophy illustrated in Figure 1 should be retained.

The control apparatus would typically consist of a potentiostat with a sufficiently large current output to support the total photoelectrochemical process. Most examples of photoelectrochemical processing are carried out at constant potential, but some examples exist of galvanostatic control. The course of the photoelectrochemical process is monitored as the integrated current, which may be related directly to the amount of etched or deposited material. A coulometer or integrating computer may be used for this purpose.

The light source for photoelectrochemical processing must put out photons of energy greater than the bandgap of the semiconductor. Lasers have the advantage of monochromaticity, thus permitting accurate calculation of the photon flux from the intensity and the reflectance and depth of penetration from the semiconductor's optical constants. However, since cw sources are usually desirable for processing, lasers of sufficient intensity for uniform processing of large areas at a reasonable rate may be prohibitively expensive compared to broadband sources. Lasers are the sources of choice for etching interferograms (e.g., diffraction gratings) into semiconductors, or for processes requiring a highly focused beam. Broadband sources are frequently used for illumination of a photoresist patterned electrode or for projection imaging. Broadband sources may be obtained in standard illuminator configurations, as might be employed for the exposure of photoresist. Table 1 summarizes the spectral characteristics of several commonly employed light sources while the wavelength equivalent of the bandgaps of some technologically significant semiconductors are included in Table 2.

Table 1

Light Sources for Photoelectrochemical Processing

Source	Spectral Range (*nanometers*)	Major Lines (*nanometers*)
NONCOHERENT SOURCES		
Quartz Tungsten-Halogen	300 to >2000 max. at 900	BB
Deuterium	180 to >400	BB, 480, 660
Hg Arc, low P	180-350	185, 253
Hg Arc, med. P	300->800	313,365,430,540,580
Hg Arc, high P	300->800	same, BB (high intensity)
Hg/Xenon	250-2000	same, BB
Xenon	350-2000	BB
COHERENT SOURCES (CW)		
Ar ion	Blue-Green	351, 457.9, 476.5 488.0, 514.5 257 (doub)
Kr	Red	530.9,647,676
He/Cd	Blue-green	345,442
He/HeNe	Red	543,632.8,1150
Semiconductor	Red, NIR	750,780,820,1300,1550
Nd/Yag	Green	532,1064,1318
Dye	Tunable	350-950

BB: broad band

Table 2

Properties of Candidate Semiconductors for Photoelectrochemical Etching

Semiconductor	Bandgap (nm)	n (e-/eq)	Rate(μm/sec) $\times 10^{-4}\lambda$I
$BaTiO_3$	388	4,6	0.56
CdS	512	2	1.25
CdSe	729	2	1.38
CdTe	795	4	0.81
GaAs	873	6	0.38
GaP	549	6	0.34
Ge	1771	4	0.29
InP	919	6	0.42
Si	1107	4	0.25
SiC	413	8	0.13
TiO_2	400	4	0.39
ZnO	370	2	0.61
ZnS	337	2	0.99

It is also important to note that many cases may be cited of photoelectrochemical processing in which control is lacking, such as using a two electrode arrangement (no reference electrode), or a non-potentiostatic power supply. Similarly, many examples exist of photo-electrochemical processing (primarily etching) of semiconductors simply immersed in the electrolyte without external contact (1). Indeed, these may be practical solutions to photoelectrochemical processing once the systems have been characterized electrochemically.

3.0 PHOTOELECTROCHEMICAL ETCHING

3.1 General Background

Photoelectrochemical etching occurs only when an optically produced minority carrier at the semiconductor-electrolyte interface is sufficiently energetic to induce a corrosion reaction. This condition is met for valence band holes for virtually all semiconductors used in electronics in contact with aqueous electrolytes (4). In order for etching to occur at a sufficiently

practical rate, kinetics must also be favorable. Processes which consume minority carriers without corrosion, such as surface recombination and reaction with dissolved electrolyte species, will detract from the overall quantum efficiency of etching by kinetic competition. Mass transfer can also kinetically inhibit the etching reaction. It is particularly important in this regard to employ an electrolyte in which the corrosion products are highly soluble. Examples of conditions which have been reported for photoelectrochemical etching of a variety of semiconductors are given in Table 3.

In a photoelectrochemical reaction with unit quantum yield, each photon absorbed by the semiconductor will give rise to one electron in the dissolution process. In a well-behaved photoelectrochemical cell, the curve of photocurrent (or quantum yield) vs. applied potential is S-shaped, as shown schematically in Figure 2. As indicated by the band bending diagrams in Figure 2, when the potential is negative of the flat band value (V_{fb}) for an n-type semiconductor, the bands are flat and there is little electron-hole separation, and hence negligible photocurrent. As a positive potential is applied, the bands become bent due to a surface depletion of electrons. A space-charge layer is thus formed, the width and magnitude of which grows as the potential becomes more positive. Above a certain potential, the space-charge region reaches a limiting width. The efficiency of separation of electron-hole pairs, and thus photocurrent production, also increases with voltage due to the fact that more pairs are created within the space-charge region and the driving force for their separation increases. In some semiconductors, typically direct bandgap materials like GaAs, only carriers produced within this space-charge region are efficiently separated due to relatively low bulk diffusion lengths. Indirect bandgap semiconductors with long diffusion lengths, like Si, derive significant photocurrent from photons absorbed well beyond the space-charge region. The plateau region of highest photocurrent quantum yield is often referred to as the photon limited region.

The beauty of photoelectrochemical etching is that the rate of etching can be controlled by the photon flux and by the potential, due to the linear relationship between light intensity and photocurrent. Since an ampere is equal to a current of 6.24×10^{18} electrons/sec, it can be shown that the current equivalent of photons is equal to $8.065 \times 10^{-5} \lambda I$ "photon amperes". The quantities λ and I are the wavelength (angstroms) and intensity (watts/cm^2) of the light source. The rate of etching may be expressed quantitatively as

$$\text{Eq. (1)} \qquad r(\mu m/sec) = 8.36 \times 10^{-6} (1 - R) \phi \lambda A I (m/n\rho)$$

where r is the normal incidence reflectance of the crystal, and ϕ is the

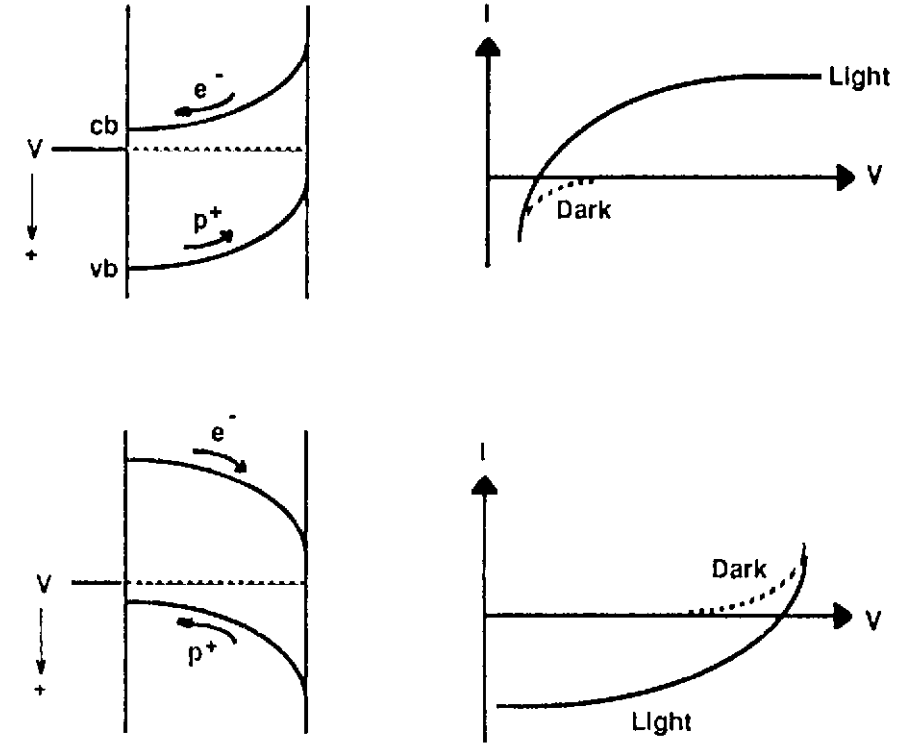

Figure 2. Idealized current-potential curves and band bending diagrams for n- and p-type semiconductor electrodes in the dark and under illumination. Conduction and valence bands are indicated (cb, vb). Voltage is applied via an ohmic contact at the Fermi level, located in the band gap near the cb (n-type) or vb (p-type).

quantum yield of conversion of photons to current in the dissolution reaction. The quantity $(m/n\rho)$ describes the etching reaction, where m is the molecular weight of the dissolving layer, ρ is its density in g/cm^3, and n is the number of equivalents/mole in the dissolution process. The relative rates of etching of some important semiconductors are compared in Table 2, the differences arising from differences in density and the stoichiometry of the corrosion process.

Table 3

Conditions for Photoelectrochemical Etching Reported for Various Semiconductors.

Material	Conditions	Electrolyte	Application	Ref.
GaAs SI	Ar^+(488,513nm) HeNe(633nm) 10^{-3} - 10^3 W/cm²	1:1.3:25 H_2SO_4:H_2O_2:H_2O	holes, holographic gratings	21
n-GaAs (100),[011] $10^{18}/cm^3$	Ar^+ (514,457nm) 300 mW/cm²	1:1:100 H_2SO_4:H_2O_2 H_2O	holographic gratings	45
n-GaAs var. faces	Ar^+ (514, 257nm) 10mW-1kW/cm² focused	1:20 HNO_3	holes, slits	22
n,p,SI-GaAs	Ar^+ (257nm) 10W/cm² focused	1:1:100 H_2SO_4:H_2O_2:H_2O 1:20(v) HNO_3:H_2O 1:20(w) KOH:H_2O	holes, vias	10
n-GaAs (100),[011]	Ar^+ (488 nm) 50mW/cm²	1:1:50 H_2SO_4:H_2O_2 H_2O	holographic gratings	11
n-GaAs (100) $1.5x10^{18}/cm^3$	HeNe (633nm) 16W/cm² - 16kW/cm²	10% KOH	character writing	24
n-GaAs (100) 10^{17} - $10^{18}/cm^3$	150W Xe ~20mA/cm² 0.2V (SCE) Metal mask	0.5M Tiron	gratings, deep grooves	14
n-GaAs (100),[011]	150W Xe ~20mA/cm²	0.5M Tiron	symmetric Echelle gratings	16

-- Continued --

Table 3 (Continued)

Material	Conditions	Electrolyte	Application	Ref.
10^{17} - 10^{18}/cm^3	0.2V (SCE) Photoresist mask			
n-GaAs off(100) $5x10^{17}$/cm^3	Hg-Xe,30mW/cm^2 0.4 volt (SCE) Photoresist mask	0.1M KCl	blazed Echelle gratings	18
p-GaAs (111) 3-$5x10^{17}$/cm^3	HeNe (633nm) 0.75W/cm^2 -0.2, +0.25V(SCE)	0.1M H_2SO_4/0.1M NaSCN (and others)	holes	5
p-GaAs (100),[011] $9x10^{17}$/cm^3	Ar^+ (257nm) 100mW/cm^2	1:1:50 H_2SO_4:H_2O_2:H_2O	holographic gratings	13
n-InP (100) 10^{18}/cm^3	Microscope lamp Au mask	40%(w) $FeCl_3/H_2O$	mesas	25
n-InP (100) var. N_D	100W W-halogen 0.1-0.4 volt (SCE) projection	2M HF/0.5M KOH	integral LED lenses	28
n-InP	HeNe, Ar^- 0.2 volt (SCE)	1:1:10 H_2SO_4:H_2O_2:H_2O, etc.	holographic gratings	7,8
n-InP $2x10^{17}$/cm^3 epi-InGaAs epi-InGaAsP $2x10^{16}$/cm^3	W lamp ion beam mask 0.25V (SCE) ~0.1μm/min.	2M HF/0.5M H_2SO_4; 2M H_2SO_4	mesas, gratings	26
n-InP (100),[011] $6x10^{18}$/cm^3	Ar^-(488nm) 0.7 volt (SCE)	1:1:20 HCl:HNO_3:H_2O	holographic gratings	12
n-Si ~$5x10^{14}$/cm^3	Ar^+ (514 nm)	5% HF	holographic gratings	47
n-Si	Ar^+ (257 nm) focused	5% HF	fiber optic coupler	23
n-SiC epi on Si; poly (CVD)	Hg-Xe arc 1 volt (SCE) Photoresist mask	1M HF	characters, gratings	48

Ostermayer et al. (5) have reported the photoelectrochemical etching of p-type III-V compounds. Under cathodic polarization, the photogenerated minority carriers (electrons) give rise to formation of the III element on the surface along with the evolution of the group V hydride (e.g., Ga and AsH_3). Subsequent anodic polarization leads to dissolution of the surface film by a majority carrier mediated reaction. As this process is repeated, the light-localized etched profile is developed.

It has been noted that light can accelerate etching of n-type semiconductors in oxidizing media, so that photoetching can be carried out without electrochemical control (1). In this "corrosion mode", the light produces minority carrier holes at the interface, while the charge compensating electrons are swept by the space charge field to adjacent non-illuminated regions. Photoselective etching can be maintained if reaction paths are available for the oxidation/dissolution of the lattice by holes and also the (non-etching) consumption of the compensating electrons. The oxidation and reduction currents must be balanced, so that the rate of either reaction can limit the overall photoetching rate. Electrolytes for photoselective etching may contain a weak or dilute oxidizing agent to accelerate reaction of conduction band electrons, or the reaction can be facilitated on a catalytic ohmic contact region of the crystal. Typically photoselective etching of this sort is conducted in known chemical etchants which have been diluted sufficiently to retard the dark reaction.

3.2 Periodic Structures

One of the most useful aspects of photoelectrochemical etching is the production of diffraction gratings and other periodic structures in semiconductor crystals for optical and electro-optical applications. Because of the different manner in which they are produced, these may be classified as holographic and non-holographic structures.

Holographic Gratings. A diffraction pattern is produced when two coherent, monochromatic beams are allowed to interfere. Today, the light source is almost always a laser. Many optical arrangements are possible to produce the desired interferogram, and the reader is referred to the excellent review by Hutley (6) for a complete discussion of the options. A typical optical arrangement is shown in Figure 3. The beam is first spatially filtered, expanded and collimated. The beam is then split into two separate beams of equal intensity, then recombined at the interference angle, θ. What is produced is a sinusoidally modulated pattern of light and dark fringes with a spacing, d, given by:

Eq. (2) $$d = \lambda_o / 2\eta \sin\theta \cos\delta$$

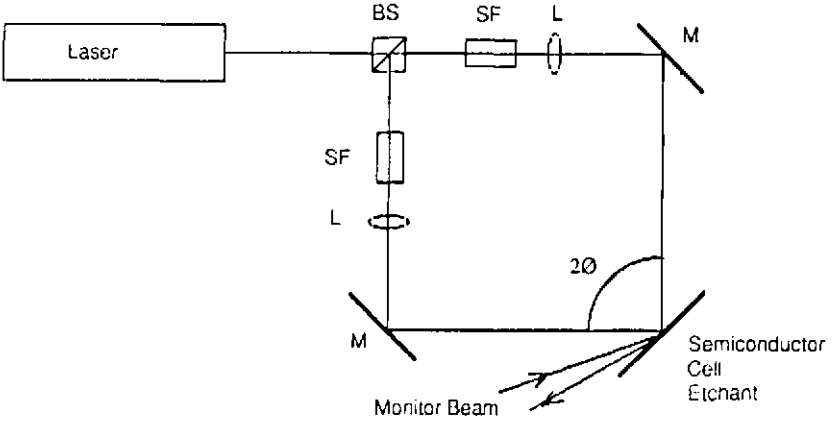

Figure 3. Arrangement for photoelectrochemical etching of interferometric gratings in semiconductor electrodes. Also shown is a weak or non-absorbed probe beam for monitoring the etching process. BS = beamsplitter; SF = spatial filter; L = collimating lens; M = mirror.

Here, λ_o is the source wavelength, η is the refractive index of the medium (electrolyte), and δ is the angle of the substrate with respect to the bisector or the interfering beams (usually 0°).

There are several practical matters which must be confronted in the photoanodic etching of holographic images. The laser generally must have a large coherence length. Spectroscopic gratings are usually fabricated using either an Ar ion or Kr ion source operating at 457.9 nm or 351 nm, respectively. These lasers must be equipped with a Fabrey-Perot etalon to produce the narrow spectral distribution required for a large coherence length. If such lasers are unavailable, then special care must be taken to equalize the pathlength of the two interfering beams to within the coherence length. Another consideration is that the time of exposure must be as short as possible to minimize the effects of vibration (vibration damped optical tables for holography should be used). Thus, higher intensity lasers and small grating areas are most favorable; the exposure time may be calculated from Eq. 1. To obtain gratings with high frequencies, it is necessary to increase θ, although ~60° is considered to be a practical limit. Using an ultraviolet line of an Ar or Kr ion laser, it appears possible to etch holographic gratings with a pitch of 6000 - 7000 lines/mm.

The resolution obtainable for etching holographic gratings in a crystal is a function not only of the optical arrangement, but also of semiconductor transport parameters and the kinetics of the dissolution reaction. The material parameters which influence the resolution have been summarized by Ostermayer and co-workers (7). These are:

— The space-charge width, w, which is related to the majority carrier density, N_D, and the potential drop, φ, across the space charge region by the equation:

Eq. (3) $$w = (2 \epsilon \varphi / q N_D)^{1/2}$$

where ϵ is the dielectric permittivity of the semiconductor and q is the unit charge.

— The diffusion constant of minority carriers, D, which is related to their mobility, μ, by the Einstein relationship:

Eq. (4) $$\mu = (q/kT) D$$

— The diffusion length of minority carriers, L, which is determined by D and by their lifetime: $L = [D \tau]^{1/2}$

— The absorption coefficient of the semiconductor at the source wavelength, α (cm^{-1}).

— The interfacial reaction velocity K ($cm\ sec^{-1}$).

The grating figure of merit is defined as the ratio of the grating amplitude to the average depth etched, and may be evaluated from micrographs of grating cross sections and from a knowledge of the charge passed per unit area during the fabrication process. The maximum value of this ratio is unity. A number of useful relationships between grating quality and the material and electrolyte parameters were developed. The following qualitative conclusions can be drawn from both the experiments reported for n-InP and the theoretical calculations:

1. A high value of K favors high resolution, since if holes are consumed more rapidly at the surface, they will have less opportunity to diffuse laterally.

2. If K is high, then the resolution will be dependent on α, while if K is low, as is most often the case for systems investigated to date, then the resolution becomes α-insensitive. In the former case, lateral diffusion in the bulk from the point of hole generation to the surface dominates the resolution loss rather than surface diffusion.

3. All else being constant, increasing w, such as by decreasing N_D, degrades the resolution. The decreased field in the space charge region causes photogenerated holes to accumulate deeper into the surface, making them less available for reaction and more susceptible to lateral diffusion.

4. The quantum yields of etching many III-V compounds are often near unity at the photon limiting potentials. Thus, under these conditions, there is very little effect of bulk recombination, and hence little effect of minority carrier diffusion length. However, higher diffusion coefficients, D, decrease the overall resolution.

In a practical sense, the studies of Ostermayer et al. allow selection of material properties which favor high grating resolution. The reaction velocity is a dominant effect, and rapid dissolution of oxidation products is necessary. Furthermore, a low lateral diffusion of surface holes is fostered by high doping density and low D. If doping densities are too high, however, then anodic dark currents may become problematic.

Numerous examples have been provided in the literature of gratings and holograms fabricated in a variety of semiconducting materials. A compilation by Gurevich and Pleskov (1) of examples primarily from the Russian literature of the 1970's cites gratings etched by both controlled potential and light stimulated corrosion techniques. Diffraction gratings have been produced in elemental semiconductors, II-VI and III-V semiconductors and alloys, and in oxides. Spatial frequencies of 1000 to 6150 /mm were reported in this earlier work. Later more extensive studies by the group at Bell Laboratories were all conducted under potential control (8)(9). These studies were aimed at fabrication of gratings for use in distributed feedback lasers, and dealt primarily with InP and GaInAsP

alloys. Reaction velocities obtained from the resolution of gratings etched in n-InP are reported in Table 4. Podlesnik et al. (10), employing frequency doubled Ar^+ ultraviolet laser excitation, etched holographic gratings in n-GaAs using light stimulated corrosion in 1:1:100 H_2O_2:H_2SO_4:H_2O. The finest gratings had a spacing of 170 to 200 nm and a depth of 35 - 40 nm. The best depth-to-space ratio was 0.8 for a 2 μm grating. The degradation of depth-to-space ratio, which is directly proportional to the grating efficiency, is due to the factors limiting grating resolution, discussed above. Matz (11)(12) demonstrated a two step process for producing high aspect ratio gratings in n-GaAs and n-InP using a similar etchant. In the first step, the crystal of (100) orientation was illuminated with the diffraction pattern along the [01$\bar{1}$] direction, resulting in a shallow profile having the shape shown in Figure 4. Following this, the etching was allowed to continue in the dark where the profile became more triangular in shape due to exposure of slow etching (111)Ga planes. Thus, the two step process was not effective for other crystal orientations. Gratings with 330 nm groove spacing and 150 - 170 nm depth were prepared in this way. Matz (13) has also reported gratings etched in p-GaAs using the aforementioned method of Ostermayer et al. (5). Structures with a spacing of 230 nm and a depth of 100 nm were reported using 257 nm light from a frequency-doubled Ar ion laser source. Crystalline orientation was seen to affect the groove profile here as well, as has been observed for photoelectrochemical chemical etching using a photomask (see below).

Table 4

Reaction Velocities for Photoelectrochemical Etching of InP in Various Electrolytes (Ref. 7).

Electrolyte	Reaction Velocity, K (cm sec^{-1})
2M HCl	890
2M HF:0.5M KOH	63
2M HBr	1500
1:1:10 H_2SO_4:H_2O_2:H_2O	2500
1:1:100 H_2SO_4:H_2O_2:H_2O	15
1:10 H_2SO_4:H_2O	1500

A detailed analysis of the effect on resolution of etching with external control versus light enhanced corrosion has not been made. Qualitatively, results seem similar for both techniques applied to III-V compounds. Since the process can be followed optically, e.g., with a weak secondary probe beam (9), coulometric monitoring may not be absolutely necessary. Certainly the polarization of the crystal by external means often yields the advantages of using a neutral or mild electrolyte and higher effective quantum yields. At this time, more work is required to assess the effect of external fabrication variables on the actual performance of the gratings in lasers and spectroscopic instrumentation.

Non-holographic Periodic Structures. The general approach for making periodic structures of non-sinusoidal cross section has been to employ a mask to define the photoetched pattern. The semiconductor is then photoelectrochemically etched in the exposed regions, after which the pattern mask is removed with a suitable solvent. In principal, the etching will occur vertically with the edges sharply defined by the edges of the mask. However, crystallographic orientation, the masking material, the electrolyte and the bulk semiconductor properties can have profound effects on the result.

Most of the results available at this time refer to III-V compounds, particularly n-GaAs. This material exhibits a strong orientational effect on the photoanodic etching process. Orientational effects of photoanodic etching of n-GaAs have been examined in this laboratory using (100) crystals with a mask defining slots oriented along three primary directions, as shown in Figure 5. In most electrolytes, the Ga-rich crystallographic surfaces are preferentially exposed in grooves defined in the (100) surface along the $[01\bar{1}]$ direction (14)(15). The other directions exhibit more or less vertical etching. The results are quite similar to oxidative chemical etching processes in this regard, e.g., by Br_2/methanol.

Effects of both orientation and doping on etching deep periodic trenches in GaAs are shown in the photographs in Figure 6. These structures were etched at a bias of 0.5 volt vs. SCE, and a broad band light intensity sufficient to yield a dissolution current of 10 mA/cm^2 in the Tiron electrolyte (4,5-dihydroxy-1,3-benzene disulfonic acid, a Ga^{+3} complexant). The masking material was an adherent Cr/Au bilayer, patterned by liftoff. The pointed bottoms of the grooves etched along the $[01\bar{1}]$ direction illustrate the exposure of the Ga-rich planes. Higher doping densities decreased the degree of undercutting of the mask, as shown in the bottom photograph. The reason for this undercutting is still uncertain, but may relate to a greater propensity for diffusion of holes into the unilluminated region beneath the growing lip of the metal mask. This explanation would be consistent with the model of Ostermayer et al. (7), which predicts greater lateral diffusion of holes as N_D is reduced.

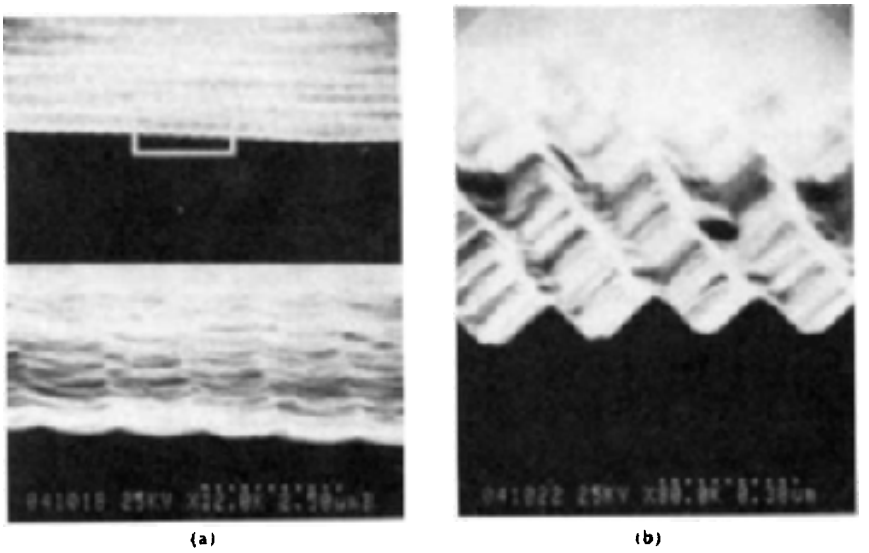

Figure 4. SEM photographs of 330 nm gratings after (a) holographic illumination, and (b) anisotropic dark etching (from Matz, ref. 12). Copyright 1986, IEEE.

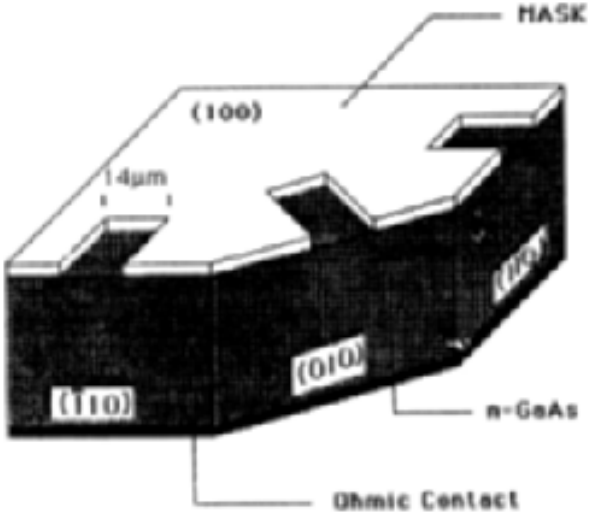

Figure 5. Patterning of (100) n-GaAs crystal surface for groove etching experiments.

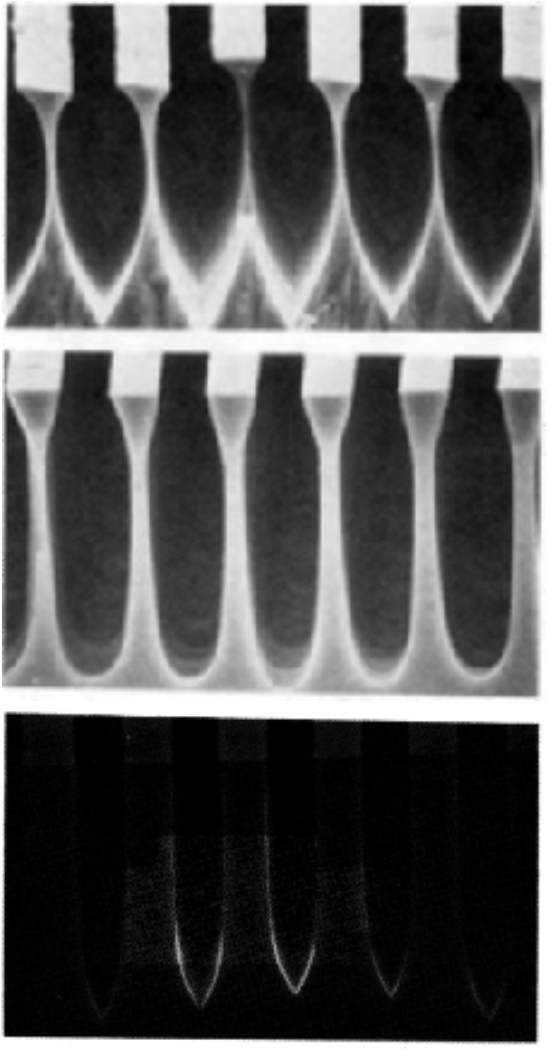

Figure 6. Cross sections of grooves photoelectrochemically etched in (100) n-GaAs. (0.5 M Tiron; 442 nm, 20 mW/cm^2; 0.5 volt vs. SCE). Top: [00$\bar{1}$] direction, N_D = 3.2 x 10^{17}/cm^3; middle: [011] direction, N_D = 3.2 x 10^{17}/cm^3; bottom: [01$\bar{1}$] direction, N_D = 1.3 x 10^{18}/cm^3. Groove width is 10 μm (from Carrabba et al., ref. 15).

The crystallographic orientational effects on the photoanodic etching profiles are particularly useful in fabricating Echelle-type diffraction gratings (16). The photoelectrochemical method permits the fabrication of these gratings with a high degree of control of lateral uniformity and of processing conditions leading to optimal smoothness of the groove walls. In general, photoresist masking materials have been employed, e.g., Shipley 1350J positive resist. The evolution of formation of the "teeth" is shown in Figure 7, in which the Ga faces become exposed and the mask becomes undercut until it floats off as the apex is formed. The interior angle of the V-groove can be influenced by the electrolyte composition, which in turn determines the relative rates of dissolution of the Ga^{+3} and As^{+3} oxidation products (17). For example, in KCl electrolytes, the angles are close to the theoretical value of 70.54° for low KCl concentrations, but become significantly wider at higher concentrations. Apparently, high Cl^- enhances Ga^{+3} dissolution and the exposed planes have more of a mixed composition.

In order to produce blazed Echelle gratings, it is necessary to cut the GaAs crystal at an angle off the (100) plane toward the (011) plane (18). As shown in Figure 8, orienting the photoresist lines in the $[01\bar{1}]$ direction then still gives rise to structures with the interior angles governed by the preferred Ga-rich surfaces. One advantage of photoelectrochemical etching for producing these structures is that the process can be followed coulometrically. The charge, Q, required to etch the V-groove sawtooth pattern is:

Eq. (5) $$Q(C/cm^2) = 3.54 \times 10^3 nN(0.5W^2/\cot(\alpha - \beta) + \cot(\alpha + \beta))$$

Here, n is the electron stoichiometry (equivalents/mole) of the photoanodic dissolution reaction, W is the width (cm) of each groove, α is the angle of the groove face with respect to the (100) surface, β is the angle of the crystal slice with respect to the (100) surface, and N is the number of grooves/cm.

An example from this laboratory demonstrates the photoelectrochemical etching of blazed structures. Crystals of n-GaAs ($N_D = 5 \times 10^{17}/cm^3$) were cut and polished with (100), (100)-8° and (100)-18° orientations. The other parameters in Eq. 5 were: n = 6, N = 500 and $W = 2 \times 10^{-3}$ cm. The electrolyte composition was 0.1 M KCl, adjusted to pH 3, and the light intensity was 30 mW/cm^2. The potential was held at the onset of the photon limited region, 0.4 volt vs. SCE. Initial structures were etched under the assumption that the interior angles were 70.54°, as defined by the (111) Ga surfaces. However, we found under closer examination that this angle was dependent on the etching conditions and on the electrolyte, and was closer to 90° under the present conditions. This would correspond most closely to the (223)Ga-rich surface. With a

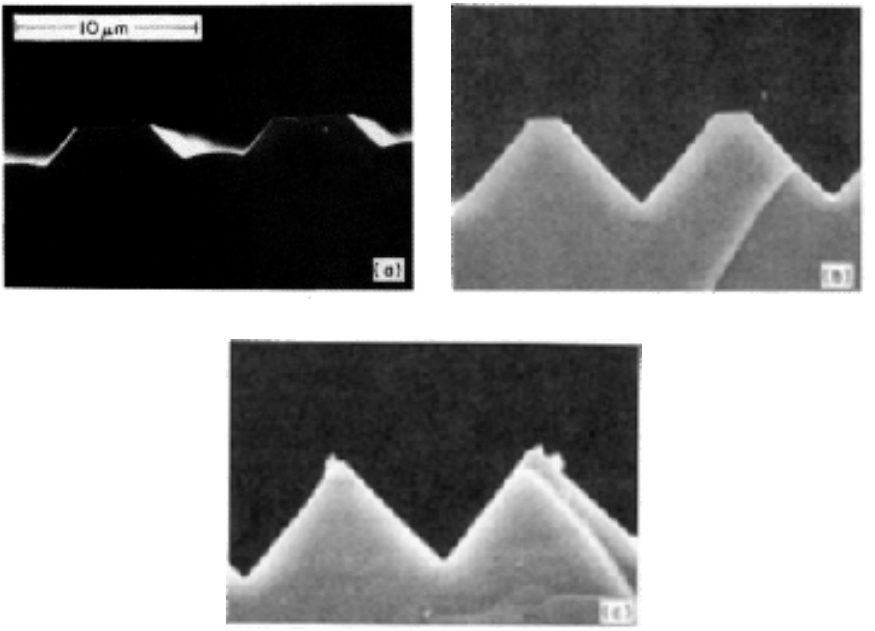

Figure 7. Scanning electron micrographs showing cross sections of grooves photoelectrochemically etched in (100) n-GaAs, [01$\bar{1}$] direction, at three stages of development (16). Copyright 1986, The Optical Society of America.

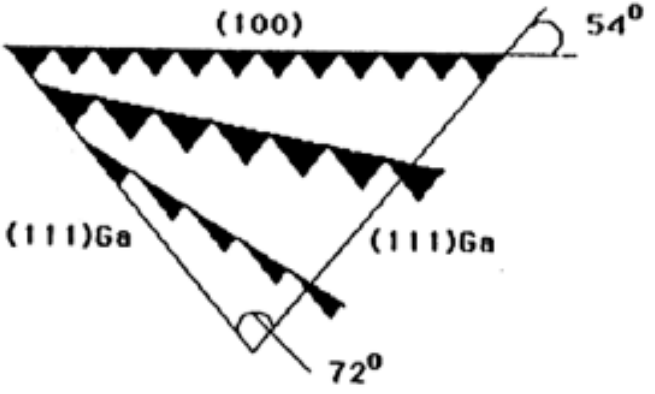

Figure 8. Schematic cross section of V-grooves arising from exposed [111]Ga planes for GaAs cut at various angles off the (100) plane.

90° interior angle, Eq. 5 predicts a charge of 10.6 and 8.6 C/cm^2 required to etch the gratings in the (100) and (100)-18° surfaces, respectively. With coulometric monitoring, both unblazed and blazed gratings were produced with pointed tops and bottoms and extremely smooth walls. A scanning electron micrograph of the blazed structure from the (100)-18° surface is shown in Figure 9. The blaze angle of 60° is slightly less than the expected value of 63°, an error probably due to inaccuracies accumulated in the cutting and polishing procedures.

Cummings et al. (19) have reported the use of a focused gallium ion beam to produce damaged regions in n-GaAs which act as a mask for photoelectrochemical etching due to a high rate of electron-hole recombination. After exposure, the undamaged GaAs was photoelectrochemically etched in 2 M H_2SO_4 at -0.2 volt vs. SCE. Ion beams can be focused to well below 0.1 μm. However, when 0.2 μm beam was used to draw the mask, the resolution of the photoetched features could be made no better than about 1 μm. The reason was determined to be the extremely low ion dose needed to deactivate the GaAs surface - only about 1 ion per 1000 angstrom^2. Hence, the gaussian tail of the ion beam can deactivate the GaAs far from the beam center.

3.3 Focused Laser and Related Techniques

A focused laser may be used for "drawing" or for "drilling" microstructures into semiconductor surfaces. In these cases, the laser beam is focused into a spot onto the crystal surface. Specific patterns may be generated by computer-controlled scanning techniques.

When using a focused laser beam to etch semiconductors photoelectrochemically, it is important to consider the limiting light intensity to preclude significant localized heating. In many situations, heating will accelerate an etching process and hence degrade selectivity and resolution. The approximate maximum temperature rise caused by an absorbed cw laser beam has been derived by Lax (20) as:

$$\text{Eq. (6)} \qquad T_{max} = P/2\pi^{1/2}\kappa W$$

where P is the nominal laser power, κ is the material thermal conductivity, and W is the beam width. For example, T_{max} caused by a 5 μm diameter beam on GaAs (κ = 0.46 W/cm deg) will be 1240 P degrees. In reality, the temperature rise will be somewhat less due to the finite depth of penetration of the light. Note that a 1 mW laser will produce a power density of 4000 W/cm^2 under these conditions, and a T_{max} of only 1.24°C.

Osgood and co-workers at Columbia University (10)(21)(22) have investigated laser hole drilling in crystals of III-V compounds simply

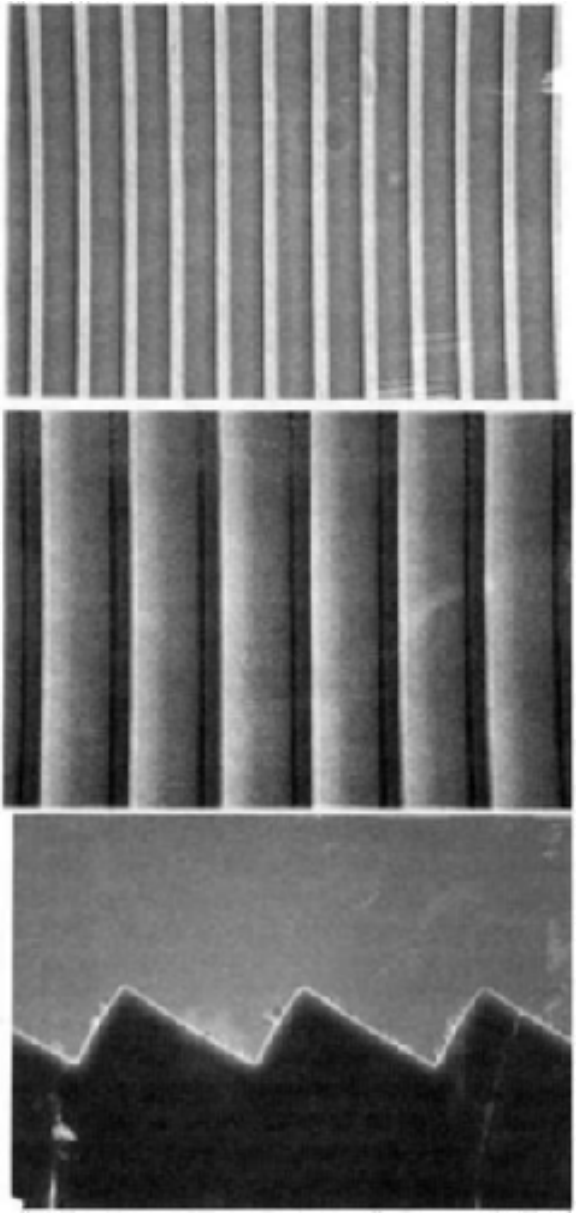

Figure 9. SEM profiles of a 60° blazed grating etched in (100)-18° cut n-GaAs (18). Reprinted by permission of the publisher, The Electrochemical Society, Inc.

immersed in etching electrolytes. As mentioned earlier, the light will generate minority carriers, thus accelerating etching in the illuminated zone. Most previous investigations of photoelectrochemical etching under these conditions have shown it to be analogous to corrosion, and a charge-balancing reduction reaction is expected to occur in neighboring non-illuminated zones.

The Columbia group has observed marked wavelength effects on the hole drilling process. Many experiments were carried out using an Ar ion laser, comparing etching using fundamental (514 nm) and frequency doubled ultraviolet excitation (257 nm), a 3 - 4 μm spot size and laser powers ranging from 10 nW to 100 mW. Ultraviolet illumination of GaAs immersed in pure water results in oxide growth, while no effect on the oxide layer was noted with visible light illumination. If the solution is made acidic or basic so that the oxide is dissolved away, etching occurs with both sources, but at a much higher rate with the ultraviolet source at the same intensity. Etching with the ultraviolet source was observed for n-, p- and semi-insulating material. Finally, holes drilled with the focused ultraviolet source are narrower, deeper and formed more rapidly than with the visible source. Using the 257 nm laser, holes 3 - 4 μm in diameter have been etched through 200 - 300 μm thick wafers. An incident focused laser intensity of 10 W/cm^2 resulted in an etch rate of 0.15 μm/sec.

The highly actinic nature of the ultraviolet light is ascribed by Osgood and co-workers to the fact that carriers are produced very near to the surface (<5 nm) and thus diffuse to the interface and react before they have a chance to relax thermally. Thus, holes are produced deeply enough in the valence band to react with redox levels of pure water located at ~ 0.4 volt below the top of the valence band. The deep holes that can be drilled with ultraviolet light are ascribed to a light guiding effect that is promoted by the high angular dependence of reflectance at these wavelengths.

One interesting application of laser drilled holes is in producing fiber optic couplers for integrated electro-optic devices. Prucnal et al. (23) reported a coupler to Si, shown in Figure 10. The well was first etched into n-Si using focused 257 nm laser light and a 5% HF electrolyte, then its internal surface converted to a p-n junction photodetector. The well acted as a receptacle for a 9 μm single mode optical fiber. Other applications include vias for connecting the front and back sides of wafers, and light guides for electro-optical circuits.

Rauh and LeLievre (24) examined the intensity and total delivered energy dependence of hole diameters etched in n-GaAs with a focused 633 nm (HeNe laser) source. Unlike the results with ultraviolet excitation, the hole diameters grew sharply with etching time and no "light guided" structures were produced. However, shallow pits could be etched with

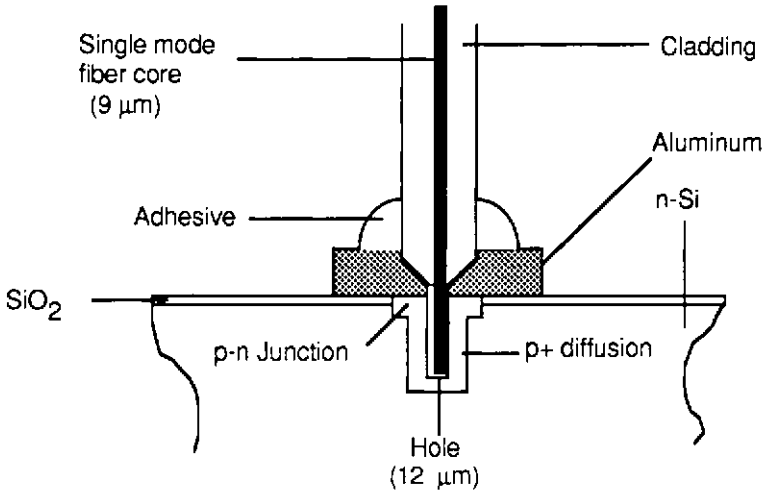

Figure 10. Schematic cross section of prototype integrated fiber-optic coupler prepared by photoelectrochemical etching (after Fig. 1, ref. 23).

high resolution. By raster scanning the stage holding the electrolyte coated crystal (10% KOH), and by computer controlling the shutter, complex patterns could be etched in relief in the surface. An example of a character set produced in this way from 2 μm diameter "pixels" is illustrated in Figure 11.

A common feature of the hole drilling experiments described above is that they were performed without electrochemical control of the semiconductor surface. As a result, quantum yields were always much less than unity and the width of the space charge region was probably very low. The latter factor doubtlessly magnified differences between quantum yields observed for ultraviolet and visible light resulting from differences in the penetration depth and hence efficiency of electron-hole separation. To date, no studies of the effects of electrode bias on the rates and profiles of laser drilled structures have been presented.

3.4 Miscellaneous Applications of Photoelectrochemical Etching

A number of examples have been reported of using photoelectrochemical etching as a step in fabricating electronic and electro- optical devices.

Lubzens (25) has demonstrated the photoelectrochemical etching of mesa structures in n-InP. The structures described were cylinders 50 μm in diameter by 18 μm high. They were prepared by first defining the circular regions by standard lithographic/liftoff procedures. The patterned crystal was immersed in a 40% $FeCl_3$ etching solution and illuminated with a broadband collimated source. The etching proceeded smoothly in the exposed areas between the mesas, although occasional removal of etching products with $Br_2/HBr/H_2O$ was necessary. The aforementioned ion beam masking technique has also been used to define mesas for definition by photoelectrochemical etching, thus avoiding the need for metallization (26). Mesa structures were demonstrated in InP, InGaAs and InGaAsP alloys.

Forrest et al. (27) described the application of photoelectrochemical etching to the fabrication of an annular photodiode, shown in Figure 12. The central hole was photoelectrochemically etched through photolithographically defined circular areas in the metallization. The process was carried out under an external bias using an electrolyte of 0.75 N KF/0.75 N HF. The photo-process continued until the p^+ region was reached, after which it was completed by a dark chemical etch.

Ostermayer et al. (28) reported the photoelectrochemical fabrication of lenses onto light emitting diodes (LEDs). The spherical lenses were formed by projection of the lens pattern onto an n-InP/InGaAsP double

Figure 11. Photoelectrochemically etched character set in unbiased n+-GaAs using scanned 2 μm diameter HeNe laser spot (160 W/cm^2, 0.2 sec/point, 10% KOH) (24). Reprinted by permission of the publisher, The Electrochemical Society, Inc.

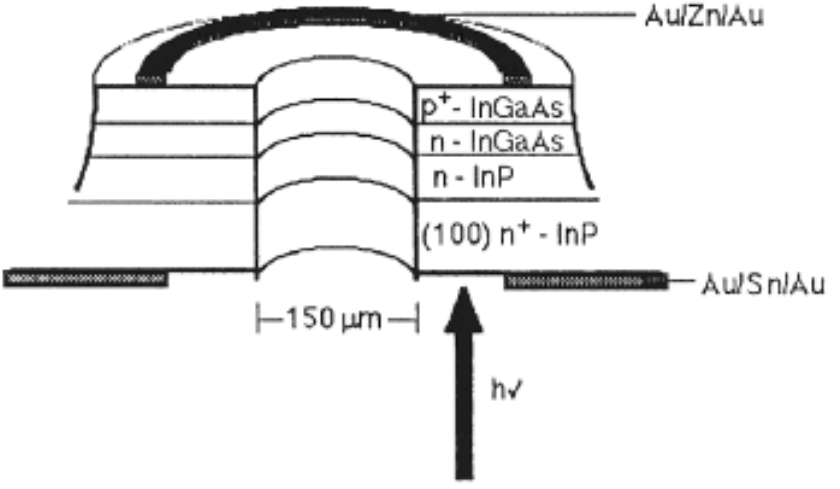

Figure 12. Schematic cross section of annular p–i–n photodetector (after Fig. 1, ref. 27).

heterostructure LED, which served as the electrode. The projection mask for the 70 μm diameter lenses was produced from concentric Cr rings lithographically fabricated from a thin Cr film evaporated onto a glass substrate. The lenses are used for coupling the output of the LED directly into optical fibers.

Cheng and Kohl (29) demonstrated that fiducial patterns on one side of an n-InP wafer, defined in photoresist, could be photoelectrochemically etched through to the other side of a wafer about 90 μm thick. The metallized mask served the dual purpose of the electrical contact, which was at the front surface in this case. The process was carried out by illumination with a collimated beam from a HeNe laser and an electrode polarization of 0.2 - 0.4 volt (SCE) in 2 - 4 N HCl. Best results were obtained at light intensities < 260 mW/cm^2 due to reduced effects of diffraction and light scattering within the growing hole.

Lin and co-workers (30) have demonstrated photoelectrochemical etching of very fine lines in n-GaAs with the tip of a scanning tunneling microscope as the counter electrode. An electrochemically machined Pt tip was used with an end < 0.1 μm in diameter. The tip was immersed in the etching electrolyte, which also contained a reducible depolarizer to avoid tip dissolution, and drawn across the GaAs electrode surface at a controlled distance of 1 μm. The n-GaAs was anodically polarized, and light was used to induce and control current flow while the tip was moving. A minimum line width of 0.3 μm was achieved.

4.0 PHOTOELECTROCHEMICAL DEPOSITION

Up to this point we have been concerned with photoelectrochemical processes for selective removal of the semiconductor substrate. As stated earlier, light-localized deposition is also feasible. In general, this is carried out by adding to the electrolyte the precursor of a material that forms the deposit when reduced or oxidized. The precursor may be a metal ion, an electropolymerizable monomer, or any compound or complex that is soluble in one oxidation state and insoluble in another. Some of the applications of photoelectrochemical deposition include formation of ohmic or rectifying contacts, plating of via (through wafer) holes, imaging for information storage and display, and fabrication of optical elements.

We first consider the localized photoelectrodeposition of metals onto semiconductor surfaces (31)(32). In almost every case the precursor to a metal in a plating bath is a positive ion, so that the deposit is formed by reduction. Thus, a p-type semiconductor is required for positive photoelectrochemical imaging. If the deposition is done in an electrochemical cell configuration, the semiconductor electrode should

Next Page

heterostructure LED, which served as the electrode. The projection mask for the 70 μm diameter lenses was produced from concentric Cr rings lithographically fabricated from a thin Cr film evaporated onto a glass substrate. The lenses are used for coupling the output of the LED directly into optical fibers.

Cheng and Kohl (29) demonstrated that fiducial patterns on one side of an n-InP wafer, defined in photoresist, could be photoelectrochemically etched through to the other side of a wafer about 90 μm thick. The metallized mask served the dual purpose of the electrical contact, which was at the front surface in this case. The process was carried out by illumination with a collimated beam from a HeNe laser and an electrode polarization of 0.2 - 0.4 volt (SCE) in 2 - 4 N HCl. Best results were obtained at light intensities < 260 mW/cm^2 due to reduced effects of diffraction and light scattering within the growing hole.

Lin and co-workers (30) have demonstrated photoelectrochemical etching of very fine lines in n-GaAs with the tip of a scanning tunneling microscope as the counter electrode. An electrochemically machined Pt tip was used with an end < 0.1 μm in diameter. The tip was immersed in the etching electrolyte, which also contained a reducible depolarizer to avoid tip dissolution, and drawn across the GaAs electrode surface at a controlled distance of 1 μm. The n-GaAs was anodically polarized, and light was used to induce and control current flow while the tip was moving. A minimum line width of 0.3 μm was achieved.

4.0 PHOTOELECTROCHEMICAL DEPOSITION

Up to this point we have been concerned with photoelectrochemical processes for selective removal of the semiconductor substrate. As stated earlier, light-localized deposition is also feasible. In general, this is carried out by adding to the electrolyte the precursor of a material that forms the deposit when reduced or oxidized. The precursor may be a metal ion, an electropolymerizable monomer, or any compound or complex that is soluble in one oxidation state and insoluble in another. Some of the applications of photoelectrochemical deposition include formation of ohmic or rectifying contacts, plating of via (through wafer) holes, imaging for information storage and display, and fabrication of optical elements.

We first consider the localized photoelectrodeposition of metals onto semiconductor surfaces (31)(32). In almost every case the precursor to a metal in a plating bath is a positive ion, so that the deposit is formed by reduction. Thus, a p-type semiconductor is required for positive photoelectrochemical imaging. If the deposition is done in an electrochemical cell configuration, the semiconductor electrode should

be operated under a negative bias to enhance the (downward) band bending. A current-voltage curve for a p-type semiconductor electrode in a plating electrolyte is shown schematically in Figure 2. At potentials more positive than V_{fb} the p-type electrode passes positive current in the dark by the injection of holes via the valence band. In an ideal junction for semiconductors with bandgaps large compared to thermal energies, cathodic current will be negligible in the dark and will be stimulated by super-bandgap illumination. When the electrolyte contains metal ions, their reduction by conduction band electrons produced by light excitation will give rise to localized metal deposition.

An important aspect of photoelectrochemical deposition is to ensure that the energy of the conduction band electrons reaching the interface is sufficient to reduce the precursor ion in the electrolyte. In reality, there are three possible situations relating the electrodeposition potential, V_{dep}, the flat band potential, V_{fb}, and the semiconductor bandgap. In the case where V_{dep} is more negative than the conduction band, photoelectrochemical deposition will not occur. The optimal potential region for V_{dep} is within the bandgap. When V_{dep} lies below V_{fb}, precursor ions may be reduced in the dark via electrons flowing in the valence band.

The progress of photoelectrochemical positive deposition of metals depends on whether the deposit forms an ohmic or rectifying contact. If the contact is ohmic, then the band bending will collapse during the deposition of the first few monolayers and the light-driven reaction will cease. The plating may continue in the dark, however, if the control potential is sufficiently negative or if the process is being conducted galvanostatically. If the deposited contact is rectifying, then the light driven reaction will continue for up to a few thousand angstroms until the growing contact blocks all of the incoming light.

The voltammetric behavior of p-Si in combination with different plating electrolytes has been investigated in this laboratory (32)(33)(40). It is seen that relatively little cathodic current passes in the dark in plating electrolytes showing the more negative deposition potentials, exemplified in Figure 13b by Zn. In $CuSO_4$, where the metal deposits at a relatively positive potential, considerable plating occurs in the dark. This is due to the fact that the plating potential is relatively near to the valence band in p-Si. Even though the plating current is accelerated by light for this electrolyte (due to additional contribution from photogenerated conduction band electrons), the selectivity is severely reduced.

The electrical characteristics of photoelectrochemically deposited Au-Zn contacts onto p-InP and p-GaAs has been reported by Kelly et al. (34). Some electrolyte compositions gave very constant Zn/Au ratios over a wide range of deposit thicknesses. In general, once the deposit was initiated photoelectrochemically, it could be continued in the dark. Rapid

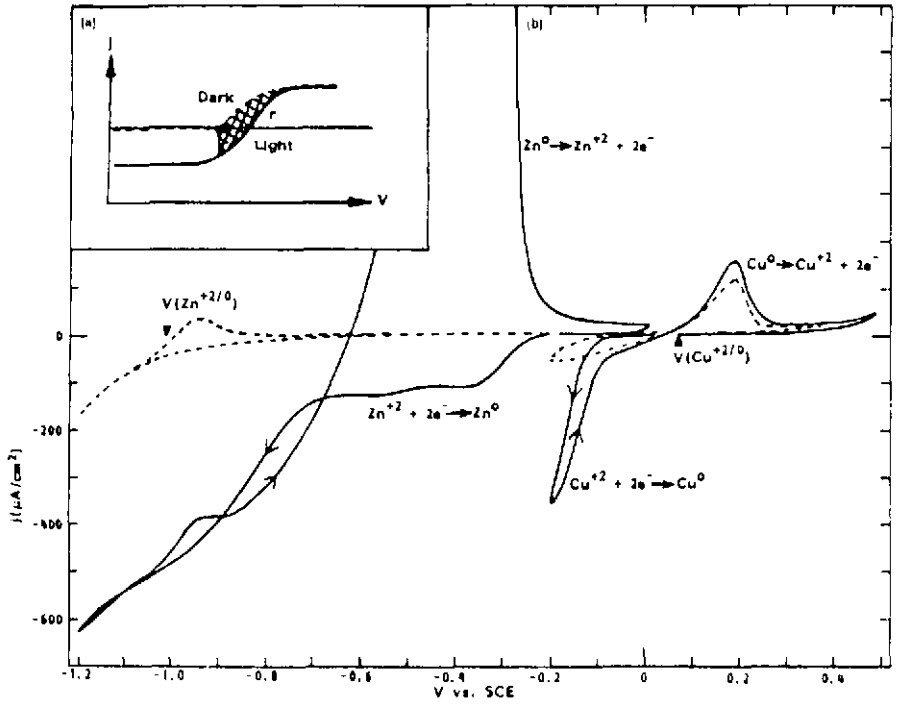

Figure 13. Current-voltage for p-Si photocathode. (a) Hypothetical curves showing overlap region (shaded) between anodic dark current and cathodic photocurrent necessary for "electroless" imaging. (b) Cyclic voltammograms for p-Si in Zn plating electrolyte and Cu plating electrolyte with 0.5 M MSO_4 and pH = 3.1. Broken line, dark; solid line, 1.2 mW/cm^2 tungsten-halogen light illumination (40). Copyright 1983, The American Institute of Physics.

annealing to 425 - 450°C in a mildly reducing atmosphere led to contact resistances on the order of $10^{-5}\ \Omega\ cm^2$.

The resolution of photoelectrochemical deposits appears to be determined by a number of factors, and its limitation is not yet understood. Figure 14 shows results obtained in this laboratory for a projection image of Au produced on p-GaAs under galvanostatic control. The minimum feature size of the 0.4 μm deposit is 10 - 20 μm (32). Jacobs and Rikken (35) have studied the nucleation and growth of Au photoelectrochemically deposited on p-GaAs under potentiostatic control. They initially observed nuclei of about 1nm in diameter at a surface density of 10^{10} to $10^{12}/cm^2$ which then grew and eventually coalesced. The dark current was observed to increase during the initial stages of deposition, indicating that Schottky barriers pinned at a low barrier height were formed at the nuclei. As a result, some degree of growth of the pattern could be expected by continuing the electrolysis in the dark following an initial photoelectrochemical "strike".

The best resolution was obtained by Jacobs and Rikken under the following conditions. The p-GaAs was Zn doped ($N_A \sim 2x10^{17}/cm^3$) and etched in 100:2:1 $H_2O/H_2O_2/NH_4OH$, then dipped in 0.2 M KOH. The plating bath consisted of $5x10^{-3}$ M $KAu(CN)_2$, 0.1 M KCN and 0.2 M KOH. The deposition was conducted potentiostatically at -1.2 volts vs. SCE and a light intensity sufficient to give a photocurrent of a few mA/cm^2. The pattern was obtained by projection imaging onto the electrode surface. A pattern similar to that in Figure 14 was reported which was the result of a 10 second exposure, with resolution of about 2 μm. The average photocurrent during deposition was approximately 1 mA/cm^2, where the growth rate of the deposit is approximately 1 nm/sec.

Inoue et al. (36) have demonstrated positive imaging of oxide layers onto n-type semiconductors, where the oxide is formed by the oxidation of a soluble precursor. The general reaction is:

$$M^{n+} + aH_2O + bp^+ \longrightarrow M_xO_y + 2aH^+$$

The technique is suitable for depositing oxides of Pb, Co, Mn and Cr, and has been reported primarily for wide bandgap n-type oxide semiconductors, such as ZnO and TiO_2. A number of the oxide deposits are electronically conductive and can be used as electrical contacts. Although not demonstrated, the process should also be suitable for semiconductors more commonly used in electronics. Imaging via oxidative photodeposition has also been reported for conductive organic polymers on ZnO and other semiconductors (37). The polymer forms on electrochemical oxidation of solutions of the monomer, e.g., pyrrole, thiophene and aniline. Since the conductive polymers are also electrochromic, the process might be

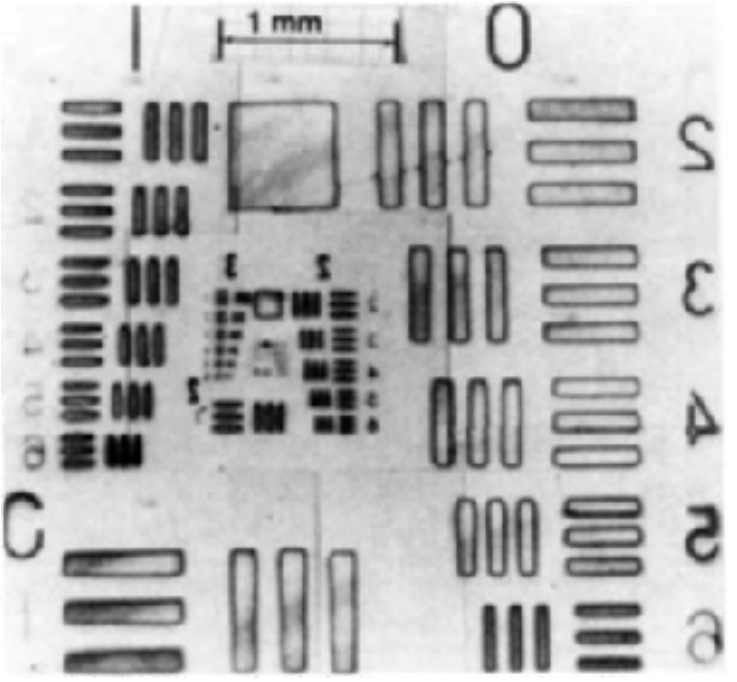

Figure 14. Photomicrograph of a photoelectrochemical Au deposit on p-GaAs, produced from the projected image of a USAF-1951 resolution target (33)(34). Copyright 1983, The Materials Research Society.

useful in the fabrication of electrochromic display elements.

As with etching, it is also possible in some cases to observe photoelectrochemical deposition of thin films without external control, i.e., an electroless process (31)(38). In this case, the semiconductor is simply immersed in the plating/precursor solution and the surface illuminated with the desired pattern. The main requirement for the electroless photodeposition of a metal to occur is to have a sacrificial reductant in solution or on the semiconductor (e.g., the semiconductor itself). Thus, when the semiconductor is illuminated with the light pattern, the metal ions will be reduced in the illuminated zones and the reductant oxidized by majority carriers in the dark zones.

One possibility is to employ the dissolution of the semiconductor itself as the sacrificial oxidation reaction. Kohl et al. (39) have demonstrated the filling of via holes through a 30 μm GaAs wafer by electroplated Au using such a photoassisted process. As illustrated in Figure 15, nucleation of the Au occurs as the dark reaction at the source pad of an FET bridging the via hole. The minority carriers (holes) produced at the semiconductor/electrolyte interface give rise to Ga^{+3} and As^{+3} formation. The equivalents of Au that are plated in the vias, which had a $6x10^{-4}$ mm^2 cross section, is very low, so that < 1 μm of the 2" wafer surface is etched away.

A particular example of electroless plating with a controlled sacrificial layer has been described by Rose et al. (40), illustrated in Figure 13. Here, a crystal of p-Si was contacted with metallic Zn on the back side, and then immersed in 0.5 M $ZnSO_4$. The Zn^{+2}/Zn potential of approximately -1 volt vs. SCE resulted in a significant band bending at the semiconductor/electrolyte interface.

On illumination, conduction band electrons reduced Zn^{+2} in solution, giving rise to a light-localized deposit. To balance the charge, holes were swept to the Zn contact where they participated in its anodic dissolution. In other words, the sacrificial Zn layer provides an anodic dark reaction which overlaps in potential with the cathodic photodeposition reaction, thus allowing the process to proceed spontaneously under illumination. The process also works for other metals with rather negative plating potentials, such as Cd, but not for more noble metals, such as Cu or Ni. In the latter cases, the metal potentials are not sufficiently negative to cause significant band bending in p-Si. (Note that putting the Zn-contacted p-Si in the Cu^{+2} bath, for example, will not work since the Cu will simply plate out onto the Zn contact by exchange). This approach may also be taken to deposit an "activation" layer of Pd, for example, for later electroless plating in the dark (see, for example, Stremsdoerfer et al. (41)).

5.0 PHOTOELECTROCHEMICAL SURFACE PROCESSING

Illumination of semiconductors immersed in liquid electrolytes often gives rise to formation of oxidation products on the surface. The nature of these products can affect strongly the energy distribution and concentration of surface states. Such surface states play an important role in the operation of solid state Schottky and metal-oxide-semiconductor (MOS) diodes. In general, processing techniques are constantly being sought where the surface state densities are reduced to a point where the Fermi level is essentially unpinned so that the band bending in the diode becomes a sensitive function of the applied voltage over a wide range. Silicon technology is successful because surface oxidation readily reduces the surface state density to below a critical concentration, typically $< 10^{10}/cm^2$. The development of integrated circuits based on III-V compounds, which generally have higher mobilities than Si, has been hampered somewhat by the absence of surface processing techniques that can reduce the surface state densities to below even $10^{13}/cm^2$ (42).

The high surface state density in GaAs is generally considered to be due to the formation of islands of elemental As. The As is formed spontaneously by the reaction of GaAs with one of its native oxides, Ga_2O_3. The oxidation of GaAs occurs spontaneously in air, as does the subsequent evolution of surface As. Using the experimental apparatus shown in Figure 16, Offsey et al. (43) demonstrated that illumination of n- or p-type GaAs while washing the surface with a jet of 18 MΩ deionized water increased greatly the intensity of photoluminescence, which is proportional to the surface state density. The technique was used to reduce surface state density to $\sim 5x10^{11}/cm^2$. Surface state densities were measured using actual MOS devices prepared by coating the treated surface with a thin nonreactive polymeric insulator. It was speculated that the light increases the hole concentration at the GaAs surface and hence the rate of formation of As and Ga and As oxides, which are simultaneously swept away by the stream of deionized water, leaving a clean surface. The positive effect is transitory, however, as the surface gradually re-oxidizes in air. Treating the surface with sulfide has been shown recently to stabilize the surface against re-oxidation.

Woodall et al. (44) determined that photochemical oxidation of GaAs immersed in 1:1 HCl/H_2O resulted in only As surface films, about 5 nm thick, if O_2 was excluded and if the H_2O was deionized (18 MΩ); without these precautions, a mixture of As and Ga oxides was formed. The As further prevented oxide formation on the surface, and could be removed by a relatively mild heat treatment at 290°C in vacuo. The surfaces so-produced were superior to those formed by much higher temperature heat treatments in vacuo that were necessary to clean typical oxide-coated

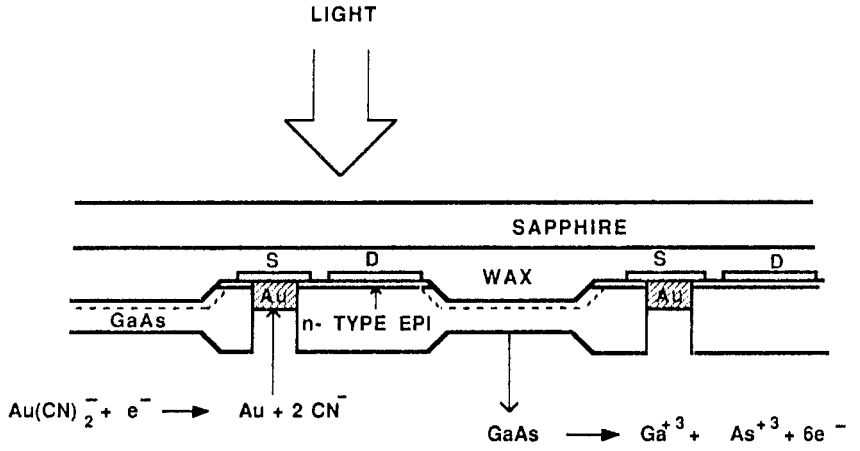

Figure 15. Schematic diagram showing photoelectrochemical deposition of Au in plasma-etched vias of a GaAs FET mounted on a sapphire substrate (after Fig. 1, ref. 39).

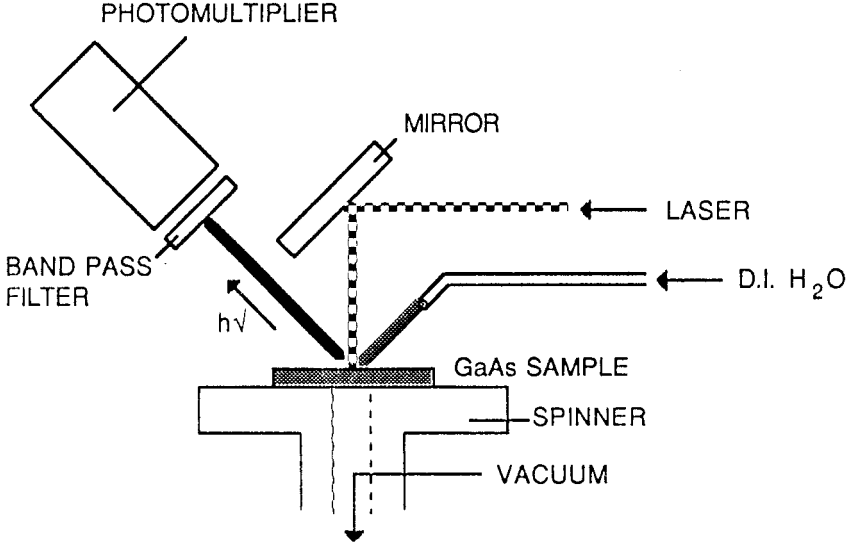

Figure 16. Apparatus for photoelectrochemical unpinning of the Fermi level in GaAs with simultaneous monitoring of the photoluminescence (after Fig. 1, ref. 44).

surfaces. The photoelectrochemical surface preparation was suggested as a precursor to molecular beam epitaxial growth onto GaAs.

6.0 CONCLUSION

The application of photoelectrochemistry to processing semiconductor materials is still at an early stage of development. Yet, numerous possibilities can be foreseen. Optical elements may now be produced in hard, thermally robust materials using simple holographic techniques that previously applied only to soft photosensitive polymers. Diffraction gratings may be produced in SiC, for example, for high efficiency in the vacuum ultraviolet or for use with high power laser sources (48). Projection photoetching of a variety of periodic structures should be feasible, such as have been proposed for beam steering, coupling and focusing in integrated electro-optics. Photoelectrochemistry has been shown to be suitable for producing extremely high aspect ratios, superior in some cases to alternative "dry" processes such as reactive ion etching. Thus, it is expected to have its place in fabrication of waveguides and vias in thick crystals, in machining of microminiature mechanical and sensor devices, and in making high surface area solar cells for enhanced light collection efficiency. The high degree of control obtainable in photoelectrochemical etching should find applications in electronics as well, e.g., in buried gate GaAs FETs which require a precisely etched channel between source and drain. Future workers in this exciting area will do well to maintain an interdisciplinary approach, since its full realization will require the expertise of electrochemists, surface scientists, solid state chemists, electrical and optical engineers.

7.0 ACKNOWLEDGEMENT

This chapter was prepared with the support of the Office of Naval Research.

8.0 REFERENCES

1. Gurevich, Y.Y. and Pleskov, Y.V., Photoelectrochemistry of Semiconductors. *Semiconductors and Semimetals* (R.K. Willardson and A.C. Beers, eds.), Vol. 19, pp. 256-328, Academic Press, New York (1983)

2. Gelchinski, M.H., Romankiw, L.T., Vigliotti, D.R. and von Gutfeld, R.J., Electrochemical and metallurgical aspects of laser-enhanced jet electroplating. *J. Electrochem. Soc.* 132: 2575-2581 (1985)

3. Haynes, R.W., Metze, G.M., Kreismanis, V.G., Eastman, L.F., Laser-photoinduced etching of semiconductors and metals. *Appl. Phys. Lett.* 37:344-346 (1980)

4. Park, S.M. and Barber, M.E., Thermodynamic stabilities of semiconductor electrodes. *J. Electroanal. Chem.* 90: 67-75 (1979)

5. Ostermayer, F.W. and Kohl, P.A., Photoelectrochemical etching of p-GaAs. *Appl. Phys. Lett.* 39:76-78 (1981)

6. Hutley, M.C., *Diffraction Gratings* Academic Press, New York (1982)

7. Ostermayer, F.W., Kohl, P.A. and Lum, R.M., Hole transport equation analysis of photoelectrochemical etching resolution. *J. Appl. Phys.* 58:4390-4396 (1985).

8. Lum, R.M., Ostermayer, F.W., Kohl, P.A., Glass, A.M., and Ballman, A.A., Improvements in the modulation amplitude of submicron gratings produced in n-InP by direct photoelectrochemical etching. *Appl. Phys. Lett.* 47:269-271 (1985)

9. Bjorkholm, J.E. and Eichner, L., Monitoring the growth of nonuniform gratings written holographically by Gaussian laser beams. *J. Appl. Phys.* 57:2402-2405 (1985)

10. Podlesnik, D.V., Gilgen, H.H., and Osgood, R.M., Deep ultraviolet induced wet etching of GaAs. *Appl. Phys. Lett.* 45:563-565 (1984)

11. Matz, R., Laser wet etching of diffraction gratings in GaAs for integrated optics. *J. Lightwave Technology* LT-4:726-729 (1986)

12. Matz, R. and Zirrgiebel, J., Fast photoelectrochemical etching of quarter-micrometer diffraction gratings in n-InP. *J. Appl. Phys.* 64:3402-3406 (1988)

13. Matz, R., Holographic photoetching of high-quality diffraction gratings in p-GaAs for distributed feedback lasers. *Mat. Res. Soc. Symp. Proc.* 75: 657-664 (1987)

14. Carrabba, M.M., Nguyen, N.M., and Rauh, R.D., Effects of doping and orientation on photoelectrochemically etched features in n-GaAs. *J. Electrochem. Soc.* 134:1855-1859 (1987)

15. Carrabba, M.M., Nguyen, N.M. and Rauh, R.D., Crystallographic effects of the photoelectrochemical etching of gratings in compound semiconductors. *Mat. Res. Soc. Symp. Proc.* 75:665-670 (1987)

16. Carrabba, N.M., Nguyen, N.M., and Rauh, R.D., Photoelectrochemical fabrication of sawtooth gratings in n-GaAs. *Applied Optics* 25:4516-4518 (1986)

17. Li, J., Carrabba, M.M. and Rauh, R.D., Morphology control of photoelectrochemically etched profiles in n-GaAs. *Extended Abstracts, Fall Meeting of the Electrochemical Society,* October 15-20 (1989)

18. Li, J.J., Carrabba, M.M., Hachey, J.P., Mathew, S., and Rauh, R.D., Photoelectrochemical etching of blazed echelle gratings in n-GaAs. *J. Electrochem. Soc.* 135: 3171-3172 (1988)

19. Cummings, K.D., Harriott, L.R., Chi, G.C., and Ostermayer, F.W., Using focused ion beam damage patterns to photoelectrochemically etch features in III-V materials. *Appl. Phys. Lett.* 48:659-661 (1986)

20. Lax, M., Temperature rise caused by a focused laser beam. *J. Appl. Phys.* 48:3919-3923 (1977)

21. Osgood, R.M., Sanchez-Rubio, A., Ehrlich, D.J., and Daneu, V., Localized laser etching of compound semiconductors in aqueous solution. *Appl. Phys. Lett.* 40:391-393 (1982)

22. Podlesnik, D.V., Gilgen, H.H., Willner, A.E., and Osgood, R.M., Interaction of deep-ultraviolet laser light with GaAs surfaces in aqueous

solution. *J. Op. Soc. Am.* B 3:775-784 (1986)

23. Prucnal, P.R., Fossum, E.R. and Osgood, R.M., Integrated fiber optic coupler for very large scale integration interconnects. *Optics Letters* 11:109-111 (1986)

24. Rauh, R.D. and LeLievre, R.A., Microphotoelectrochemical etching of n-GaAs using a scanned focused laser. *J. Electrochem. Soc.* 132:2811-2812 (1985)

25. Lubzens, D., Photoetching of InP mesas for production of mm wave transferred electron oscillators. *Electron. Lett.* 13: 171-172 (1977)

26. Chi, G.C., Ostermayer, K.D., Cummings, K.D. and Harriott, L.R., Ion beam damage-induced masking for photoelectrochemical etching of III-V semiconductors. *J. Appl. Phys.* 60:4012-4014 (1986)

27. Forrest, S.R., Kohl, P.A., Panock, R., DeWinter, J.C., Nahory, R.E. and Yanowski, E., A long-wavelength annular InGaAs pin photodetector. *IEEE Electron. Dev. Lett.* EDL-3415:415-417 (1982)

28. Ostermayer, F.W., Kohl, P.A. and Burton, R.H., Photoelectrochemical etching of integral lenses on InGaAsP/InP light-emitting diodes. *Appl. Phys. Lett.* 43:642-644 (1983)

29. Cheng, J. and Kohl, P.A., The resolution of photoelectrochemically etched features. *Mat. Res. Soc. Symp. Proc.* 29:127-132 (1984)

30. Lin, C.W., Fan, F.F. and Bard, A.J., High resolution photoelectrochemical etching of n-GaAs with the scanning electrochemical and tunneling microscope. *J. Electrochem. Soc.* 134:1038-1039 (1987)

31. Haisty, R.W., Photoetching and plating of GaAs. *J. Electrochem. Soc.* 108:790-794 (1961)

32. Rose, T.L., Micheels, R.H., Longendorfer, D.H. and Rauh, R.D., Photoelectrochemical deposition of metal patterns on semiconductors. *Mat. Res. Soc. Symp. Proc.* 17:265-272 (1983)

33. Micheels, R.H., Darrow, A.D. and Rauh, R.D., Photoelectrochemical deposition of microscopic metal film patterns on Si and GaAs. *Appl. Phys. Lett.* 39:418-420 (1981)

34. Kelly, J.J., Rikken, J.M.G., Jacobs, J.W.M. and Vaister, A., Photocathodic deposition of gold alloys for ohmic contacts to III-V materials. *J. Vac. Sci. Technol.* B6:48-52 (1988)

35. Jacobs, J.W.M. and Rikken, J.M.G., Oxygen-diffusion size effect in electroless metal deposition. *J. Electrochem. Soc.* 135:2822-2827 (1988)

36. Inoue, T., Fujishima, A. and Honda, K., Photoelectrochemical imaging processes using semiconductor electrodes. *Chem. Lett.* 1978:1197-1200 (1978)

37. Okano, M., Kikuchi, E., Itoh, K. and Fujishima, A., Photoelectrochemical polymerization of pyrrole on ZnO and its application to conducting pattern generation. *J. Electrochem. Soc.* 135:1641-1645,(1988)

38. Silverman, S.J. and Benn, D.R., Junction delineation in silicon by gold chemiplating. *J. Electrochem. Soc.* 105:170-173 (1958)

39. Kohl, P.A., D'Asaro, L.A., Wolowodiuk, C. and Ostermayer, F.W., Photoelectrochemical plating of via GaAs FET's. *IEEE Electron. Dev. Lett.* EDL-57:7-9 (1984)

40. Rose, T.L., Longendorfer, D.H. and Rauh, R.D., Photoelectrochemical deposition of metals onto p-silicon using an internal cell. *Appl. Phys. Lett.* 42:193-195 (1983)

41. Stremsdoerfer, G., Martin, J.R., Garrigues, M. and Perossier, J.L., Localized photoactivation with Pd of p-InP previous to an electroless gold plating. *J. Electrochem. Soc.* 133:851-852 (1986)

42. Robinson, A.L., Chemical coat helps semiconductor prospects. *Science* 238: 27-29 (1987)

43. Offsey, S. D., Woodall, J.M., Warren, A.C., Kirchner, P.D., Chappell, T.I. and Pettit, G.D., Unpinned (100) GaAs surfaces in air using photochemistry. *Appl. Phys. Lett.* 48: 475-477 (1986)

44. Woodall, J.M., Oelhafen, P., Jackson, T.N., Freeouf, J.L. and Pettit, G.D., Photoelectrochemical passivation of GaAs surfaces. *J. Vac. Sci. Technol.* B1:795-798 (1983)

45. Podlesnik, D.V., Gilgen, H.H. and Osgood, R.M., Maskless, chemical etching of submicrometer gratings in single crystalline GaAs. *Appl. Phys. Lett.* 43: 1083-1085 (1983)

46. Kohl, P.A., Wolowodiuk, C. and Ostermayer, F.W. Jr., The photoelectrochemical oxidation of (100), (110), and (111) n-InP and n-GaAs. *J. Electrochem. Soc.* 130: 2288 (1983)

47. Dalisa, A.A., Zwicker, W.K., DeBitetto,D.J. and Harnack, P., Photoanodic engraving of holograms on silicon. *Appl. Phys. Letters* 17: 208-210 (1970)

48. Rauh, R.D. and Carrabba, M.M., Photoelectrochemical fabrication of gratings in silicon carbide. *Extended Abstracts, Fall Meeting of the Electrochemical Society,* October 15-20 (1989)

5

PHOTOELECTROCHEMICAL CHARACTERIZATION

Micha Tomkiewicz

1.0 INTRODUCTION

This chapter will cover possible applications of liquid junctions in "noncontact" characterization of semiconductor electronic devices. Wherever possible, we use examples from characterization of materials that play a central role in the electronic industry, primarily Si and GaAs. Review articles that focus on non-solar applications of semiconductor-liquid junctions (1) and on experimental techniques for the study of such junctions (2) were recently published. Conceptually, liquid junctions are well suited for semiconductor characterization, since they have almost "contactless" junctions and are most adaptable for on-line characterization. Nevertheless, they have yet to significantly penetrate the electronics industry. One reason is an apparent reluctance of the solid-state community to get involved with "wet chemistry". Even the widespread use of "wet" etching is now being replaced by "dry" Reactive Ion Etching (RIE) (3). Another reason for slow acceptance is that liquid junctions are perceived as more complex than their solid counterpart. Some aspects of this complexity are real and involve problems of corrosion and chemisorption that do not have a solid-state counterpart. However, much of the perceived complexity reflects a traditional oversimplification of the solid state junctions as abrupt junction devices. The simplest solid state contact, Schottky barriers, are rich in uncontrollable chemistry during contact formation (4) and only recently are attempts being made to control this chemistry either through the use of liquid junctions (5) or through submonolayer metal deposition under vacuum (4).

The science of semiconductor-liquid junctions has its roots in the

same work as that of solid state junctions (6)(7). However, the explosive development of solid state devices, reflecting the growth in the volume and diversity of their practical applications, has left their liquid junction counterparts far behind.

Renewed interest in semiconductor-liquid junctions started to emerge after it was demonstrated that a device based on partially reduced TiO_2 in contact with an aqueous electrolyte can sensitize photoelectrolysis of water (8). Immediately following that work, the need to find alternative fuel sources rekindled interest in solar energy. As a result, the study of energy conversion at semiconductor-liquid junctions grew to form almost a separate discipline that was named "photoelectrochemistry."

Before liquid-junctions can enter in force as an alternative junction technique to MOS and Schottky barriers for the characterization of semiconductors, a careful delineation of parameters that are independent of the nature of the junction will have to be compiled. To accomplish this, more fundamental work has to be done in comparative studies of the potential distribution under different junction configurations (9).

While liquid-junction devices cannot yet compete with solid-state devices, stable photovoltaic liquid junctions devices can be made with conversion efficiencies in the 12 - 15% range (10)(11). Furthermore, some niche applications are already emerging. Prominent among these applications are the etching and photoetching of semiconductors (12)(13). At present, probably the broadest application of liquid junctions is for characterizing semiconductor surfaces: an electrolyte provides a convenient, reversible, junction medium in which the interfacial chemistry can be modified and the transport and optical properties can be monitored in a nondestructive way. Excellent examples of such applications can be found in the literature. Lewis et al. (5) have used liquid junctions to probe the origin of Fermi level pinning at metal junctions with Si and GaAs. Similarly, Morrison et al. (14) have used liquid junctions to investigate the effects of dislocation loops on Si, on the transport properties. They compared transport parameters, in averaged and scanned modes, in both liquid junction and MOS devices, as a function of the surface treatment that produces the dislocations.

Photoelectrochemistry is still an emerging discipline in that it is not yet possible to write this chapter in the form of a tutorial in which one can give a series of steps and techniques that, once applied to a given system, results in a "complete" understanding of the system in terms of structure, mechanism and kinetics. There is no single semiconductor/electrolyte system of which our understanding is sufficient for its predictive power to provide any degree of satisfaction. A few systems such as Si and InP come close.

Per definition, semiconductor/liquid junctions act as a focal point for

convergence of interdisciplinary methodologies of inquiry. Characterization techniques are no exception. Almost every technique applied in electrochemistry and solid state physics has found its way into photoelectrochemistry. The scope of these techniques is too broad for any attempt to cover them in a single chapter. We will exclude all the techniques that primarily probe the semiconductor in an ex situ configuration; this will include all the high vacuum surface spectroscopies and the ion beam techniques. This is done in spite of recent progress in adapting many of these techniques for "almost" in situ configuration by applying sophisticated cell construction and transfer techniques (15). If one includes the fundamental principles and recent relevant work, almost every technique that will be mentioned in this chapter deserves a chapter, if not an entire book, for a comprehensive exposure. This review will not cover all available references, and we apologize for the omissions. It will be somewhat tilted to our own work and priorities that recently focused on the possible applications of some of these techniques for process characterization in the electronics industry.

The chapter is organized as follows: We begin by discussing the response of photoelectrodes to d.c. perturbation, focusing first on current-voltage behavior of static and rotating electrodes and the applications of various spectroscopic techniques. Next, we discuss responses to a.c. modulated electric fields, covering impedance, photocapacitance and optical/spectroscopic techniques. The third area of focus is on time-resolved techniques, in which short lived transient responses are considered. Finally, brief mention is made of photothermal methods and of topographical studies.

2.0 DIRECT RESPONSE

Figure 1 shows the combined energy diagrams of n-Si (100) in liquid junction under short circuit conditions (16a). The electrolyte is a methanolic solution of ferrocene/ferrocinium with $LiClO_4$ as the supporting electrolyte. The data for the energy diagrams were taken from impedance spectroscopy, current-voltage measurements and electroreflectance, details of which will follow. The electrolyte here is one of the simplest since it was demonstrated that Si is not corroding in the electrolyte and the ferrocene is an outer sphere complex that, at least over a limited potential range, is not absorbed on the surface of the electrode. Yet, in spite of this, the complexity of the potential distribution at the solid-liquid interface, is evident. One can compare this complexity with the relative simplicity of the potential distribution of a Ti Schottky structure made with material with similar characteristics (16e). In both cases a small fraction of a monolayer

is covered with surface states. These states tail from the conduction band in the metal junction while they are more isolated in the liquid junction. In addition, in the liquid junction, even after HF etching, a thin layer of a porous oxide is observed. In the solid junction, the Fermi level is not pinned until it reaches the position of the surface states, while in the liquid junction case, the Fermi level is pinned at reverse bias probably due to surface accumulation of minority carriers, and then it gets pinned again (or the band edges unpinned) due to charging of the surface states. The filled surface states also catalyze precipitation of nearly a monolayer of the electrolyte.

2.1 Current-Voltage

Figure 2 shows the current-voltage characteristics of the cell for which the energy level diagram was shown in Fig. 1 (16a). The figure shows current-voltage characteristics of the semiconductor in a three electrode configuration: one electrode (Pt) serves as a counter electrode and the third electrode serves as a reference electrode. The potentials are given against the solution potential. The photocurrent was measured with a low frequency chopped light source (using a hand as a shutter) such that one can observe the light induced current and the dark current on the same chart. One also can see that the most negative potential (for n-type materials), in which light induced charge separation starts, is around -0.6 volt. This potential is usually a rough estimate of the position of the flat band potential. In addition, one can observe the irreversible reduction in the dark of the electrolyte, shown also in the energy diagram. This information, combined with knowledge of the band gap, flat band potential, doping level, interface states and presence or absence of an interfacial layer, is essential for construction of a band diagram such as the one presented in Fig. 1. Such a diagram serves as a starting point in understanding the semiconductor-electrolyte interface and in the interpretation of the results from the dielectric techniques that will be described below.

2.2 Rotating Ring Disc Electrodes

In a typical experiment with semiconductor-liquid junctions, one of the most important experimental problems is the differentiation between reactions that involve chemical changes at the semiconductor electrode (corrosion with insoluble products) and chemical changes in the electrolyte that might be subject to mass transfer limitations. The technique of Rotating Ring Disc Electrode (RRDE) (17-19) provides an opportunity to differentiate between these two types of reactions under controlled hydrodynamic conditions. In its simplest form, the metallic ring is isolated

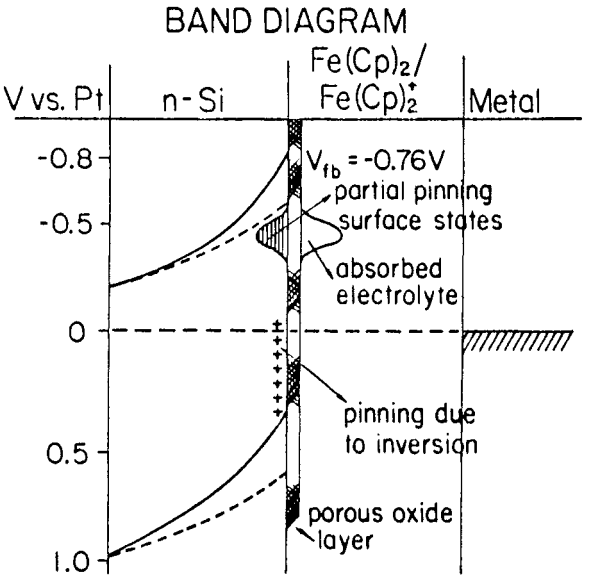

Figure 1. The proposed band structure diagram of the Si/methanol that is described in the text (16a).

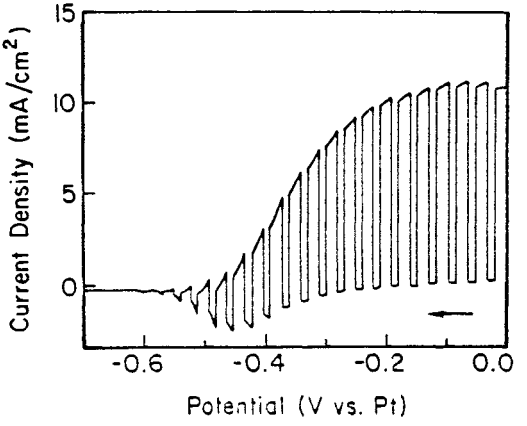

Figure 2. Current-potential response with chopped white light for unetched <100> n-Si in methanolic solution of oxidize and reduced dimethylferrocene in the following concentrations: 0.2 M $FeCp_2$, 1 mM $FeCp_2^+$ and 1 M $LiClO_4$ supporting electrolyte under nitrogen atmosphere. Tungsten Halogen ELH lamp with light intensity at the electrode surface of 100 mW/cm². Sweep rate: 10 mV/sec (16a).

from the semiconductor disc. Both rotate at a certain angular frequency. The voltammogram of the disc is similar to the one we have previously described. The metallic ring is kept at a potential characteristic of one of the anticipated reaction products. The ring current, at this potential, is being monitored simultaneously with the disc voltammogram. The procedure can be repeated with other products to provide sufficient information for construction of a unique reaction mechanism.

2.3 Absorption, Reflection and Photoluminescence Spectroscopies

These techniques are covered in standard text books (20), review articles (21) and books (22) dedicated to the individual techniques. The subject of applications of any of these techniques in the study of properties of semiconductors is too broad to be covered here. We will just provide a short outline focused on specific applications for study of liquid-junction devices.

The use of direct absorption spectroscopy, with photon energies above the band gap, for study of liquid junction devices is limited due to the special requirements of thin, optically transparent, crystals. Electric field modulated absorption was reported (23). Reflection spectroscopy is of wider use but its application is also limited, primarily due to advances in techniques such as Electrolyte Electroreflectance, Photoreflectance and Ellipsometry which will be described later, techniques that can provide the same information and offer higher spectral sensitivity and higher surface sensitivity. Nevertheless rotating light-pipe reflectivity (RLPR) studies were used for in situ study of the growth of anodic oxide films on GaAs (24). One can greatly increase the sensitivity of reflection studies to interfacial phenomena by employing subband gap irradiation and by giving the crystal a shape that allows multiple internal reflection (25). An example of the applications of this technique in detecting surface states on cleaved Ge and Si can be found in Ref. 26. The technique was also applied in the presence of an electrolyte (27). The sensitivity of this technique to the interface can also be greatly improved by modulation of the electric field and will be described in the section that describes modulation techniques.

Among the direct optical spectroscopic techniques, photoluminescence is probably the most widely used in both in situ and ex situ configurations. Since, as with many other techniques, the temperature window in which one can measure in the in situ configuration is limited, one can usually find in the literature comparative studies between in situ and ex situ conditions. A short review article relevant to applications in liquid junction devices was written by Ellis (28). The technique also can

be applied in an electric field modulated form and in the time-resolve form that will be addressed later. In addition to its utility as a characterization tool that provides information on the electronic states involved in emissive transitions and the kinetics of excited state processes, photoluminescence can be used as an in situ diagnostic tool to monitor effects of etching (29), aging of photoelectrochemical devices (30) and much more. An interesting application being pursued recently is the ability of photoluminescence to provide information on the distribution of electric field at the interface. This is based on the assumption that the electric field in the space-charge layer provides a strong enough driving force to separate the electron-hole pair, thus preventing them from radiative recombination. This gives rise to a "dead layer" in which the luminescence is totally quenched. Often the "dead layer" coincides with the space charge layer (31)(32). Under these conditions the intensity of the PL signal will be given by:

Eq. (1) $$I_f = \Phi I_a \exp(-\alpha d)$$

where Φ is the quantum efficiency, α the absorption coefficient, d the thickness of the "dead layer" and I_a the intensity of the incident irradiation. If d is associated with the thickness of the space-charge layer, it will change with the electrode potential according to:

Eq. (2) $$d \sim [(2K\epsilon/eN_d)(U - U_{fb} - kT/e)]^{1/2}$$

where ϵ is the permittivity of free space, K is the relative dielectric constant, e the electronic charge, N_d the effective dopant concentration, k the Boltzman constant, T the absolute temperature, U the electrode potential and U_{fb} the flat band potential. Application of these equations to the potential dependence of the PL intensity should provide information on the flat band potential and the doping level. This was demonstrated on a number of systems.

A variant of photoluminescence that in some cases requires the presence of a liquid junction is electroluminescence (EL) (28). In this case, the luminescence is not induced by optical excitation but by charge-transfer processes. The most widely used electrolyte for this purpose is alkaline peroxydisulfate (33) in which the $S_2O_8^{2-}$ ions are reduced by the conduction band electrons of an n-type semiconductor to yield the highly oxidizing sulfate radical anions that can inject a hole into the valence band. Recombination of an electron with the injected hole yields the luminescence. This process is much more localized to the surface as compared with photoluminescence. Comparison between the two can

yield valuable information about location and energetics of traps localized near the interface (31). Under strong reverse-bias conditions, electroluminescence due to avalanche breakdown was also observed (34).

2.4 Ellipsometry

Ellipsometry is a reflectance method in which the change of the state of polarization upon reflection is determined. This change is described in terms of two ellipsometric angles Δ and Ψ given by:

Eq. (3) $$\Delta = (\delta_{||}^{r} - \delta_{||}^{i}) - (\delta_{\perp}^{r} - \delta_{\perp}^{i}), \text{ and}$$

Eq. (4) $$\Psi = \tan (A_{||}^{r} A_{\perp}^{i} / A_{||}^{i} A_{\perp}^{r})$$

where δ and A are the phase and amplitude of the parallel and perpendicular components of the electric field of the incident (i) and reflected (r) beams. One can show that these angles can be correlated with the real and imaginary parts of the dielectric constant of the reflecting medium. In this form the results are analogous to other dielectric techniques such as impedance with its model sensitive interpretation. The advantage of this technique is the high sensitivity to the surface. Spectroscopic ellipsometry (35) takes out much of the guesswork, at least concerning the chemical composition of the surface. One can analyze the data in terms of energy dependence of the dielectric constant and compare the results with electroreflectance. The results of such a study were interpreted in terms of extension of the low field theory of electroreflectance to include interactions of the modulating electric field with defects (36). The technique is widely used for in situ characterization of surface modifications either through adsorption or under electrochemical conditions in a liquid junction environment (37-40).

3.0 ELECTRIC FIELD MODULATION OF SYSTEM'S RESPONSE

These techniques are based on the sensitivity of the system's response to the electric field. Since the electric field is localized at the interface, phase sensitive detection of the component that is modulated by the electric field can differentiate between interfacial response and bulk response.

3.1 Impedance

The system's response here is the dark current. Excellent recent reviews on impedance spectroscopy, that cover also many aspects of semiconductor-liquid interfaces, are available (41)(42). Details about the instrumental setups can be found there. In principle, if the frequency range is broad enough, the technique is sensitive to all the charge accumulation modes and to the charge transport kinetics and mechanism. The difficulty, as with most of the dielectric techniques, is to establish the uniqueness of the proposed model for the interface. The most heavily used practice is to measure the "capacitance" or the "conductance" at a fixed frequency and to deduce the physics from the voltage or temperature dependence. The next degree of complexity is found when the real and/or the imaginary part of the impedance are measured over a wide frequency regime, an equivalent circuit is proposed and the physical nature of the elements in the equivalent circuit are determined from their dependence on external parameters such as voltage, temperature, electrolyte, etc. Alternatively one can model the interface as a capacitor with a composite dielectric and apply some form of an effective medium model to characterize the interface (43). Another widely used practice, particularly among electrochemists, is to measure the impedance in a voltage regime in which charge transfer takes place, propose a mechanism, solve the kinetic equations in terms of frequency dispersion of the impedance and get the kinetic parameters from the fit to the experimental results (41). The main difficulty in all these schemes is the necessity to show the uniqueness of the original assumption, be it the equivalent circuit, the form of the effective medium theory or the proposed charge transfer mechanism. The technique described here attempts to satisfy this requirement by analyzing the data in terms of a generalized equivalent circuits, the details of which emerge from the analysis. Figure 3 shows a generalized equivalent circuit for a simple case where one measures the impedance of a single dielectric (abrupt junction between a semiconductor and a metal or a concentrated electrolyte). C_{sc} is usually the capacitance due to the space charge layer, assumed to be the fastest relaxing element. C_i and $\tau_i = C_i R_i$ are the capacitances, and their corresponding relaxation times, of charge accumulation modes such as various surface states, minority carriers and bulk states. Z_d is a generalized CPA (Constant Phase Angle) element given by:

Eq. (5) $$Z_d = N(1 + J\omega\tau)^{-n}$$

where ω is the angular frequency and N, τ and n are parameters. R_s is the series resistance and R_p is the shunt resistance.

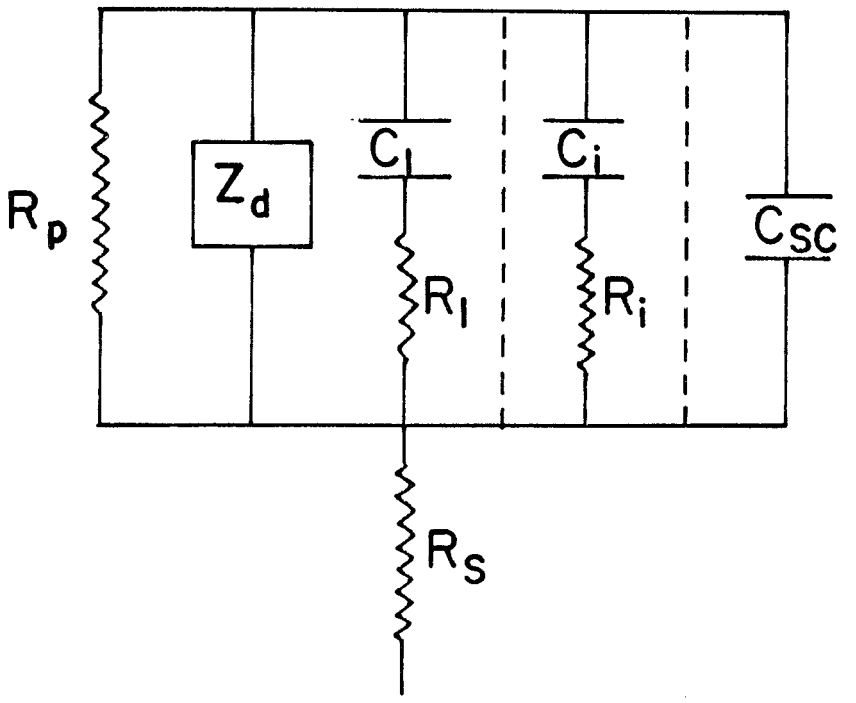

Figure 3. The generalized equivalent circuit of a single interface. R_p is the resistance associated with the Faradaic current flow, Z_d is a generalized impedance associated with disorder either in the structure or in the dynamics (diffusion), C_i and R_i are associated with parallel charge accumulation modes with different relaxation times than the majority carriers such as surface states or minority carriers, C_{sc} is the space charge capacitance and R_s is the series resistance (16a).

The inclusion of Z_d extends the previously reported procedure of Relaxation Spectrum Analysis (44). Z_d in this form can include contributions from static disorder such as porosity (45), random mixture of conductor and insulator that can be described by the effective medium approximation at percolation (46), or an interface that can be described by a fractal geometry (47). It can also include contributions from dynamic disorder such as diffusion. To provide one specific example: if Z_d originates from diffusion capacitance in the semiconductor, then τ is the minority carriers' diffusion time, n = 0.5 and

Eq. (6) $$N = (kT/q)(L_p/qD_pP_{n0})\exp(-qV_0/kT)$$ (see Ref. 48)

where T is the temperature, k the Boltzmann constant, q the electronic charge, L_p the minority carriers' diffusion length, D_p their diffusion coefficient, P_{n0} their concentration in the bulk and V_0 is the forward bias. As with all the other elements, the origin for this contribution can be determined by the voltage and the temperature dependence.

If one subtracts the frequency-independent, high frequency resistance

Eq. (7) $$Z' = Z - R_s$$

and calculates the resulting admittance, it is easy to show that:

Eq. (8) $$\frac{1}{Z'} = \frac{1}{R_p} + J\omega C_{sc} + \omega^2 \sum_i \frac{C_i \tau_i}{1 + \omega^2\tau_i^2} + J\omega \sum_i \frac{C_i}{1 + \omega^2\tau_i^2} + N^{-1}(1 + \omega^2\tau_i^2)^{n/2}(\cos n\theta + J\sin n\theta)$$

where $\tan\theta = \tau$. For $\tau >> 1$, Eq. 8 can be viewed as superposition of a constant term, linear term, power law term and superposition of Lorentzian terms with respect to the frequency. If the separation between the time constants is large enough one can isolate the respective terms and obtain all the parameters directly. The contributions of the parallel RC elements can be most conveniently obtained through the following two functions:

Eq. (9a) $$\frac{Gss}{\omega} = \omega \sum_i \frac{C_i \tau_i}{1 + \omega^2\tau_i^2}$$

Eq. (9b) $$Bss = \omega \sum_i \frac{C_i}{1 + \omega^2\tau_i^2}$$

Bss is sensitive to the fast relaxing elements and Gss to the slow elements. If the separation between the time constants is large enough one can isolate the respective terms and obtain all the parameters directly. If it is not large enough and/or the system cannot be represented in terms of a simple abrupt junction due to film formation, multiple junction etc., some data fitting will be necessary. In the latter case, a degree of confidence is obtained by fitting the real or imaginary component and checking it against the other component. The uniqueness of the interpretation is then checked against other techniques that provide complementary information. Figure 4 illustrates the impedance spectra of n-Si in contact with the methanolic solution (a) for which the band diagram was presented in Fig. 1 (16a), (b) n-Si/Ti Schottky structure (16e), and (c) n-Si MOS device (16e), together with the equivalent circuits and the corresponding calculated spectra. The equivalent circuits of the solid-state devices are as expected from ideal structures. The equivalent circuit of the liquid junction is much more complicated (16a). Z_d is due to a porous oxide layer that can be almost completely removed by HF etching. R_H and C_H are due to absorption of the electrolyte at potentials negative to the surface states. Figures 5(a) and (b) depict the Mott-Schottky plots (49)(50) of the fastest relaxing element, the space charge layer capacitance C_{sc}, for the HF-etched Si and for the unetched one, in the liquid junction configuration. The flat band potentials, obtained from the intercept, are -0.76 volt vs. Pt for the HF-etched sample, and -0.86 volt vs. Pt for the unetched one. The doping levels, obtained from the slopes, yielded $4.7 \times 10^{15}/cm^3$ for the etched sample and $2.2 \times 10^{15}/cm^3$ for the unetched sample. The apparent difference in the doping level is due to the increase in roughness due to etching. The pinning of the Fermi level around -0.4 volt vs. Pt can be easily observed.

Figure 6 shows a typical Gss/ω and Bss spectra of n-InSe electrode in iodide solution (51), from which two surface state elements were assigned, with relaxation times of 1 ms. and 10 ms., respectively. An example of the dependence of the surface state capacitances on the electrode potential, is shown in Fig 7. The data were fitted to a Gaussian distribution of surface states (52). For the fast surface state, the distribution is centered around -0.23 volt (vs. Pt) with area density of $1.05 \times 10^{13}/cm^2$ and width of 0.11 eV. For the slow surface state, the distribution is centered around -0.21 volt (vs. Pt) with area density of $3.12 \times 10^{13}/cm^2$ and width of 0.13 eV. If we take $10^{15}/cm^2$ as typical density for a monolayer, both states occupy a small fraction of a monolayer. Similar analysis of the impedance data was done on other semiconductor/electrolyte systems that include TiO_2, CdSe, $CuIn_2Se_3$ etc.

An interesting variance of impedance spectroscopy is the time domain spectroscopy (53) in which a voltage function (a Heavyside function, for example) is sent along a line of fixed constant impedance. At

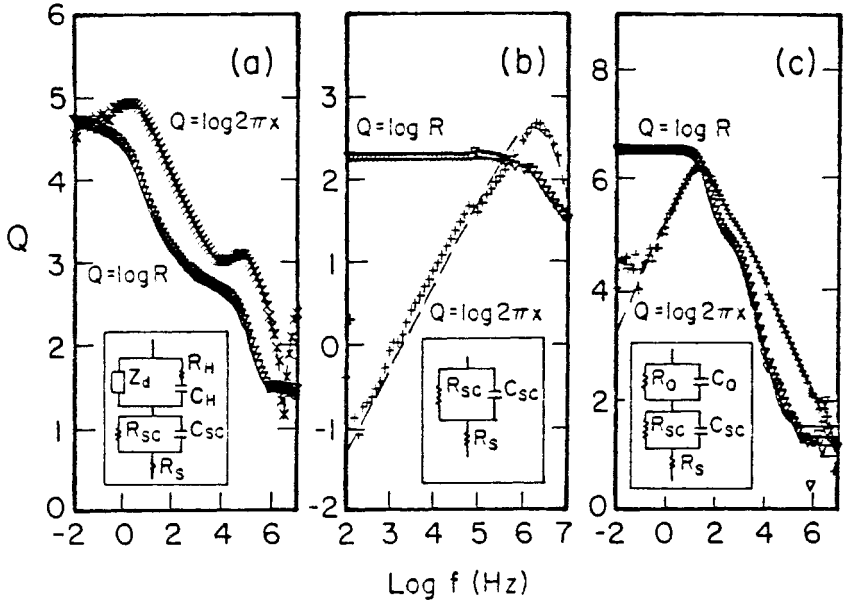

Figure 4. Impedance response curves for n-Si in three different junctions: a. HF etched n-Si in a methanolic solution of oxidized and reduced dimethylferrocene in the following concentrations: 0.2 M $FeCp_2$, 1 mM $FeCp_2^+$ and 1 M $LiClO_4$ supporting electrolyte under nitrogen atmosphere. Potential: 0.2 volt vs. Pt; b. Ti/Schottky-Barrier at 0 volt; c. Ti/MOS device at -0.5 volt. Symbols: experimental data for the real and imaginary parts of the impedance. Solid lines: numerical fits to the equivalent circuit shown in the inserts (16a and 16e).

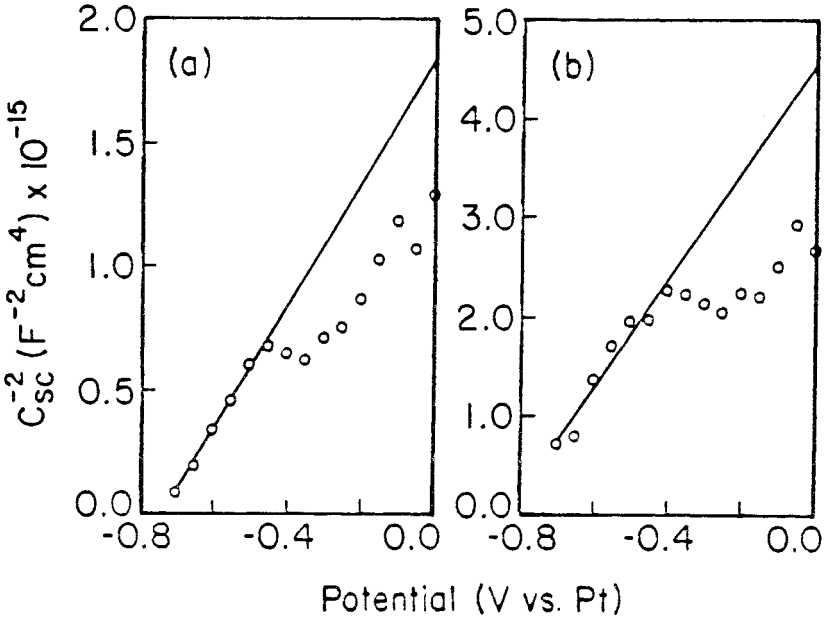

Figure 5. Mott-Schottky plots of n-Si in the methanolic Solution described in Fig. 2(a). (a) HF etched sample. V_{fb} = -0.76 volt vs. Pt and N_d = 4.7x10^{15}/ cm^3. (b) original sample. V_{fb} = -0.86 volt vs. Pt, N_d = 2.2x10^{15}/cm^3 (16a).

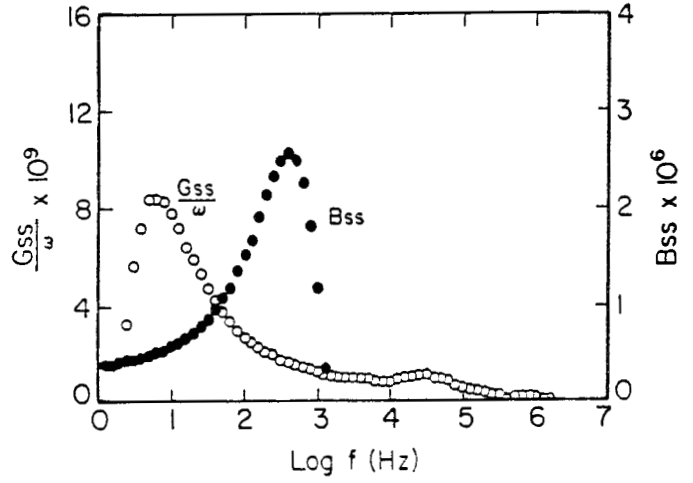

Figure 6. Gss/ω and Bss spectra of n-InSe in the electrolyte: 1 M KI/ 0.05 M I_2/2 M H_2SO_4, electrode potential: 0 volt vs Pt. The capacitive and resistive elements of the surface states are evaluated from the amplitude and the position of the peaks (51).

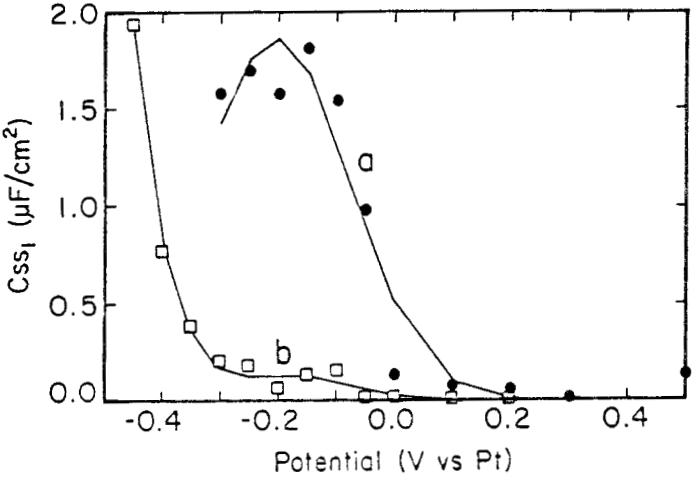

Figure 7. Variation of Css_1 of the slow surface states, with electrode potential for (a) n-InSe and (b) modified InSe. The solid lines are theoretical fits to Gaussian line shapes (51).

the point of intersection between this impedance line and a different impedance (the electrochemical cell) part of the original voltage function is reflected back along the line and provides information about the encountered impedance. The promised advantage of this technique is its high speed. In principle the technique should provide the same information as the frequency domain analog.

3.2 Photocapacitance

Under this heading one can include all the techniques that use impedance spectroscopy under illumination. With band gap illumination one has the usual difficulty of a unique interpretation, particularly the need to separate the light-induced kinetic effects from changes in the light induced "equilibrium" potential distribution. Nevertheless routine analysis of the high frequency capacitance in terms of the Mott-Schottky relation was interpreted in terms of light induced shift in the flat band potential and/or change in the dopant distribution (54). A technique that does not suffer from these difficulties is the photocapacitance or its liquid junction version Electrochemical Photocapacitance (EPS) (55). In EPS, the capacitance of a reversed biased semiconductor electrode is measured as a function of the wavelength of incident sub-band gap illumination. It is assumed that the origin of the capacitance signal (imaginary part of the impedance) is the space-charge layer and that the sub-band gap illumination is absorbed by the deep traps and interface states and induce exchange of charge with the space-charge layer that results in capacitance changes. Typical plots of capacitance vs. wavelength yield a series of plateaus and/or peaks that correspond to population/depopulation of band gap states. The results usually complement those obtained using Deep Level Transient Spectroscopy (DLTS) (56). Since, as a rule, the available temperature window in liquid junction devices is very narrow, EPS is much more suitable than DLTS for evaluation of deep traps in these devices.

3.3 Optical Techniques

A cost effective experimental setup for optical modulation experiments, recently built in our laboratory, is shown in Fig. 8 (57). Similar setup was recently reported by Tian et al. (58). Experiments performed with this system include: photoreflectance (PR), electrolyte electroreflectance (EER), surface photovoltage spectroscopy (SPV), 1st. and 2nd. harmonics photoinduced current-voltage characteristics, spectral response and d.c. current-voltage characteristics. One can switch electronically between experiments and perform any number of techniques without moving the cell or removing the electrode from the electrolyte. A variable neutral

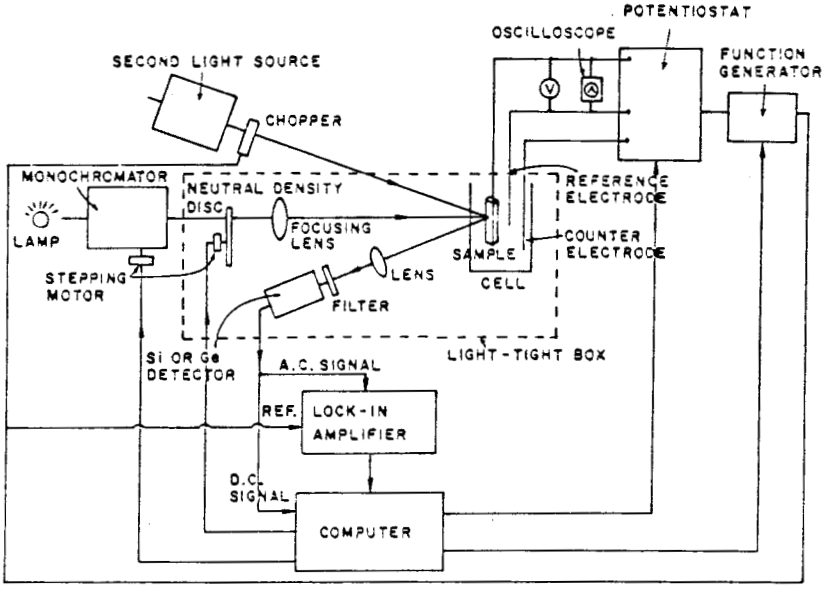

Figure 8. The experimental arrangement of the modulation spectroscopy workstation (16b).

density filter, placed between the monochromator and the sample, is adjusted by a computer controlled motor to fit the requirements of each experiment. For EER and PR experiments the filter is adjusted to keep the d.c. reflectivity constant. For SPV experiments the filter is adjusted to keep the open circuit voltage constant, and for spectral response the filter is adjusted to keep the intensity of the probe beam constant enabling direct measurements of unnormalized quantum efficiencies.

Electroreflectance. The system's response here is the surface reflectivity. The technique is based on modulating the reflectivity of the semiconductor with low frequency bias voltage across the device. If the junction is being formed with an electrolyte, the technique becomes known as Electrolyte Electroreflectance (EER). Excellent review articles cover the applications of this technique for analysis of optical properties of semiconductors and in the determination of the potential distribution across the interface of a solid or a liquid junction (59).

Often one can work within a theoretical framework known as the "low field regime" (60). If one includes the possibility that the Fermi level is pinned at the surface (61), then the ratio between the modulated reflectance (ΔR) and the reflectivity (R) is given by:

$$\text{Eq. (10)} \qquad \Delta R/R = -(2eN_d/\epsilon)\,[1 - (e/C_h)(dN_{ss}/dV)] \bullet \Delta V \bullet L(E)$$

where e is the electronic charge, E the energy, N_d the doping level, ϵ the dielectric constant, C_h the capacitance of the Helmholtz layer (that corresponds to the entire surface covered with states that can be charged and discharged upon modulation of the surface potential), N_{ss} is the density of the surface states, ΔV is the amplitude of the modulating voltage and L(E) is a spectral line-shape function given by:

$$\text{Eq. (11)} \qquad L(E) = \mathrm{Re}[C(E - E_g + i\Gamma)^{-n} \exp(i\theta)]$$

where C and θ are amplitude and phase factors, n is a number characteristic of the interband critical point, E_g is the energy gap and Γ is a broadening parameter related to the lifetime of the majority carriers.

From analysis of the spectral line-shape one can get information about the optical properties through evaluation of n and E_g and about properties of the majority carriers, hence presence of defects that act as scattering centers, through evaluation of θ and Γ.

From analysis of the variations of the spectral amplitude with the d.c. bias voltage and the modulation amplitude (Eq. 10), one can obtain a measure of the flat band voltage that directly relates to the properties of the surface and serves as a reference point in any attempt to understand

the distribution of the electric field at the interface. One also can obtain the doping level through evaluation of N_d and actively trace the shifts of the Fermi level with the applied bias. When $(e/C_h)dN_{ss}/dV = 1$, the Fermi level is completely pinned, all the potential drop is at the surface and the electroreflectance signal reduces to zero. If, on the other hand, $dN_{ss}/dV = 0$ either because there are no surface states or because their energy is such that they do not charge and discharge as the surface potential is changed, all the potential drop falls on the space-charge layer, the junction behaves as an abrupt junction and the electroreflectance signal is independent of the d.c. bias. From the quantitative evaluation of the functional dependence of the spectral amplitude with the d.c. bias, the density and energy of the surface states responsible for the pinning of the Fermi level can be obtained (61). An example, seen in Fig. 9, was taken from the dependence of the E_1 transition of Si in the methanolic solution, previously discussed (16a). The flat band can be seen at the potential in which the signal inverts sign and two potentials ranges can be seen in which the Fermi level is pinned: one narrow range around -0.4 volt vs. Pt. due the surface states mentioned before, and another one at potentials positive to -0.2 volt vs. Pt, probably due to accumulation of minority carriers at the surface. Recently it was demonstrated that one can determine the potential distribution under illumination by performing the experiments with a second light source (62).

The power of the technique can be appreciated if one considers that in a multicomponent system one can obtain the electric field distribution, with all its implications, for each component, if the spectral transitions can be resolved.

Photoreflectance. This technique is almost identical to electroreflectance except that the electric field is not modulated by changing the bias voltage across the device, but instead, the system is irradiated with a second light source that induces a photovoltage between the surface and the bulk. Since the photovoltage can be correlated with the light intensity, it is possible to analyze the data using the theoretical machinery that was developed for electroreflectance. This is demonstrated in Figs. 10 and 11. In Fig. 10 we compare photoreflectance in air with the electroreflectance and the photoreflectance in the methanolic solution of the E_1 transition of Si (16b). One can observe some differences in line shape due to the difference in the penetration depth of the electric field and the light, but the similarity is obvious. Figure 11 shows the variation of the PR amplitude of Si with the intensity of the pumping beam (16b). The logarithmic relationship, the same as the one observed for the photovoltage, is evident. Although this method is somewhat indirect compared with electroreflectance, it offers a unique opportunity to obtain electrical transport properties without the need to form a junction. The power of

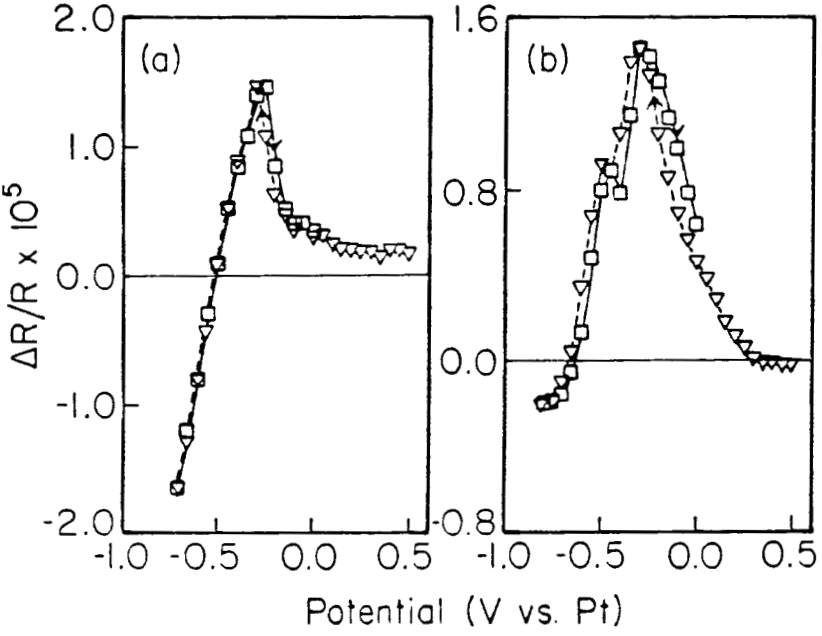

Figure 9. Variation of the amplitudes of the 3.4 eV EER peaks with the electrode potential: (a) after HF etching; (b) before etching. The potential sweep rate was 5 min. per experimental point. The lines are drawn for convenience of inspection. The arrows indicate the direction of the potential sweep (16a).

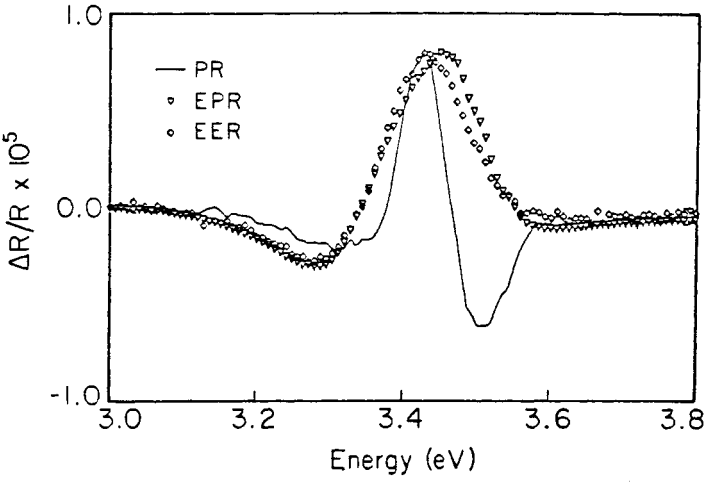

Figure 10. Comparison between Photoreflectance (PR), Electrolyte-Electroreflectance (EER) and Photoreflectance in an electrolyte (EPR) of n-Si. The EPR and the EER were measured in the methanolic solution of oxidized and reduced dimethylferrocene in the following concentrations: 0.01 M $FeCp_2$, 50 μM $FeCp_2^+$ and 1 M $LiClO_4$ supporting electrolyte under nitrogen atmosphere. The EPR was measured under open circuit conditions and the EER at a potential of 0.0 volt vs. Pt. The chopping frequency in all cases is 750 Hz (16b).

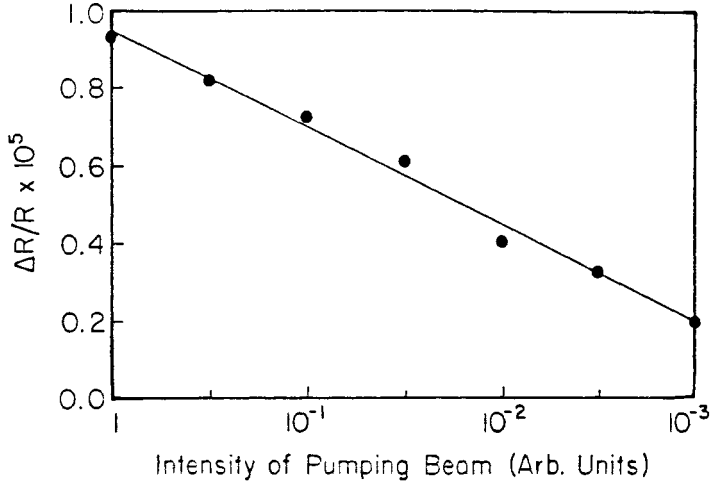

Figure 11. Dependence of the PR signal of n-Si, on the light intensity of the modulated beam (16b).

photoreflectance as a nondestructive spectroscopic tool can be seen in Fig. 12, which shows the spectrum of the various confined and unconfined PR transitions of a multiple quantum well, made of $GaAs/Ga_{0.82}Al_{0.18}As$, with well and barrier widths of 71 Å. Also shown is the theoretical fit of the line shape to superposition of Gaussian derivatives that were found to be more suitable for quantum well structures than the Lorenztian line shapes of Eq. 11 (63). Figure 13 shows the PR spectra of Si samples that were subject to various RIE etchants (16c). The shift in peak position was interpreted in terms of strain induced by the damage to the Si surface by the treatment.

Since PR is a contactless technique, one cannot induce electric field with a power supply, instead the space-charge layer is being formed by equilibration of charge between the bulk and surface or interface states (64). The surface states can either be traced to modified intrinsic states or be induced by absorption of impurities. Since this is a contactless technique, at equilibrium charge neutrality requires that the amount of charge needed to form the space-charge layer will originate from the surface (65). From Eq. 2, within the Schottky approximation for an abrupt junction, the barrier height at the surface is given by:

Eq. (12) $$V_s = eN_d d^2/2\epsilon$$

where e is the electronic charge, N_d is the concentration of the donors, d is the thickness of the space charge layer and ϵ is the dielectric constant. The number of charges per unit area on the surface, N_{ss}, arising from electrons or holes exhausted from a distance d from the surface, is given by:

Eq. (13) $$N_{ss} = -N_d d$$

Combining Eqs. 12 and 13 results in:

Eq. (14) $$V_s = eN_{ss}^2/2\epsilon N_d$$

Weisz (66) was first to point out that for a constant V_s, since N_{ss} varies as the square root of the impurity concentration, no matter how impure the sample, one is limited to a fraction of a percent of a monolayer of equilibrium ionosorption, when depletion layer is present.

The last argument can also be taken in reverse: for charge neutrality

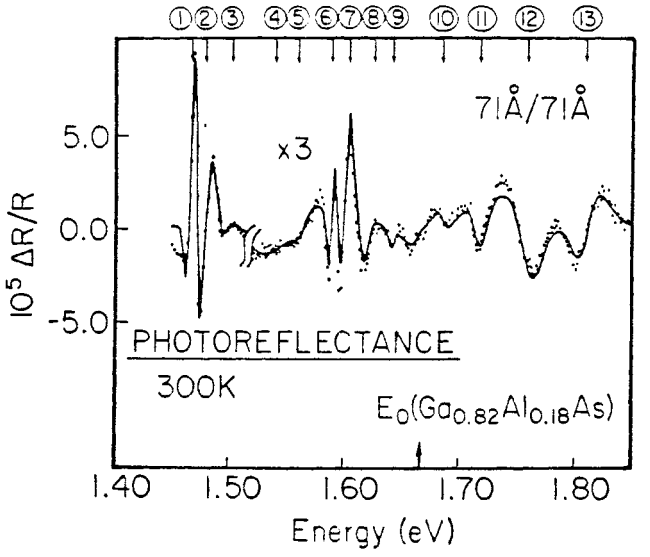

Figure 12. Photoreflectance spectrum at 300K (dotted line) of GaAs/$Ga_{0.82}Al_{0.18}As$ multiple quantum well, with well and barrier widths of 71 Å. The solid line is a least-square fit of the experimental data to a first-derivative of a Gaussian line shape form. The arrows indicate the energies of the various transitions as obtained from the fit (63).

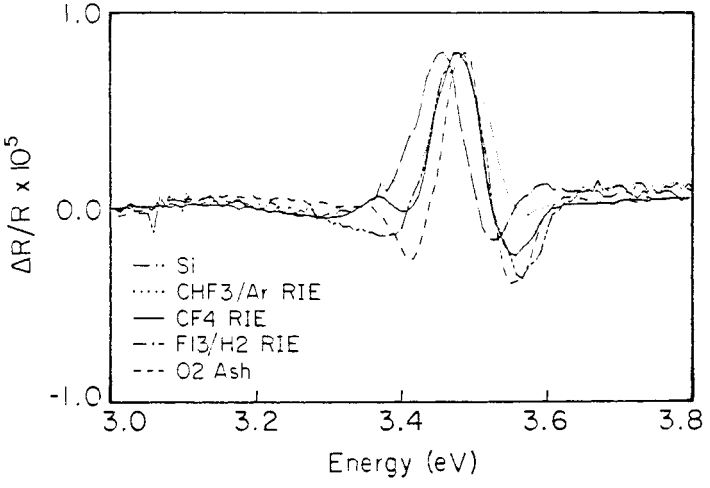

Figure 13. Photoreflectance spectra of n-Si subjected to various RIE treatments. Temperature 77°K. The modulation source is 7.5 mW He-Ne laser; modulation frequency: 750 Hz (16c).

to be maintained, only small modulation of the surface charge can produce a very large modulation of the surface potential and produce a large PR signal. To our knowledge, this aspect of photoreflectance has not yet been credibly demonstrated. Both, EER and PR can also be used for measurements of the impedance of the system. It was shown (67) that if one measures the amplitude of an EER signal as a function of the modulating frequency over a broad frequency regime, it is possible to correlate the results with the impedance response over the same frequency regime.

Surface Photovoltage. This technique was first proposed by Goodman (68), and has since been used both with solid and liquid junctions. It is based on the observation that for most "good" semiconductors the photovoltage is related to the minority carriers' diffusion length through the following expression:

Eq. (15) $$Ia\alpha/(1 + \alpha Lp) = f(V_{oc})$$

where Ia is the light intensity, α the absorption coefficient, Lp the minority carrier diffusion length and V_{oc} the photovoltage. Ia is being adjusted at various wavelengths to give the same photovoltage. From Eq. (15), the plot of the light intensity against the absorption coefficient directly gives the value of the minority carriers' diffusion length that in turn correlates with presence of defects in the bulk of the semiconductor. Direct comparison between results taken with Al Schottky barrier and liquid junction on silicon ribbon gave identical results for the minority carriers' diffusion length (69).

A variance that usually appears in the literature as Surface Photovoltage Spectroscopy (21) uses either a vibrating metal electrode in close proximity to the surface of the semiconductor (Kelvin probe), or a semitransparent metal electrode with a modulated light source to make contact with the semiconductor, and monitors the spectral response of the photovoltage with subband gap illumination. This technique can also be viewed as a non-contact technique that can be used for in situ characterization during device fabrication.

Electromodulated Infrared Spectroscopy. The form most widely in use is the electromodulated attenuated-total-reflection-spectroscopy. This is the electromodulated form of the multiple internal reflection spectroscopy that was previously discussed. The practice here is to modulate, by switching the potential between two values, and monitor the absorption changes by lock-in techniques. Description of this technique with an emphasis on metal-electrolyte interfaces can be found in (70). The modulation here is different from all the other techniques that were mentioned in the sense that the modulation is not a small perturbation of an equilibrium state but a shift between two equilibrium states. Whether

or not one achieves equilibrium in the two states depends on the modulation frequency. But since this is a true spectroscopic technique in which one can resolve vibrational modes at the interface and the modulation is used primarily to increase sensitivity to voltage-induced chemical change at the interface, the issue of switching between two real equilibrium states might be irrelevant as long as information is not being derived from line-shapes.

The semiconductor/electrolyte system most thoroughly investigated using this technique is the Si/acetonitrile (71-74). The researchers were able to observe vibrational transition due to Si-H, CH, and distinguish between isolated and hydrogen bonded Si-O-H. They were able directly to observe absorption due to surface states, correlate these states with the surface chemistry and with treatments such as etching, aging and oxidation (72). They were able to estimate the reorganization energy (71) of the surface states and estimate the potential distribution from the free carriers' absorption (74). By itself this series of papers constitutes a tour-de-force. When and if these or similar data will be correlated with transport properties and UHV spectroscopies, they will provide a solid framework for our understanding of semiconductor-liquid interfaces.

Other Modulation Techniques. Electric field modulated photoluminescence in a liquid junction device was reported in Ref. 75. The results agreed with the "dead layer" model previously discussed. Quantitative comparison of differentiation of Eq. 1 with respect to the electrode potential and impedance measurements yielded an agreement between the "dead Layer" and the space-charge layer.

Electroabsorption was demonstrated in Ref. 76 and the line shape was found to fit Eq. 11. Theoretical justification for this fit was not given.

A summary of other modulation techniques such as wavelength modulation, temperature modulation and stress modulation can be found in Ref. 77. These modulation techniques have not yet found any significant applications in the study of semiconductor-liquid junction devices.

4.0 TIME RESOLVED TECHNIQUES

The overall charge separation process across a semiconductor liquid junction involves various contributions to the mechanism, details of which are still lacking. These include the light induced electron-hole formation, their various recombination mechanisms and their transport across the interface to react with the electrolyte. Time resolved techniques, that can now reach the femtoseconds time scale, should be a powerful tool to elucidate many mechanistic and kinetic aspects of these processes and provide the best interface with theory. Care should be exercised in

correlating many of the pulsed experiments with their steady-state analogs: typical laser power of 1 mJ/cm^2 per pulse (30 ns) corresponds to steady-state illumination power of 33 kW/cm^2, close to five orders of magnitude higher than a typical steady-state measurement (78).

4.1 Current

Perhaps the simplest of these techniques are the potentiostatic photocurrent transients (79) that were shown to be sensitive to the semiconductor electrodes down to 1 ns. (80) and below (81). Often the time resolution is limited by the RC of the system and the technique is most valuable in the longer time scales for identification of intermediates and products of photo redox reactions (79). The interpretation of the data follows the routine in some of the methods that we have explored to interpret impedance data, i.e., assume an equivalent circuit and analyze the decay as a superposition of exponential decays where the time constants are correlated with the elements of the equivalent circuit (79)(80)(82). The time constant that was associated with the space charge layer was in reasonable agreement with the Mott-Schottky data (79)(80). The time-scale of the predicted response (83) is much faster than the one observed by the authors of Ref. 79, but the much faster resolution reported in Ref. 81 was in agreement with the time-dependent version of Gartner's model. Etching was found to have a large effect on the amplitude and decay time of the transients (82). This method was also applied to the study of dye sensitization and the role of a "super sensitizers" in these systems (84).

4.2 Potential

An alternative method is the coulostatic-flash technique (85) in which the system is perturbed by a pulse of charge induced by a pulse of supra-band-gap photons. The subsequent time-resolved return of the electrode potential to equilibrium is observed at open circuit. In principle, in this mode, the system is not limited by the RC of the interface but only by the parasitic capacitance of the setup. The correlations with the kinetics of charge transfer are less direct compared to the potentiostatic mode. The results with TiO_2 in aqueous electrolyte were in general agreement with the theory (86) of double layer relaxation. These experiments were extended to non-aqueous electrolytes (87) where it was found that surface modification through silanation has a significant effect on the slower components of the time evolution of the photopotential that was interpreted in terms of induced surface states that can enhance the charge transfer to the electrolyte. An algorithm that relates the number of

photogenerated carriers with the observed transients was developed (88). This theory was applied to the investigation of the time-resolved photopotential of one of the best characterized semiconductor-liquid junctions, InP both n and p types, in aqueous and non aqueous electrolytes (89). In this system one can control to a certain degree the distribution of surface states by controlled deposition of various metals and the system appears to be stable to corrosion. This method was also used to determine barrier height of a leaky Schottky barrier junction between SnO_2 and p-SiC (90).

4.3 Photoluminescence

Perhaps the most informative variant of the time-resolved techniques is the one based on photoluminescence (91). The time resolution can extend below the picosecond regime. In addition to band-gap emission one can monitor the emission due to specific recombination centers. The disadvantages are that one is confined to materials that emit light and the sensitivity is such that most of the work is reported under high injection conditions where the system was driven to flat band. The one dimensional continuity equation under these conditions was solved and the experimental results with CdS were analyzed to yield the surface recombination velocity that was found to be affected by the choice of electrolyte (91). The time-resolved study of cathodic and anodic electroluminescence of ZnO in the μsec time scale was reported (92).

4.4 Microwave Conductivity

The method uses the proportionality between the relative change of reflected microwave power and the conductivity induced by a light pulse in a solid embedded in a waveguide system (93). Time resolution of nanoseconds was reported.

4.5 Surface Restricted Transient Grating

This powerful method was only recently applied to semiconductor-liquid interfaces by R.J. Dwayne Miller et al. (94). Two time coincident supra-band-gap beams are used to image an optical interference pattern on the semiconductor surface. The excitation promotes electron-hole pairs that decay into free carriers. The spatial modulation of the carrier concentration creates a periodic variation in the material index of refraction that mimics the optical interference pattern. The holographic diffraction grating thus formed is being probed with a variably delayed sub-band-gap probe. The grating image decays according to the carrier population and

thus measures directly the dynamics of the carriers. The strong electric field at the solid-electrolyte interface can focus the pattern at the interface by driving minority carriers to the surface and majority carriers away from the surface in a time scale that is short compared to the measurement. In addition the grating image excites a surface acoustic mode (94) with its own temporal and spatial resolution that increases considerably the information contents of these experiments. The time scales that were probed are from subpicoseconds to nanoseconds. The experimental work is supported by Monte Carlo computer simulations (95) of the dynamics of some of these systems to offer the hope that our understanding of the dynamics of charge carriers at the solid-liquid interfaces will approach our understanding of charge transport processes in homogeneous systems.

5.0 PHOTOTHERMAL METHODS

During the course of photoelectrochemical reactions only a portion of the light energy absorbed by the semiconductor can be utilized in the electrode reaction. The remaining energy is being dissipated as heat. The heat should cause a local temperature change that can be monitored by placing a suitable sensor near the surface of the electrode (96).

The simplest sensing device is a thermistor that can directly measure the temperature changes (97). The temperature changes were correlated with the quantum efficiency. A serious deficiency of this method is the slow equilibration time of the thermistor ($\sim$1 sec.). The equilibration time can be considerably reduced by shifting to photoacoustic detection either in the form of a microphone (98) or a piezoelectric transducer (99). These developments follow the success that photoacoustic spectroscopy had in determining absorption spectra of solids (100) and efficiency of photovoltaic devices (101).

Variants of these techniques are the Photothermal Deflection Spectroscopy (PDS or "Mirage" effect) and Photothermal Displacement Spectroscopy (102). These techniques are based on deflection of a light beam due to refractive index gradients either in a fluid (or air) in contact with a light absorbing solid or in the solid itself. If the fluid is inert the technique can be used to measure absorption spectra of solid materials and transport properties. A version of these techniques was applied to electrochemical and photoelectrochemical systems (103). The authors describe the experimental conditions needed to separate the contributions from the temperature and concentration gradients. Once this is done the results can be correlated with the kinetics and mechanism of the electrochemical reactions.

6.0 TOPOGRAPHICAL STUDIES

One of the most convenient features of liquid junctions is that almost every one of the various techniques mentioned so far can be used in conjunction with a computer-controlled X-Y stage to provide a topographical image of a particular parameter to which the technique is sensitive. The simplest one is the photocurrent (104). Since many of the corrosion products are semiconducting oxides, this technique was used to detect corrosion on metal structures (105). Figure 14 shows an example of an electroreflectance scan (106) across the surface of GaAs. From Eq. 10, one can see that the amplitude of the EER signal is proportional to the doping level. The scan was interpreted to represent contours of doping levels. The resolution reported in most of these studies is of the order of fractions of a millimeter. Yet, the optics and the stage can bring the resolution down to that of an optical microscope, that is, in the μm range. The resolution limiting factor in many of the modulated optical techniques is the low signal to noise ratio. For a typical EER signal of 10^{-4}, the signal accumulation time is about 1 sec. that will amount to a resolution of 0.2 mm for one hour experiment on a 1 cm^2 crystal. If, in addition, one has to monitor the peak position in every point the spatial resolution will be further reduced.

7.0 ACKNOWLEDGEMENT

This work was supported by ONR.

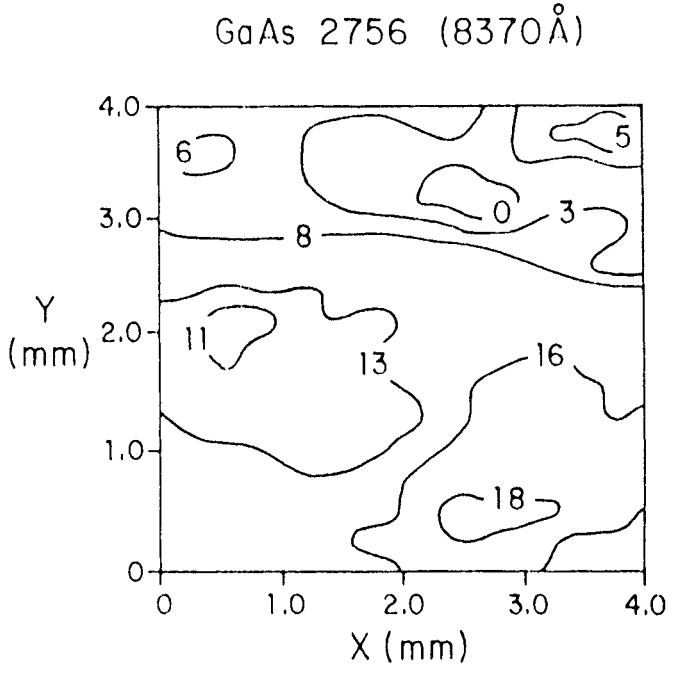

Figure 14. Contours of the variations in carrier concentrations across the surface of GaAs utilizing the electrolyte electroreflectance signal at 8370Å. The numbers in the contours indicate percentage variations relative to the lowest concentration (106).

8.0 REFERENCES

1. See for example:
   Tomkiewicz, M., *Proc. SPIE,* 452:120 (1984)

2. See for example:
   Chazalviel, J-N., *Electrochimia Acta,* 33:461 (1988)

3. See for example:
   Oehrlein, G.S., *Phys. Today,* 39:26 (1986)

4. See for example:
   a. Brillson, L.J., *J. Vac. Sci. Technol.,* 16:1137 (1979)
   b. Spicer, W.E., Chye, P.W., Skeath, P.R., Su, C.Y. and Lindau, I., *J. Vac. Sci. Technol.,* 16:1422 (1979)
   c. Freeouf, J.L. and Woodall, J.M., *Appl. Phys. Lett.,* 39:727 (1981)

5. See for example:
   Lewis, N.S., Rosenbluth, M.L., Casagrande, L.G. and Tufts, B.J., in: *Homogeneous and Heterogenous Photo-catalysis,* (E. Pelizzetti and N. Serpone eds.), 343, D. Reidel Pub. Co. (1986)

6. For references that cover the early work at Bell Telephone Laboratories see: Brattain, W.H. and Boddy, P.J., *J. Electroch. Soc.,* 109:574 (1962)

7. See for example:
   a. Gerischer, H. in: *Physical Chemistry: An Advanced Treatise,* (H. Eyring, D. Henderson and W. Yost, eds.), p. 463, Academic Press, New York (1970)
   b. Memming, R., *J. Electroch.Soc.,* 116:785 (1969).
   c. Myamlin, V.A. and Pleskov, Y.V., *Electrochemistry of Semiconductors,* Plenum Press, New York (1967)

8. Fujishima, A. and Honda, K., *Nature,* 238:37 (1972)

9. See for example: Horowitz, G., Allongue, P. and Cachet, H., *J. Electroch. Soc.,* 131:2563 (1984)

10. Rosenbluth, M.L. and Lewis, N.S., *J. Am. Chem. Soc.,* 108:4689 (1986)

11. Licht, S., Tenne, R., Dagan, G., Hodes, G., Manassen, J., Triboulet, R., Rioux, J. and Levy-Clement, C., *Appl. Phys. Lett.,* 46:608 (1985)

12. See for example:
Kern, W. and Deckert, C.A., in: *Thin Film Processes,* (J.L. Vossen and W. Kern eds.), p. 401, Academic Press, New York (1978)

13. a. Tenne, R., *Appl. Phys.,* 25:13 (1981)
b. Ostermayer, F.W. Jr., Kohl, P.A. and Burton, R.H., *Appl. Phys. Lett.,* 43:642 (1983)

14. See for example:
Divigalpitya, W.M.R. and Morrison, S.R., *J. Appl. Phys.,* 60:406 (1986)

15. Yeager, E., Homa, H., Cahan, B.D. and Scherson, D., *J. Vac. Sci. Tech.,* 628 (1982)

16. Series of five papers by the common title "Liquid Junctions for Characterization of Electronic Materials" in J. Appl. Phys. (1989)
a. Fantini, M.C.A., Shen, W.M., Tomkiewicz, M. and Gambino, J.P., *J. Appl. Phys.,* 65:4884 (1989)
b. Shen, W.M., Fantini, M.C.A., Tomkiewicz, M. and Gambino, J.P., *J. Appl. Phys.,* 66:1759 (1989)
c. Shen, W.M., Fantini, M.C.A., Pollack, F.H., Tomkiewicz, M., Leary, H. and Gambino, J.P., *J. Appl. Phys.,* 66:1765 (1989)
d. Fantini, M.C.A., Shen, W.M., Tomkiewicz, M. and Gambino, J.P., *J. Appl. Phys.,* 66:2148 (1989)
e. Fantini, M.C.A., Shen, W.M., Tomkiewicz, M. and Gambino, J.P., *J. Appl. Phys.,* 66:4846 (1989)

17. Bard, A.J. and Faulkner, L.R., in: *Electrochemical Methods,* p. 298., John Wiley & Sons, 1980

18. Memming, R., *Ber. Bunsenges. Physik. Chem.,* 81:732 (1977)

19. Miller, B., Menezes, S. and Heller, A., *J. Electroch. Soc.,* 127:1483 (1979)

20. See for example:
Burns, G., in: *Solid State Physics,* Ch. 13, Academic Press (1985)

21. Luth, H., *Appl. Phys.*, 8:1 (1975)

22. See for example:
Luminescence of Inorganic Solids, (P. Goldberg, ed.), Academic Press (1966)

23. Pujadas, M., Gandia, J., Salvador, P. and Decker, F., *J. Electroanal. Chem.*, 218:347 (1987)

24. Silberstein, R.P. and Pollak, F.H., *J. Appl. Phys.*, 51:1743 (1980)

25. Harrik, N.J., in: *Internal Reflection Spectroscopy,* John Wiley and Sons (1967)

26. Chiarotti, G., Nannarone, S., Pastore, R. and Chiaradia, P., *Phys. Rev.*, B4:3398 (1971)

27. See for example:
a. Palik, E.D., Holm, R.T. and Stella, A., *J. Appl. Phys.*, 57:843 (1984)
b. Spitler, M.T., in: *Electrochemistry: Fundamental Processes and Measurement Techniques,* (W. Wallace, A. Nozik and S. Deb eds.), p. 282. Electrochemical Society (1982)

28. Ellis, A.B., *J. Chem. Educ.*, 60:332 (1983)

29. Garuthara, R., Tomkiewicz, M. and Tenne, R., *Phys. Rev.*, B31:7844 (1985)

30. Garuthara, R. and Tomkiewicz, M., *J. Appl. Phys.*, 58:1662 (1985)

31. Streckert, H.H., Tong, J., Carpenter, M.K. and Ellis, A.B., *J. Electroch. Soc.*, 129:772 (1982)

32. Garuthara, R., Tomkiewicz, M. and Silberstein, R.P., *J. Appl. Phys.*, 54:6787 (1983)

33. Memming, R., *J. Electroch. Soc.*, 116:785 (1969)

34. Gautron, J., Delbera, J-P. and Lemasson, P., *Surf. Sci.*, 99:300 (1980).

35. See for example:
Aspnes, D.E., *J. Phys.*, 44:C10-3 (1983) and *Surf. Sci.*, 101:84 (1980)

36. Raccah, P.M., Garland, J.W., Zhang, Z., Lee, U., Xue, D.Z, Abels, L.L., Ugur, S. and Wilinsky, W., *Phys. Rev. Lett.*, 53:1958 (1984)

37. Meyer, F., *Phys. Rev.*, B9:3622 (1974)

38. Dorn, R. and Luth, H., *Phys. Rev. Lett.*, 33:1024 (1974)

39. McIntyre, J.D.E. and Aspnes, D.E., *Surf. Sci.*, 24:417 (1971)

40. Mu, X.C., Fonash, S.J., Yang, B.Y., Vedam, K., Rohatgi, A. and Rieger, J., *J. Appl. Phys.*, 58:4282 (1985)

41. MacDonald, J.R., in: *Impedance Spectroscopy,* John Wiley & Sons (1987)

42. Raistrick, I.D., *Ann. Rev. Mater. Sci.*, 16:343 (1986)

43. Shen, W.M., Aurian-Blajeni, B., Tomkiewicz, M. and Cahen, D., *J. Electroch. Soc.*, 133:930 (1986)

44. Tomkiewicz, M., *J. Electroch. Soc.*, 126:2220 (1979)

45. Kramer, M. and Tomkiewicz, M., *J. Electroch. Soc.*, 131:1283 (1984)

46. Tomkiewicz, M. and Aurian-Blajeni, B., *J. Electroch. Soc.*, (1988)

47. Liu, H.S., *Phys. Rev. Lett.*, 55:529 (1985)

48. Sze, S.M., *Physics of Semiconductor Devices,* John Wiley & Sons, New York (1981)

49. Schottky, W., *Z. Phys.*, 113:367 (1939); 118:539 (1942)

50. Mott, N.F., *Proc. R. Soc. London,* Ser A, 171:27 (1939)

51. Shen, W.M., Tomkiewicz, M., Sedaries, D. and Levy-Clement, C., *J. Electroch. Soc.*, 137:2656 (1990)

52. Tomkiewicz, M., *Surf. Sci.,* 101:286 (1980)

53. Braun, C.M., Fujishima, A. and Honda, K., *Surf. Sci.,* 163:369 (1985)

54. See for example:
    a. McEvov, A.J., Etman, M. and Memming, R., *J. Electroanal. Chem.,* 190:225 (1985)
    b. Chandrasekaran, K., Kainthla, R.C. and Bockris, J. O'M., *Electrochimica Acta,* 33:327 (1988)

55. Haak, R. and Tench, D., *J. Electroch. Soc.,* 129:275 (1984)

56. Lang, D., *J. Appl. Phys.,* 45:3023 (1974)

57. Tomkiewicz, M. and Shen, W.M., in: *Photoelectrochemistry and Electrosynthesis On Semiconducting Materials,* (D.S. Ginley, A.J. Nozik, N. Armstrong, K. Honda, A. Fujishima, T. Sakata and T. Kawai eds.), The Electrochemical Soc., Inc. (1987)

58. Luo, J., Lin, Z.H. and Tian, Z.W., *Photochemical Conversion and Storage of Solar Energy,* Abst. E41, Proc. 7th. Internat. Conf., Evanston, Ill (1988)

59. See for example:
    Pollak, F.H., in: *Photoelectrochemistry: Fundamental Processes and Measurement Techniques,* (W.L. Wallace, A.J. Nozik, S.K. Deb and R.H. Wilson, eds.), The Electrochemical Soc. (1982)

60. Aspnes, D.E., *Surf. Sci.,* 37:418 (1973)

61. Tomkiewicz, M., Siripala, W. and Tenne, R.. *J. Electroch. Soc.,* 131:736 (1984)

62. Tafalla, D., Pujadas, M. and Salvador, P., *Photochemical Conversion and Storage of Solar Energy,* Abst. E13, Proc. 7th. Internat. Conf., Evanston, Ill (1988)

63. Shen, H., Pan, S.H., Hang, Z., Pollak, F.H. and Sacks, R.N., *Sol. St. Comm.,* 65:929 (1988)

64. Risch, L., *Phys. Stat. Sol.,* 88:111 (1978)

65. Morrison, S.R., in: *The Chemical Physics of Surfaces,* Plenum Press, NY (1977)

66. Weisz, P.B., *J. Chem. Phys.,* 21:1531 (1953)

67. Silberstein, R.P., Lyden, J.K., Tomkiewicz, M. and Pollak, F.H., *J. Vac. Sci. Technol.,* 19:406 (1981)

68. Goodman, A.M., *J. Appl. Phys.,* 32:2550 (1961)

69. Micheels, R.H. and Rauh, R.D., *J. Electroch. Soc.,* 131:217 (1984)

70. Bewick, A. and Pons, S., in: *Advances in Infrared and Raman Spectroscopy,* Vol. 12, (R.J.H. Clark and R.E. Hesler eds.), p. 1., Wiley-Heyden, Chichester (1985)

71. Chazalviel, J-N. and Rao, A.V., *J. Electroch. Soc.,* 134:1138 (1987).

72. Rao, A.V. and Chazalviel, J-N., *J. Electroch. Soc.,* 134:2777 (1987)

73. Rao, A.V., Chazalviel, J-N. and Ozanam, F., *J. Appl. Phys.,* 60:696 (1986)

74. Tardella, A. and Chazalviel, J-N., *Phys. Rev.,* B32:2439 (1985)

75. Garuthara, R., Tomkiewicz, M. and Silberstein, R.P., *J. Appl. Phys.,* 54:6787 (1983)

76. Pujadas, M., Gandia, J., Salvador, P. and Decker, F., *J. Electroanal. Chem.,* 218:347 (1987)

77. Cardona, M., in: Modulation Spectroscopy, *Solid State Physics,* Supp. 11, (F. Seitz, D. Turnbull and H. Ehrenreich, eds.), Academic Press (1969)

78. Jaegermann, W., Sakata, T., Janata, E. and Tributsch, H., *J. Electranal. Chem.,* 189:65 (1985)

79. See for example:
Deutscher, S.B., Richardson, J.H., Perone, S.P., Rosental, J and Ziemer, J., *Far. Disc.* 70:33 (1980)

80. Willig, F., Bitterling, K., Charle, K.P. and Decker, F., *Ber. Bunsenges. Phys. Chem.*, 88:374 (1984)

81. Bitterling, K. and Willig, F., *J. Electroanal. Chem.*, 204:211 (1986)

82. Harzion, Z., Croitoru, N. and Gottesfeld, S., *J. Electroch. Soc.*, 128:551 (1981)

83. Laser, D. and Bard, A.J., *J. Electroch. Soc.*, 123:1837 (1976)

84. Kojima, T., Ban, T., Kasatani, K., Kawasaki, M. and Sato, H., *Chem. Phys. Lett.*, 91:319 (1982)

85. Perone, S.P., Richardson, J.H., Deutscher, S.B., Rosenthal, J. and Ziemer, J.W., *J. Electroch. Soc.*, 127:2580 (1980)

86. Feldberg, S.W., *J. Phys. Chem.*, 74:87 (1970)

87. Kamat, P.V. and Fox, M.A., *J. Phys. Chem.*, 87:59 (1983)

88. Gottesfeld, S. and Feldberg, S.W., *J. Electroanal. Chem.*, 146:47 (1983)

89. Cook, R.L., Dempsey, P.F. and Sammells, A.F., *J. Electroch. Soc.*, 133:2287 (1986)

90. Itoh, K., Matsumoto, H., Kobata, T. and Fujishima, A., *Appl. Phys. Lett.*, 51:1685 (1987)

91. Evenor, M., Gottesfeld, S., Harzion, Z. and Huppert; D., *J. Phys. Chem.*, 88:6213 (1984)

92. Fichou, D. and Kossaney, J., *J. Electroch. Soc.*, 133:1607 (1986)

93. Kunst, M., Beck, G. and Tributsch, H., *J. Electroch. Soc.*, 131:954 (1984)

94. Kasinski, J.J., Gomez-Jahn, L.A., Faran, K.J., Gracewski, S.M. and Miller, R.J. Dwayne, *J. Chem. Phys.*, 90:1253 (1989)

95. Zhou, X., Hsiang, T.Y. and Miller, R.J. Dwayne, *J. Appl. Phys.* -- in press

96. Fujishima, A., Maeda, Y. and Honda, K., *Bull. Chem. Soc. Jap.*, 2735 (1980)

97. Fujishima, A., Maeda, Y., Honda, K., Brilmyer, G.H. and Bard, A.J., *J. Electroch. Soc.*, 127:840 (1980)

98. Masuda, H., Fujishima, A. and Honda, K., *Chemistry Letters*, 1153 (1980)

99. Yoshihara, S., Aruchamy, A. and Fujishima, A., *Bull. Chem. Soc. Jap.*, 61:1017 (1988)

100. Rosencwaig, A., *Opt. Comm.*, 7:305 (1973)

101. Cahen, D., *Appl. Phys. Lett.*, 33:810 (1978)

102. Amer, N.M., *Proc. SPIE*, 294:11 (1987)

103. Decker, F. and Fracastoro-Decker, M., *J. Electroanal. Chem.*, 243:187 (1988)

104. Furtak, T.E., Canfield, D.C. and Parkinson, B.A., *J. Appl. Phys.*, 5:6018 (1980)

105. See for example:
    a. Butler, M.A., *J. Electroch. Soc.*, 130:2358 (1983)
    b. Shukla, D. and Stimming, U., *Werkstoffe und Korrosion*, 40:43 (1989)

106. Pollak, F.H., Okeke, C.E., Vanier, P.E. and Raccah, P.M., *J. Appl. Phys.*, 50:5375 (1979)

6

ELECTROCHEMICAL MIGRATION

Giulio Di Giacomo

1.0 INTRODUCTION

Electrolytic metal migration is a mechanism that affects microelectronic devices causing failure (1). The failure consists of dendritic growth bridging across adjacent conductors due to metallic ions. The migration occurs between biased lands and under conditions conducive to electrocrystallization (2)(3).

A number of conditions must be satisfied to form a dendrite: 1) the current density must reach high levels at the tip of the dendrite (e.g., 10^3 A/cm^2), e.g., achieved through spherical diffusion: 2) a sufficient liquid medium (polar), such as condensed water, must be present in the migration path so that adequate ionic flux is developed to sustain the required dendritic growth rate (3)(4); and 3) the applied voltage must exceed the sum of the anodic and cathodic potential in equilibrium with the electrolyte. The conditions dictate that the materials surfaces or interfaces must have the physical and chemical properties for adequate water condensation to the extent that the current density requirement at the tip of the growing dendrite is satisfied (2).

Based on literature findings, there is a minimum rate below which a dendrite cannot continue to grow because of lattice poisoning at the surface by contaminants which deposit on the crystallographic facets and obstruct the process.

To produce a metal dendrite, the current density at the whisker's tip must be orders of magnitude greater than the average current. The growth is possible only through spherical diffusion of the ionic current on the dendrite tip, which can be expressed in terms of its radius of curvature, r. (The current density, however, must be above a critical value, Jc.)

To achieve dendritic growth successfully, the mass flux density Q_{tip} must be equal to or greater than the minimum rate below which dendrite poisoning by contaminants occurs:

Eq. (1) $$Q_{tip} \geq d\sigma / Mt_m$$

where:

- M = Atomic weight,
- d = Distance between electrodes,
- σ = Density of dendrite,
- t_m = Maximum time to bridge across electrodes beyond which poisoning takes place.

Since the impurities and metal ion concentrations are probably not the same from site to site, i.e., within a module, the critical current value will vary accordingly.

It must be emphasized, however, that the magnitude of the critical current depends not only on the level but also the type of impurities (among other things) and therefore its value must be considered a characteristic of the particular process.

According to Price et al. (3), the minimum time required to completely block the dendrite's growth can be approximated from the rate of impurity diffusion to the dendrite's tip and the number of molecules needed to block a unit area. The time, therefore, will vary from impurity to impurity and from metal to metal.

The strong effect of impurity atoms and molecules on the dendrite crystal growth can be explained in terms of the edge energy of the lattice step per unit area (s) and the free energy decrease per unit volume (ΔG) accompanying the deposition process (3). The atomic step can advance (during deposition) between two strongly adsorbed impurities only if the distance between them is greater than twice the critical radius of curvature, Rc, of the advancing step. In terms of energy, the steps that will advance and add to dendritic growth are those having radii of curvature greater than the critical value (2) given by $Rc = s/\Delta G$. Schematically,

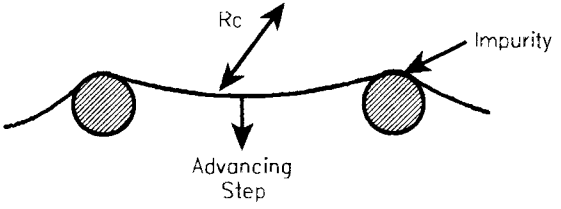

On a statistical basis, as the impurity concentration increases, the critical current density of the metal ions, Jc, required to sustain dendritic

growth also must increase. For a given metal ion concentration, type of impurity, temperature and dendrite radius, the critical current density for dendrite growth is proportional to the cube root of the impurity concentration. As lower voltages across the gap reduce the current density below the critical value in more impure sites, the average dendrite growth will decrease approaching zero with the applied voltage and will show a superlinear growth dependence on voltage.

Another factor is the capability of the adsorbed layer of water to carry the mass of ions required by the dendritic growth rate which defeats poisoning. If t_m is of the order of one minute and the electrodes are Ag lands on a substrate 0.1 mm apart, then the required ionic flux to bridge across the gap is 1.75×10^{-3} g/cm^2 s. For a Ag^+ mobility of 7×10^{-4} cm^2/s V and 5 volt bias, an ionic Ag^+ concentration of 5×10^{-3} g/cm^3 would be required to meet the flux density rate and therefore the t_m requirement. This assumes the electric field to be parallel to the dendrite and no distortion around the dendrite tip. In reality, the field focuses on the tip due to the spherical shape of the equipotential lines around it, and therefore the flux density is larger and the Ag^+ concentration required lower. On the other hand, if the thickness of the adsorbed water film is thinner than the minimum dendrite thickness which is possible, then theoretically not only the ionic concentration must be greater but the dendritic growth will be impaired. For a dendrite to succeed, therefore, all these factors must be in tune and satisfy the requirement of dendrite growth without poisoning. But even when the ionic concentration is sufficient to start a dendrite, it may be that the ionic supply is source limited. This would be the case when just enough ions were produced during a period of incubation but not enough to sustain a dendritic growth to its completion or to prevent it from being poisoned. A period of incubation is usually required before any dendrite is discovered between lands in test vehicles. The time varies depending on the chemical environment created by process and test conditions.

Dendrite failures have been observed for most metals used in the electronics industry during accelerated tests and under field conditions. The empirical models are usually a product of three factors (which are assumed to be separable), each being a function of one variable. These factors are voltage, temperature, and relative humidity. This last one has assumed different forms varying from a simple exponential, e^{BRH}, to B.E.T. form, $CRH/(1-RH)[1+(C-1)]RH$ (5)(6), and to the statistical pore distribution $\mathrm{erfc}\,(1/2\sigma)\ln[KTr\ln RH/(2\nu_m\gamma)]^2$, where RH is the relative humidity, B and C are process parameters, r is the pore radius, γ the surface tension, ν_m the molar volume, and σ the pore distribution sigma. The parameter C is a function of temperature, heat of adsorption and the condensation (5-7). The other two factors usually take the form of $e^{(-\Delta H/KT)}$ and V^n where n can

vary from 1 to 2. Because of the migration, strong dependence on RH and the long testing time required at the low RH levels, most of the test data available to date were obtained above 50% RH; therefore, the empirical models do not cover the dry field condition within the module, to which the data is projected by extrapolation. When contaminants and process residues are present, the migration dependence on relative humidity may be shifted to lower RH values because adsorption of moisture by reaction products and hygroscopic particles will allow condensation to occur at RH values lower than saturation.

Another aspect of migration that is least explored, therefore least known, is its behavior in the presence of polymer coatings (4)(8)(9). Polymers absorb water and other pollutants from the environment and, under the driving force of an electric field, current leakages are generated between electrodes. Consequently, the insulation resistance of the polymer is curtailed. Soluble ionic species within the polymer (e.g., hydrolyzable chloride...) contribute to the mechanism. Water not only may be the solvent and vehicle for ionic transport but it can also participate pervasively in the conduction through electrolysis, especially at the higher voltages.

First, however, the species must be transported to the vicinity of the electrodes (within the sphere of the electric field influence) via diffusion under the driving force of the concentration gradient before participating in the leakage process, thus closing the electrochemical cycle. A steady state is eventually achieved which will determine the local concentration of the species and the limiting ionic current across the electrodes. Generally, at steady state, such transport mechanisms are controlled by diffusion, which tends to simplify the analysis; however, the process can be very slow, which makes it necessary to deal with the transient aspect and time-dependent factors.

In practice, the interfacial insulation resistance of polymers degrades as the films are exposed to humidity under electric bias (8). Indeed, the resistance tends to level off with time unless defects in the film or at the polymer-ceramic interface act as shorts. The process of interfacial adhesion degradation can continue as a function of time as the bond weakens under the degrading action of some of the electrolytes. Under these conditions the leakage steadily increases with time. Much higher leakages between biased electrodes can occur because of polymer bond degradation in humid environments rich in sulfurous and nitrous pollutants.

Water drop tests are not very revealing and do not necessarily predict the migration susceptibility of metals in microelectronics under field conditions (1). The reason is that metal migration and dendritic formation depend on the state of the metal surface, whether it is oxidized or not, and on whether the oxide passivates the surface or it dissolves in water. For instance, copper will rarely produce dendrites when it is

oxidized due to the oxide tenacity and insolubility in water, but it will migrate if the oxide is removed. On the other hand, silver will migrate whether it is oxidized or not since the oxide is water soluble. Insoluble oxides (and other insoluble compounds) tend to prevent metal migration because they limit or stop the ionic and electronic exchange required at electrodes to fulfill the electrochemical cycle (1). Another element that migrates massively is molybdenum which forms water soluble oxides and hydroxides. The migration, however, does not result in distinct dendrites but rather mass growth along the entire electrode. Under field conditions of relative humidity, temperature, and contamination, the propensity for dendritic formation depends on a host of other variables: process variables, materials variables, and test condition variables. Therefore, the water drop test is only an indicator for migration susceptibility between metals for different surface conditions, to screen out those which would perform badly in the field under a very high relative humidity condition. Even under these restrictions, metals which would perform well in the field can also be rejected by the test.

Another key variable in metal migration is the critical current density, Jc, which determines whether an electrode will passivate or be inhibited by adsorption (10-13).

It is known that dissolving anodes begin to passivate when the value of J exceeds a critical value (J_{cr}) which depends on the nature of the metal, the composition of the electrolyte, and temperature. According to Savchenkov and Uvarov (11), at current densities below J_{cr} of the metal, all the anodic current is spent on the dissolution of the metal, while at current densities $> J_{cr}$, the metal may be in the active state only a limited time, t, before the metal changes to passive state. Usually the higher the current density of the anode, the smaller the value of t, which is referred to as the transition time. The length of the transition time depends on the ratio between the rates of formation and removal of the passive layer products. Most investigators present this relationship as:

Eq. (2) $$(J - J_{cr})\, t^n = K$$

where K is a constant for values of $J - J_{cr} \leq 10\, J_{cr}$, and n may vary between 0.5 and 3. The value of J_{cr} is obtained by measuring t for different values of J and extrapolating J to $1/t^n = 0$. The value of J_{cr} represents the capacity of the metal for active dissolution. For metals of the iron group in acid solutions at 25°C, the value of J_{cr} increased from Ni to Co to Fe (12). According to Okamoto et al. (13), the pH of the solution has a significant effect on J_{cr}, expressible (at 25°C) as:

Eq. (3) $$\log J_{cr} = 1 \cdot 1 - 0.83\, pH$$

Equation 3 indicates that the more acidic the electrolyte is, the higher the value of J_{cr} and the harder it is to achieve passivation which requires current values $> J_{cr}$. For a water drop test at room temperature (pH 7), J_{cr} is 1.3×10^{-6} A/cm^2 which allows passivation to occur.

Savchenkov and Uvarov found that the dependence of the transition time of Ni passivation on the current density at 25°C can be expressed as $(J - J_{cr})t = 0.52$, and at 160°C as $(J - J_{cr})\,t^{0.5} = 1.64$, where J is in A/cm^2 and t in seconds. At room temperature for current densities of the order of 3.8×10^{-4} A/cm^2, the transition time is 23 minutes. At the higher temperature, a much longer transition time is required to begin passivating as J_{cr} increases with temperature. According to Savchenkov, this behavior indicates that the electrode is in the active state at a higher temperature (for which $T < T_{cr}$), which may be due to the decrease of the degree of irreversibility of adsorption of foreign particles (hydroxide, oxide) on the Ni surface.

According to Vagramyan and Uranov (14) at lower temperature the rate of inhibition is high because the adsorbed particles bind themselves firmly to the electrode surface so that, in effect, reduction of the metal ions proceeds through a continuous layer of foreign particles that form a barrier (cathode). Because this diffusion process requires a relatively high activation energy, it will control the deposition of Ni which occurs uniformly. At higher temperature, however, the inhibition effects diminish, the discharge of Ni ions occurs at very low overvoltages, and the deposition of the metal takes place only on the active areas of the cathode surface. As a result, isolated aggregates of Ni form whose rate of deposition depends primarily on the supply of the Ni ions to the electrode. The high polarization during Ni deposition is due mainly to oxides, hydroxides, hydrogen, and other foreign particles.

Vagramyan and Zhamagortsyants (10) have indicated that the sharp decrease in the overvoltage of cathodic and anodic processes with increase in temperature may be due to two cases: (1) the direct effect of temperature on the electrochemical reaction, and (2) the elimination of the inhibiting effect of adsorbed foreign particles by means of temperature. The overvoltage for Ni at room temperature for 1 N $MeSO_4$ solution is about 3/4 of one volt (10), while for Ag, Cu, and Pb, the overvoltage is about an order of magnitude lower.

2.0 MODEL

2.1 Current Density through an Electrolyte

The current density, J, can be expressed as a function of the drift

velocity, ν_d, and the ionic concentration C (4):

Eq. (4) $$J = ZFC\nu_d$$

where F = Faraday's electrochemical equivalent, and Z = valence. The drift velocity is the difference between the ions' velocity in the direction of the field ($\vec{\nu}$) and their velocity against it ($\overleftarrow{\nu}$):

$$\nu_d = \vec{\nu} - \overleftarrow{\nu} = l\,[KT/h]\, e^{(-\Delta H_D/KT)}\,[e^{(\Delta H_E/KT)} - e^{(-\Delta H_E/KT)}]$$

Eq. (5) $$\nu_d = 2\,l\,[KT/h]\, e^{(-\Delta H_D/KT)} \sinh(\Delta H_E/KT)$$

where:

- l = jump distance,
- ΔH_D = diffusion component of free energy of activation,
- ΔH_E = 1/2 ZFlE, electric component of free energy of activation representing the electric work from the equilibrium position to the top of the barrier,
- h = Planck's constant,
- K = Boltzmann constant.

Substituting ν_d from Eq. 5 into Eq. 4:

$$J = 2ZFCl\,[KT/h]\, e^{(-\Delta H_D/KT)} \sinh ZFlE/2RT$$

For low electric fields such that $1/2\ ZFlE/RT << 1$:

$$J = (ZF)^2C\,[l^2KT/h]\, e^{(-\Delta H_D/KT)} \cdot E/RT$$

$$J = \{[(ZF)^2CE]/RT\}\, D_0\, e^{(-\Delta H_D/RT)}$$

Eq. (6) $$J = [(ZF)^2CDE]\,/\,RT$$

For higher fields,

Eq. (7) $$J = (2ZFCD/l)\, e^{pE}$$

where $p = ZFl/2RT$.

Water Availability as a Function of RH. The ionic current is rate-controlled by the availability of water in the form of an adsorbed layer or condensate within interconnected pores (15). There exists a probability

that the current density J, and therefore the dendritic growth, will take place. The probability is assumed to be proportional to the adsorbed or condensed water film cross section characterized by its thickness (such as given by the B.E.T. adsorption isotherm) or based on pores cross-sectional area distribution (15). A time-to-failure, t_f, will, therefore, depend on the product of the current density, J, and the relative humidity or probability function, P(RH) which can be termed statistical J_s:

Eq. (8) $$t_f = A/J \times P(RH) = A/J_s$$

where A is a proportionality constant. It is assumed that t_f is inversely proportional to J_s and, for simplicity, that the current density is entirely due to the metallic ions. The migration process in humid environment, therefore, must rely on the presence of a water film as the medium in which the metal ions will dissolve and through which they will migrate under the influence of an electric field. The water film thickness at any point dictates the ionic flux density and concentration requirements for dendrite growth without being poisoned by impurities. The average thickness of the water film adsorbed on a substrate is a function of relative humidity and temperature, which can be expressed by adsorption isotherms. It is assumed that the probability of successfully growing a dendrite across an electrically biased gap between the two conductors is proportional to the average thickness of the water film or its cross section participating in the ionic transport for the dendritic growth. As the water film grows with relative humidity, more and more sites within a gap will achieve adequate film thickness to meet the physical and chemical requirements to satisfy the dendritic growth demands. The concept of film thickness applies equally to water films at interfaces when porous polymeric coatings are applied at the surface.

B.E.T. RH - Function. The most used adsorption isotherm function is the B.E.T., named after Brunauer, Emmett, and Teller (5). It expresses the number of water monolayers or cross-sectional area, S, as follows:

Eq. (9) $$S \propto [m\,RH]/\{(1-RH)[1+(m-1)RH]\} = P(RH)$$

where: $m \simeq e^{[-(\Delta H_V - \Delta H_A)/RT]}$ determined experimentally,
ΔH_V = Heat of water vaporization, 10.5 kcal/mol,
ΔH_A = Heat of adsorption which depends on the material and surface conditions. It is determined from the knowledge of m and ΔH_V.

Equation 9 has a singularity at 100% RH; however, it is suitable for relative

humidities below 90% where the adsorption theory reasonably applies.

B.E.T Time-to-Failure Model for Dendrites. Substituting Eqs. 6 and 9 into Eq. 8, we have,

Eq. (10) $$t_{50} = A/\{[(ZF)^2CDE]/RT\} \cdot mRH/\{(1- RH)[1+(m-1)RH]\}$$

where: $D = D_o e^{(-\Delta H_D/RT)}$, ionic diffusivity in water,
A = a function of the material and process.

Equation 10 allows the determination of ΔH_D by experimentally determining the time-to-failure, t_f at two or more temperatures with fixed RH and E, assuming a constant C in the process. On this basis, Eq. 10 is rewritten as:

Eq. (11) $$t_{50} = B / mRH/\{(1- RH)[1+(m-1)RH]\} \cdot [e^{(-\Delta H_D/RT)}/T] \cdot E$$

where $B = AK/(ZF)^2CD_o$, experimentally determined. For known C, the constant A can be determined and C could be exercised as a variable if so desired; otherwise C is an unknown in practice and plays no role except if it represents ionic contaminants, in which case it would have to take the appropriate empirical form from a suitable experiment. The time-to-failure is not the time that a dendrite takes to bridge across a gap after it has succeeded to start, but rather the time determined from the statistical current density which is based on the probability of having sufficient water and propitious conditions for nucleation and growth. The probability of occurrence among the many sites increases as the test conditions become more stressful.

The model expressed by Eq. 11 is used to project the time-to-failure from test to field conditions, making use of the failure acceleration due to relative humidity, temperature, and electric field. The model has been verified experimentally and has been consistent. The values of B, m, and ΔH_D will vary with contaminants, material and surface condition. The ionic impurity environment is assumed not to vary among all samples under test within the same experiment. The metallic ion concentration will vary with the samples' contamination due to process residues and other ionic species that may be present in the system. Adding chemicals to enhance the oxidation/reduction process, therefore the electrodeposition, is another way to accelerate the formation of dendrites, however, it would be difficult to relate the results to field conditions if a new mechanism is introduced.

RH Function Based on Pore Distribution. Another way of expressing the relative humidity effect on metal migration is derived from the assumption that a surface or an interface between a film and a substrate can be imagined as consisting of a log-normally distributed pore-network in which water condensation will first occur in the smaller pores as the

relative humidity is raised. The condensation in pores occurs according to the Kelvin equation which expresses the vapor pressure, p, at which condensation occurs within a cylindrical pore as a function of the pore radius, r, the surface tension, γ, the molar volume, ν_m, and temperature, T:

Eq. (12) $$p = p_o e^{[-2\nu_m\gamma/KTr]}$$

where p_o is the saturated vapor pressure above a flat surface ($r = \infty$), and p/p_o is the relative humidity at which condensation occurs in a pore of radius r (5)(6). For a given material and pore frequency distribution, the ionic current density and mass flux density are assumed proportional to the cumulative cross section of the pores where water has condensed. For a log-normal distribution, the fractional area P in which condensation has occurred (small pores first) can be written as (1):

Eq. (13) $$P = (1/2)\,\mathrm{erfc}\,(1/2\sigma)\,\ln(\bar{r}/r)^2$$

where:
σ = $\ln(r_{50}/r_{16})$, which defines sigma,
r_{50} = marks 50% of cumulative cross-sectional area made up by pores having $r < r_{50}$,
r_{16} = marks 16% of the area.

Equation 13 is assumed to be the probability to have a water path. Substituting r from Eq. 12 into Eq. 13, we express such probability in terms of relative humidity, temperature, water surface tension:

Eq. (14) $$P(RH) = \mathrm{erfc}\,(1/2\sigma)\,\ln[KT\bar{r}\ln RH/(2\gamma\nu_m)]^2$$

Note that since RH replaces the variable r and full condensation is assumed in all pores (not just up to $\bar{r}$) when RH = 1, Eq. 14 had to drop the 1/2 coefficient, thus conforming to the conditions: P(RH) = 1 when RH = 1, P(RH) = 0 when RH = 0.

t_f for Dendrites Based on Pore Distribution. Substituting Eqs. 6 and 14 into Eq. 8, we have,

Eq. (15) $$t_f = B^1/E \cdot (e^{(-\Delta H_D/KT)}/T) \cdot \mathrm{erfc}\,(1/2\sigma)\,\ln[KT\bar{r}\ln RH/(2\gamma\nu_m)]^2$$

where:
B^1 = $A^1 K/(ZF)^2 CD_o$
E = V/d
d = gap between conductors.

The parameters B, ΔH, $\bar{r}$, and σ are experimentally determined from the time-to-failure (i.e., t_{50}) as a function of one variable at a time: RH, T,

and E. The parameters r and σ are determined from the t_{50} values obtained from two or more test cells run at different relative humidities and fixed T and E. Similarly, ΔH_D is determined from the t_{50} results obtained at two or more different temperatures, while RH and E remain constant. The same is done with the electric field as a variable.

Both models, Eqs. 11 and 15, are functions of the same three test variables and both have been used to interpret the results of Ag migration in vehicles having epoxy and silicone backseals. The models have been used to project electric failures (due to Ag dendrites grown under accelerated test conditions) to field conditions, thus allowing the calculations of failure rate based on a distribution of fails in time.

2.2 Current Density through a Polymer Coating

The model must deal with the situation encountered when the electrodes are coated with a polymer and ionic leakage eventually causes failure. Ionic species and molecules diffuse to the electrodes as migration takes place under the effect of the electric field, the latter governed by the electrolytic process. Before steady state is attained, there is a transient period during which the incoming diffused species and the migration component establish concentration profiles and an equilibrium ionic concentration at the electrodes.

At equilibrium, the rate of ionic transport due to the diffusion component i_D from the sample surface equals the transport component i_E between the electrodes.

The mass flux density, Q, of water and other species that diffuse from the outside through the polymeric film, destined to be electrolized on arrival at the electrodes, can be expressed as:

Eq. (16) $$Q = D(C_o - C_i) / L$$

where C_o is the molar concentration of the species at the polymer surface, C_i is the prevailing concentration near the electrodes, and L the average distance traveled to reach the electrodes driven by the concentration gradient. Upon electrolysis, the ionic current density, J_D produced from such mass flux is equivalent to:

Eq. (17) $$J_D = ZFD (C_o - C_i) / L$$

at steady state, the rate of ionic transport due to the diffusion component, J_D, equals the transport rate between the electrodes, J_E, given by Eq. 6. However, steady state is achieved after a transient period during which the ionic concentration, C_i, within the polymer film between the electrodes

tends to approach a constant value at a rate of dC_i/dt.

The following differential equation describes the process to a first approximation:

Eq. (18) $J_D - J_E = [ZFD(C_o - C_i)/L] - [(ZF)^2 DEC_i/(RT)] = ZFd(dC_i/dt)$

from which the solution, given the fact that $ZFDE/(RT) >> D/L$, is:

Eq. (19) $J = (ZFDC_o/L)\{1 - \exp[-ZFDE/(RTd)\,t]\}$

where $D = D_o e^{(-\Delta H_D/RT)}$.

The statistical function, J_s, is:

Eq. (20)
$J_s \propto i = ARH e^{(-\Delta H_D/RT)} / \{(1-RH)[1+(m-1)RH]\}\{1-\exp[-ZFDE/(RTd)t]\}$

The time-to-failure, t_f (which is implicit in Eq. 20) occurs when the current reaches a fail criterion i_c. For $ZFDE/(RTd)\,t << 1$, which requires $t < 1000$ hrs at test temperature, Eq. 20 can be rewritten as:

$$t_f \simeq B / RH / \{(1-RH)[1+(m-1)RH]\} \cdot [e^{(-2\Delta H_D/KT)}/T] \cdot E$$

Eq. (21) $B = i_c Rd/AZFD_o$

3.0 EXPERIMENTAL

3.1 Parameters for Dendrite Model

The work deals with Ag-migration between tinned Ag-Pd lands (free Ag along edges) in an encapsulated vehicle consisting of a polyimide-amide surface coating, aluminum cap and silicone rubber or epoxy backseal. Figure 1 shows the test site.

The tests were conducted in temperature-humidity chambers. The lands were biased with 5, 10, and 20 volts, and in-situ voltage-drop measurements (across 10 MΩ limiting resistor in series with each gap) were made at intervals to generate a cumulative fail distribution as a function of time. A fail is defined as a resistance $\leq 5 \times 10^6 \Omega$.

Failure analysis was performed on each failed unit. Leakages were first analyzed electrically to ascertain that they were caused by dendrites (and not other conductive paths), and then by an electron microprobe to determine the elements responsible for the high conductivity. Typical Ag dendrites are shown in Fig. 2. Those obtained at the lower voltage are

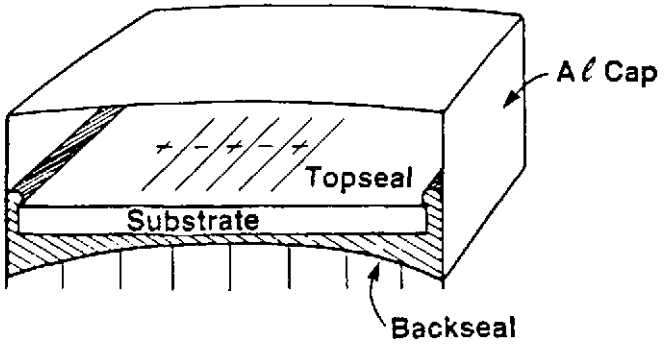

Figure 1. Vehicle (1), © 1982, IEEE

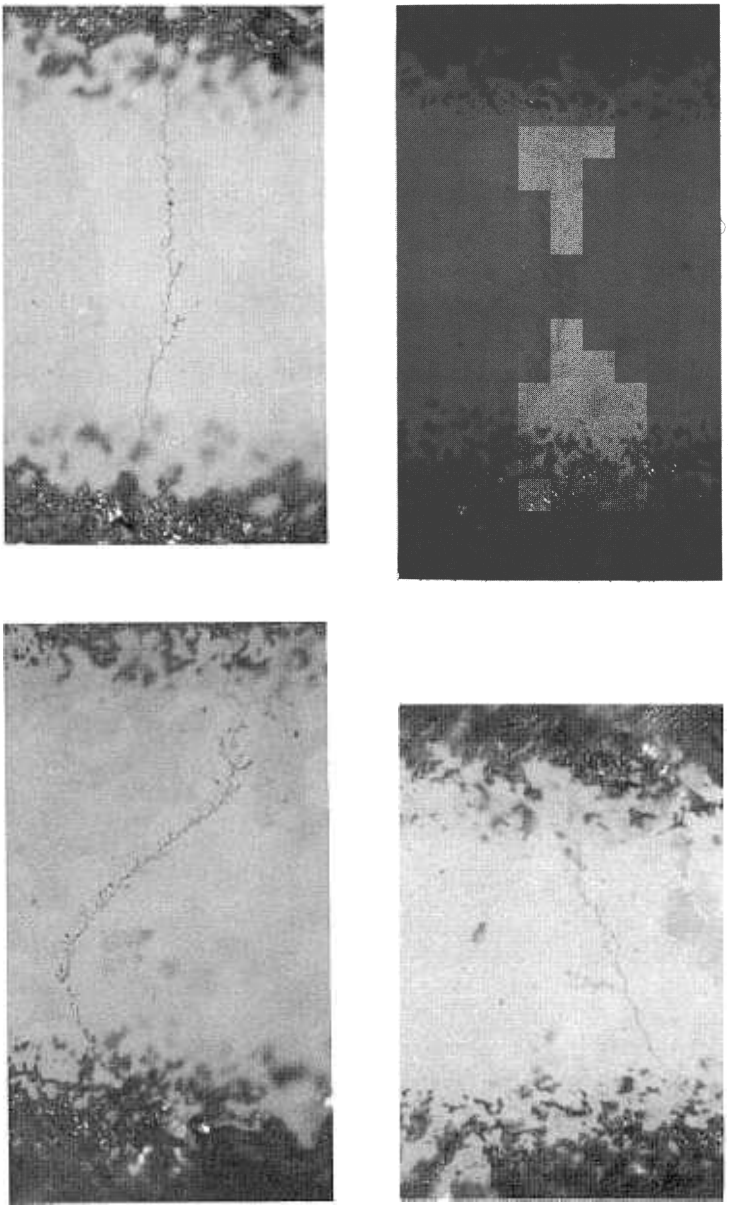

Figure 2. Typical Silver Dendrites

somewhat heavier than those grown at the higher bias.

The cumulative percentage of failures obtained from each stress condition were plotted versus time on lognormal paper. Figures 3 and 4 show the fail distribution for silicone rubber and epoxy backseals respectively at each voltage.

The reciprocal t_{50} values for both backseals are plotted against the applied voltage in Fig. 5 showing a linear dependence and an intercept of four volts. The results suggest that the current density distribution may be falling to subcritical values.

There is a notable difference between the results obtained with the two backseals. The modules encapsulated with silicone rubber show a constant sigma (~ 0.9) independent of the bias, while those encapsulated with epoxy have a sigma ranging from 0.7 to 2.5, increasing as the bias falls from 20 to 5 volts so that, at low fallout, the cumulative percentage of failures is practically independent on the applied voltage.

Based on the results at 85°C/80%RH/20V and 95°C/80%RH/20V, which are presented in Fig. 6, the activation energy for the migration process is ~ 0.15 eV, in agreement with literature values for ionic diffusion (17). The time-to-fail dependence on relative humidity is seen in Fig. 7, which best satisfies the model for an average pore size $\bar{r}$ = 17.5 nm and a lognormal-distribution σ = 1.45. Figure 8 shows the humidity factor versus relative humidity (RH) calculated from the model and how well it agrees with the experimental data and the B.E.T. adsorption isotherm.

The actual pore-size distribution should, however, be measured experimentally to provide materials characterization and direct model verification. Meanwhile $\bar{r}$ and σ are just parameters.

The experimental results show that below 4 volts no failures were observed, which is consistent with a critical current. Based on the t_{50} data for the silicone rubber backsealed modules, the parameters in the pore-based model, Eq. 15, are:

$$
\begin{aligned}
B^1 &= 0.88\ \text{hV/cm °C} \\
\sigma &= 1.45 \\
\bar{r} &= 175\text{x}10^{-8}\text{cm} \\
\Delta H_D &= 0.15\ \text{eV} \\
E &= (V - 4)/d
\end{aligned}
$$

The parameters for the B.E.T.-based model, Eq. 11, based on the same data, are:

$$
\begin{aligned}
B^1 &= 0.88\ \text{hV/cm °C} \\
m &= 0.0065 \\
\Delta H_D &= 0.15\ \text{eV} \\
E &= (V - 4)/d
\end{aligned}
$$

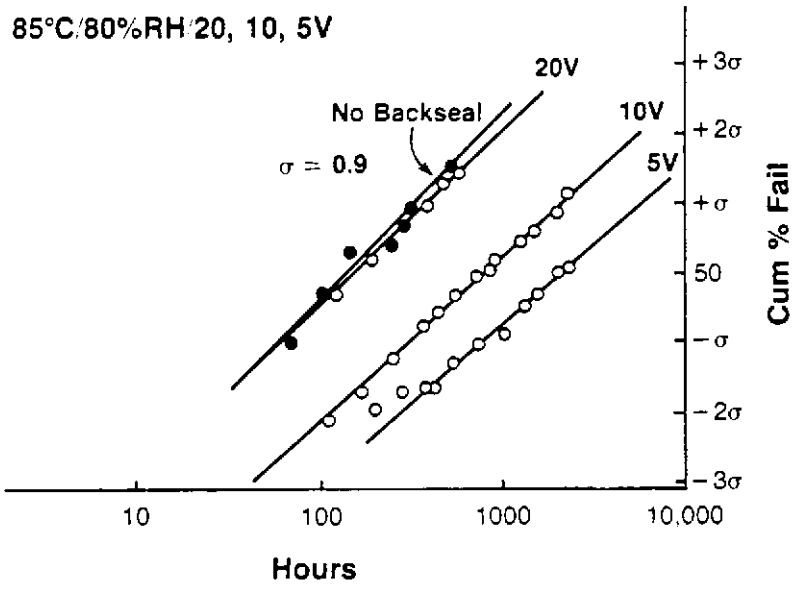

Figure 3. Migration-Fail Distribution, Silicon Rubber Backseal (1), © 1982. IEEE.

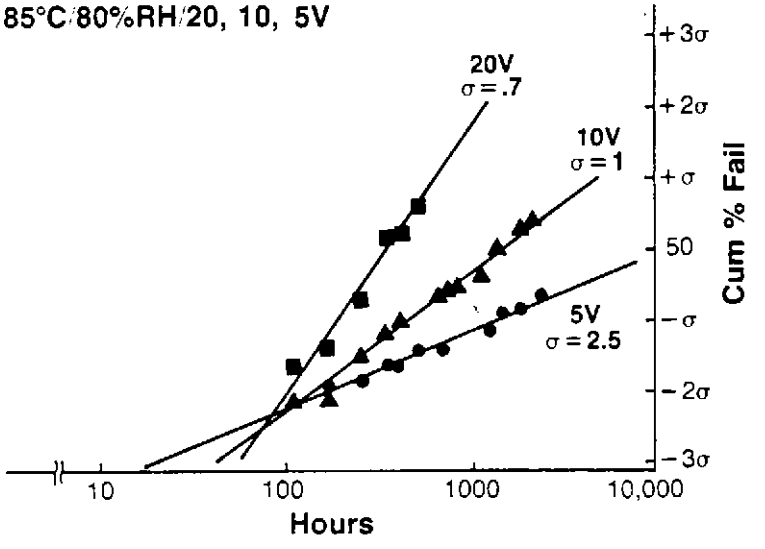

Figure 4. Silver Migration, Epoxy Backseal, Voltage as a Parameter (1), © 1982, IEEE.

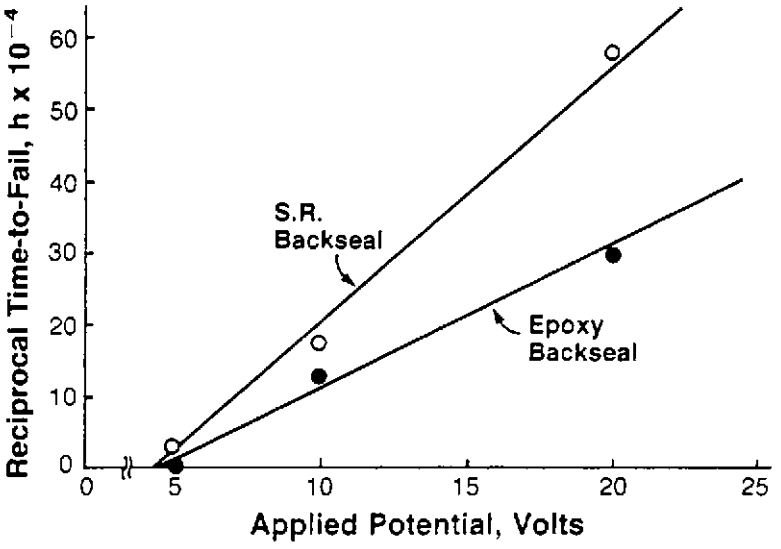

Figure 5. Reciprocal Time-to-Fail (t_{50}) vs. Applied Voltage (1), © 1982, IEEE.

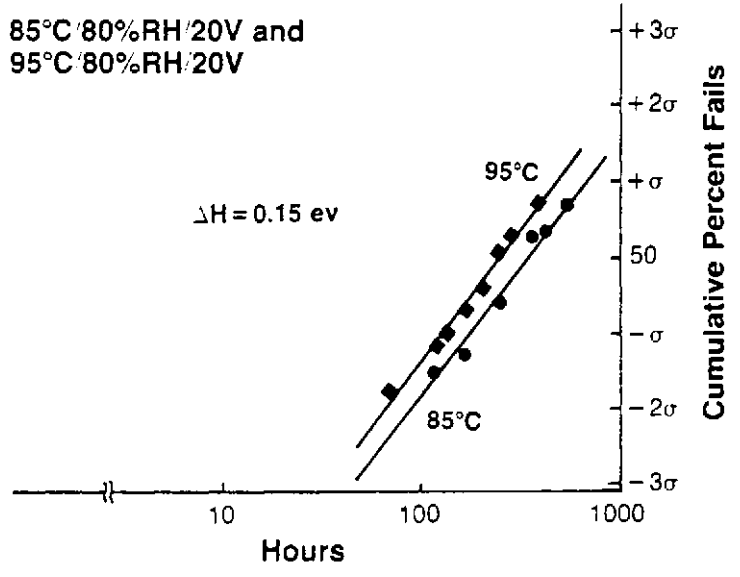

Figure 6. Silver Migration, Epoxy Backseal, Temperature as a Parameter (1), © 1982, IEEE.

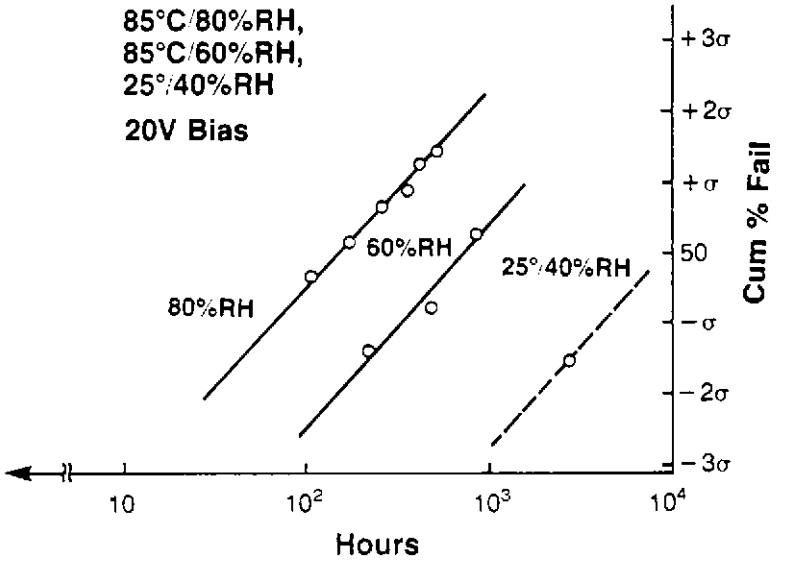

Figure 7. Silver Migration, Silicon Rubber Backseal, Relative Humidity as a Parameter (1), © 1982, IEEE.

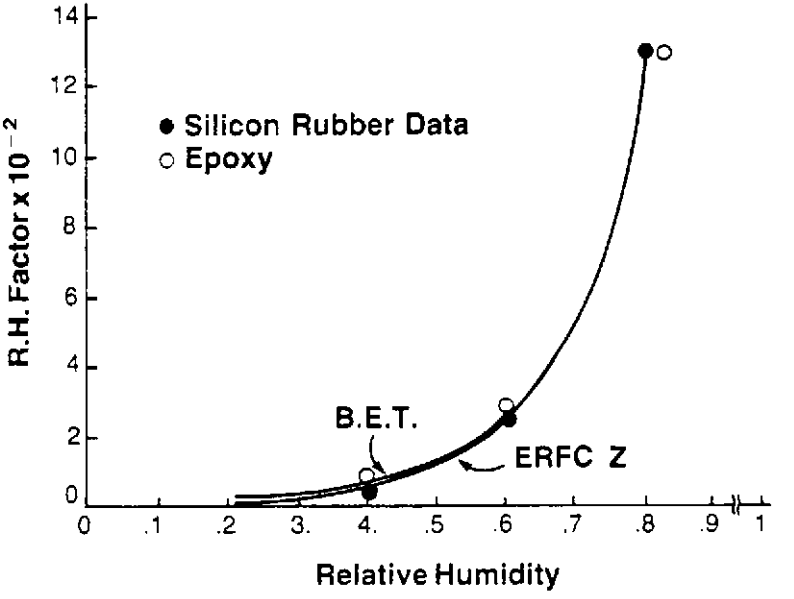

Figure 8. Relative Humidity Factor vs. RH (1), © 1982, IEEE.

The epoxy back-sealed modules show similar t_{50} results for which the parameters in Eq. 15 are:

$$B^1 = 2.0\ hV/cm\,°C$$
$$\sigma = 1.70$$
$$\bar{r} = 175 \times 10^{-8} cm$$
$$E = (V - 4) / d$$

However, the statistical sigma increases as the voltage decreases such that for < 1% cumulative fails, there is no distinction among the three voltages, that is, the time-to-failure becomes independent of voltage (See Fig. 3A). This behavior is attributed to a second mechanism which must prevail at the lower voltages and must not depend on the voltage itself. Species which enhance metal migration may be diffusing from the epoxy backseal. The result is a larger sigma at the lower voltages.

3.2. Parameters for Leakage Model

The experiment deals with the measurement and interpretation of electric leakage between parallel tinned and non-tinned Cr/Cu lands on a ceramic substrate, covered with an epoxy overlay about 1mm thick. The lands are 0.254 cm wide and spaced 0.0127 cm, 0.0254 cm, and 0.038 cm, while the thickness of Cr, Cu, and Pb-10%Sn in the land structure are 100 nm, 800 nm, and $\sim 10^4$ nm, respectively. Chromium is used for adhesion.

The experiment is conducted under various stress conditions to develop leakage kinetics to verify the model and to make projections to field conditions as a function of temperature, relative humidity, voltage, electrode gap, geometry, diffusivity parameters, and time.

From a mechanistic point of view, the process is apparently controlled by the permeation of moisture and other soluble species that participate in the leakage. The tests were conducted under three electrical biases (50 V, 30 V, and 10 V) and three electrode gaps (0.0127 cm, 0.0254 cm, and 0.038 cm) for the following temperature and relative humidity conditions: 70°C at 70%RH, 70°C at 81%RH, and 85°C at 81%RH. The leakage is measured in situ and plotted versus time. Figures 9 and 10 show the data from the three test cells (solid lines) which are used to determine the model's parameters and, therefore, the leakage dependence on temperature, RH, and voltage from which the time-to-failure dependence is determined based on a fail criterion. Initially, the leakage increases linearly with voltage but become sublinear as the test progresses, which implies ionic depletion. (See Fig. 11 showing leakage versus voltage after 1500 hours at 85°C.) The trend indicates that the voltage dependence will continue to

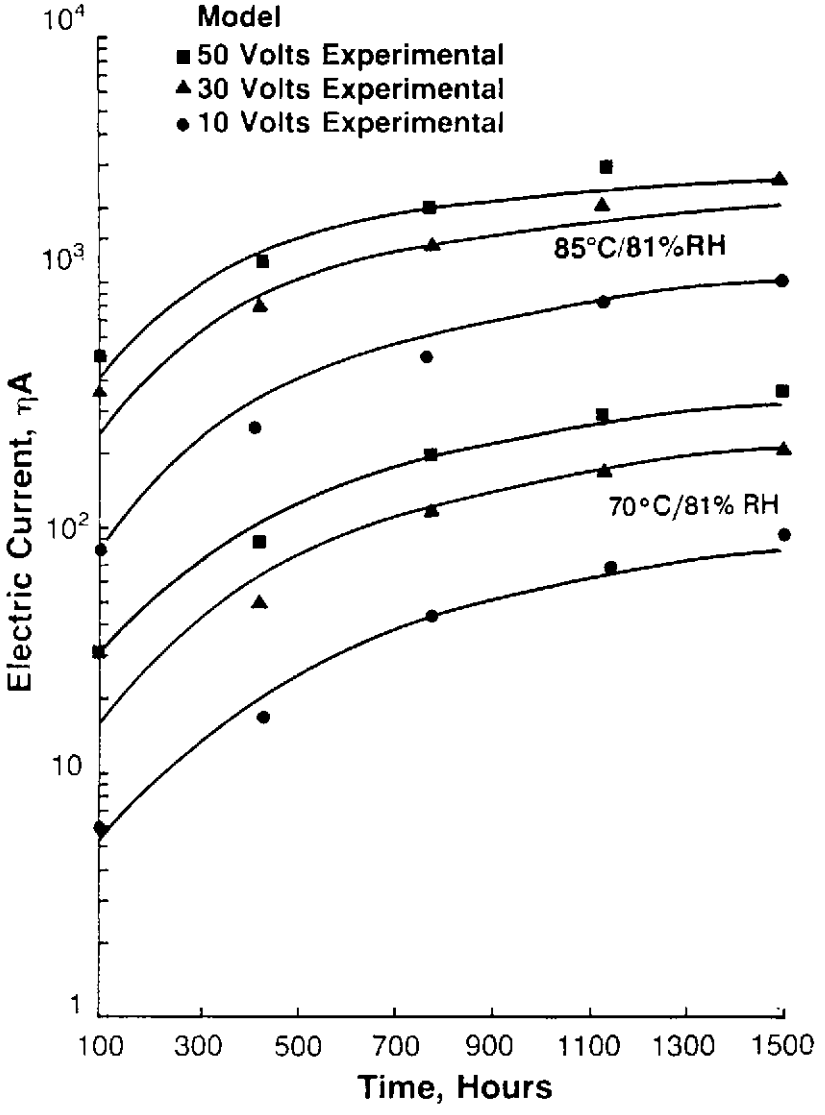

Figure 9. Electric Leakage Current Versus Time on Test at 70°C/81% RH and 85°C/81% RH for Three Different Voltages (8),© 1985, IEEE.

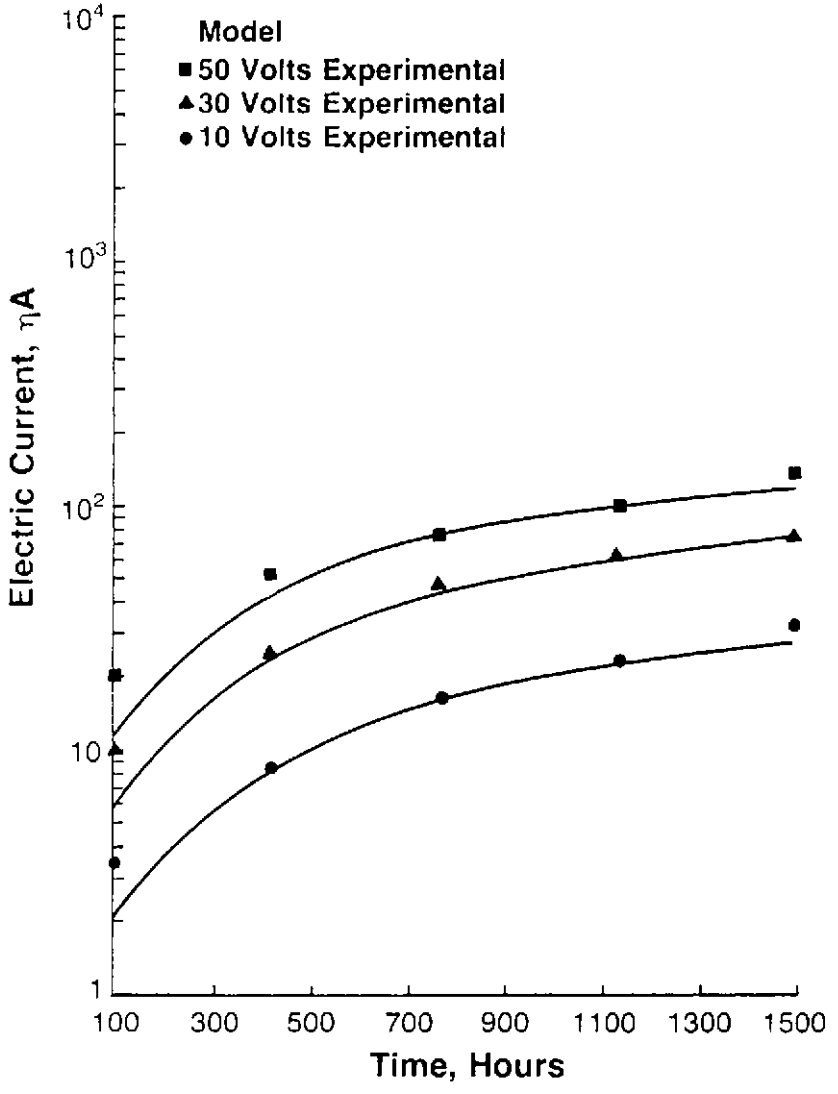

Figure 10. Electric Leakage Current Versus Time on Test at 70°C/70% RH for Three Different Voltages (8), © 1985, IEEE.

erode as the system approaches a steady state, consistent with the model's transient form with respect to voltage, whose effect is, therefore, time dependent.

The parameters in Eq. 20 were determined experimentally:

$$\begin{aligned} m &= 0.0065 \\ \Delta H_D &= 1.0\ eV \\ A &= 1.83 \times 10^{15}\ nA \end{aligned}$$

Using these parameters, the leakage criterion i_c can be expressed as a function of t_f:

Eq. (22)

$$i \simeq 1.83 \times 10^{15} \frac{RH}{(1-RH)^2} e^{\frac{-1.16 \times 10^4}{T}} \{1 - \exp[-8.87 \times 10^7 \frac{ZFV}{RT} e^{\frac{-1.16 \times 10^4}{T}} t]\}$$

To reach a fail criterion of $10^{-8}\Omega$ from an insulation resistance of $10^{11}\Omega$, it will take 10^5 hrs. at 40°C/40%RH/10V. The leakage dependence on d is practically nil. This may be the result of the polymer thickness being considerably larger than the gaps.

3.3 Water-Drop Migration.

Ag, Pb, and Cu Films. Evaporated Ag, Pb, and Cu land patterns on ceramic substrates were tested in water-drop experiments under 10 volt bias: as-evaporated, after being oxidized, "sulphized" and exposed to HCl dilute solution to form metal chlorides. Five samples for each metal and surface condition were stressed. The reaction surface layers were ≤ 50 nm thick and rather spotty (discontinuous) as determined by electron microprobe. The oxide and sulphide layers either halted migration or reduced its occurrence dramatically. It was obvious that dendrites, whenever they occurred, were associated with incomplete passivation and, in general, the surface treatment was very effective.

Metal chlorides did not improve the migration resistance. Actually the chlorides made it worse, which can be explained by their high solubility in water. Table I summarizes the results in terms of the time to grow the dendrite and the current recorded during the process. The results show how important the surface condition is and explains why metals that grow stubborn insoluble oxide (e.g., Cu) are much more resistant to metal migration than those whose oxides are water-soluble (e.g., Ag). These differences reflect in the pre-exponential factor A which is a function of the material and process. These affect the critical current requirement and

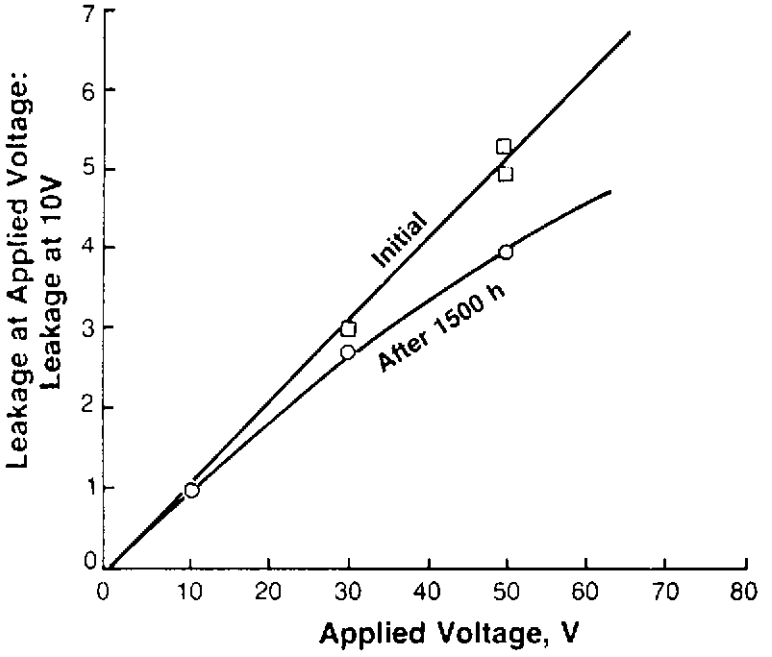

Figure 11. Voltage Dependence Drift (8), © 1985, IEEE.

Table 1. Migration Across Evaporated Lands (Water-Drop) (1), © 1982, IEEE.

Metal	Untreated	Chloride	Oxide	Sulfide	Current for Migration
Ag	50 Sec	53 Sec	45 Sec	≥3 Min	10-19 μA
Cu	7 Min	5 Min	None	None	10-16 μA
Pb	1 Min	30 Sec	20 Min	30 Min	18-47 μA

Cu (Wire) None
Cu (.01% H_2SO_4) 30 Sec

determine whether a dendrite will or will not grow in given materials following certain processes through which contamination occurs.

In addition, when the experiment is conducted with acidic solutions, e.g., 10^{-3} M H_2SO_4 solution, the Cu will readily migrate all over, across the electrodes. Figure 12 shows a number of dendrites across parallel Cu wires (0.005 cm diameter) in water drops having a pH of 3.2. No dendrites were obtained with water having pH 7. Therefore, acidic environments that can dissolve the oxide will promote metal migration.

It appears that as long as the metal is protected by an insoluble layer of oxide, sulphide, etc., metals will not be able to migrate as the exchanging of ions and electrons across the anode and cathode interfaces (essential for the oxidation-reduction process) will cease.

In the present experiment we have observed threshold voltages of 0.5 to 1 volt for Cu, Ag, and Pb utilizing evaporated film electrodes separated by a gap 20 mils. Similar limiting voltages were observed with test vehicles having Ag paste and evaporated Cu patterns, all lands spaced 3 mils apart. Cr had been etched off the Cu lands. When a 0.01 M electrolyte solution of $Cu(NO_3)_2$ was used, however, the dendrites between the Cu lands were produced with 0.1 V bias. This reaffirms the fact that the threshold voltage varies inversely with concentration in maintaining a critical current or a certain dendrite growth rate for a given set of conditions. In fact, literature data shows that, for low current densities, the dendrite rate of formation is linear with the ion concentration and the applied voltage.

Therefore, for very low ion concentration, one requires a correspondingly higher voltage to produce the current density necessary for dendritic growth.

Ni Films. This section deals with nickel migration and how it compares with the migration of Ag, Cu, and Pb. Ni films were evaporated on ceramic blank substrates leaving a 15 mil gap between two halves of the film. The gap was covered with a water drop (~ 1 mm diameter) and biased at various voltages ranging from 0.5 to 15 volts. Ni dendrites formed under these conditions. Dendrite growth rates were calculated from the time that each dendrite took to bridge the gap. The ionic current density was 0.1 A/cm^2.

Results at room ambience show that a voltage threshold exists at 1.60 volts, below which no dendrite grew (see Fig. 13). This voltage threshold is much higher than those of Ag and Ag 20%Pd paste which are 0.80 and 0.75 volt respectively (17). For Cu and Pb, it was 0.5 volt (6).

The dendrites which were produced under higher voltages are heavier and have a ramiform structure, while those at lower voltages are thinner and occur in fascicles aligned with the field. The growth rate is nearly linear with the voltage in excess of the threshold and has a value of ~0.17

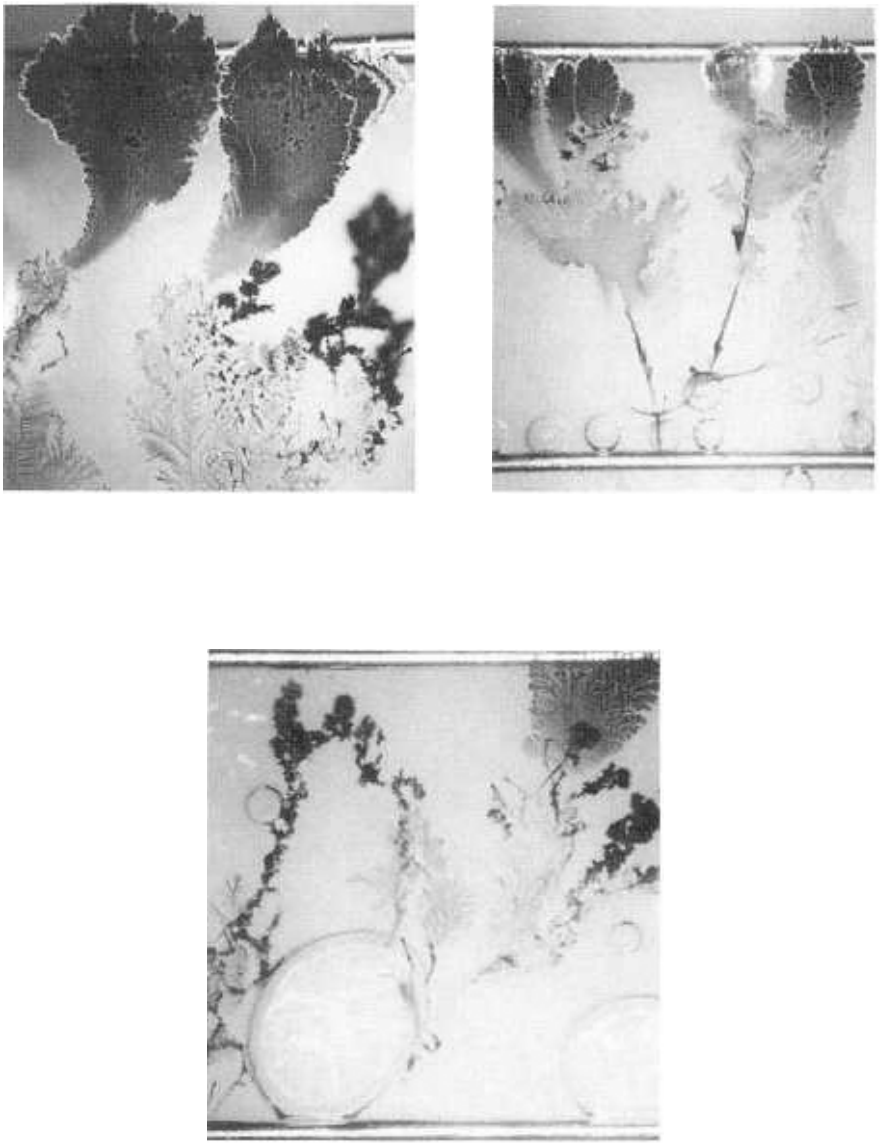

Figure 12. Cu Dendrites Across Parallel Copper Wires

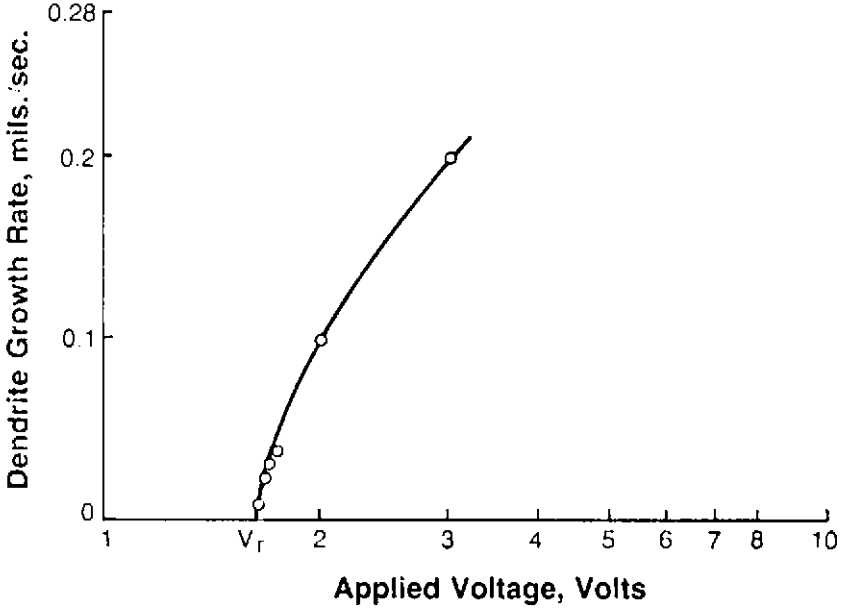

Figure 13. Ni Dendrite Growth Rate vs. Applied Voltage

mils/sec x volt. Ni dendrite growth rates of 1.5 mils/sec x volt have been reported in the literature (17) at 105°C using aqueous solution of $NiCl_2$ (18). The two results are consistent if it is assumed that the activation energy is 0.3 eV and the electrolyte has no effect or has a lower activation and only some electrolyte effect. Oxidized Ni, however, did not migrate under the same conditions. All dendrites occurred in the first few minutes, and no additional ones formed after 23 minutes. This indicates that passivation takes place under the low temperature test conditions and neutral pH. Based on literature findings and the results of this experiment, it is evident that the high-threshold voltage must be due to the high overvoltage resulting from the effect of surface contaminants and oxide/hydroxide formation. Indeed the literature shows that above a critical current density, J_{cr}, the Ni cathode passivates such that Ni reduction or deposition is governed by the activation energy of Ni^{++} diffusion through the passivating impurity layer (~ 10.5 kcal/mol). Since the critical current increases with temperature, the critical value, J_{cr}, is more easily exceeded at room temperature, thus satisfying the conditions for passivation. Therefore, the voltage threshold is expected to increase at higher temperatures as it will depend on the critical current density which limits the process. In addition, drastic reduction in the migration of Ni is, therefore, possible by introducing substances which decrease the acidity and increase the rate of impurity deposition at the cathode. It appears that oxidation or the production of a layer of hydroxide at the cathode are very effective in reducing Ni migration. Because dendritic growth is occurring at both temperatures, one may assume that the mechanism of passivation is not significant in both cases.

It should be noted that Fe and Co behaved quite similarly. These three elements (Fe, Co, Ni) are called metals of the iron group. The outer electrons' free atoms of iron, cobalt, and nickel have configurations d^6S^2, d^7S^2, and d^8S^2 respectively. Their high chemical activity is due to the presence of unfilled d-levels. Among the characteristics of these metals is high overvoltage during deposition and dissolution of the metals in simple salt solutions. Because of their high reactivity, when one of the metals comes into contact with a solution, foreign particles are adsorbed on its surface leading to the passivation of the electrode.

Cu-15%Ag-2.5%P Wires. The wire is 10 mils in diameter and has a Cu core. Other wires used in the experiment were pure Cu and Ag-coated Cu.

The preliminary experiment consists of placing sets of parallel wires of each type on a ceramic substrate (~ 50 mils apart), sandwiching a water layer between the substrate and a glass slide such that a water path is established across the electrodes, applying the bias, and observing dendritic growth as a function of time. Two electrolytic media were used:

(1) DI water, and (2) dilute H_2SO_4 solution ($\sim 10^{-3}$ M, pH = 3.2), which is representative of SO_2 in a humid environment.

Results show that in DI water the Ag-coated Cu wire grew about 30 dendrites per centimeter of wire in ten minutes starting at 1 1/2 minute with the first dendrite, while the Cu-Ag-P wire produced no dendritic growth even after 90 minutes, at which time the test was terminated.

In the acidic electrolyte, however, the Cu-Ag-P wire grew an average of 1 1/2 Cu dendrites per centimeter of wire in ten minutes—about the same as the Cu wire which grew ~2 dendrites/cm. In any case, all dendritic growths approached a limit and practically ceased growing after 10 minutes of exposure. It appears that there is a finite number of active sites that are amenable to dendritic growth and that their exhaustion ends the process. This appears to be the case even before any one dendrite shorts the electrodes. Figure 14 shows typical dendrites from both Cu and Cu-Ag-P wires.

Based on the results, it can be stated that the Cu-15Ag-2.5P braze wire behaves like a Cu wire in terms of metal migration in the system used. It appears that the metallurgical state of Ag in the quenched wire structure is not amenable to migration. Considering the Ag dispersed phase in the Cu matrix and its composition, it appears that, thermodynamically, Cu is favored. Figure 15 shows the number of dendrites per cm of wire as a function of time for the three wires in the given electrolytes.

Wire samples were also tested in a standard migration cell, and I-V curves were measure to determine the Tafel slope during anodic dissolution in various aqueous media. The results of the migration cell tests in O_2 + H_2O and 350 ppm HCL showed no dendrite formation; however, the anode was roughened (dissolution) and there was Cu in solution. No silver was detected. The Tafel slope was identical to that of Cu, though there was a slight shilft in the noble metal direction. These results support the observations in the water-drop experiment that only Cu dendrites form and that the Cu-15%Ag-2.5%P wire behaves like pure Cu.

4.0 DISCUSSION

4.1 Model Acceleration and Materials/Process Effects

The time-to-failure model expressed by Eqs. 11, 15, and 20 are used to determine an acceleration factor between test conditions T_T, RH_T, V_T, and field conditions T_F, RH_F, V_F assuming that the process is invariant. The proportionality constant B is, in effect, a function of all the process and materials variables. The assumption is that the prevailing mechanism at test conditions is the same as under field conditions, and projection of test

Next Page

(1) DI water, and (2) dilute H_2SO_4 solution ($\sim 10^{-3}$ M, pH = 3.2), which is representative of SO_2 in a humid environment.

Results show that in DI water the Ag-coated Cu wire grew about 30 dendrites per centimeter of wire in ten minutes starting at 1 1/2 minute with the first dendrite, while the Cu-Ag-P wire produced no dendritic growth even after 90 minutes, at which time the test was terminated.

In the acidic electrolyte, however, the Cu-Ag-P wire grew an average of 1 1/2 Cu dendrites per centimeter of wire in ten minutes—about the same as the Cu wire which grew ~2 dendrites/cm. In any case, all dendritic growths approached a limit and practically ceased growing after 10 minutes of exposure. It appears that there is a finite number of active sites that are amenable to dendritic growth and that their exhaustion ends the process. This appears to be the case even before any one dendrite shorts the electrodes. Figure 14 shows typical dendrites from both Cu and Cu-Ag-P wires.

Based on the results, it can be stated that the Cu-15Ag-2.5P braze wire behaves like a Cu wire in terms of metal migration in the system used. It appears that the metallurgical state of Ag in the quenched wire structure is not amenable to migration. Considering the Ag dispersed phase in the Cu matrix and its composition, it appears that, thermodynamically, Cu is favored. Figure 15 shows the number of dendrites per cm of wire as a function of time for the three wires in the given electrolytes.

Wire samples were also tested in a standard migration cell, and I-V curves were measure to determine the Tafel slope during anodic dissolution in various aqueous media. The results of the migration cell tests in O_2 + H_2O and 350 ppm HCL showed no dendrite formation; however, the anode was roughened (dissolution) and there was Cu in solution. No silver was detected. The Tafel slope was identical to that of Cu, though there was a slight shilft in the noble metal direction. These results support the observations in the water-drop experiment that only Cu dendrites form and that the Cu-15%Ag-2.5%P wire behaves like pure Cu.

4.0 DISCUSSION

4.1 Model Acceleration and Materials/Process Effects

The time-to-failure model expressed by Eqs. 11, 15, and 20 are used to determine an acceleration factor between test conditions T_T, RH_T, V_T, and field conditions T_F, RH_F, V_F assuming that the process is invariant. The proportionality constant B is, in effect, a function of all the process and materials variables. The assumption is that the prevailing mechanism at test conditions is the same as under field conditions, and projection of test

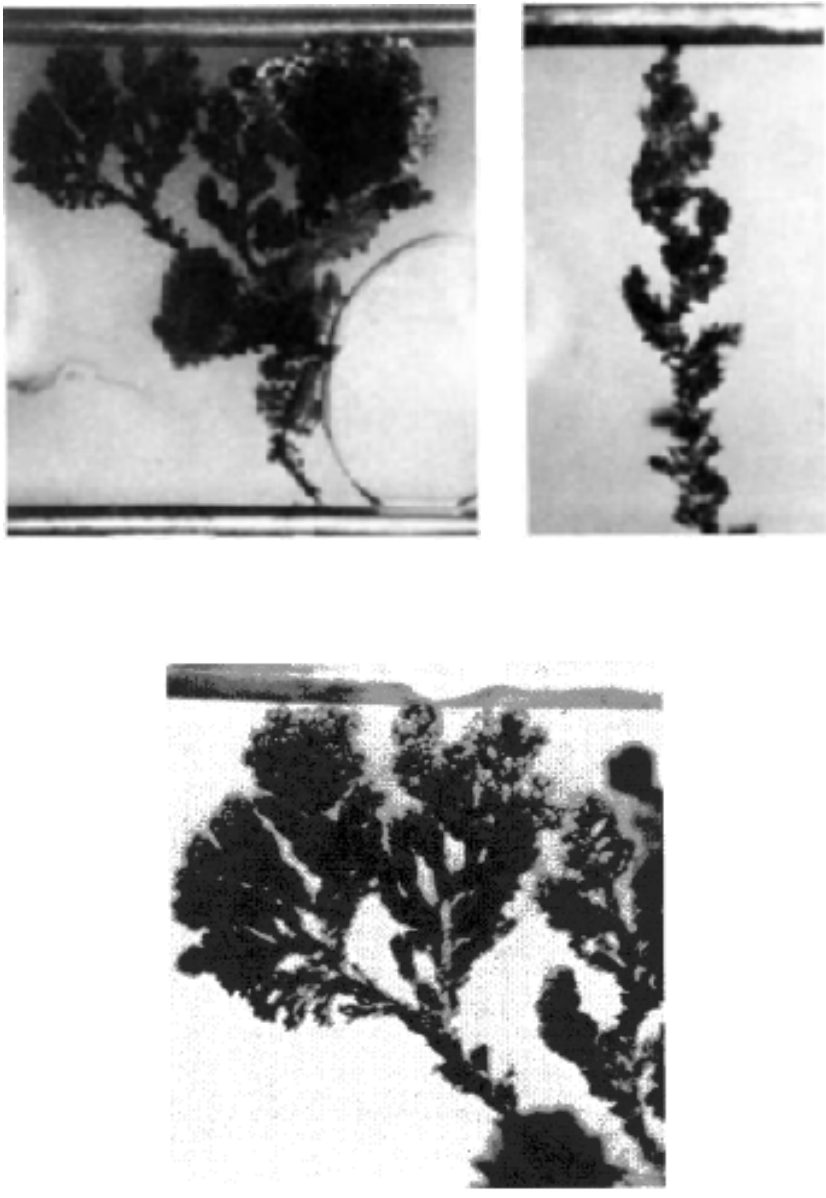

Figure 14. Cu Dendrites Grown From Cu-Ag-P Wires in 10^{-3} M H_2SO_4

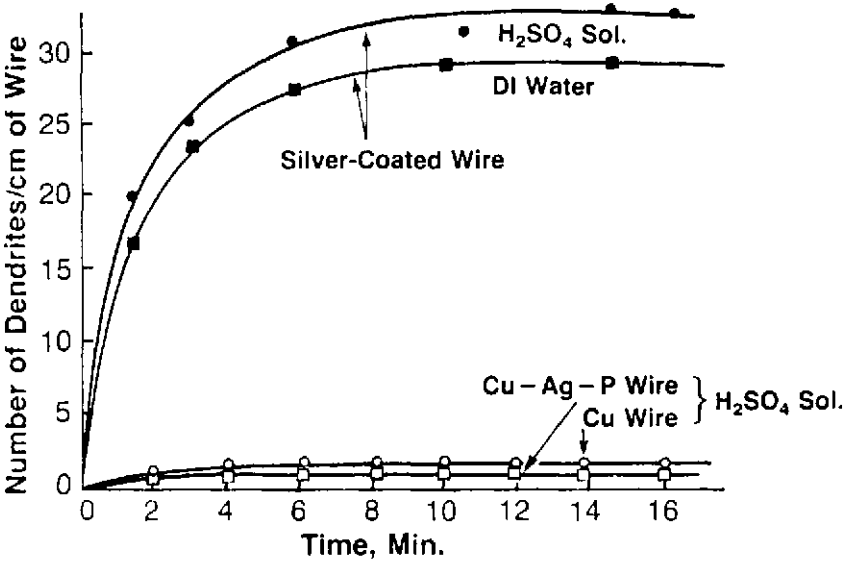

Figure 15. Number of Dendrites Per Centimeter of Wire vs. Time

results can be safely made. It must be ascertained that no abrupt change in the migration behavior is expected outside the experimental range; process and materials variables, on the other hand, are usually kept under control. These variables include the nature and the concentration of impurities. If the impurities are characterizable and their effect on dendritic growth is known, one can often use such species to accelerate or decelerate the process depending on whether they have a catalytic or poisoning effect on the dendrites. In any case, any new test variable introduced for acceleration purposes must not upset the mechanism and the effect on migration kinetics must be understood and quantified. In addition, the surfaces of the conductor may be in a different state of oxidation as a result of process temperature variation, thus altering the migration kinetics. Such changes in migration due to subtle process variation cannot be easily isolated because of the interference of other variables which are either unknown or not controllable to the desired extent. Thus, the characteristics which affect the nucleation and growth kinetics of a dendrite (ionic species, passivation, poisoning, film roughness) are all reflected in the parameter B which can be termed the process-material characteristic function. To some extent, this function can be explored by studying the electrochemical behavior of material systems in aqueous solutions and water-drop tests with respect to specific contaminants, their concentrations, and temperature. The model, therefore, has two parts: (1) the acceleration function which depends on the test conditions (and any process variable which is well characterized) and provides an acceleration factor for the given mechanism no matter what the extent or magnitude of migration is, and (2) the characteristic function, which represents the reciprocal of the magnitude, and which is determined experimentally from the fail distribution, t_{50}, under controlled test conditions employing the appropriate model, e.g., Eq. 11. The objective is to minimize B with the proper choice of process and materials. Knowing the characteristic function means having the tools to design the optimum metallization system for the given environment.

4.2 Materials Characterization by Water-Drop

Some of the water-drop experiments reported here have illustrated the usefulness of such data in terms of combating migration under specific environmental conditions and state of surface oxidation. Other important factors are process residues, pH, etc., which likewise must be studied to determine their level of tolerance for the given situation. It is no wonder that B, as an experimental parameter, varies from metal to metal and from process to process. The key is to identify and quantify the variables responsible for the change.

The metal oxides have shown a considerable slowing of the migration process which resulted in much longer times to produce a dendrite. The effect of the metal oxide on migration is dependent on the film oxide thickness. For instance, a film 50 - 100 Å thick will barely produce detectable changes. One must produce films of the order of 1000 Å to slow down the dendrite growth rate considerably. For instance, a copper oxide film of this magnitude, grown on a substrate, slowed down the process by about two orders of magnitude. Thinner films of copper oxide, as well as Pb oxides, have shown various degrees of effectiveness in reducing the rate of dendritic growth. The effect of oxides is also observed in terms of raising the threshold voltage of pure metals by one half and even one volt for comparable migration times. In addition, the thicker the oxide film the fewer the number of sites at which the dendrite can grow as it is restricted to grow through defects. That dendrites grow selectively is illustrated by the fact that at times growths have been observed in a 30 mil gap in preference to a 3 mil gap under the same voltage. The observations were made in Cu oxide and sulfide films, and only after a substantial delay. The sites were characterized to be defects.

In addition, the oxide provides a high resistance path through which a potential drop occurs. This voltage loss reduces the field across the electrolyte and, therefore, can cause the current to fall below the critical value.

4.3 Effect of Active Impurities

Another important aspect of migration is the concentration of active impurities. For one metal ion concentration and one type of impurity at a given temperature, the critical current density for dendrite growth is (3)

Eq. (23) $$J_{cr} = (\text{Constant})\,(C_i'/r)^{1/3}$$

where C_i' is the concentration of surface active impurities and r is the dendrite diameter. It is theorized that when a constant current is passed through a cell, one crystal will form at the cathode and, as it grows, the current density on its faces decreases. When the current density becomes less that J_{cr} the crystal will become contaminated and will stop growing; a new crystal will then be nucleated and it will grow. Occasionally, it will happen that all but one face of the crystal will become blocked. The last crystal face will then adjust its size so that the current density is equal to J_{cr} and will grow as a whisker or dendrite.

Measurements of critical current densities in solutions containing known concentrations of additives are available only for the growth of Ag whiskers in $AgNO_3$ solutions containing gelatin. At 25°C the constant in

Eq. 23 is equal to 14 $Acm^{4/3}/mol^{1/3}$. From known C_i and r, J_{cr} was calculated. The results show that one can quantify the effect of impurities and incorporate Eq. 23 into the model as a $(J - J_{cr})$ factor.

Ionic species are also responsible for the enhanced conductivity of water films. The species can originate from the process residues left on the substrate (chlorides), from environmental gases dissolved in the water film, or from the corrosion process providing water soluble compounds (19-26). The addition of Cl_2 gas, for instance, can promote dendritic growth in situations where no growth had been possible without the gas. Sbar and Feinstein (19) found no sign of dendrites after Ti-Pd-Cu-Ni-Au biased conductors had been exposed to 85°C/85%RH for 1000 hours. Metal dendrites were observed, however, when the Cl_2 was added. In many instances chlorine acts as a catalyst by forming intermediate compounds which are soluble in water. The controlling electrochemical process usually ends up with lower activation energy. Since the effect of chlorides may be considerable even for surface concentrations which escape detection, quantification of the effect is limited by the analytical capability. When other active species are present, even an accurate analysis would probably not allow a fair prediction of their effect on metal migration because the entire mechanism may change. Therefore, one must know the system well and must know the prevailing mechanism and its sensitivity to secondary effects from other interacting species. Unless the metallurgical and pollutant system is understood, migration quantification on the basis of species concentration and other electrochemical data is difficult. For this reason, we can only speak of modelling in terms of acceleration factor which is based on test variables and is in compliance with the general theory of migration. Models that go beyond the test variables by including the effect of specific species and their concentrations are usually justified on the basis of empirical relationships that quantify the systems' migration behavior with respect to the specific variable.

4.4 Mechanism and Time-to-Failure Results

Relevant works in the electronics packaging industry have dealt with silver, copper, cobalt, zinc, lead, iron, tin, nickel, and gold; however, Ag migration has been the most widely reported (2)(27-35). Barton and Bockris (2) have measured the rate of Ag dendrite growth from the silver and silver nitrate system (0.33 to 12%$AgNO_3$). The current density during dendritic growth is superlinear with respect to the overpotential and proportional to the concentration of silver ions. A critical current density (J_{cr}) exists for the initiation of dendritic growth, which is proportional to the silver concentration and increases as the radius of the electrode decreases. The dendritic growth tip is parabolic with a radius of curvature of $\sim 10^{-6}$

cm. The current density is controlled by diffusion at all conditions and obeys laws characteristic of spherical diffusion for small radii. The rate of dendrite growth is also controlled by the kinetics of the Ag^+ ion position on the dendrite tip (charge exchange and spherical diffusion controlled). For low exchange currents the dendritic growth rate is linear with overvoltage, but for high current densities, the velocity of growth is proportional to the square of the applied overvoltage.

Barton and Bockris have, in fact, verified the electrochemical kinetics with $AgNO_3$ solutions within the concentrations mentioned. For diffusion controlled migration and low current density,

Eq. (24) $$J = (ZFDC/\delta) \cdot (ZF/RT)\, V$$

For these conditions:

V = 20mV, applied overvoltage,
C = 10^{-5} mole/liter,
S = 10^{-2}, diffusion layer,
D = 2×10^{-5} cm^2/sec,

the value of $J \approx 1$ A/cm^2 at room temperature.

In general the current density is expressed as an hyperbolic sine (6)(7) which reduces to Eq. 24 for low voltage [$(ZF/RT)\, V << 1$].

The superlinear behavior, therefore, is expected at the higher voltage. The results in Fig. 4, which is a plot of the reciprocal of t_f versus the voltage, show a threshold of 4 volts in both silicone rubber and epoxy backsealed modules with a linear fit. Another fit can be obtained by forcing the curve to pass through the origin, in which case the reciprocal time-to-failure would depend on V^2. If one considers that the voltage-drop at the anode and cathode is ~1/2 volt and that the water-drop experiments with Ag electrodes have shown dendrites growing under 1/2 volt bias, the fit through the origin is not unreasonable for analytical purpose, to show its consistency with the theory.

On a statistical basis, a V^2 dependence is also in line with the fact that impurities are not homogeneously distributed. As voltages across the gap raise the current density from below the critical value at the various sites, having different thresholds, the dependence of dendrite growth on applied voltage appears stronger than it actually is due to the tail of the J_{cr} distribution dictated by the impurities. This means that there cannot be a cessation of migration activity at a specific voltage since we are dealing with statistics. Therefore, a voltage intercept must be more of a gradual fading than an abrupt ending of the migration process. In any case, the level of activity is obviously very low below four volts and is inconsequential

from a fail rate point of view regardless of interpretation. Again, it must be emphasized that since the threshold depends on the level and type of impurities (among other things), the voltage intercept value must be considered a characteristic of the particular process.

4.5 Polymer Coating

The leakage current may include extremely low components of metallic ions derived from the anode, but the predominance is due to indifferent ions and electrolyzed substances, mainly water through hydrogen reduction. Gaseous pollutants dissolve into the water film or polymer and maintain concentration levels proportional to the outside vapor pressure according to Henry's law applicable to dilute solutions. Among the notorious pollutants are SO_2, NO_2, and CO_2, which provide the ionic species for conduction through electrolysis.

Water electrolysis, as mentioned, is probably a large contributor to the current. It increases with voltage and, consequently, the migration component of the metal ions grows with it, as it is proportional to the total current via the transport number. Despite the initial very low concentration of metallic ions, the rate of metal deposition is increased when the electrolysis is carried out with a large current caused by the reduction of another substance. This phenomenon is called "exaltation of the migration current" by simultaneous electrolysis of another compound or substance (3).

In the case of a polymeric coating, the electrolytic process must eventually achieve equilibrium with the diffusion process originating at the polymer surface, which interacts with the outside environment through adsorption. It is assumed that initially the external pollutants have not significantly permeated the film and that considerable time would be required to reach the steady-state concentration, thus satisfying the diffusion and migration components near the electrodes. During the transient period, a certain volume of the polymer around the electrodes, extending to the limits of field interaction, will have to be "charged" with ions at some rate zFC_i, which will vanish at steady state, whatever the time required. Likewise, the voltage effect diminishes with time, as predicted by the model and supported by the experimental results (Fig. 10). The process of achieving steady state is quite slow because the small diffusivity, estimated at $\sim 10^{-9}$ cm^2/hrs. and 85°C. This is considerably lower than the diffusivity of water through epoxies. This may be due to solvation and complexing which can curtail the diffusion process ascribable to ionic size increase and alteration of the electric interaction. Such an argument can also be made to explain the relatively high activation energy.

5.0 SUMMARY

The time-to-failure models, derived on the basis of the electrochemistry of solutions, theory of adsorption and condensation, and transport through water films and polymers are characterized by the product of four functions:

$$t_f = B(M,P)\ F(T)\ G(RH,T)\ H(E,T)$$

where B(M,P) is a function of materials and process parameters and must be studied with respect to materials properties, contaminants, and prevailing mechanism. It is a constant for the same material system under controlled process. F(T) is the integrated form of the Arrhenius equation. G(RH,T) is the relative humidity function (which also depends on T) which can assume the B.E.T. form or the pore-condensation probability form, both conforming to established physical interactions between liquids and solids. Other forms such as pure exponential (e^{BRH}), relative humidity to a power (RH^n) and other similar fitted functions are not sufficiently flexible to express water film adsorption throughout the practical RH range, and their extrapolation to low RH values from test conditions is questionable. They are not unique and fall within the reach of the two basic functions above. H(E,T) is the electric field or voltage function, which also depends on temperature. When a polymer coating is present which adheres well to the substrate and electrodes, the function assumes a transient form to express current leakage as a function of time, which is the result of non steady-state between migration and diffusion, the latter becoming rate controlling with time. For short times, the function reduces to the same form applicable to dendritic growth, however, for long times the leakage follows an exponential decay growth such that the insulation resistance approaches a limit. This is the point when migration is completely dependent on the electrolyzable species diffused from the outside.

The most important variable in metal migration is relative humidity because, in the absence of a surface water film, no electrolytic process can take place.

The activation energy for the migration process (leakage) in the presence of a polymeric film is much higher than that for dendritic growths because in the former the diffusion through the polymer is rate-controlling, while in dendritic growth the diffusion through the water film controls the process.

Common metal films used in the electronics and semiconductor industry show voltage thresholds between 0.5 and 1.6 volts when tested by water-drop (DI water) with a clean unoxidized surface. On the other hand, the voltage threshold established through the time-to-failure statistics obtained from T/H testing at 85°C/80%RH show higher threshold (e.g. 4

volts for silver) by extrapolation from 20, 10, and 5 volts data. It is difficult to determine the actual shape of the curve (t_f^{-1} vs V) below 5 volts because the probability of producing a fail under those conditions is very low, such that no fails are possible for the test duration.

The dramatic difference between Ag-migration results in the presence of a silicone rubber backseal and epoxy backseal indicates that species that can be leached out from a polymer play an important role in the failure mechanism, and can introduce a bimodal fail distribution.

A critical current density must be achieved before dendritic growth can occur. In many instances the critical current has ranged from 0.1 to 1 A/cm^2, depending on temperature, type of metal, and impurities.

At critical current density, dendrites begin to form in cathodic regions which have achieved sharp "macro-rough" geometries, where extremely high localized currents of the order of 10^3 A/cm^2 develop as a result of parabolic or spherical diffusion to the tip of the dendrite. Dendritic growth is, therefore, a special case of migration, the case which must satisfy the requirement of current density and suitable conditions for single crystal formation.

Migration-induced failures strongly depend on the environmental atmosphere which modifies the metal migration behavior by altering the leakage current and even the rate limiting step as a result of surface passivation or other gating mechanism. In addition, process residues also play an important role in metal migration through water adsorption and conductivity enhancement.

Oxidation and other insoluble film formation curtail migration and even stop it if the films are of sufficient thickness and tenacity. For instance, the low migration associated with Cu-oxide films indicates that such oxide is a good barrier to ion exchange at the oxide-metal interface and that the oxide has a very low solubility. Other oxides with such properties behave similarly.

Ni has the highest voltage threshold among the various metals tested by water-drop test. Its migration is drastically reduced by the formation of an oxide or hydroxide layer. Introduction of impurities which raise the pH of the system and favor the formation of $Ni(OH)_2$ is an important consideration in the prevention of Ni-migration. At temperatures greater than 100°C, the hydroxide impurity layer is not formed, while at the lower temperatures the migration process can be practically stopped by such a layer.

The basic model in its general form presents a good base for wide coverage over the diverse applications. The experimental data on Ag-migration and leakage kinetics through epoxy coating for acceleration purpose, serve a starting point and set the stage for further evaluation with other metals, which are expected to produce different parameters values for H, M, V_{TH}, F and B. The model's ability to be expressed as a function

of different materials and process contamination depends on how well the variables can be controlled and studied and to what extent they affect metal migration and leakage.

6.0 ACKNOWLEDGEMENT

Stephen Drofitz is acknowledged for performing the water-drop experiments on thin films and Cheryl Hamilton for typing the manuscript.

7.0 REFERENCES

1. Di Giacomo, G., Metal Migration (Ag, Cu, Pb) in Encapsulated Modules and Time-to-Fail Model as a Function of the Environment and Package Properties, *Proceedings Reliability Physics Symposium* (1982)

2. Barton, J.L. and Bockris, J.O., The Electrolytic Growth of Dendrites from Ionic Solutions, *J. Electrochem. Soc.*, Vol 268A (1962)

3. Price, P.B. et al., On the Growth and Properties of Electrolytic Whiskers, *Acta Metallurgica*, Vol. 6, August (1968)

4. Bockris and Reddy, *Modern Electrochemistry*, Vol. 1 and 2, Plenum Press, New York (1970)

5. Adamson, A.W., *Physical Chemistry of Surfaces*, Interscience Publishers, New York (1967)

6. Overbeck, J.Th.G., Colloid and Surface Chemistry, *Center for Advanced Engineering Studies*, MIT (1971)

7. Bowden, F.P. and Throssell, W.R., Adsorption of Water Vapors on Solid Surfaces, *Proc. Roy. Soc.*, Vol. A209, p. 29 (1951)

8. Di Giacomo, G., Current Leakage Kinetics Across Tinned Cr/Cu Lands Having Epoxy Overlay, *IEEE Transaction on Components, Hybrids, and Manufacturing Technology*, Vol. CHMT8, No. 4, December (1985)

9. Chariot, G., Badoz-Lambling, J. and Tremillon, B., *Electrochemical Reactions*, pp 3-30, Elsevier, New York (1962)

10. Vagramyan, A.T. and Zhamagortsyants, M.A., *Electrodeposition of Metals and Inhibiting Adsorption*, TT-72-51030, Translated from Russian (1969)

11. Savchenkov, G.F. and Uvarov, L.A, Study of the Anodic Behavior of Metals of the Iron Group in a Wide Range of Temperatures; The Influence of Temperature on the Critical Passivation Current of Nickel, *Zashchita Metallov*, 1:636 (1965)

12. Bond, A.P. and Uhlig, H.H., *J. Electrochem. Soc.*, 107:488 (1960)

13. Okamoto, G. et al, *J. Electrochem. Soc.*, Japan, 25:199 (1957)

14. Vagramyan, A.T. and Uvarov, L.A., Effect of Inhibition on the Electrodeposition of Metals, *Transactions of Institute of Metal Finishing*, Vol. 39 (1962)

15. Ohya, H., A Study of Pore Size Distribution of Modified Ultra Thin Membranes, *J. Applied Polymer Sci.*, Vol. 18 (1974)

16. Gregg, S.J. and Sing, K.S.W., *Adsorption Surface Area and Porosity*, Academic Press, 1967

17. Hills, G.J., Kinetic Studies of Ionic Migration, *International Symposium of the Electrochemical Society*, 1964

18. Tajima, S. and Ogata, M., Electrocrystallization of Ni and Co Dendrites From Aqueous Solutions II, *Electrochimica Acta*, Vol. 15, pp 61-64 (1970)

19. Sbar, N.L. and Feinstein, L.G., *IEEE Trans. Parts Hybrids Packaging*, PHP 13, 3, 208 (1977)

20. Shumka, A. and Piety, R.R. *13th Annual Proc. Reliability Physics Symp. IEEE*, p 93 (1975)

21. Hakim, E.B. and Shappirio, J.M., *Solid State Technol.*, p 66, April (1975)

22. Kozakiewicz, R.P. and Sbar, N.S., *Extended Abstracts, Spring Meet. Electrochem. Soc.*, p 123 (1977)

23. Labuda, E.F., Herb, G.K., Ryden, W.D., Fritzinger, L.B. and Szabo, J.M. Jr., *Extended Abstracts, Spring Meet. Electrochem. Soc.*, p 195 (1974)

24. Sbar, N.L., *IEEE Trans. Parts Hybrids Packaging*, PHP 12, n 3, p 176 (1976)

25. Fuss, F.N., Hartwig, C.T. and Morabito, J.M., *Thin Solid Films*, Vol 43, 12, p 189 (1977)

26. Sbar, N.S. and Kozakiewicz, R.P., *IEEE Trans. Electron Devices*, ED-26, n 1, p 56 (1979)

27. Kohman, G.T., Hermance, H.W. and Downes, G.H., *Bell Syst. Techn. J,* Vol. 34, p 1115 (1955)

28. Williams and Herrmann, *IRE Trans. Reliability Quality Control,* PGRQC, 11 (1956)

29. Chaikin, Janney, Church and McClelland, *Ind. Eng. Chem,* 51, 299 (1959)

30. Wirtz, G.P., *Proc 22nd Electronic Components Conf,* P 840 (1971)

31. Stein, S.J., Huang, C., Cang, L. and Schultz, G., *Solid State Tech.,* p 25 (1975)

32. Licari, J.J., Perkins, K.L. Caruso, S.V., *Proc. Int. Microelectronic Symp. (ISHM),* p 65 (1975)

33. Rogren, P.E., *Proc. Int. Microelectronic Symp. (ISHM),* p 267 (1976)

34. Pantanelli, G.P., and Sedora, E.J., *Int. Conf. on Manufacturing and Packaging Technology for Hybrid Circuits,* Paris, France (1976)

35. Naguib, H.M. and McLaurin, B.K., *IEEE Trans. Components Hybrids Manuf. Technol.,* CHMT 2, p 196-207 (1979)

7

ELECTROCHEMICAL CAPACITORS

Ian D. Raistrick

1.0 INTRODUCTION

Electrochemical capacitors differ fundamentally from both conventional capacitors and batteries in their mechanism of charge separation and energy storage. Conventional types of capacitors store *electrostatic* energy when an electric field is applied across a dielectric. Batteries store *chemical* energy in the form of reactants that combine and release the Gibbs free energy of reaction when an external electronic connection is made. In the simplest case, an electrochemical capacitor makes use of the double-layer of charge that forms spontaneously at the interface between a metallic electrode and an ionically conducting electrolyte. Depending on the origin of the interaction between the electrode and the electrolyte, the associated capacitance is usually in the range of tens to hundreds of μF per cm^2 of interface area. It is therefore evident that, if an electrode with a large specific surface area is used, significant energy storage is possible at this type of interface. Suppose, for example, that a material with a specific surface area of 100 m^2/g and a density of 3 g/cm^3 is employed in a 10-μm-thick layer. Each electrode would then have an effective capacitance of about 10 mF/cm^2. Such a large capacitance is of obvious interest in energy storage and power conditioning applications. The earliest suggestion that practical devices may be constructed on this principle appears to be due to Becker (1).

A schematic drawing of an electrochemical capacitor, based on symmetric electrodes is shown in Fig. 1. Here, the active plates are arranged in a *bipolar* configuration (a current collector acts as a positive electrode for one cell and a negative electrode for the neighboring cell).

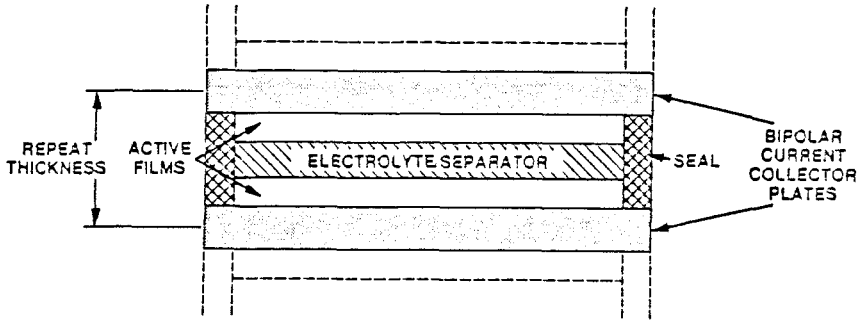

Figure 1. Bipolar arrangement of electrodes in an electrochemical capacitor.

The electrolyte compartments are electrically isolated from one another. This is the simplest and most common arrangement for this type of device. It ensures a uniform current density through the structure, thus minimizing ohmic losses caused by current bunching at collector tabs, and has the minimum intrinsic inductance (important for pulse applications). A characteristic of capacitors is that they are usually built with identical positive and negative electrodes. This is not always the case (see Section 4.4 for examples), but, if the electrodes are composed of different materials, the cells will not typically have zero voltage when uncharged.

In general, the properties of electrochemical capacitors are quite different from those of other types of capacitors. Like batteries, electrochemical capacitors are essentially low-voltage devices: their breakdown occurs by electrolysis of the electrolyte. For aqueous electrolytes, the thermodynamic potential at which this occurs is about 1.2 volts. For organic solvent-based systems, it may be as high as 3 or 4 volts, whereas, for silver and copper solid electrolytes, it is less than 1 volt. This property severely limits the amount of stored energy (U) for a given capacitance because $U = 1/2CV^2$.

In an ideal capacitor, the amount of charge stored, Q, is proportional to the potential difference across the dielectric, $Q = CV$. Due to the nature of the interfaces, electrochemical capacitors seldom show this simple behavior. Usually, the dependence of C on V is complicated by chemical interactions. Even in the simplest double-layer capacitors (see Section 2.2), the presence of mobile electrolyte ions ensures a nonlinear dependence of charge on potential. Overall, however, the total quantity of stored charge is usually very much higher than that available from a conventional capacitor.

Probably more important for many applications than the total energy storage capability of a device, however, are its ability to deliver current and the nature of its electrical response, as compared to that of an ideal capacitor. Electrolytes have an appreciable, and sometimes very large, resistivity that often dominates the electrical behavior of the device, not only in the sense that it controls the time constant of the discharge process, but also in that the current distribution within the electrode structure is strongly dependent on this quantity. The microstructure of the high surface-area electrode is often of great importance. Electrochemical capacitors, therefore, are usually characterized by a relatively large effective series resistance (esr).

The principal application of electrochemical capacitors to date is as backup energy for integrated electronics. Here, the long life, small size, wide temperature range, and low cost of carbon electrochemical capacitors give them a distinct advantage over, for example, rechargeable batteries. This mode of operation, where the capacitor is kept continually charged

by line power, is clearly favorable to capacitors, whose absolute energy storage capability is not as high as that of batteries (especially primary batteries). A similar consideration holds for applications such as weapons fusing, where the capacitor is charged only a short time before being needed, and until that time has no energy content. Various types of energy conditioning applications may also prove attractive. In this case, primary energy is supplied from another source, but peak or pulse power is provided by the capacitor. Such an application takes advantage of the high power capability of electrochemical capacitors, compared with batteries. In contrast, the large capacitance per unit volume of electrochemical devices, compared with conventional (including electrolytic) capacitors, offers the possibility of using them in compact filters for power supplies. Clearly, the relatively high series resistance and poor a.c. performance to date are hindrances for this last application.

In the next two sections, the principal mechanisms of charge storage and the electrical behavior of electrochemical capacitors are discussed in a general way. In the remaining sections, individual families of devices and materials that have either found, or show promise for, applications are covered in more detail.

2.0 MECHANISMS OF CHARGE STORAGE AT THE ELECTROCHEMICAL INTERFACE

In this section, the main types of electrode processes that may be used for capacitative electrochemical energy storage are briefly described. Detailed description of specific systems is reserved for later sections. A formal distinction is made here between electrochemical processes that are localized at, or near, the electrolyte/electrode boundary and those that involve bulk phases. The latter type of reactions are more appropriately classified as belonging to batteries. The distinction is not always clear, since in some 'capacitor' materials, reactions apparently extend over a significant distance from the surface, and in some batteries, the active materials may be deployed in very thin films, with the objective of improving power. Further, in very high surface-area materials such as some transition metal oxides and the conducting polymers, the active material is present in such a small particle size and is so completely penetrated by the electrolyte phase that almost the entire material may be regarded as a surface species. In the following paragraphs, however, we treat idealized situations, in which the distinctions are clear.

2.1 Double-Layer Capacitors

In the absence of any chemical interactions between a metal and an

electrolyte solution, a double-layer capacitance spontaneously occurs. This is due to the difference in work function between the two phases, which causes a small charge to flow across the interface to equalize the electrochemical potentials.

The excess charge is accommodated in a surface layer on the metal side of the interface, but on the electrolyte side the charged layer has a more complex structure (2). Farthest from the interface is the 'diffuse region' in which the excess charge decays to zero in the bulk of the electrolyte according to Boltzmann statistics.

Eq. (1) $$\rho(x) = \Sigma z_i F c_i^{\circ} \exp\{ [-z_i F \phi(x)] / [RT] \}$$

Here x is the distance from a reference plane, corresponding to the distance of closest approach of hydrated ions; z_i and c_i° are the charge number and unperturbed concentration of the i^{th} ionic species; ϕ is the local electric potential; and R, F, and T are the gas constant, Faraday's constant, and the absolute temperature. The situation is quite analogous to the junction between a semiconductor and a metal, except that, in an electrolyte, the density of ionic states close to the interface is large compared with the electronic density of states, and therefore an ionic rather than an electronic space charge forms. This perturbation in concentration extends into the electrolyte for a characteristic distance known as the Debye length:

Eq. (2) $$L_d = \left[\frac{RT \epsilon \epsilon_o}{2 z_i^2 F^2 c_i^{\circ}} \right]^{1/2}$$

Here ϵ is the relative dielectric constant of the electrolyte, and ϵ_o is the permittivity of free space. Electrically, the diffuse part of the double layer behaves as a potential-dependent capacitor with a plate separation given by the Debye length. The capacitance is

Eq. (3) $$C_d = \left[\frac{2 z_i^2 F^2 \epsilon \epsilon_o c_i^{\circ}}{RT} \right]^{1/2} \cosh \left[\frac{zF\phi_o}{2RT} \right]$$

where ϕ_o is the potential at $x = 0$ (measured relative to $\phi = 0$ at $x = \infty$).

In dilute solutions, the potential drop in the diffuse region is significant, but in energy storage devices, where high-conductivity situations are usually encountered, this component is less important than that associated with the 'compact' part of the double layer.

This component is normally described in terms of a 'molecular capacitor' model. According to this description, the electrode is covered with a monolayer of solvent molecules. The electrolyte ions are essentially excluded from this layer, except when strong chemical interactions result

in desolvation and specific adsorption. The solvent molecules are highly oriented in the field and, for the case of water, have a much reduced dielectric constant. A layer of partially oriented water, which also contributes to the hydration sheath of the first layer of solvated ions, lies outside the first solvent layer (2). In recent years, an alternative description of the compact layer has also been considered. This is the 'jellium' or 'electronic capacitor' model. At the interface, the wave function of the electrons extends significantly out into the electrolyte, leading to an effective charge separation. Clearly, the two models differ conceptually to a significant degree. The experimental evidence which relates to the two models has recently been reviewed by Martynov and Salem (3).

From the point of view of charge storage devices, the main properties of the double layer are as follows:

— The double layer behaves as a capacitance in series with the electrolyte resistance.

— For metallic conductors, the capacitance is on the order of a few tens of μF per cm^2. In order to achieve significant stored energy density, very high surface-area electrodes must be employed. This raises problems of *distributed* charging processes, which will be addressed in a later section.

— For a smooth electrode, the double-layer capacitance shows no frequency dependence up to ionic relaxation frequencies. This frequency lies well outside the range of times useful for energy storage, which are of the order of the RC time constant or longer.

— The capacitance does show a significant potential dependence because of non-electrostatic (chemical) factors, as well as purely coulombic interactions.

2.2 Electrosorption Capacitance

The double-layer charging process described in the previous section may be regarded as taking place without complete charge-transfer to or from ionic species either in the solution or adsorbed at the interface. Evidently, specifically adsorbed species undergo some chemical interaction with the electrode and there is, therefore, some degree of charge transference between the metal and the adsorbate. Using surface analytical techniques, it is possible to assess the degree of covalency of the bond.

Some species, however, can undergo a well-defined Faradaic charge-

transfer process to become adsorbed on the surface. Well-known examples of this type of reaction involve electrosorption of protons at noble metal surfaces, e.g.,

$$H_{aq}^{+} + Pt + 1e^{-} \longrightarrow Pt - H_{ads}$$

This reaction has been suggested as a vehicle for capacitative energy storage (4) and demonstrated in a solid polymer electrolyte configuration (5-7). At least some of the transition metal oxide systems, discussed in greater detail later, also fall into this category, e.g., thermal RuO_2 and IrO_2.

Because an electron is transferred for every adsorbed proton, much greater charge densities and capacitances are possible than is the case for the pure double-layer behavior discussed above. For the example of H electrosorption on polycrystalline platinum, the charge density associated with a fully covered surface is 210 $\mu C/cm^2$. The advantage of this is that less material, i.e., a thinner active layer, is required. Greater charge densities and capacitances not only reduce the mass and volume of a device; they also render distributed charging effects less significant. The differential capacitance associated with electrosorption processes is often called a 'pseudocapacitance' (8):

Eq. (4)
$$C_{ads} = \frac{\partial q}{\partial E} = q_o \frac{\partial \theta}{\partial E}$$

where θ is the fractional surface coverage by the adsorbed species and q_o is the charge associated with the adsorption of a monolayer ($\theta = 1$).

Because the proton adsorbs at a specific site on the surface, with a well-defined enthalpy of adsorption, the dependence of differential capacitance on electrode potential may be quite strong. On platinum, for example, several different site energies may be resolved in the underpotential deposition region.

Each adsorption process may be described in terms of an adsorption isotherm, which quantifies the relationship between the degree of coverage, θ, and the electrode potential. The simplest example is the Langmuir isotherm (9), which assumes no interaction between the adsorbed species (i.e., a constant free energy of adsorption, ΔG°). The coverage is just the balance between an enthalpic term (driving the adsorption process) and the entropic term, giving the isotherm:

Eq. (5)
$$\frac{\theta}{1 - \theta} = c_i \exp\frac{-\Delta G^{\circ}}{RT} \quad \exp\frac{-z_i EF}{RT}$$

where c_i is the bulk concentration of i.

More sophisticated treatments of electrosorption equilibria lead to other formulations of the isotherms (10)(11). Terms that may be included are those due to surface heterogeneity and lateral interactions between the adsorbed species. In the Temkin isotherm, these terms appear as a parameter, r, which reduces the free energy of adsorption :

Eq. (6) $$\frac{\theta}{1-\theta} = c_i \exp \frac{-\Delta G^\circ - r\theta}{RT} \exp \frac{-z_i EF}{RT}$$

In Fig. 2(a), this isotherm is plotted for different values of the interaction parameter, r. For the case of r = 0, the isotherm corresponds to that of Langmuir. From the coverage equations, it is straightforward to derive the equations for the differential capacitance.

Eq. (7) $$C_{ads}^{\text{Langmuir}} = q_o \frac{zF}{RT} \theta(1-\theta)$$

Eq. (8) $$C_{ads}^{\text{Temkin}} = q_o \frac{zF}{RT} \frac{\theta(1-\theta)}{1+r\theta(1-\theta)}$$

The potential dependence of C_{ads} is shown graphically in Fig. 2(b), corresponding to the r values in Fig. 2(a). Dolin and Ershler (12) were the first to investigate pseudocapacitance experimentally. Using a.c. methods they found C_{ads}'s as high as 2 mF/cm^2 for H on platinum. For a more complete discussion of interaction terms and pseudocapacitance, see Conway et al. (13).

The strong dependence of charge on electrode potential exhibited by a system such as H/Pt may be a disadvantage in capacitor applications. A symmetrical device would operate over a rather narrow potential range. Some conducting metal oxides of the transition and noble metals, however, show very broad capacitance/potential behavior. This implies that adsorption sites with a very wide distribution of free energies are available for the protons. This behavior may be formally described in terms of several broad, overlapping Temkin isotherms. It is likely that the origin of this behavior is to be found in the following effects:

— a broad distribution of enthalpies of ionic interactions, and

— a strong dependence of Fermi level on amount of injected electronic charge, i.e., a rather small density of states function over the potential range.

In contrast to the true double-layer capacitor situation, we may also

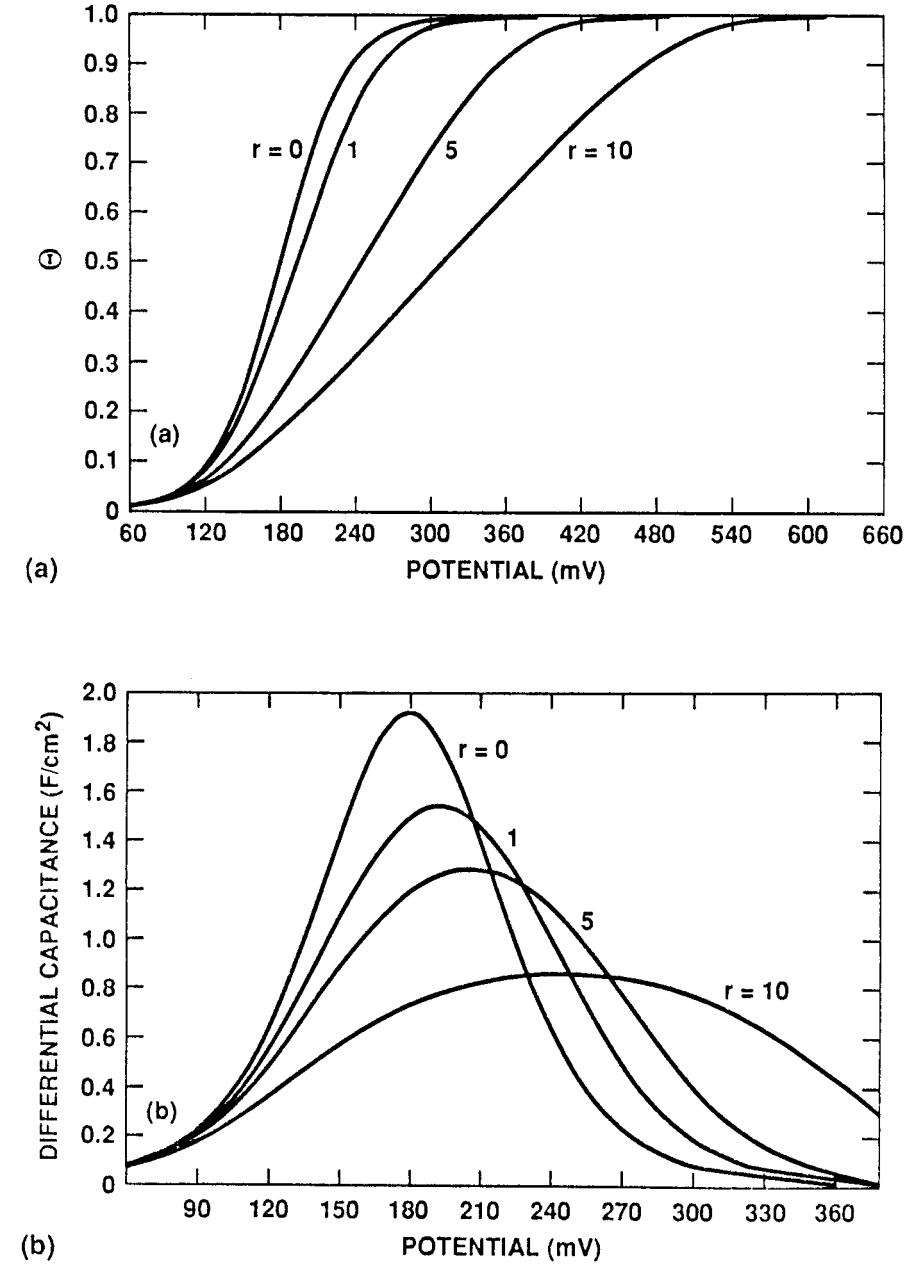

Figure 2. (a) Plot of Temkin isotherm for various values of the interaction parameter, r. (b) Differential capacitance corresponding to the same r-values.

have to consider the kinetic aspects of the charge-storage reaction. If a heterogeneous electron-transfer reaction is involved, then this reaction proceeds at a finite rate, which may be slow enough to appear as an additional resistance in the charging process. An equivalent circuit which describes the *small-signal* response of an electrosorption capacitor (C_2) with finite charging kinetics, as well as finite series electrolyte resistance, R_1, is shown in Fig. 3. The true double-layer capacitance, corresponding to the effects discussed in the previous section is also included as C_1. The charge-transfer resistance, R_2, is related to the exchange current density by the equation

Eq. (9) $$R_2 = RT/z_i Fi_o$$

The exchange current may also vary with the electrode potential through the dependence of the surface coverage on potential. It should be noted, however, that the kinetics will not be of the usual Butler-Volmer type, which describes steady-state behavior, because, in the type of reaction we are considering, there is no true steady-state current, and a continuous series of open circuit potentials occurs depending on the amount of charge that has been passed to or from the electrode. The kinetics are most conveniently discussed in terms of small-signal behavior, where the kinetic parameters can be assumed fixed by the d.c. potential and then investigated by a small-signal perturbation around the d.c. level. In this way it proves possible, in principle, to study the d.c. potential dependence of R_2 and C_2. There appear to have been rather few attempts to make electrochemical studies of this type. For the case of platinum, the kinetic parameters governing the electrosorption of hydrogen have been determined (Volmer reaction) (14).

In principle, of course, mass transport limitations can also occur in the electrolyte phase. However, this would usually occur (at least for protons) only at very low concentrations. Under these circumstances, diffusion as well as migration would play a role in limiting the interface charging rate, and the electrolyte could no longer be represented as a pure resistance in the circuit above.

2.3 Surface Redox Processes

In the previous section, the electrosorption of mobile ionic species onto an electrode surface was discussed. It is also possible to imagine the oxidation and reduction (with charge transfer) of immobile surface-bonded species.

$$S\text{-}Ox + e^- + C^+ \longrightarrow S\text{-}Red$$

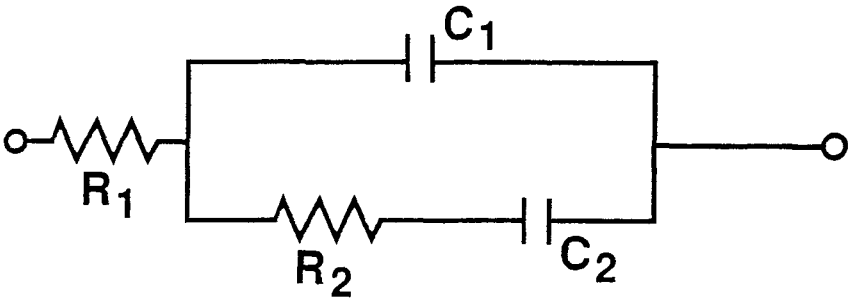

Figure 3. Equivalent circuit for an electrosorption process: R_1 is the bulk solution resistance, R_2 is the charge transfer (kinetic) resistance, C_1 is the double-layer capacitance, and C_2 is the adsorption pseudocapacitance.

Here, S represents the electrode surface. As indicated in this equation, counterion movement, C^+, in or out of the interface region is necessary to restore local electroneutrality. Note that either anions or cations or both may be involved. The extent to which the charge is localized on the surface and the detailed involvement of the counterion must be determined for each individual case. The clearest example of this type of behavior might be that found in chemically modified electrodes, in which a redox species is bound to an electrode surface by means of an electrochemically inactive polymer (15)(16). An example of the modification of a surface by an adsorbed redox species is to be found in a patent by Calahan et al. (17), where metallorganic molecules are adsorbed onto the surface of carbon, thus increasing the charge-storage capability of the surface. In fact, it is likely that many carbons derive a significant fraction of their charge-storage capacity from the oxidation and reduction of surface functional groups, e.g., the quinone-hydroquinone type of reaction (18):

$$Q + 2H^+ + 2e^- \rightarrow H_2Q$$

As in the previous section, electrode kinetics may be important in determining the total series resistance and hence the charge and discharge rate. As mentioned above, movement of the counterion may also be important. This aspect may be easily overlooked, because the counterion may not be directly involved in a formal description of the charge-transfer reaction. It is probably important in determining the rates of oxidation and reduction at immobilized electroactive layers (e.g., in Langmuir-Blodgett films) and in conducting polymers (e.g., polyacetylene).

2.4 Thin-Film Bulk Reaction

Depending on the system, it could certainly be argued that reactions involving charge storage in conducting polymer electrodes and in some thin-film oxide systems (e.g., anodically grown IrO_2 and nickel oxide) are actually bulk reactions which extend throughout the layer of electroactive material. Charge is injected into a π electron system in the polymer and an electrolyte cation or anion moves in or out of the polymer as the charge-compensating species. Here, the polymer macromolecule behaves as a giant redox system. The conceptual distinction between polymers and some metal oxide systems (especially highly hydrated anodic films) may not be large. The bands of the inorganic crystal act in the same way as the extended π electron systems in the polymers, and the transition metal ions undergo redox processes. For a thin film, the electrical response will appear to be capacitative, as long as solid-state diffusion kinetics are

rapid enough to allow equilibration of the concentration profiles throughout the film at the times of interest (see Section 3.5).

In addition to considerations of solid-state diffusion coefficients and the intrinsic kinetics of the interfacial electrochemistry, we may also have to consider nucleation and growth kinetics of new phases that are produced or removed during the reaction.

As was mentioned in the introduction, this type of reaction is more usually associated with secondary batteries than with capacitors. Most battery systems are designed to produce a relatively flat potential vs. charge relationship during discharge (Fig. 4a), in contrast to the linear fall in potential expected from a capacitor (Fig. 4b). In a chemical reaction that involves the coexistence of multiple phases, the equilibrium potential is, in fact, independent of the degree of discharge throughout the multiphase region. If such electrodes are deployed in thin films, then the entire charge will be delivered in a narrow range of voltage, followed by a precipitous fall after the reactants have been consumed. The cyclic voltammograms for a single electrode corresponding to the 'battery' and 'capacitor' situations, measured with respect to an arbitrary reference electrode, are shown schematically in Figs. 4c and 4d. The behavior of a 'capacitor' constructed from symmetric electrodes of these two systems is shown in Figs. 4e and 4f. Depending on the application, these alternative characteristics may be an advantage or a disadvantage. The possibility also exists of combining two chemically different electrodes into a single device. This would have the effect of shifting the origins of Figs. 4e and 4f.

Solid-state reactions leading to useful energy storage or conditioning processes have been intensively investigated during the last two decades from a battery development point of view (19-21).

The amount of charge stored in an electrode is a function of the potential, and is related to the amount of stored energy:

Eq. (10) $$U = \int_{E_1}^{E_2} Q(E)dE$$

We can therefore define an equivalent integral capacitance per electrode

Eq. (11) $$C = 2U/\Delta E^2$$

where ΔE is the potential range over which the device is to be used. We can also define a differential capacitance dQ/dE, which will be useful later when discussing the kinetics of these types of devices.

Eq. (12) $$C = \int (dQ/dE)dE$$

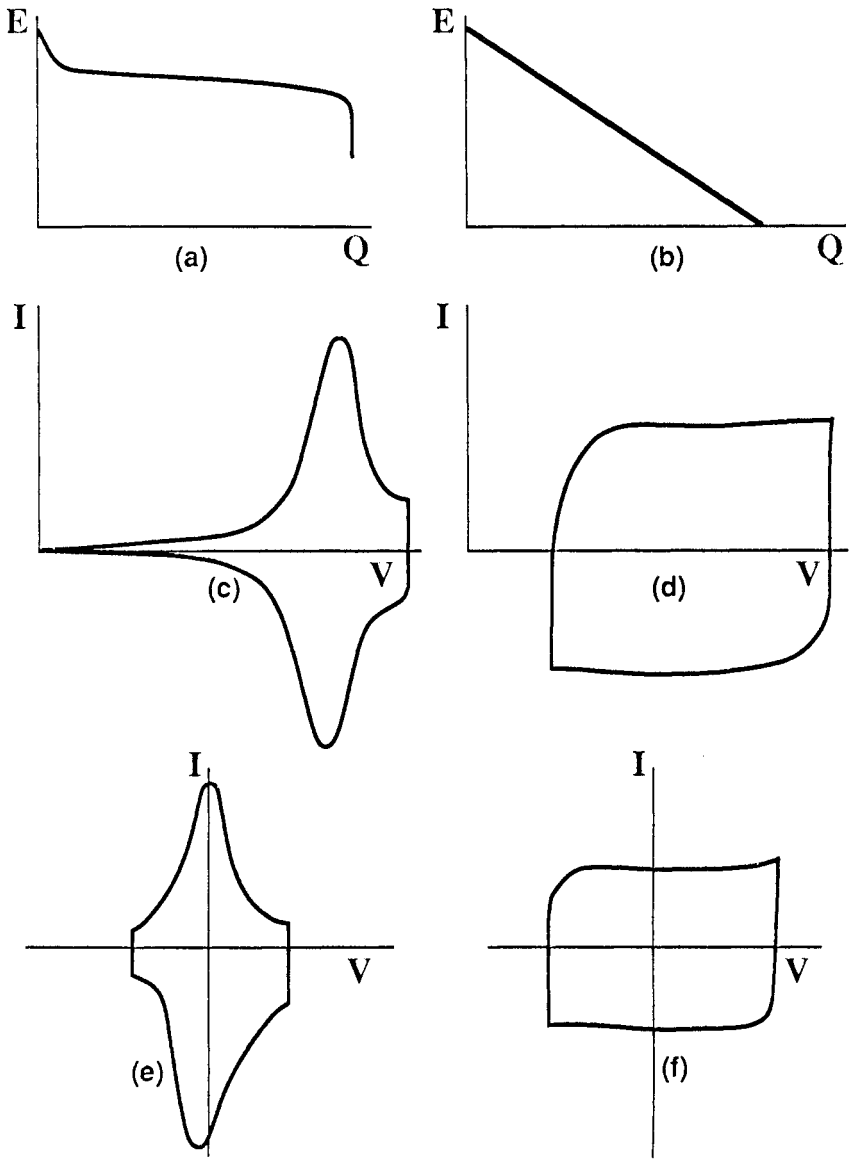

Figure 4. Schematics of discharge curves for (a) 'battery-like' and (b) 'capacitor-like' electrodes; (c) and (d) are corresponding single-electrode cyclic voltammograms; (e) and (f) are corresponding voltammograms for a symmetrical electrochemical capacitor.

When E vs. Q is as shown in Fig. 4a, then clearly the differential capacitance can be very large. If operation over a narrow potential range is required, then very high capacitances can be obtained.

3.0 DYNAMIC BEHAVIOR OF ELECTROCHEMICAL CAPACITORS

3.1 General Considerations

In this section, the dynamic electrical behavior of electrochemical capacitors will be considered. Details of specific systems will be discussed later, as appropriate.

The traditional approach to understanding both the steady-state and transient behavior of battery systems is based on the porous electrode models of Newman and Tobias (22), and Newman and Tiedermann (23). This is a macroscopic approach, in that no attempt is made to describe the microscopic details of the geometry. Volume-averaged properties are used to describe the electrode kinetics, species concentrations, etc. One-dimensional expressions are written for the fluxes of electroactive species in terms of concentration gradients, preferably using the concentrated solution theory of Newman (24). Expressions are also written for the species continuity conditions, which relate the time dependence of concentrations to interfacial current density and the spatial variation of the flux. These equations are combined with expressions for the interfacial current density (heterogeneous rate equation), electroneutrality condition, potential drop in the electrode, and potential drop in the electrolyte (which includes spatial variation of the electrolyte concentration). These coupled equations are linearized using finite-difference techniques and then solved numerically.

This approach has been used to model the behavior of several different types of battery systems, including a recent study by Lafollette (25) of a very high-rate lead-acid battery. An important conclusion of this work was that for thin electrodes, operated at very high rates, electrolyte depletion at the pore wall is very significant, a factor not usually considered in more conventional battery situations in which the actual interfacial current densities are not particularly high.

Although this approach has not been explicitly applied to electrochemical capacitor modelling, some variation will probably be necessary when large-signal pulse behavior of, for example, the metal oxide systems is studied in depth.

The second approach to modelling the behavior of high surface-area electrodes, is to consider explicitly the geometry of the microstructure and to solve the linearized response. The simplest model is that of the

uniform cylindrical pore (or rectangular slot, in one dimension), which is discussed in the next section. An equivalent circuit approach is usually adopted which makes use of the concepts of distributed impedance and transmission lines. Variations of this type of model allow for nonuniform pores, curvature of potential surfaces (in the case of shallow pores or a rough surface), and a biporous geometry. They are briefly considered here.

Solid-state mass transport and its effect on the electrical response are considered in Section 3.5. Again, the discussion is given in terms of the small-signal response, i.e., the linear behavior of the system. In the final part of this section, consideration is given to some aspects of the large-signal response, which are important for real applications, and which may be difficult to predict on the basis of linear-response considerations.

3.2 Uniform Transmission Line Model of the Response of Porous Electrodes

The simplest approach to understanding interfacial charging processes in porous electrodes is through the use of uniform transmission line models (26), such as that shown in Fig. 5. Here, the electrode is supposed to consist of a set of uniform cylindrical pores, each of length l. The electrolyte resistance per unit length is r (ohm/cm), and the capacitance per unit length is c (F/cm). The differential equations describing the current and potential variation with distance are

Eq. (13) $$-\partial\phi / \partial x = ir \text{, and}$$

Eq. (14) $$\partial i / \partial x = c\, \partial\phi/\partial t$$

Differentiating the first equation again with respect to x and substituting into the second, we obtain

Eq. (15) $$\partial^2\phi/\partial x^2 = rc\, \partial\phi/\partial t$$

The impedance of this line, for the case in which it has an open termination ($[\partial\phi/\partial x]|_{x=l} = 0$), is given by the expression:

Eq. (16) $$Z(j\omega) = [r/(j\omega c)]^{1/2} \coth l\,(j\omega rc)^{1/2}$$

This impedance is plotted in the complex plane representation in Fig. 6. Qualitatively, the impedance appears to be a pure capacitance at low frequencies, where the phase angle tends toward $\pi/2$. At higher frequencies,

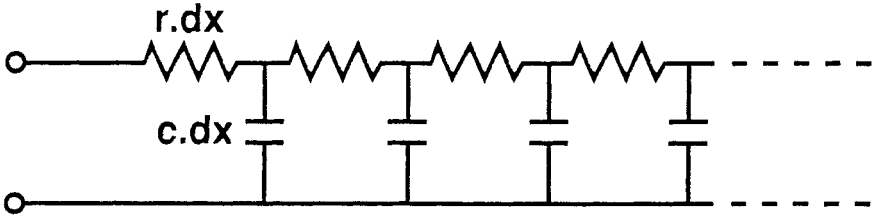

Figure 5. Uniform transmission line equivalent circuit.

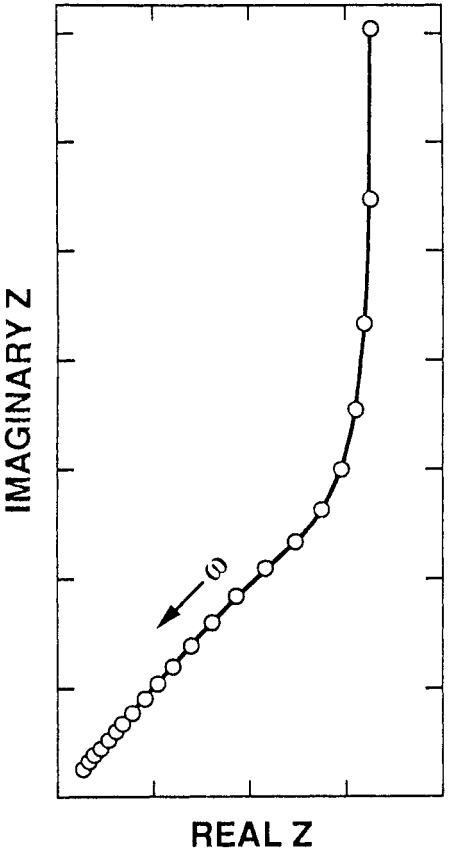

Figure 6. Impedance plot corresponding to a uniform, finite-length rc transmission line with an open termination.

the differential phase is $\pi/4$. The critical point to note is that there is a *real* part associated with the impedance which arises from the distributed pore resistance, through which the low-frequency capacitance must be charged. This is, of course, in addition to any high frequency resistance associated with the electrolyte *outside* the porous structure. In a porous structure it is therefore not possible to charge the interface as quickly as would be expected on the basis of a single RC time constant, where the value for R is calculated solely from the electrode plate separation. The additional distributed resistance can be shown to be equal to rl/3.

This, therefore is the fundamental problem with high surface-area electrochemical capacitors. In order to achieve the desired high energy densities, large surface-area materials must be used in a layer of finite thickness. This automatically ensures that an additional resistance associated with current penetration of the porous structure will be present. Whether this additional resistance interferes with a proposed application is a separate question. Obviously, since r is equal to $\rho/\pi a^2$, where ρ is the specific electrolyte resistance and a is the pore radius, then the greater the values of ρ and l and the smaller the pore radius, the more severe is the distributed resistance problem.

In this simple explanation of the fundamental nature of double-layer charging in porous materials, the following assumptions were made:

1. Curvature of the potential surfaces was neglected. This is a good approximation for pores that are long compared with their diameter. For shallow pores and 'rough' electrodes, this is no longer a good assumption, and Laplace's equation must be solved to give the current distribution. This topic is addressed below.

2. Electrode resistance has been neglected in this treatment. It may be included in the equivalent circuit of Fig. 5 by including distributed resistance in the ground line of the circuit.

3. Concentration polarization within the electrolyte has been neglected.

4. The model is strictly valid only for an identical set of uniform (constant diameter) pores. As will be seen below, however, this simple model provides a good description of the electrical response of carbon electrochemical capacitors. The model is evidently qualitatively descriptive of the *average* properties of some porous materials. It is expected that the model will apply to a material composed of a set of pores in which r and

c do not vary with position. It is therefore not useful if these quantities vary with depth of current penetration, as in a material with a well-defined biporosity, or one in which all length scales are present, as is found for the case of a fractal geometry.

3.3 Rough Electrode Surfaces

Under some conditions, it is necessary to calculate the current distribution in the system from first principles, rather than by merely assuming a transmission-line-like behavior. This will be the case when the pores are not long compared with their radius. This type of electrode has been called a rough electrode by de Levie (27). The equipotential surfaces cannot be assumed to be perpendicular to the axis of the pores. Here, it is necessary to solve Laplace's equation

Eq. (17) $$\nabla^2 \phi = 0$$

throughout the electrolyte for the particular geometry and condition at the boundary. Although numerous methods exist for the time independent solution to this problem, little attention has been given to the a.c. or transient solution. This problem has recently been approached numerically using a boundary integral method (28). This method, in which the potential in the bulk of the electrolyte is calculated by an integration around the surface of the region, is particularly suited to electrochemical problems in that the boundary conditions can be dealt with in a manner appropriate to the problem. At any frequency and potential, an electrochemical interface can be represented as a parallel combination of a resistor and a capacitor. This means that the boundary condition can be expressed as a linear combination of a Dirichlet and a von Neumann condition. An example of the results of a calculation for a sawtooth rough electrode is shown in Fig. 7. In Fig. 7a, the equipotential lines are shown at a low and a high frequency. In Fig. 7b, the computed complex impedance plot for the whole frequency range is shown for several aspect ratios (amplitude of sawtooth divided by peak-to-peak spacing). Several features are noteworthy. First, the numerical calculation shows some strong similarities to the transmission line model, in which a region of lower phase angle is succeeded by purely capacitative behavior at lower frequencies. The high-frequency phase angle is not $\pi/4$ however, as would be true for a uniform pore. Rather, it is greater than $\pi/4$ to an extent determined by the aspect ratio of the pore. In addition, the effect of curvature of the equipotential lines is to lead to a higher effective resistance at very high frequencies. Instead of asymptotically approaching the real

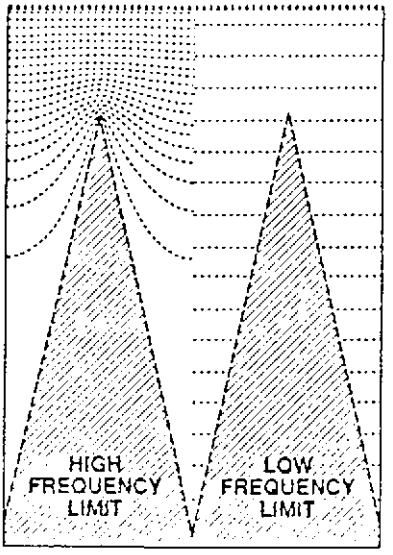

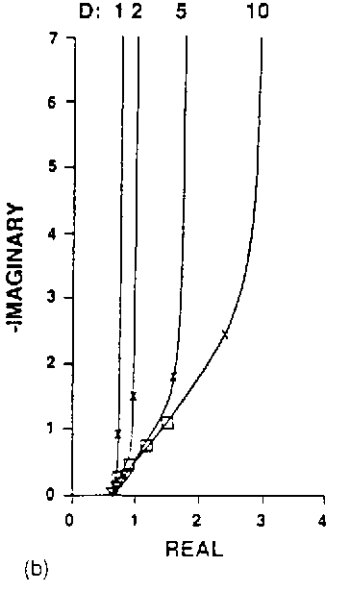

Figure 7. (a) Equipotential lines in the electrolyte for a sawtooth electrode surface in the high and low frequency limits, (b) complex impedance plots corresponding to (a) for different aspect ratios (height to half-width ratio) of the groove .

axis at $\pi/4$, the locus of the impedance approaches the real axis at $\pi/2$ and at a higher value of resistance than would be expected for a smooth electrode at the same distance from the reference potential plane. The cause for this is that the current lines concentrate at the points of the sawteeth. One conclusion is therefore that for a very thin, high resistivity electrolyte, the theoretical high frequency resistance cannot be achieved for a rough front surface.

3.4 Nonuniform Pores

An example of the electrical response of a nonuniform pore structure was given in the previous section. An alternative approach is to use the transmission line approximation discussed in Section 3.2. The model is modified by allowing r and c to be functions of x. Equation (15) is then replaced by:

Eq. (18)
$$-c(x)\frac{\partial \phi}{\partial t} = \frac{1}{r(x)^2}\left[\frac{\partial \phi}{\partial x}\frac{\partial r(x)}{\partial x} - r(x)\frac{\partial^2 \phi}{\partial x^2}\right]$$

which can be solved analytically for certain functional forms for r and c, or, in general, may be solved numerically. This approach has been adopted by Keiser et al. (29), who examined the frequency response of various assumed pore geometries, ranging from the sawtooth, discussed above, to a very occluded pore (ink-bottle pore). A qualitative representation of their results, plotted in the complex impedance plane, is shown in Fig. 8. Sometimes, a particular geometry can be approximated by a combination of transmission line circuits. An example is the occluded pore (shown in Fig. 8), which may be modelled by two transmission lines, the first being terminated by the second. The result of such a calculation is shown in Fig. 9. Note that all geometries have one thing in common. At low enough frequencies, the result tends to a purely capacitative behavior. It is at intermediate and high frequencies that the geometry affects the form of the impedance.

One type of behavior is observed experimentally to be particularly widespread. It is described by the constant-phase element (CPE):

Eq. (19)
$$Z_{cpe} = A(j\omega)^{-\alpha}$$

In the complex plane, this element appears as a straight line inclined at the angle $\alpha\,\pi/2$ to the real axis. Macdonald has shown that, for physical situations in which a relaxation time description is appropriate, CPE behavior may arise from an exponential distribution of activation energies for the relaxation process (30). For porous electrodes, such a description

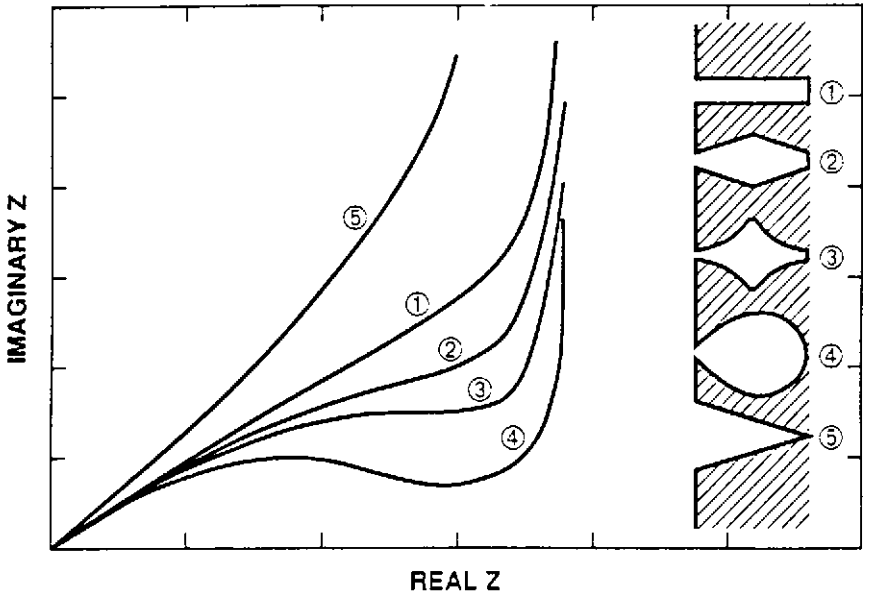

Figure 8. Results of the calculations of Keiser et al. (29) of the influence of pore geometry on impedance. *(Adapted with permission from Ref. 29).*

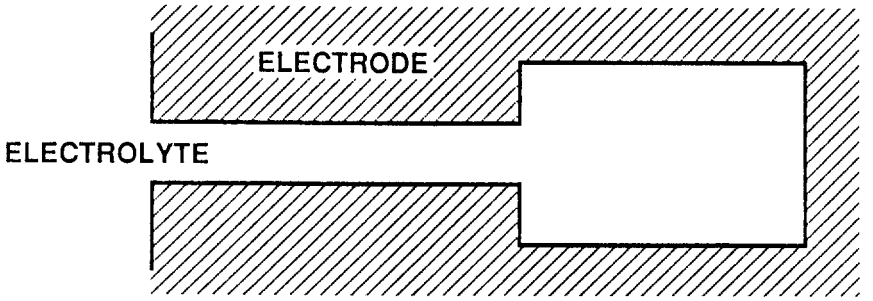

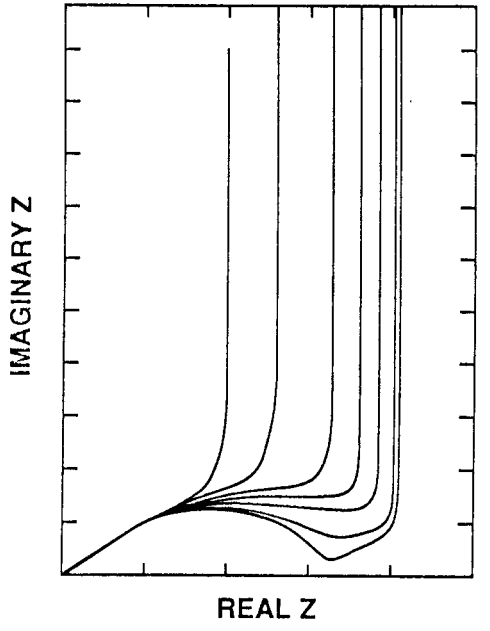

Figure 9. Simple two-transmission line approach to the calculation of the impedance of a pore with two characteristic radii. The different impedance plots correspond to different relative sizes of the two regions.

is not necessarily helpful, and other explanations should be considered. If we assume that some geometrical aspect of the porosity is responsible for this behavior, then an obvious extension of Macdonald's approach is to inquire whether a particular distribution function of pore sizes or shapes might lead to this behavior.

The transmission line response itself, in the region where the current penetration is not complete, is an example of CPE behavior. It should perhaps be emphasized here that CPE behavior cannot continue indefinitely to either infinitely high or low frequencies. At low frequencies, the behavior will ultimately become purely capacitative and the phase angle will approach $\pi/2$. At high frequencies, the current will ultimately withdraw from even the shallowest pores, and the phase angle will approach $\pi/4$ in the simple transmission line case or $\pi/2$, according to the more realistic calculations based on Laplace's equation described above.

It has been suggested that *fractal* pore structures lead to CPE behavior during double-layer charging (31)(32). In a fractal structure, all length scales are present, and for a process, such as diffusion, that contains a well-defined size scale ($\approx [D/\omega]^{1/2}$), it seems to be true that a CPE with an exponent closely related to the fractal dimension occurs in the response (33). For the case of double-layer charging, however, the situation is not so clear because there is no similar characteristic distance involved (34)(35). It appears that the fractal blocking interface does lead to CPE behavior, but the exponent is not simply related to the fractal dimension.

3.5 Mass Transport into a Thin Film

Electrochemical charge storage in a bulk film of material consists of the movement of two types of species, into or out of the film. These may be, for example, a cation and an electron. The requirement of charge neutrality stipulates that the two species move essentially together. We may therefore solve the coupled transport equations to give an equation that describes the flux of the neutral combination of species, in terms of the gradient in concentration (36). This allows us to define the *chemical diffusion coefficient*, which describes the motion of a neutral species in a non-ideal solid solution.

Eq. (20) $$j_i = -\tilde{D}(dc_i/dx)$$

Eq. (21) $$= -D_i \left[(1 - t_i) \frac{d \log a_i^*}{d \log c_i^*} - \sum_{j \neq i,e,h} t_j \frac{z_i}{z_j} \frac{d \log a_j^*}{d \log c_i^*} \right] \frac{dc_i}{dx}$$

Here $\tilde{D}$ is the chemical diffusion coefficient, and D is the component

diffusion coefficient (which is proportional to individual particle mobilities). The asterisk indicates a *neutral* combination of species, e.g., the ion plus electron. This equation is valid for general transference numbers and thermodynamic conditions. From the point of view of overall electrical response, the most important point is that this equation is still of the Fick's law form, even though thermodynamically the solution may be non-ideal.

The a.c. response has been calculated for such an electode, subject to a change in the applied potential or current. The complex impedance is of the form (37)

$$\text{Eq.(22)} \qquad Z(j\omega) = \frac{1}{zF}\frac{dE}{dc^*}\frac{\coth[j\omega/\tilde{D}]^{1/2}}{(j\omega\tilde{D})^{1/2}}$$

where $(1/zF)dE/dc$ is the thermodynamic enhancement factor. This term may be recognized as being the reciprocal of the differential capacitance, defined in Eq. (12). It specifies the relationship between the charge and the potential in the electrode. The small-signal response to a voltage or current step has also been calculated (36)(38-40). Diffusion coefficients have been measured, based on such experiments, for proton and alkali cation diffusion into a number of different materials in the form of thin films. Particular attention has been given to tungsten trioxide (37) and iridium oxide (41), from the point of view of electrochromic applications.

The same equations are also applicable to the kinetics of charge diffusion in redox systems. For example, Hunter et al. (42) have studied the charging behavior of polyvinylferrocene films using this methodology.

It is very important to note the identical forms of Eqs. (22) and (16). Electrochemically, they correspond to very different processes, even though the essential physics, that of a distributed storage/dissipation process is the same. The mathematical similarity is a source of ambiguity in the interpretation of a.c. and transient data. The presence of a 'Warburg' impedance ($\omega^{1/2}$ dependence of the impedance) is often taken as proof of the existence of a diffusion process, as in Eq. (22). It may often, however, be caused by the presence of porosity or even roughness in the electrode.

3.6 Large-Signal Response

Most of the discussion of the transient and frequency-dependent response has been given in terms of the small-signal or linear behavior. This is obviously a significant simplification, which allows, for example, analysis of processes in terms of a perturbation around a well-defined thermodynamic state. However, when larger signals are involved this will not be a good description of the system. This observation is particularly important for pulse applications of electrochemical devices or in conventional

time-domain studies, where large-amplitude cyclic voltammetry (CV) is the usual experimental technique.

First, in a porous electrode, an ionic species may be removed during an interfacial or a bulk discharge process. This may deplete the concentration of the species in the electrolyte phase within the pore. The fall in concentration may only be replenished by diffusion into the pore. This situation may be contrasted with the small-signal case in which the concentration within the pore may be regarded as constant in the axial direction and only gradients in a radial direction have to be considered. Depending on the magnitude of the perturbation, a strong nonlinear response may be expected. As mentioned in Section 3.1, Lafollette (25) found this to be important in thin electrodes operated at high current density. A second class of examples is associated with situations in which a critical property of the electrode material depends very strongly on potential or injected charge. Gottesfeld et al. (43) have theoretically examined the cyclic voltammetric behavior of films (such as sputtered IrO_2 and polyaniline) in which the film resistance is a strongly nonlinear function of Q. These types of films often show a 'prepeak' in the anodic sweep, which comes before the main film oxidation peak. No corresponding cathodic peak is seen. The characteristic of these materials is that, in the reduced state, the film resistance is very much greater than it is in the oxidized state. Gottesfeld et al. (43) found, that under these circumstances, the onset of oxidation is delayed because of IR losses, until sufficient charge has entered the film to make it conducting. At this point, the thermodynamically required charge will then flow into the film. The prepeak corresponds to this required charge. Once the film is conducting, subsequent charge movement is reversible. From an applications point of view, it is clear that such behavior is of great importance for large-signal pulse applications, where the kinetics of charging cannot easily be predicted from a small-amplitude measurement. A closely related example (the nickel oxide electrode) has been analyzed experimentally (44).

4.0 CARBON ELECTROCHEMICAL CAPACITORS

4.1 Introduction

In the last two sections, we have considered in a general way the mechanism of charge storage and the electrical response we might expect for different types of systems. In the next three sections, we will consider the properties of specific materials systems and try to relate those properties to the earlier discussion.

Electrochemical capacitors, based on high surface-area carbon

electrode materials and a variety of electrolytes, are the most highly developed of the systems discussed in this chapter. Capacitors using sulphuric acid as the electrolyte are commercially available and are used as backup power for memory. They have also found a number of military applications, including fusing. After the initial patent of Becker (1), much development work has been carried out at Sohio (45)(46). Much of the recent work on carbon systems (especially involving the development of nonaqueous electrolyte systems) is to be found in the Japanese patent literature.

Carbon is available with a wide variety of morphologies and physical and chemical properties. The subject is comprehensively reviewed in a recent book by Kinoshita (18). To a large extent, the actual carbon used in commercial electrochemical capacitors has remained proprietary, but most would appear to be carbon blacks (47) and very high-surface-area active carbons. The latter materials are prepared from carbonaceous precursor materials by steam activation. Recent Japanese patents indicate that a carbon obtained by activation of a carbonized phenolic resin is particularly suitable, especially for organic solvent-based systems. This material may have a specific surface area up to 2500 m^2/g.

Some data on the capacitance of different activated carbons has been given by Currie (46). In addition, the double-layer capacitance of carbon electrodes has been studied by a variety of techniques. These data have been collected by Kinoshita (18) and Randin (48). Both carbon blacks and activated carbons appear to have double-layer capacitances of about 10 $\mu F/cm^2$. This is somewhat less than the value expected for a good metal and is ascribed to the semi-metallic nature of carbon, which allows a semiconducting space charge to form on the carbon side of the interface. This space-charge capacitance is significantly less than the electrolyte double-layer capacitor and therefore dominates the behavior. The values for the capacitance are typically obtained by dividing the measured capacitance of a flooded electrode by the BET surface area. Some reservation must be associated with this type of measurement, as very small pores (< 20 angstroms in diameter) may not easily be wetted.

The contribution of surface active groups to the interface capacitance is increased by oxidation, and decreased by a heat treatment in an inert or reducing atmosphere. Kinoshita and Bett (49) have studied the oxidation of carbon black (Vulcan XC72) in chromic acid and found that a reversible peak develops in the cyclic voltammogram at 0.5 - 0.6 volt vs. SHE) with an increasing level of oxidation. This type of reaction is associated with oxidation and reduction of carbonyl/quinone groups. Numerous other studies of the electrochemical activity of species on carbon surfaces have been reported and are collected and summarized by Kinoshita (18).

4.2 Systems with Aqueous Electrolytes

By far the most commonly used electrolyte in electrochemical capacitors is aqueous sulphuric acid, largely because of its high conductivity, wide temperature range of applicability, and low cost. If a concentration of 35% - 40% H_2SO_4 is used, performance remains good down to a least -55°C, although freezing caused by concentration polarization during discharge of the electrode would seem to be a possibility at low temperature. Performance generally increases up to at least 100°C, the reason presumably being improved electrolyte conductivity that gives better access to charge stored in pores at the end of long resistive paths.

This type of capacitor is commercially available with an energy density of about 1.5 J/cm^3 (46)(50). This may be compared with a Ni-Cd rechargeable battery (450 J/cm^3) and a typical electrolytic capacitor (0.02 J/cm^3). Volumetric capacitance density scales as $1/V^2$ for electrochemical capacitors; electrolytic capacitors decrease less quickly, and thus the biggest advantage of the electrochemical devices is to be found at low voltage. Cycle life is excellent ($> 10^5$) and shelf life is also very good. These devices can be manufactured from very low-cost components. Typical failure modes are solvent evaporation, which can be eliminated by incorporation of a hermetic seal, and container corrosion leading to high contact resistances and increased leakage currents.

As mentioned earlier, leakage currents are an important consideration in memory backup applications, where they may represent a significant fraction of the needed current to maintain memory voltage. Typical leakage currents for this type of device are about 4 $\mu A/cm^2$, and are strongly temperature dependent. Currie (46) has reported an activation energy of 14 kJ/g for leakage currents in H_2SO_4. The current is caused by electrochemical reactions involving active species dissolved in the electrolyte. Various attempts have been made to reduce leakage currents, including addition of inert material, such as SiO_2, Al_2O_3, and SiC, to the electrolyte (51) and saturation of the electrode compartments with nonproton-containing salts, such as Li_2SO_4 (52). Currie (46) has reported that the leakage current of a C capacitor using a K_2SO_4 electrolyte is much reduced compared with a H_2SO_4 electrolyte. A comparison of the rate of voltage decay for a 5 volt capacitor using these two electrolytes is shown in Fig. 10. Leakage current decreases with decreasing specific surface area of the carbon.

A further problem with leakage currents is that they lead to cell balancing problems. Individual cells with high leakage rates do not charge to the same voltage as low-leakage cells, leading to failure of the higher voltage cells. This problem may be addressed by (1) de-rating the overall voltage, (2) incorporating redox couples with an appropriate

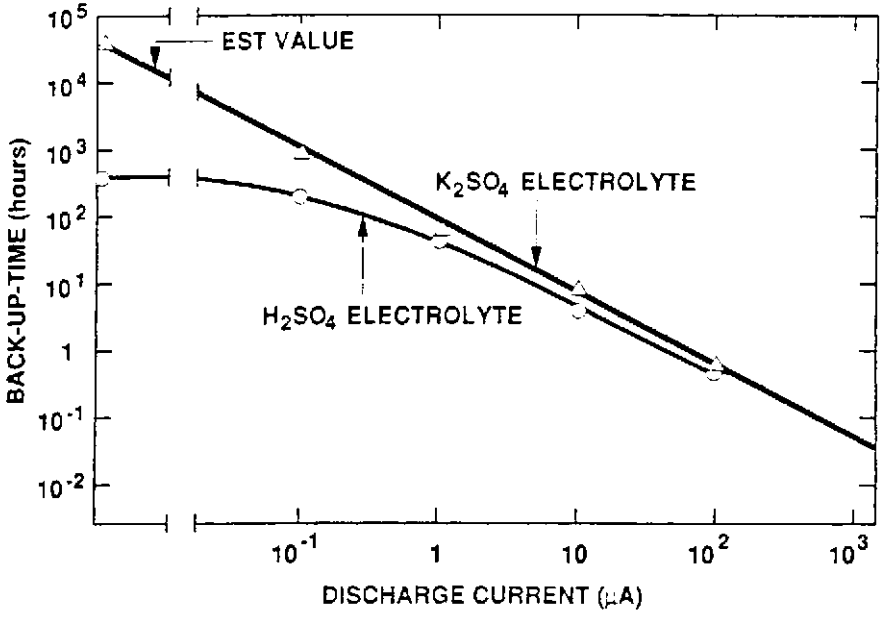

Figure 10. Rate of self-discharge of carbon double-layer capacitors with H_2SO_4 and K_2SO_4 electrolytes, expressed as back-up time (time for a capacitor to discharge from 5.0 to 2.0 volts) at a particular discharge current. *(Adapted with permission from Ref. 46.)*

potential to buffer the overcharge, or (3) electronic cell balancing using shunt resistors or zener diodes.

A great variety of carbons have been used for electrode materials, some of them exhibiting surface areas significantly in excess of 2500 m^2/g, although values around 1100 m^2/g are more normal. Important considerations in the choice of carbon will include the way the surface area is distributed (micropores vs. mesopores, for example) and the distribution function of pore sizes. An interesting recent concept is the addition of an inorganic redox substance to the surface of an active carbon, e.g., $H_4PMo_{11}VO_{40}$, to add storage capacity (17). This idea could undoubtedly be extended to other substrates and redox couples.

Small-signal impedance data for a carbon capacitor are presented in complex impedance-plane form in Fig. 11. The best fit to Eq. (16), which describes the behavior of a uniform transmission line, is also plotted. It is clear that, to a first approximation, the transmission line model is quite good, and can certainly be used for predicting the small-signal behavior of the device, once the transfer-function parameters have been obtained. It is also obvious that, in order to access the low frequency capacitance, the devices have a high esr. As was discussed in an earlier section, this is due to the contribution of the electrolyte resistance within the pores of the electrode. Currie (46) has also examined the effect of carbon type on the electrical response. Figure 12 shows some of his results on the frequency dispersion of the phase angle for several types of carbon. The frequency response of devices with 60 Å diameter pores is significantly better than that of an activated carbon with 20 Å pores, and is improved even more if a carbon with a controlled 170 Å pore size is used.

Another consequence of the delay associated with the transmission line behavior is voltage recovery after termination of a constant current discharge. This is caused by a redistribution of the remaining charge in parts of the electrode with a longer time constant.

4.3. Nonaqueous Electrolyte Systems

Much recent development work has focused on the use of organic solvent-based electrolyte systems for use with carbon electrodes. The principal advantage of this approach is the removal of the limitation on cell voltage imposed by the electrolysis of water and the consequent increase in energy density, which is proportional to V^2 (53). Because cell voltages of 3 volts or more are easily attained, an order of magnitude increase in energy density is possible if the stored charge density were the same as in aqueous systems. Several Japanese patents claim cell voltages in the range of 4 to 5.5 volts and specific capacitances greater than 100 F/g. A list of the more common electrolytes and solvents is given in Table 1.

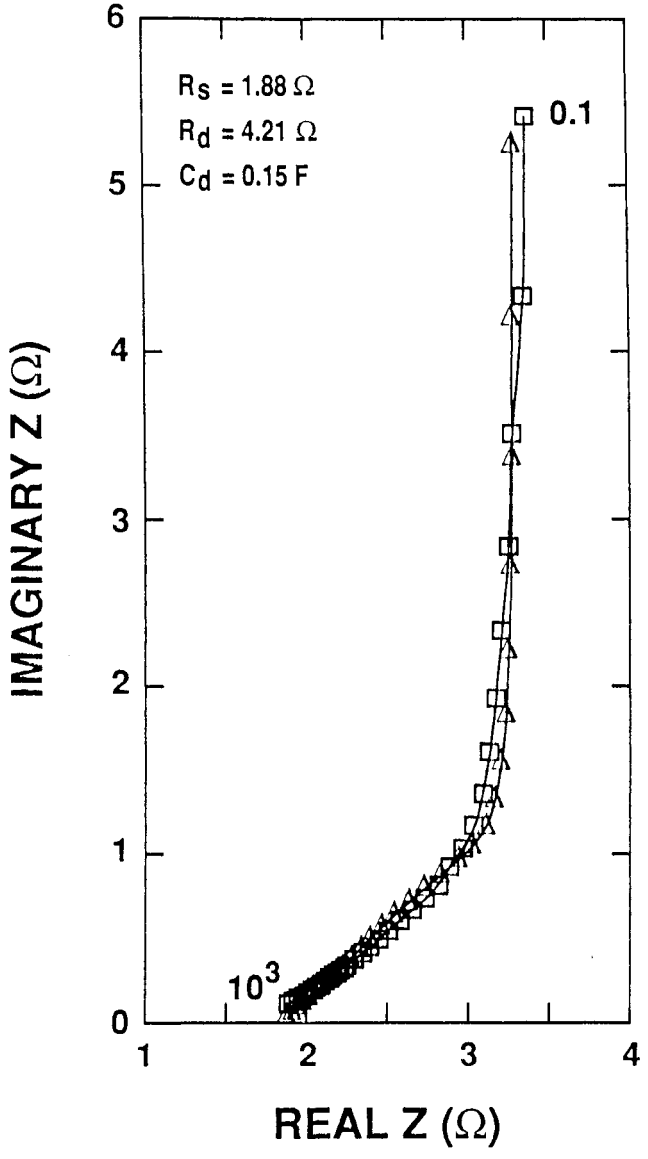

Figure 11. Impedance plot (□) for a commercial carbon/H_2SO_4 double-layer capacitor at room temperature. Calculated data points (Δ), based on the fit to Eq. (16) are also shown.

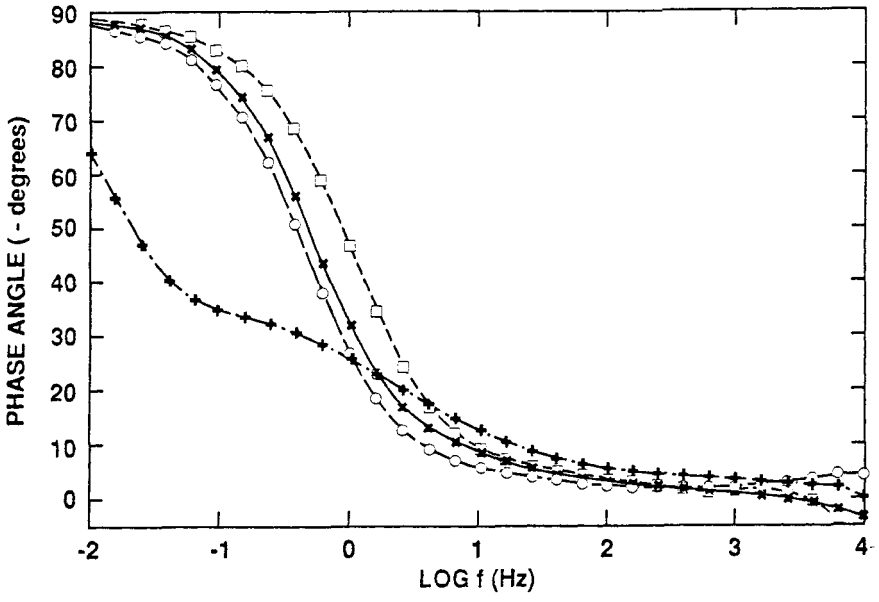

Figure 12. Effect of pore size and distribution on the electrical behavior of various types of carbon. Dependence of phase angle on frequency for: (o) 76-angstrom controlled porosity carbon; (□) 166-angstrom controlled porosity carbon; (×) C black (Black-Pearls); (+) high surface-area activated carbon. *(Adapted with permission from Ref. 46.)*

Table 1
Nonaqueous Solvents and Solutes Used
in Carbon-Based Electrochemical Capacitors

Solvents	Electrolytes
propylene carbonate	$LiClO_4$
γ-butyrolactone	$R_4N^+A^-$ where R = Et, Pr, Bu etc. A = BF_4, ClO_4, CF_3SO_3
sulpholane	RSO_3M where M = alkali, NH_4^+, NR_4^+

These are essentially the same electrolyte solutions that have been found useful for nonaqueous lithium batteries, and their properties relevant to that application have been reviewed (54). Other advantages may include low leakage currents and absence of gas evolution on overcharge. The conductivities of these electrolytes, however, are much lower than those of aqueous solutions and an increase in series resistance is unavoidably associated with their use. Although detailed transient or impedance studies appear not to have been published, it is safe to assume that the increase in electrolyte resistivity is also detrimental to dynamic response, because of increased transmission line effects in the porous electrode structures.

A partial description of the Matsushita 'Gold' capacitor has been given (55). The carbon is based on a carbonized and activated (800°C - 1100°C for 1 - 2 hrs. in water vapor carried in nitrogen) phenolic resin and has a surface area of up to 2500 m^2/g. This type of carbon also has a rather high electrical conductivity, of about 60 $\Omega^{-1}cm^{-1}$. It can be made in various forms, such as felts, fiber, cloth, and paper, and is thus quite suitable for electrode fabrication. Specific capacitance vs. specific surface area was found to be linear at room temperature. In order to get good performance at low temperatures (-25°C), it was found necessary to have more than 50% of the pore volume in pores with a diameter of 200 Å or greater. Plasma-sprayed aluminum was used for making contacts.

Nawa et al. (56) have also described a capacitor based on the same type of carbon using $LiClO_4$ and γ-butyrolactone as the electrolyte. These authors believe that cell capacity is due to a superimposition of a double-layer charging process and an electrolyte intercalation process (galvanic

cell mode). The intercalated species are Li^+ and ClO_4^-. Evidence for the Faradaic processes is found in the dependence of charge recovered on cell voltage. It was found that more charge was stored in the cell than would be expected from the linear dependence of Q on V associated with double-layer charging. Intercalation in this type of carbon is not unlikely, as its high conductivity implies a well-developed graphitic nature. Specific capacitance of the system was 36.5 F/g of carbon, and specific energy and power were 130 kJ/kg and 11.1 kW/kg, respectively, based on carbon and necessary electrolyte. Self-discharge was reported to be 40% - 50% after one day.

Yashima et al. (57) have investigated the self-discharge in activated carbon fiber - $LiClO_4$/PC cells. Water and oxygen, dissolved and adsorbed, were found to be the principal sources of self-discharge. After removal of these impurities, residual reactions were probably the reduction of propylene carbonate at the negative electrode, irreversible dopant reactions with the carbon and the presence of surface functional groups, e.g., -OH, -COOH and -CHO. About 70% of the self discharge apparently occurred at the negative electrode.

Nogami et al. (58) have described a symmetrical activated carbon fiber cell using Bu_4NClO_4 as the electrolyte.

4.4 Solid Electrolyte Systems

From the point of view of lifetime, mechanical ruggedness, and, possibly, ease of manufacture, solid electrolyte systems are very attractive. Two main difficulties are, however, apparent. The first of these is the difficulty in making an intimate high-surface-area solid-solid interface and maintaining it over a wide temperature range. Even if the electrolyte can be introduced into the pores as a liquid, it may prove difficult to maintain contact on solidification by cooling or solvent evaporation. The second problem is that most solid electrolytes are distinctly inferior to liquid electrolytes in terms of their resistivity and the temperature coefficient of that resistivity.

An early solid-state device, based on the solid electrolyte AgBr, was patented by Raleigh (59). The solid Ag^+ conductor $RbAg_4I_5$, however, has a much higher room temperature ionic conductivity ($\approx 0.27\,\Omega^{-1}cm^{-1}$) (60). Oxley (61)(62) studied an electrochemical device that made use of this electrolyte with an asymmetric arrangement of electrodes, $Ag\,|\,RbAg_4I_5\,|\,C$. Within the potential range of 0 to +500 mV (vs. Ag^+/Ag), the device behaved almost perfectly. Interface areas up to 10 m^2/g were obtained, leading to packaged energy densities of 1 to 1.7 J/cm^3. The device had excellent charge retention properties, because of the very low electronic conductivity of this electrolyte, and also an attractively wide temperature

range. At -55°C, the conductivity only falls to 0.09 $\Omega^{-1}cm^{-1}$, and at +75°C it is 0.39 $\Omega^{-1}cm^{-1}$. Other silver ion conductors have also been proposed (63).

Although they have lower ionic conductivities, analogous and related copper compounds have also been used (64). They appear to have about half of the specific energy achieved with the Ag^+ conductor. The best of the Cu^+ electrolytes is $Rb_2Cu_8I_3Cl_7$ which has a 25°C conductivity of $6.4x10^{-3}$ $\Omega^{-1}cm^{-1}$. The copper electrolytes seem to show considerably more self-discharge through electronic conductivity than does $RbAg_4I_5$.

Other inorganic solid electrolytes have also been employed in electrochemical capacitor applications, including hydrogen uranyl phosphate, ($H_3OUO_2PO_4$) and $Zr(HPO_4)_2 \cdot xH_2O$ (proton conductors) (65), Li and Na β-alumina (66), $LiNaSO_4$ (67). Clearly, these systems will only be satisfactory for relatively slow applications.

Devices based on ionically-conducting polymers appear perhaps to be more attractive than the inorganic solid electrolytes. U.S. patents describe a capacitor based on the use of polyethylene oxide (PEO) containing dispersed lithium salts as an electrolyte (68)(69). The PEO acts as a solvent for the electrolyte salt, and can be applied as a liquid (in a solvent such as acetonitrile) to the high surface-area electrode, ensuring good penetration of the pores. Much research has been carried out on polymeric lithium ion conductors for lithium-battery applications (70), and PEO is no longer considered one of the best (i.e., highest conductivity) systems (71). We can presume that improved capacitor performance could also be obtained if some of the more recently developed systems were tried, particularly close to room temperature.

5.0 TRANSITION AND NOBLE METAL OXIDE CAPACITORS

5.1 Introduction

In this section, we will consider the properties of perhaps the second most well developed of the electrochemical capacitor systems: those based on the oxides of the transition and noble metals. In general, a distinction is made between the metal oxide systems and the carbon systems on the basis that the former are redox active materials, i.e., charge is stored by means of changes in the oxidation state of the metal when an ionic species (e.g., a proton) reacts with the surface (or bulk) of the oxide, and the 'chemisorption' is accompanied by the simultaneous injection of an electron into the oxide. The carbon capacitors are supposed to be more purely of the double-layer or space-charge variety. In fact, as was pointed out earlier, the distinction is less clear. In the case of carbon, surface functional groups may be oxidized and reduced in very much the

Next Page

Previous Page

range. At -55°C, the conductivity only falls to 0.09 $\Omega^{-1}cm^{-1}$, and at +75°C it is 0.39 $\Omega^{-1}cm^{-1}$. Other silver ion conductors have also been proposed (63).

Although they have lower ionic conductivities, analogous and related copper compounds have also been used (64). They appear to have about half of the specific energy achieved with the Ag^+ conductor. The best of the Cu^+ electrolytes is $Rb_2Cu_8I_3Cl_7$ which has a 25°C conductivity of $6.4x10^{-3}$ $\Omega^{-1}cm^{-1}$. The copper electrolytes seem to show considerably more self-discharge through electronic conductivity than does $RbAg_4I_5$.

Other inorganic solid electrolytes have also been employed in electrochemical capacitor applications, including hydrogen uranyl phosphate, ($H_3OUO_2PO_4$) and $Zr(HPO_4)_2 \cdot xH_2O$ (proton conductors) (65), Li and Na β-alumina (66), $LiNaSO_4$ (67). Clearly, these systems will only be satisfactory for relatively slow applications.

Devices based on ionically-conducting polymers appear perhaps to be more attractive than the inorganic solid electrolytes. U.S. patents describe a capacitor based on the use of polyethylene oxide (PEO) containing dispersed lithium salts as an electrolyte (68)(69). The PEO acts as a solvent for the electrolyte salt, and can be applied as a liquid (in a solvent such as acetonitrile) to the high surface-area electrode, ensuring good penetration of the pores. Much research has been carried out on polymeric lithium ion conductors for lithium-battery applications (70), and PEO is no longer considered one of the best (i.e., highest conductivity) systems (71). We can presume that improved capacitor performance could also be obtained if some of the more recently developed systems were tried, particularly close to room temperature.

5.0 TRANSITION AND NOBLE METAL OXIDE CAPACITORS

5.1 Introduction

In this section, we will consider the properties of perhaps the second most well developed of the electrochemical capacitor systems: those based on the oxides of the transition and noble metals. In general, a distinction is made between the metal oxide systems and the carbon systems on the basis that the former are redox active materials, i.e., charge is stored by means of changes in the oxidation state of the metal when an ionic species (e.g., a proton) reacts with the surface (or bulk) of the oxide, and the 'chemisorption' is accompanied by the simultaneous injection of an electron into the oxide. The carbon capacitors are supposed to be more purely of the double-layer or space-charge variety. In fact, as was pointed out earlier, the distinction is less clear. In the case of carbon, surface functional groups may be oxidized and reduced in very much the

same way as surface oxide and hydroxide groups on oxides, and intercalation reactions are a real possibility. Also, the term redox is perhaps misleading, in that most of the oxides are good electronic conductors and it is to be expected that crystallographically-equivalent individual metal ions will have the same oxidation state, which is intermediate between those of the formal redox states. This is not necessarily always the case, since electrons may be localized in surface states, or other defects, in which case specific ions may be said to have different oxidation states. This is also true of some transition metal oxides that are intrinsically semiconducting (e.g., the vanadium oxides) and will, in general, require electronically conducting additives to function well as battery or capacitor electrodes.

Other features also blur the distinctions. As will be described below, the evidence suggests that, in the case of thermal RuO_2, the ionic processes involved are largely restricted to the surfaces of individual oxide grains. In the case of nickel oxide, however, it is much more likely that the bulk of the lattice is readily accessed by protons. For IrO_2, it seems that anodically grown films behave rather like nickel oxide, whereas thermal films behave almost identically to RuO_2. There is thus a continuous spectrum of behavior which, in principle, may be defined in terms of bulk vs. surface ionic reactions and delocalized vs. localized electronic behavior. From the point of view of the energetics of the charging process, both the ionic and electronic components may formally be said to contribute to the total free energy of the interaction. Clearly the availability of empty electronic states (either bulk or surface) is a prerequisite for any type of interaction, and the density of such states is probably a dominant feature in the voltage vs. charge characteristic of many electrodes. However, the ionic contribution to the enthalpy is also important and it controls the ion exchange and acid-base behavior of oxide interfaces. The ionic interactions may in turn modify the electronic states and, therefore, the assumption of rigid bands may not be a good basis for predicting the energetics of the charging process. Unfortunately, the degree to which these features are important for individual oxides has scarcely been addressed, and conflicting opinions are widely found in the literature.

5.2 Thermally Prepared Oxide Films

Because of its importance as a dimensionally stable anode material (DSA) for the evolution of chlorine and oxygen, RuO_2 in pure form, or mixed with the oxides of other metals, including Ta, Ti and Ir (72), has received considerable attention. IrO_2 has also been investigated, but to a lesser extent, presumably due to its greater cost. Several books and review articles have been devoted to the physical, chemical, and electrochemical properties of these and related oxides (73).

Films are prepared by thermal decomposition and oxidation of soluble precursor materials. For RuO_2, the most common precursor is $RuCl_3 \cdot xH_2O$, dissolved in water or an alcohol, such as isopropanol. The solution is applied to a valve-metal substrate, the most common material being titanium, by painting, dipping, or spraying. The chloride can then be decomposed and oxidized in air or oxygen to RuO_2 at relatively low temperatures (300°C - 500°C). The properties of the oxide, e.g., surface area, depend significantly on the preparation temperature.

The highly capacitive nature of thin films of these oxides, when immersed in an aqueous electrolyte, is well known. Cyclic voltammograms of RuO_2 and IrO_2 are shown in Figs. 13a and b. The specific capacitance of the RuO_2, determined by Rutherford backscattering and cyclic voltammetry is about 350 F/g (74). This may be compared with about 100 C/g for carbon, achieved on much higher surface-area material. A striking feature of these data is the broad range of potential over which charge is stored. This is actually an important distinguishing feature between 'chemisorption' on these oxides and the underpotential deposition of, for example, hydrogen on platinum, in which case adsorption takes place over a rather narrow potential range.

In situ quartz crystal microbalance studies (75)(76) have confirmed the cationic nature of the charging process: the film mass decreases proportionately to charge as the potential is made more positive (Fig. 14). Attempts have been made to determine the real charge density on RuO_2 by comparing BET surface areas and electrochemically measured capacitance. Burke et al. (77) found a value of about 160 $\mu C/cm^2$, and Raistrick and Sherman (74) found somewhat higher values, in the range of 200 - 300 $\mu C/cm^2$, on oxide optimized for capacitor applications. The specific surface area of the RuO_2 was about 120 m^2/g, a value in line with transmission electron micrographs that indicated a microcrystalline structure with a particle diameter of about 200 angstroms. A straightforward calculation of the density of -OH groups on the surface of a rutile-structure oxide (78) indicates that a charge density of 200 $\mu C/cm^2$ is expected if each surface group is singly ionizable, i.e.,

$$M\text{-}OH + H^+ + e^- = M\text{-}OH_2$$

Obviously, if multiple ionization processes are possible, then more charge can be accommodated on the surface. It is therefore unnecessary to postulate *bulk* reaction of protons with RuO_2. Other evidence that points to the same conclusion may briefly be summarized as follows:

— Although the a.c. impedance behavior of the electrodes is not well explained by solid-state bulk diffusion, it is understandable

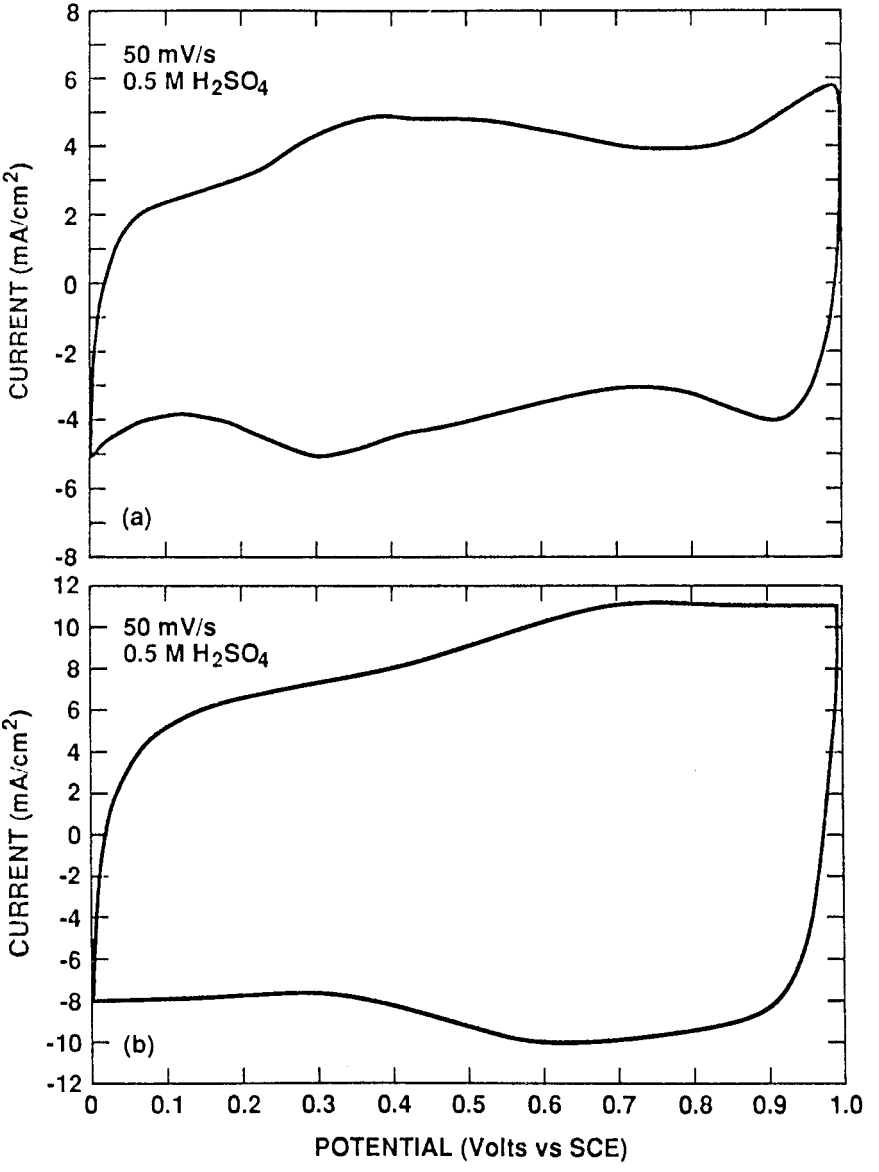

Figure 13. Cyclic voltammograms in 0.5 M H_2SO_4 at 50 mV/s sweep rate, for (a) thermal RuO_2 and (b) thermal IrO_2.

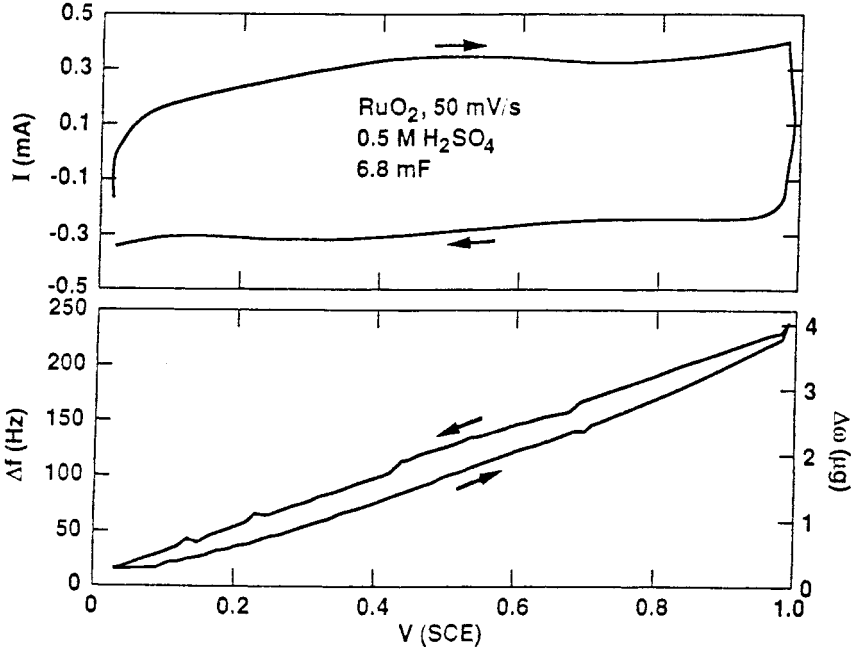

Figure 14. Dependence of frequency of RuO_2-coated-quartz crystal microbalance electrode on potential in 0.5 M H_2SO_4 shown below the corresponding cyclic voltammogram.

in terms of the charging of a porous medium (see below).

— Other ions (e.g., the alkali metals) also interact strongly with these oxides, and, although the charge density is somewhat lower, the kinetics of charging are essentially identical to those found with protons, if the differing conductivities of the electrolytes are taken into account. This result is expected for a fast surface electrosorption process, but is quite incompatible with solid-state diffusion.

The kinetics of the charging process have been studied in some detail using a.c. impedance spectroscopy (74)(79)(80). The nature of the response depends on the method of film preparation, but usually two time constants are clearly seen in the impedance data, a result which suggests an approximate equivalent circuit of the type shown in Fig. 3. Various authors have proposed differing explanations for the origin of the two time constants. Rishpon and Gottesfeld (79) have suggested that two mass-transport processes are involved, the faster being associated with the surface of the grains and the second with diffusion into the bulk. The possibility that the high-frequency time constant was associated with finite interfacial kinetic processes (i.e., a charge transfer resistance in parallel with a double-layer capacitance) was suggested by Abraham and Rajeshwar (80), who also attribute the low-frequency behavior to a diffusion process. Raistrick et al. (74) have examined the possibility of charge-transfer kinetic limitations by varying the proton concentration and the conductivity of the electrolyte separately. It was found that both R_1 and R_2 were proportional to the electrolyte conductivity, but independent of the proton concentration. This suggests that the form of the response is determined by charging in a porous medium, but with an effective geometry which is significantly different from that encountered in the case of the carbon electrodes.

Films of oxides may also be prepared by sputtering. The most intensively studied material is IrO_2 because of its possible application as an electrochromic material (81-83). Films prepared by this method seem to be more similar to films prepared thermally, than to those prepared by anodic oxidation (see next section). Aurian-Blajeni et al. (81) have interpreted the two time constants in the impedance spectrum as caused by a two-layer structure in the oxide.

5.3 Anodically Prepared Films

Many transition and noble metal oxides can be anodically oxidized in aqueous electrolyte solutions to form oxide coatings. In some cases,

these special electrochemical treatments, e.g., cycling or pulsing, allow very thick layers to be built up, which have significant charge-storage capacity. Besides Ir, other metals that show this behavior are Ru (84), Ni (44)(85), Rh (86), and Mn (87).

In some cases, the behavior of the anodic films is significantly different from the thermally prepared materials. Hepel et al. (88) found that the energy of interaction of protons with IrO_2 was about the same for sputtered films and for single crystals, but differed significantly from that associated with anodic films.

The growth of an iridium oxide film in acid solution is shown in Fig. 15. (Note the small anodic pre-peak discussed in section 3.6.) The charge increases steadily with number of growth cycles and approaches values comparable to those found in thick thermal films. A comparison with the cyclic voltammogram of a thermal film of IrO_2 in the same electrolyte (Fig. 13b) illustrates some of the differences. At cathodic potentials, the capacity of the anodic films is rather low, but it shows a strong peak at about 0.7 volt (SCE) and a broad highly capacitive response at more positive potentials. Small-amplitude impedance data for such a film are presented in Fig. 16 for several different potentials which cover the complete range of behavior. At anodic potentials, the data are well explained in terms of a single, almost ideal capacitor in series with the electrolyte resistance. As the potential is made more negative, it is clear that a second resistance enters into the description of the response. At the lowest potentials, this resistance dominates the behavior and allows only a very limited degree of charging of the film. This resistance may safely be ascribed to the film itself and presumably corresponds to a dramatic change in the electronic properties. From the point of view of applications, this change in the capacitance and conductance of the film is a disadvantage. Equally striking, however, is the almost perfectly capacitive behavior of the film at positive potentials. Data at 0.9 volts show no evidence of distributed charging behavior. This behavior is intriguing in that the electrode is behaving as if it were nonporous (i.e., no frequency dispersion) and yet shows very high charge-storage capacity. The likely explanation is that the oxide is, in fact, exceedingly porous, with a structure similar to that of a polymer, in which chains or small numbers of atoms or molecules are completely permeated by and accessible to electrolyte species. A hexagonal structure has been proposed for anodic IrO_2 (89).

Confirmation of cationic (H_3O^+) involvement in the charging process for anodic IrO_2 was obtained by McIntyre et al. (90) who examined the composition of oxidized and reduced films using RBS and nuclear reaction analysis of deuterated specimens. The average D:Ir ratio was found to be 1.51 in oxidized and 2.28 in bleached films. The composition of the films was also found to be nonuniform. The interior of the films becomes

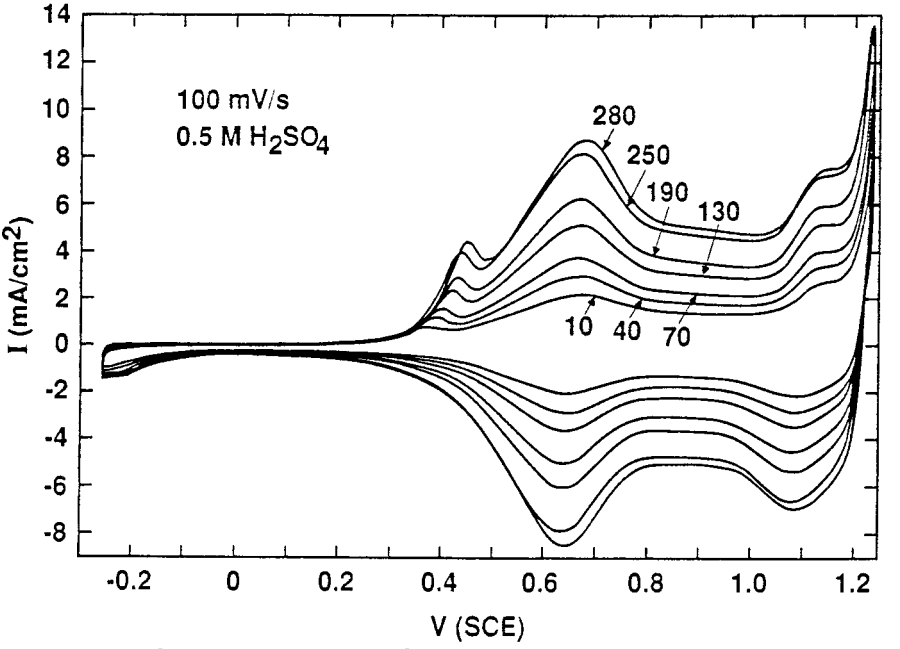

Figure 15. Growth of anodic IrO_2 on an Ir wire in 0.5 M H_2SO_4. The number of cycles is indicated.

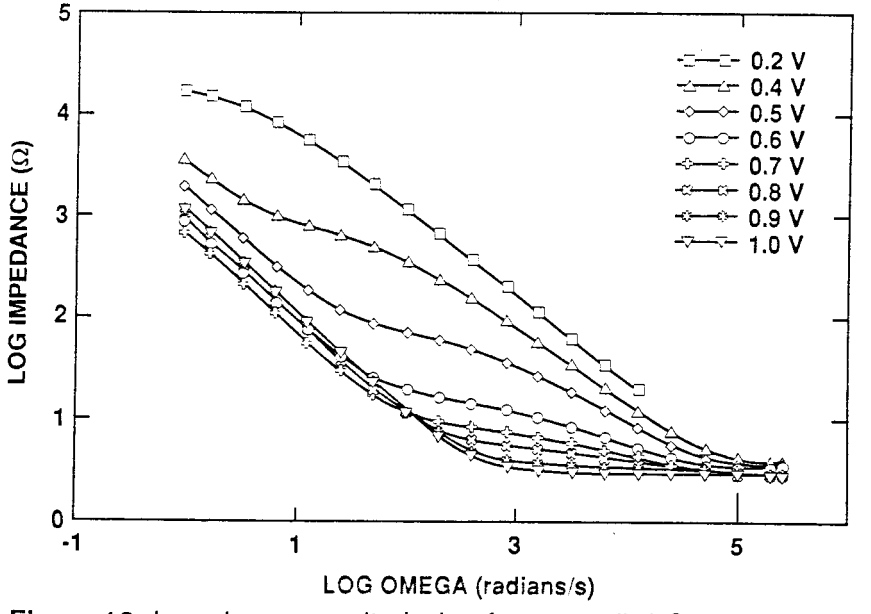

Figure 16. Impedance magnitude data for an anodic IrO_2 film measured at different electrode potentials (vs. SCE).

increasingly anhydrous with almost no water being found at the metal/oxide interface. The composition of the outer layer was $IrO_2 \cdot 2D_2O$ in oxidized and $IrO_2 \cdot D \cdot 3D_2O$ in reduced films. The same authors found that in aprotic solvents, lithium and sodium ions could be inserted into the structure, to a composition of about $LiIrO_2$; however, K^+ could not be inserted.

Using chemical analysis, Pickup and Birss (91) found evidence of non proton cation involvement in the redox processes in aqueous solutions.

5.4 Other Oxides

Many transition metal oxides are electrochemically active and can therefore be used as the electrode material in an electrochemical capacitor. Most of these oxides, however, are more justifiably considered as battery materials because extensive bulk involvement is normal. Well-known examples are the oxides of manganese, nickel, vanadium, tungsten, chromium, copper, cobalt, and molybdenum. Some of these materials are among the most important components of well-established secondary battery systems and have been extensively studied and the results reviewed (19)(20)(80). Many of them are used with both aqueous and nonaqueous electrolyte systems. In the table below, the charge densities of some oxide electrode systems are given. These numbers give some indication of the energy-storage capability of a 'capacitor' constructed from these materials. The corresponding charge density for RuO_2 in H_2SO_4 is about 350 C/g.

Table 2
Rechargeable Oxide Electrodes and Charge Densities.

Oxide	Charge Density (C/g)
$Li_xV_2O_5$	$\approx$ 650
$Li_xV_6O_{13}$	$\approx$ 1400
$Li_xCr_2O_5$	$\approx$ 972
MnO_2	1120
Li_xCoO_2	670
NiOOH	1040
AgO	1570
PbO_2	810

These oxides will not be considered further here as little work has been carried out with the express purpose of optimizing them in capacitor-like configurations. Exceptions are the patent of Elliot and Huff (92) and the recent work of Rauh (93) (see below).

5.5 Metal Oxide Capacitors Utilizing Solid and Polymeric Electrolytes

As is the case for carbon-based devices, polymeric electrolytes have been used with transition metal oxides. McHardy (5-7) has used IrO_2 (and also platinum metal) as electrodes deposited in and on the surface of Nafion. (Nafion is a registered trademark of E. I. duPont de Nemours, Inc.) The electrode fabrication is achieved by ion-exchanging hydrazine for polymer protons and then immersing the structure in a salt of the noble metal. Charge storage capacities in excess of 10 mC/cm^2 were obtained. The best performance was obtained with very thin (1 mil) membranes, and excellent discharge characteristics were obtained on millisecond time scales. Between 0.5 and 1.1 volts the charge was proportional to the voltage.

A similar concept has been explored by Rauh (93) who prepared highly dispersed, very thin electrodes of a number of oxides and organic polymers, including VO_x, IrO_x, RuO_x, and NiO, in a capacitor configuration. Vacuum and electrochemical deposition techniques were used to deposit very thin layers of metals and oxides on ion-exchange or other polymeric electrolytes and separators. Clearly, these types of configurations show much promise for very high rate applications.

6.0 CONDUCTING POLYMERS

6.1 Introduction

Although little direct developmental work appears to have been carried out, the possibility exists of using conducting organic polymers as active materials in electrochemical capacitors. They have certainly been actively investigated as battery electrode materials (94), and many of the same requirements hold for the capacitor case. Superficially at least, conducting organic polymers resemble the inorganic oxides discussed in the previous section, especially low-density anodic oxide films, such as anodic IrO_2. Although the possibility of an all-polymer capacitor or battery is very attractive (using for example a PEO-type of electrolyte) (95)(96), the conducting polymeric materials are not particularly processable, being neither meltable nor soluble (although poly 3-alkyl thiophenes have been made soluble) (97).

6.2 Charge-Storage Mechanism

The main classes of organic materials are as follows: polyacetylene, polypyrrole, polyaniline, polyphenylene, and polythiophene. These materials share the characteristic that, on ionic doping, electronic carriers are introduced into a delocalized π system, rendering them very good conductors (98). As in the case of the oxides, this is a double-injection process, with counterions entering the polymer structure. Several of the polymers can be produced by in situ electrochemical processes. Their microstructure is typically very dependent on preparation conditions.

Some of the polymers, e.g., polyacetylene, can be either p- or n-doped. For example, the empirical equations describing potential vs. a lithium electrode, as a function of doping for this material are (99):

$$V_p = 3.43 + 0.14 \log Q \text{, and}$$

$$V_n = 1.5 - (0.13 + 0.02Q) \log Q$$

where Q is the % oxidation. There is thus a gap in the density of states. For a symmetrical cell with an electrolyte such as n-$Bu_4N^+PF_6^-$ in propylene carbonate or sulpholane, there is a potential difference of about 2.5 volts at 7% doping. A capacitor based on this arrangement would not have a linear Q-V behavior; the potential would fall rapidly to zero once the gap potential difference is reached on discharge. The behavior is more 'battery-like' than 'capacitor-like'. Polyacetylene prepared by the Shirakawa method (100) is about 33% dense and consists of a mat of interconnected fibrils with a diameter of about 200 angstroms. The surface area is 60 - 100 m^2/g. Both the n- and p-doped materials are very sensitive to air and water. Recently, new preparative routes have led to polyacetylene with conductivity comparable to that of metallic copper (101).

Polyaniline can be prepared electrochemically, and its microstructure depends on the preparative conditions (102). The charge capacity is comparable to the inorganic oxides: Gottesfeld et al. (103) report a capacity of 800 C/cm^3 in an aqueous acidic electrolyte and Genies et al. (102) a value of 450 C/g in propylene carbonate/$LiClO_4$.

The use of aqueous electrolytes is certainly an advantage for high-rate applications, and polyaniline can be cycled in water over a limited potential range. Polyacetylene, however, is very unstable, in both n- and p-doped forms, to traces of water and oxygen. At more positive potentials, polyaniline is unstable to oxidation and undergoes fragmentation and dissolution (104). Similarly, polypyrrole is fatally oxidized above 1 volt vs. SCE in aqueous solutions (105).

6.3 Electrical Response

A cyclic voltammogram for electrochemically grown polyaniline is shown in Fig. 17. The electrical response of the conducting polymers, like that of the anodic oxide films, is not understood in great detail (106). The film resistances typically vary strongly with potential through the doping process, and there appear to be two time constants associated with charge storage. One explanation is that a fast double-layer charging process occurs on the surface of the polymer fibrils, and then a slow diffusive process involving penetration of the fibrils by ions takes place. An alternative explanation may be that there are two phases which are dynamically distinguishable. Rubinstein (107) has pointed out, however, that the fact that the two capacitances are potential dependent argues against this hypothesis. Clearly, charging kinetics may depend profoundly on microstructure, and a wide range of size scales and geometries have been found in all these materials, depending on the conditions of preparation. It is to be expected that charging kinetics will depend specifically on the ion size, charge etc.

Jow and Shacklette (108) have interpreted their results on n-doped polyacetylene in terms of a charge-transfer resistance and a diffusion process. (See Section 3.5). The measured double-layer capacitance, however, does not scale with thickness of the films, and is far smaller than would be expected for a material with the observed surface area (50 - 150 m^2/g). This suggests, perhaps, that the observed high-frequency process is controlled by the porosity rather than a charge-transfer reaction, as in the case of RuO_2. Specific capacitances for n-doping are voltage dependent and range from 95 F/g at 1.1 volts vs. Na ($NaB\phi_4$ in THF) to 320 F/g at 0.6 volts.

7.0 CONCLUSIONS

In this section, the performance characteristics of electrochemical capacitors, both realized and projected, are discussed. The limited data available are presented in the form of a specific energy vs. specific power plot (Fig. 18). Although this type of plot is not particularly useful or significant for assessment of conventional capacitors, where other considerations, such as average power capability at some working frequency, prevail, it provides a useful method of separating different characteristics of energy storage devices.

The power capability of a capacitor-like device may be quantified in several different ways. The power delivered into a load resistance, R_L, by a capacitor, C, with an internal resistance, R_i, is given by the equation:

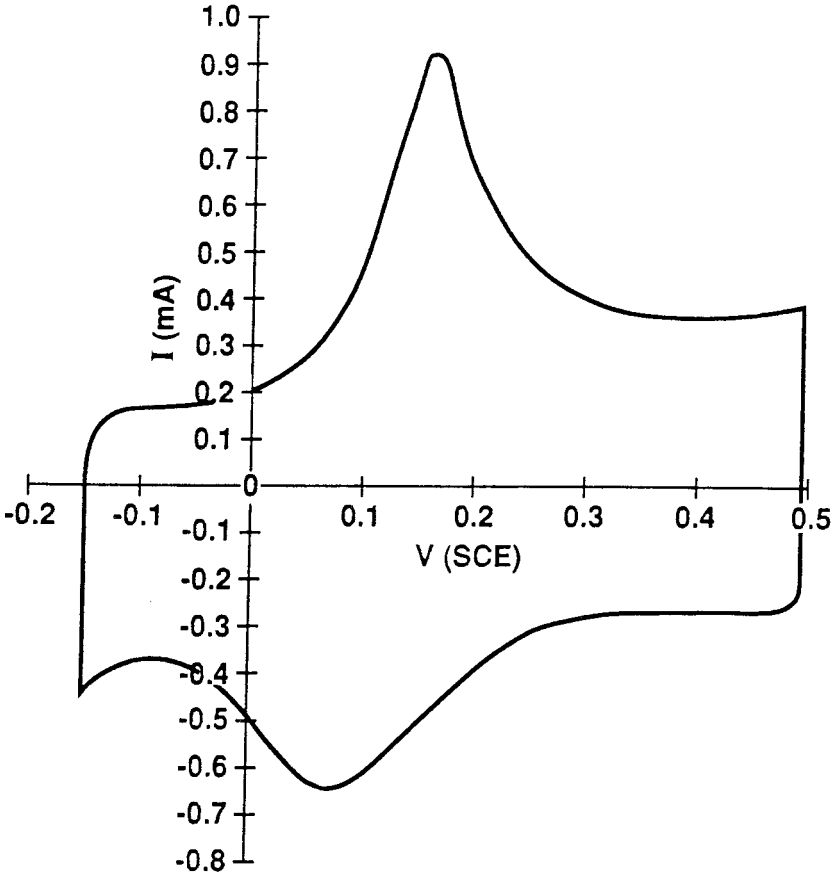

Figure 17. Cyclic voltammogram of electrochemically prepared polyaniline on a platinum electrode. 50mV/s in 0.1 M HCl.

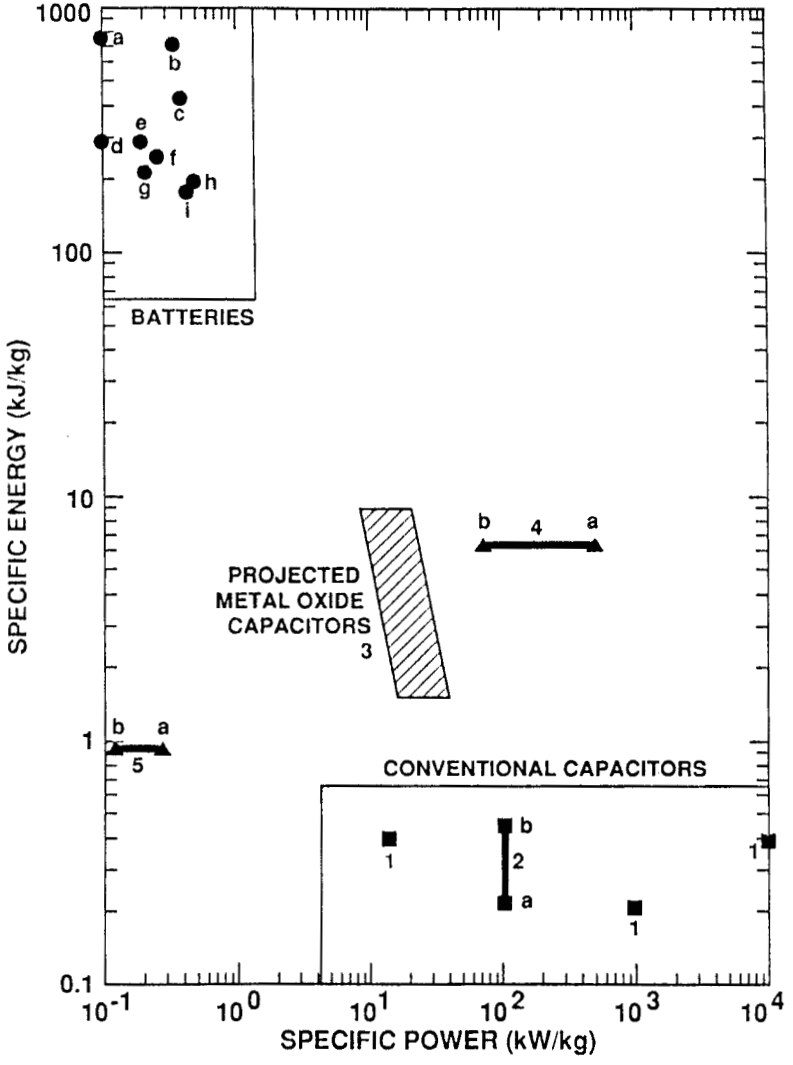

Figure 18. Specific energy vs. specific power for a number of batteries and capacitors. 1 = electrolytic capacitors (maximum power); 2 = Maxwell polycarbonate, with 2a = average energy at 1kHz repetition rate, 2b = single-shot energy density; 3 = projected RuO_2-based devices (see text); 4 = Pinnacle Ultracapacitor (110), 4a = maximum power, 4b = power at 1 msec ($\approx\tau/25$); 5 = Sohio Maxcap (46)(50) 5a = maximum power, 5b power at τ. Batteries (from Ref. 19): a = Li/MnO_2; b = Na/S; c = Ag/Zn; d = alkaline; e = Li/V_2O_5; f = Ni/Zn, g = Ni/Cd; h = Ni/H; i = Pb/H_2SO_4.

Eq. (23) $$P(t) = \frac{V^2}{R_L + R_i} \exp \frac{-2t}{C(R_L + R_i)}$$

In the absence of any information besides V and R_i, it is therefore possible to define a maximum power at zero time equal to V^2/R_i. Clearly, however, the time and load requirements should be matched to the properties of the capacitor (time $\sim \tau$, where $\tau = R_i C$, $R_L \sim R_i$) for efficient power transfer. V^2/R may be very large for a small capacitor, but if $t >> \tau$ then little useful power is available at times of interest. If weight and size are not critical then more power can be obtained by making $t < \tau$, i.e., by using a larger capacitor.

The average power delivered to time t

Eq. (24) $$\bar{P}(t) = 1/t \int_0^t P(t')\, dt'$$

is equal to

Eq. (25) $$\bar{P}(t) = \frac{V^2 C}{2t} \left[1 - \exp - \frac{2t}{C(R_L + R_i)}\right]$$

Significant quantities can be defined for P and $\bar{P}$ into matched loads ($R_i = R_L$), and at the time constant. In Fig. 18, the method for calculating the power is indicated where appropriate.

The specific energies and powers of a number of secondary battery systems are collected in the same figure. Their relatively large energy storage capability is a consequence of the fact that most batteries utilize *bulk* electrochemical reactions as their storage mode. Relatively few attempts have been made to optimize conventional batteries for power output, rather than energy storage. It is clear that by developing multicell, thin-layer, bipolar stacks, great improvements in battery power would be possible. The recent work of Lafollette (25) and Gibbard (109) illustrates the potential of this approach. Lafollette has reported power densities up to 800 kW/kg, for a bipolar lead-acid battery, and Gibbard has reported 75 kW/kg at 10 msec for a high temperature Li-Si/FeS_2 stack. Battery current density is, in some cases, limited by kinetic considerations (electrode kinetics, solid-state diffusion, or phase nucleation) and, in others, by ohmic losses caused by low electrolyte conductivity.

Conventional capacitors, on the other hand, have very low specific capacitances, and hence rely on a high cell potential difference to give them appreciable energy-storage capability. They are characterized by very high power output for short times. Their energy density is limited by dielectric breakdown. It seems that, even in systems specifically engineered for high energy content, a value of 0.5 J/cm^3 (or J/g) is difficult to achieve,

and values several times less than this are usual upper limits on energy density.

The properties of electrochemical capacitors should be intermediate between those of conventional capacitors and of batteries, both from an energy and power density point of view. In battery terms, bulk mass transport in the electrode structure is avoided by the confinement of chemical reactivity to a surface region. Surface electrosorption processes reduce the importance of electrode kinetics. (In the case of a pure double-layer process, of course, there is no kinetic component.) From a conventional capacitor perspective, electrochemical capacitors achieve high charge densities by using the equivalent of very large area plates. This last advantage is offset considerably by low operating voltages and high effective series resistances.

As may be seen from Fig. 18, commercial carbon-based electrochemical capacitors exhibit a relatively low energy density, approximately 1 to 2 J/cm^3 and less than 0.5 J/g. It should be remembered, however, that this is still several times greater than the energy density of most electrolytic capacitors. Further, the complications caused by distributed charging ensure a relatively low power density. (The value shown in the figure is the maximum power based on an esr measured at 1 kHz. In fact, as has been seen, most of the capacitance is accessed through a somewhat greater esr.) Carbon electrochemical capacitors, therefore, owe their commercial success, not to superior energy and power capability so much as to low cost, extremely high cyclability, and wide temperature range of operation. Because of their much higher operating cell voltage, the organic electrolyte-based carbon capacitors offer significantly higher energy densities.

In many respects, the use of metal oxides as active materials for electrochemical capacitors promises much improved performance over that of the carbon type. Particularly for applications in which fast response is important (e.g., pulse power, filtering), the high charge density in these materials means that thinner active layers are possible for the same overall capacitance. The main advantage of this is not in the associated improvements in energy density, but in the improved electrical response. As we saw in an earlier section, the effects of distributed charging are not completely eliminated in metal oxide capacitors, but they are significantly reduced compared with those in carbon capacitors.

Based on the small-signal response of RuO_2 capacitors, it is possible to estimate their performance, assuming that no *large-signal* problems arise (such as concentration polarization). In Fig. 18, a region of expected performance is shown for devices based on RuO_2. The calculation included measured pore resistance (based on the data in Ref. 74) and the weight of all materials except for the package. A factor of 2 - 3 reduction

in specific quantities might be expected if the packaging were included. The power densities are calculated at the capacitor time constant, for discharge into a matched load. It was assumed that bipolar plates would be constructed from 1 mil-thick Ti, and that the separator would also be 1 mil thick. A reduction in sulphuric acid conductivity of 50% was assumed to account for separator tortuosity.

Pinnacle Research Inc. has published performance data on metal oxide capacitors (of undisclosed composition) in which H_2SO_4 was used as the electrolyte (110). A 10-volt bipolar device, with an active electrode area of 2 cm^2, gave a volumetric energy density of 0.9 J/cm^3. Although this is comparable to presently available carbon electrochemical capacitors, the esr is significantly better at 30 mΩ per repeat, and the energy density of the active region (23 J/cm^3) indicates that the packaging of the device is not optimized. A prototype 20-kW device demonstrated some of the potential of this technology. It was an 84-volt package with 0.49 F capacity. The esr (at 1 kHz) was 50 mΩ. The energy density was 6.4 J/g and 20 J/cm^3. This result is quite close to estimates of projected metal oxide performance. The power densities quoted by Pinnacle are for a 1 msec pulse, whereas the actual time constant of the capacitor was closer to 25 msec. The power at the time constant would be significantly less than the 1 msec power level, as discussed above.

Conducting polymers offer a charge density similar to that of metal oxides. In addition, it seems possible that all-plastic, electrochemical capacitors may become a reality. A more detailed understanding of the kinetics of charging in both polymers and metal oxides is clearly desirable if their potential is to be realized.

From the point of view of future applications, it seems that, at the moment, the limiting feature of electrochemical capacitors is their poor frequency response. Good performance at 60 Hz would be an important achievement, opening up the area of compact power supply application for these devices.

8.0 ACKNOWLEDGEMENTS

The author would like to thank Thomas Springer (Los Alamos) for many contributions to the mathematical modelling aspects mentioned here, Ruth Sherman (Los Alamos) who gathered much experimental data on RuO_2, Judith Rishpon (University of Tel Aviv) who made the quartz crystal microbalance measurements of Fig. 14, and Bernard Boukamp (University of Twente) who has allowed the author to use his non-linear least-squared error fitting routines for impedance data analysis.

9.0 REFERENCES

1. Becker, H. I., U.S. Patent 2,800,616, July 23, (1957)

2. (a) Bockris, J. O'M., Devanathan, M. A. V. and Muller, K., *Proc. Roy. Soc.*, Ser. A 274, 55 (1963)
   (b) Bockris, J. O'M. and Reddy, A. K. N., *Modern Electrochemistry*, Plenum, New York (1970)

3. Martynov, G. A. and Salem, R. R., *Adv. Coll. Interface Sci.*, 22:229 (1985)

4. Craig, D. R., European Patent Application No. 78,404 A2, September 30 (1983)

5. McHardy, J., *Proc. IECEC.* 22:306 (1987)

6. McHardy, J., Ludwig, F. A., Higley, L. R., Kindler, A. and Townsend, C. W., U. S. Patent 4,766,522, August 23 (1988)

7. McHardy, J., in: *Proc. U. S. Army Workshop on Capacitors and Batteries for Pulse Power Applications,* Laboratory of the U. S. Army, LABCOM, Asbury Park, NJ, Nov. 17-18 (1987)

8. Grahame, D. C., *J. Electrochem. Soc.,* 99:370c (1952)

9. Langmuir, I., *J. Am. Chem. Soc.,* 40:1361 (1918)

10. Frumkin, A. N., *Z. Physik,* 35:792 (1926)

11. Temkin, M. I., *Zh. Fiz. Khim.,* 15:296 (1941)

12. Dolin, P. and Ershler, B., *Acta Physicochim.,* USSR 13:747 (1940)

13. Conway, B. E., Tellefsen, K. and Marshall, S., in: *The Chemistry and Physics of Electrocatalysis,* (J. D. E. McIntyre, M. J. Weaver, and E. B. Yaeger, eds.), Proceedings Vol. 84-12, p. 15. The Electrochemical Society, Pennington, NJ (1984)

14. Breiter, M., in: *Trans. Symp. on Electrode Processes,* (E. Yaeger, ed.), p. 307, John Wiley and Sons, New York (1961)

15. Iwakura, C., Kawai, T., Nojima, M. and Yoneyama, H., *J. Electrochem. Soc.,* 134:791 (1987)

16. (a) Neff, V. D., *J. Electrochem. Soc.,* 132:1382 (1985)
(b) Honda, K. and Hayashi, H., *J. Electrochem. Soc.,* 134:1330 (1987)

17. Calahan, J. L., Cuellar, E. A., Desmond, M. J. and Currie, J. C., U.S. Patent 4,633,372, December 30 (1986)

18. Kinoshita, K., *Carbon, Electrochemical and Physicochemical Properties,* John Wiley & Sons, New York (1988)

19. Desilvstro, J. and Haas, O., *J. Electrochem. Soc.,* 137:5c (1990)

20. Eichinger, G. and Besenhard, J. O., *J. Electroanal. Chem.,* 72:1 (1976)

21. Abraham, K. M., *J. Power Sources,* 7:1 (1981)

22. Newman, J. and Tobias, C. W., *J. Electrochem. Soc.,* 109:1183 (1962)

23. Newman, J. and Tiedermann, W., *AIChE Journal,* 21:25 (1975)

24. Newman, J., *Electrochemical Systems,* Prentice-Hall, Princeton, NJ (1973)

25. Lafollette, R. M., *Design Fundamentals of High Power Density, Pulsed Discharged, Lead Acid Batteries,* Ph. D. dissertation, Brigham Young University, Provo, Utah (1988)

26. de Levie, R., in: *Advances in Electrochemistry and Electrochemical Engineering,* (P. Delahay and C. W. Tobias, eds.), Vol. 6, p. 329, Interscience, New York (1967)

27. de Levie, R., *Electrochim. Acta,* 10:113 (1965)

28. Springer, T. E. and Raistrick, I. D., To be published

29. Keiser, H., Beccu, K. D. and Gutjahr, M. A., *Electrochim. Acta,* 21:539 (1976)

30. Macdonald, J. R., *J. Appl. Phys.,* 61:700 (1987)

31. Liu, S. H., *Phys. Rev. Lett.,* 55:529 (1985)

32. Nyikos, L. and Pajkossi, T., *Electrochim. Acta.,* 30:1533 (1985)

33. Nyikos, L. and Pajkossi, T. *Electrochim. Acta.,* 31:1347 (1986)

34. Wang, J. C., *Electrochim. Acta.,* 34:987 (1989)

35. Keddam, M. and Takenouti, H., *Electrochim. Acta,* 33:445 (1988)

36. Weppner, W. and Huggins, R. A., *J. Electrochem. Soc.,* 124:1569 (1977)

37. Ho, C., Raistrick, I. D. and Huggins, R. A., *J. Electrochem. Soc.,* 127:343 (1980)

38. Weppner, W. and Huggins, R. A., in *Annual Review of Materials Science,* (R. A. Huggins, ed.), Vol. 8, p. 269, Annual Reviews Inc., Palo Alto (1978)

39. Wen, C. J., Ho, C., Boukamp, B. A., Raistrick, I. D., Weppner, W. and Huggins, R. A., *Int. Met. Rev.,* 5:253 (1981)

40. Raistrick, I. D. and Huggins, R. A., *Solid State Ionics,* 7:213 (1982)

41. Glarum, S. H. and Marshall, J. H., *J. Electrochem. Soc.,* 127:1467 (1980)

42. Hunter, T. B., Tyler, P. S., Smyrl, W. H. and White, H. S., *J. Electrochem. Soc.,* 134:2198 (1987)

43. Gottesfeld, S., Redondo, A., Rubinstein, I. and Feldberg, S. W., *J. Electroanal. Chem.,* 265:15 (1989)

44. Glarum, S. H. and Marshall, J. H., *J. Electrochem. Soc.,* 129:535 (1982)

45. (a) Boos, D. L., U. S. Patent 3,536,963, Oct. 27, 1970
    (b) Boos, D. L., Adams, H. A., Hacha, T. H. and Metcalfe, J. E., in: *21st Electronics Component Conference,* p. 338, Washington, DC (1971)

46. (a) Currie, J. C., in: *Proc. U. S. Army Workshop on Capacitors and Batteries for Pulse Power Applications,* Laboratory of

the U. S. Army, LABCOM, Asbury Park, NJ, November 17-18 (1987)

(b) Currie, J. C., Boos, D. L., Gaylor, V. F. and Bennet, P. D., in: *The Chemistry and Physics of Composite Media,* (M. Tomkiewicz and P. N. Sen, eds.), Proceedings Vol. 85-8, The Electrochemical Society, Pennington, NJ (1985)

47. Watanabe, A., Mori, K., Ishikawa, H. and Nakamura, Y., *J. Electrochem. Soc.,* 134:1318 (1987)

48. Randin, J. P., in: *Encyclopedia of the Electrochemistry of the Elements,* Vol VII, (A. J. Bard, ed.), p1, Dekker, New York (1976)

49. Kinoshita, K., and Bett, J. A. S., *Carbon,* 11:403 (1973)

50. *Maxcap Double Layer Capacitor, Characteristics, Operation and Use,* Sohio Engineered Materials Company, Niagara Falls, NY (1985)

51. Marse, A. V., Bennett, P. D. and Boos, D. L., U.S. Patent 4,605,989, August 12 (1986)

52. Bennett, P. D. and Currie, J. C., Eur. Pat. Appl. 200,327, December 10 (1986)

53. Butherus, A. D. and Newby, K. R., U. S. Patent 3,700,975, October 24 (1972)

54. Besenhard, J. O. and Eichinger, G., *J. Electroanal. Chem.,* 68:1 (1976)

55. Yoshida, A., Tanahashi, I., Takeuchi, Y. and Nishino, A., *IEEE Trans. Components, Hybrids and Manufacturing Tech.,* 10:100 (1987)

56. Nawa, M., Nogami, T. and Mikawa, H., *J. Electrochem. Soc.,* 131:1457 (1984)

57. Yashima, H., Nogami, T. and Mikawa, J., *Synth. Metals,* 10:229 (1985)

58. Nogami, T., Mikawa, H. and Nawa, M., *J. Phys. (Paris),* 44:C3 (1983)

59. Raleigh, D. O., U.S. Patent 3,419,760, December 31 (1968)

60. (a) Bradley, J. N. and Greene, P. D., *Trans. Farad. Soc.*, 62:2069 (1966)
(b) Ibid. 63:424 (1967)
(c) Owens, B. B., and Argue, G. R., *Science*, 157:308 (1967)

61. Oxley, J. E., in: *Proc. 24th. Power Sources Conference*, p. 20 (1970)

62. Oxley, J. E., in: *Proc. U. S. Army Workshop on Capacitors and Batteries for Pulse Power Applications*, Laboratory of the U. S. Army, LABCOM, Asbury Park, NJ, November 17-18 (1987)

63. Portier, J., Reau, J. M., Sun, H. W., Tanguy, B., Astier, R., Cambie, C., Maurin, M., Pradel, A. and Ribes, M., *Fr. Demande*, 2594116:14 August (1987)

64. (a) Sekido, S. and Ninomiya, Y., *Solid State Ionics*, 3/4:153 (1981)
(b) Sekido, S., ibid. 9/10:777 (1983)
(c) *J. Electrochem. Soc.*, 126:1654 (1979)

65. Velasco, G., Colomban, P., Adet, P. and Pham, T. M., *Eur. Pat. Appl.*, 208:589, January 14 (1987)

66. (a) Xue, R. and Chen, L., *Solid State Ionics*. 18-19:1134 (1986)
(b) Matsushita Electric Industrial Co., Ltd. Japanese Patent 57/11139 B4, March 2 (1982)

67. Matsushita Electric Industrial Co., Ltd. Japanese Patent 57/14019 B4, March 20 (1982)

68. Lundsgaard, J. S., U. S. Patent 4,638,407, January 20 (1987)

69. Currie, J. C., Difranco, L. F. and Bennett, P. D., U.S. Patent 4,730,239, March 8 (1988)

70. Armand, M., in: *Ann. Rev. Mat. Sci.*, (R. A. Huggins, ed.), Vol. 16, p. 245, Annual Reviews Inc., Palo Alto (1986)

71. Scrosati, B., *J. Electrochem. Soc.*, 136:2774 (1989)

72. See, for example:
Beer, H. B., U. S. Patent 3,632,498, January 4 (1972)

73. (a) Trasatti, S., in: *Electrodes of Conductive Metal Oxides (Part B)* (S. Trasatti, ed.), Elsevier/North Holland, New York (1981)
(b) Daghetti, A.. Lodi, G. and Trasatti, S., *Mat. Chem. Physics,* 8:1 (1983)
(c) Trasatti, S., and O'Grady, W. E., in: *Advances in Electrochemistry and Electrochemical Engineering,* (H. Gerischer and C. W. Tobias, eds.), 12, p177, Wiley, New York (1981)

74. (a) Raistrick, I. D. and Sherman, R. J., in: *Proceedings of the Symposium on Materials and Processes for Energy Conversion and Storage,* (S. Srinivasan, S. Wagner and H. Wroblowa, eds.), Proc. Vol. 87-12, The Electrochemical Society, Pennington, NJ (1987)
(b) Raistrick, I. D., Beery, J. G. and Sherman, R. J., in: *Proceedings of the Symposium on Electroceramics and Solid-State Ionics,* (H. L. Tuller and D. M. Smyth, eds.), Proc. Vol. 88-3, The Electrochemical Society, Pennington, NJ (1988)

75. Buttry, D. and Gottesfeld, S., *Electrochem. Soc. Ext. Abstracts,* Abstract No. 1404, Honolulu Mtg (1987)

76. Raistrick, I. D. and Rishpon, J., unpublished work

77. Burke, L. D., Murphy, O. J., O'Neill, J. F. and Venkatesan, S., *J. Chem. Soc. Faraday Trans.,* 1:73 (1977)

78. Furlong, D. N., Yates, D. E. and Healy, T. W., in: *Electrodes of Conductive Metal Oxides (Part B),* (S. Trasatti, ed.), Chapter 8, Elsevier/North Holland, New York (1981)

79. Rishpon, J. and Gottesfeld, S., *J. Electrochem. Soc.,* 131:1960 (1984)

80. Abraham, P. and Rajeshwar, K. (To be published.)

81. Aurian-Blajeni, B., Boucher, M. M., Kimball, A. G. and Roblee, L. S., *J. Mat. Res.,* 4:440 (1989)

82. Gottesfeld, S., *J. Electrochem. Soc.,* 126:742 (1979)

83. Kang, K. S. and Shay, J. L., *J. Electrochem. Soc.*, 130:766 (1983)

84. Burke, L. D. and Whelan, D. P., *J. Electroanal. Chem.*, 103:179 (1979)

85. Burke, L. D. and Whelan, D. P., *J. Electroanal. Chem.*, 109:385 (1980)

86. Burke, L. D. and O'Sullivan, E. J. M., *J. Electroanal. Chem.*, 93:11 (1978)

87. Burke, L. D. and Murphy, O. J., *J. Electroanal. Chem.*, 109:373 (1980)

88. Hepel, T., Pollack, F. H. and O'Grady, W. E., *J. Electrochem. Soc.*, 132:2385 (1985)

89. Michell, D., Rand, D. A. J. and Woods, R., *J. Electroanal. Chem.*, 84:117 (1977)

90. McIntyre, J. D. E., Basu, S., Peck, W. F., Brown, W. L. and Augustyniak, W. M., *Phys. Rev.*, B25:7242 (1982)

91. Pickup, R. and Birss, V., *J. Electroanal. Chem.*, 240:171 (1988)

92. Elliot, W. E. and Huff, J. R., U. S. Patent 3,317,349, May 2 (1967)

93. Rauh, D., in: *Proc. U. S. Army Workshop on Capacitors and Batteries for Pulse Power Applications,* Laboratory of the U. S. Army, LABCOM, Asbury Park, NJ, November 17-18 (1987)

94. See for example:
    (a) Synth. Metals 28 (1989)
    (b) *Proceedings of the International Conference on Sci. and Techn. of Synthetic Metals,* Santa Fe, NM, June 26-July 2 (1988)

95. Chiang, C. K., *Polym. Comm.*, 22:1454 (1981)

96. Nagatomo, T., Ichikawa, C., and Omoto, O., *J. Electrochem. Soc.*, 134:305 (1987)

97. Feldhues, M., Kampf, G., Litterer, H., Mecklenberg, T. and Wegener, P., *Synth. Met.*, 28:C487 (1989)

98. *Electronic Properties of Conjugated Polymers,* Springer Ser. in Solid State Sciences, (H. Kuzmany, M. Mehring, and S. Roth, eds.), Springer Verlag, Berlin (1987)

99. MacDairmid, A. G. and Kaner, R. B., in: *Handbook of Conducting Polymers,* (T. A. Skotheim, ed.), Volume 1, p. 689, Marcel Dekker, New York (1986)

100. Shirakawa, H. and Ikeda, S., *J. Polym.,* 2:231 (1971)

101. Naarman, H. and Theolon, N., *Synth. Met.,* 22:1 (1987)

102. Genies, E., Hany, P. and Santier, C., *Synth. Met.,* 28:C647 (1989)

103. Gottesfeld, S., Redondo, A., and Feldberg, S. W., *Electrochemical Soc. Extended Abstracts,* No. 507, San Diego, CA (1986)

104. Glarum, S. and Marshall, J., *J. Electrochem. Soc.,* 134:2160 (1987)

105. Asavapiriyanony, S., Chandler, G. K., Gunawardena, G. A. and Pletcher, D., *J. Electroanal. Chem.,* 177:229 (1984)

106. Feldberg, S., *J. Amer. Chem. Soc.,* 106:4671 (1984)

107. Rubinstein, I., *J. Electrochem. Soc.,* 134:3078 (1987)

108. Jow, T. R., and Shacklette, L. W., *J. Electrochem. Soc.,* 135:541 (1988)

109. Gibbard, F., in: *Proceedings of the Symposium on Electrochemical and Thermal Modelling of Battery, Fuel Cell and Photoenergy Conversion Systems,* (J. R. Selman and H. C. Maru, eds.), Proc. Vol. 86-12, p. 193, The Electrochemical Society, Pennington, NJ (1986)

110. Tong, R. R., Mason, G. E., Lee, H. L., Bullard, G. L., in: *Proc. 34th. Power Sources Symposium* (1988)

INDEX